UNIVERSITY OF SOUTHAMPTON

FACULTY OF ENGINEERING AND THE ENVIRONMENT

INSTITUTE OF SOUND AND VIBRATION RESEARCH

Airfoil noise reduction by edge treatments

by

Mathieu Gruber

Thesis for the degree of Doctor of Philosophy

February 2012

UNIVERSITY OF SOUTHAMPTON

ABSTRACT

FACULTY OF ENGINEERING AND THE ENVIRONMENT
INSTITUTE OF SOUND AND VIBRATION RESEARCH

Doctor of Philosophy

Airfoil noise reduction by edge treatments

by Mathieu Gruber

The general aim of this thesis is to investigate experimentally airfoil trailing edge noise reduction using various trailing edge geometries. The work presented in this thesis is part of the FP7 European Project FLOCON. This thesis focuses on sawtooth serrations and a detailed study is conducted in which thirty seven sawtooth trailing edges are tested for reducing the noise at various flow velocities and angles of attack. Broadband noise reductions of up to 5 dB are obtained below some critical frequency above which the noise is increased. The mechanisms by which the noise is changed in the presence of sawtooth serrations are also investigated experimentally by measuring the changes introduced in the unsteady surface pressure near the edge, the turbulence in the boundary layer and in the near wake, and also using Howe's model [66] as a reference for comparisons. Generally, it is shown that noise reductions occur due to an attenuation of the interaction between incident and scattered pressures, which results in a decrease of up to a half of the phase speed along the edges compared with the corresponding straight edge. The noise increase is shown to be caused by a cross-flow being forced through the valleys of the serrations by the pressure difference between the two sides of the airfoil near the trailing edge.

Four novel trailing edge geometries are also tested to address the high frequency noise increase observed with sawtooth serrations. These are the slits, the sawtooth with holes, the slitted sawtooth and the random trailing edges. The slitted sawtooth are shown to provide a good alternative to sawtooth serrations, and afford similar levels of noise reductions while limiting the high frequency noise increase to no more than 1 dB. Random trailing edges also show reasonable levels of broadband noise reductions of up to 3 dB and no increase at high frequencies.

Finally, serrations are used simultaneously at the trailing edge of an upstream airfoil and at the leading edge of a downstream airfoil to reduce trailing edge noise and interaction noise of the airfoils in a tandem configuration. Broadband reductions of up to 8.5 dB are obtained using the slitted sawtooth trailing edge and the leading edge serrations designed by ONERA. It is shown that most of the noise reduction is provided by a reduction of the airfoil leading edge response due to the leading edge serrations, but that sawtooth slitted serrations provide up to about 3.5 dB additional broadband noise reductions due to a reduction in its wake turbulence.

Contents

List of Figures

List of Tables

Declaration Of Authorship

I, MATHIEU GRUBER, declare that this thesis entitled ‘Airfoil noise reduction by edge treatments’ and the work presented in it are my own and have been generated by me as the result of my own original research. I confirm that:

1. This work was done wholly or mainly while in candidature for a research degree at this University;

2. Where any part of this thesis has previously been submitted for a degree or any other qualification at this University or any other institution, this has been clearly stated;

3. Where I have consulted the published work of others, this is always clearly attributed;

4. Where I have quoted from the work of others, the source is always given. With the exception of such quotations, this thesis is entirely my own work;

5. I have acknowledged all main sources of help;

6. Where the thesis is based on work done by myself jointly with others, I have made clear exactly what was done by others and what I have contributed myself;

7. Either none of this work has been published before submission, or parts of this work have been published as:

- M. Gruber, P. Joseph, and TP. Chong: '*Experimental investigation of airfoil self noise and turbulent wake reduction by the use of trailing edge serrations.*', In 16th AIAA/CEAS Aeroacoustics Conference, 2010.
- M. Gruber, M. Azarpeyvand, and P. Joseph: '*Airfoil trailing edge noise reduction by the introduction of sawtooth and slitted trailing edge geometries.*', In 20th ICA conference, 2010.
- M. Gruber, P. Joseph, and TP. Chong: '*On the mechanisms of serrated airfoil trailing edge noise reduction.*' In 17th AIAA/CEAS Aeroacoustics Conference, 2011.

Signed:..

Date:...

Acknowledgments

I would like to thank my supervisor Phillip Joseph for giving me the opportunity to work with him and for his contribution to this thesis. Phil, I am very grateful for all the insightful suggestions, discussions, advice, guidance and most of all for your constant availability throughout my PhD. Thank you also for your positive attitude and for the good laughs.

I would also like to thank Gwénaël Gabard and Keith Holland for their very useful input as internal examiners during the annual reviews.

This work was funded by the European Commission, FP7 project FLOCON and by Rolls Royce plc through the University of Technology Centre in Gas Turbine Noise in the ISVR.

I would also like to acknowledge Cyril Polacsek from ONERA and Constantin Sandu from SM-CPFA for kindly lending their airfoils for the tandem tests presented in Chapter 7.

Special thanks to Claire Relun and Sawitri Tiavonksombat who greatly participated to the beamforming experiments and the wall jet test presented in Chapters 2 and 5, respectively.

I would like to thank Sue Brindle for taking care of all the administrative paper work and issues. I also want to thank Phil Oxborrow, Chris Oliver, Steve White and Mike Street for the good laughs and their very useful insights into the design and manufacturing of most of the equipment used in this thesis and for responding so fast to last minute requests!

Thank you to all my colleagues at ISVR, who for many became very good friends, for the interesting discussions in the office and of course in the pub.

I would like to thank all my friends, my family and especially my parents who have given me great support for the past 10 years.

Finally, thank you Helen for putting up with late night and week ends of work during these three years, and for finding the right words to bring the motivation back. I will also be forever grateful for all the house chores that you did in the last 6 months without which this thesis would not have happened! Most of all thank you for being at my side at all times and for being so special to me.

Nomenclature

f	frequency vector [Hz]
c_0	speed of sound [m/s]
$k = \omega/c_0$	acoustic wave number [m^{-1}]
U_0	mean flow velocity [m/s]
U_c	convection velocity [m/s]
U_{ph}	phase velocity [m/s]
c	airfoil chord [m]
L	length of trailing edge wetted by the flow [m]
M	Mach number
$2h$	amplitude of sawtooth [m]
λ	spatial periodicity of sawtooth [m]
St_δ	$St_\delta = f\delta/U_0$
$\overline{u'^2}$	mean square unsteady velocity [$(\mathrm{m/s})^2$]
TI	streamwise turbulence intensity $TI = \sqrt{\overline{u'^2}}/U_0$
$\mathbf{x}$	observer location
(x, y, z)	airfoil Cartesian coordinates
(X, Y, Z)	open-jet Cartesian coordinates
τ	time lag [s]
$R_{uu}(x, y, \tau)$	instantaneous velocity auto-correlation
$\mathbf{k}$	turbulence wave number vector
(k_x, k_y, k_z)	turbulence wave number components
$k_x = \omega/U_0$	freestream wave number component [m^{-1}]
k_y	spanwise wave number component [m^{-1}]
k_z	$k_z = 0$
$l_y(\omega)$	spanwise correlation length $l_y(\omega) = b_c U_c/\omega$ [m]
Re_c	chord based Reynolds number
C_p	static pressure coefficient
C_d	drag coefficient
C_L	lift coefficient

Greek letters

$\omega = 2\pi f$	$\omega = 2\pi f$ [rad/Hz]
α_g	geometrical angle of attack [^{o}]
α_e	effective angle of attack[^{o}]
α_s	angle of the sawtooth edge to the flow direction [^{o}]
ρ	air density [$\mathrm{kg.m}^{-3}$]

δ	turbulent boundary layer thickness [m]
δ^*	turbulent boundary layer displacement thickness [m]
Λ_{uu}	freestream turbulent length scale [m]
ϕ_{pp}	far field acoustic spectral density [$\mathrm{Pa}^2/\mathrm{Hz}$]
ϕ_{qq}	unsteady surface pressure spectral density [$\mathrm{Pa}^2/\mathrm{Hz}$]
η_x	streamwise sensor separation distance [m]
η_y	spanwise sensor separation distance [m]

Abbreviations

AoA	Angle of Attack
DNS	Direct Numerical Simulation
CFD	Computational Fluid Dynamics
TKE	Turbulent Kinetic Energy
RANS	Reynolds Averaged Navier Stokes
WPS	Wall Pressure Spectrum
LE	Leading Edge
TE	Trailing Edge
PWL	sound PoWer Level spectrum [dB/Hz]
SPL	Sound Pressure Level spectrum [dB/Hz]
OAPWL	OverAll PoWer Level [dB]

Symbols

$(.)_{\mathbf{b}}$	quantity expressed for the baseline straight edge airfoil
$(.)_{\mathbf{s}}$	quantity expressed for the serrated airfoil

Chapter 1

Introduction

1.1 Context and aim

The expanding network of transportation and the use of new sources of energy other than fossils have transformed society over the past century. With an increasing demand due to the growth of the population in modern society, regulations on environmental pollution arise continuously and become more and more strict, especially in terms of fuel emissions and noise. The aircraft industry, for example, is a growing market and the air traffic demand is predicted to nearly triple by 2030, with an increase of 5 % per year in civil aviation and about 6 % in military [116]. In addition, a constant effort has been ongoing for the past 50 years to research and exploit renewable and more environmentally friendly sources of energy supplies, such as wind power. On-shore and off-shore wind turbine farms are consequently expected to approximately double by 2030 and triple by 2050 [3]. The noise pollution is a particular concern for communities living nearby airports and wind turbine farms.

Aircraft noise is of main concern at the take-off and landing stages. It is generated through the interaction of the aircraft body with the air, the landing gears and most importantly the engines, amongst which the various dominant sources are the fan, the jet and the compressor. Fan noise has been identified as an aerodynamic source of tonal and broadband noise. Tonal fan noise mainly results from the interaction of the wakes and tip vortices shed from the rotor with the stator blades of the fan OGV. Broadband fan noise is mainly due to the interaction of incoming turbulence with the leading edge of the blades, i.e., airfoil leading edge (LE) noise and the interaction of the boundary layer with the airfoil trailing edge, i.e., airfoil trailing edge (TE) noise. Airfoil TE noise is also believed to be the dominant source of broadband noise on wind turbines.

The work described in this thesis was undertaken as part of the FP7 European project FLOCON [1], which aims at reducing fan broadband noise using adaptive and passive FLOw CONtrol methods. The work presented in this thesis is focused on investigating the TE noise reduction achievable using serrated edges and novel geometries located at the trailing edge. Particular attention is given to sawtooth serrations as a means of reducing airfoil TE noise and the understanding of the noise mechanisms involved in the noise reduction process. The study is conducted experimentally in the open-jet anechoic wind tunnel in the ISVR.

1.2 Literature review

This Section contains a review of trailing edge noise reduction using passive treatments. A brief history of the research conducted on trailing edge analytical and semi-empirical noise predictions is first presented.

1.2.1 Airfoil TE noise

Airfoil self noise refers to the noise radiation resulting from the interaction of the flow structures with the airfoil trailing edge. As shown by Brooks *et al* [19], five mechanisms of self noise can be defined:

- Turbulent boundary layer trailing edge noise
- Laminar boundary layer vortex shedding
- Separation stall noise
- Trailing edge bluntness - vortex shedding noise
- Tip vortex noise

The current study focuses on the scattering of the boundary layer turbulence structures into sound by the edge discontinuity. As mentioned by Brooks *et al* [19] the noise radiation can be tonal due to instabilities developing in a laminar boundary layer (and to vortex shedding), or broadband if the boundary layer is turbulent and the boundary layer flow remains attached.

Turbulent boundary layer trailing edge noise is investigated in this thesis. It has been extensively researched by many scientists and detailed reviews have been published (see Howe [62], Roger [97, 98], Rozenberg [100]). Powell [95] in 1959 first presented an experimental and analytical study of trailing edge self noise. Further fundamental work has been presented by Ffowcs Williams and Hall [117] and Chase [24] amongst others.

Brooks [18] published an extensive database of measured airfoil trailing edge noise on a NACA0012 airfoil. Later, the measured surface pressure spectra were used to predict the far field noise radiation [19]. Amiet [7] and Howe [62, 68] proposed an analytical radiation model for the interaction of a turbulent boundary layer convected past a semi-infinite rigid flat plate at 0^{o} incidence in a subsonic flow. These two models mainly differ in the way the aerodynamic near field is related to the acoustic radiation. Both lead to the following similar conclusion that the sound radiated in the far field follows a velocity power law of U^5 for the pressure density spectrum, as introduced by Ffowcs Williams & Hall [117] in 1970. Both models are valid for acoustic wavelength smaller than the airfoil chord (due to the semi-infinite flat plate assumption). Amiet's model is valid for all subsonic flows while Howe's model is valid for very low Mach numbers only.

Amiet's model [7] is used in this thesis to validate the accuracy of measurement of trailing edge noise on the isolated baseline NACA65(12)-10 airfoil in the ISVR's open-jet wind tunnel (see Chapters 2 and 3) and is therefore shortly reviewed below.

Amiet's model

Amiet [7, 8] proposed a semi-analytical model for calculating the broadband far field noise radiation from a single airfoil in a 'clean' uniform flow due to a turbulent boundary layer convecting over the trailing edge. The statistical properties of the turbulent boundary layer are assumed to remain unchanged at the trailing edge and upstream of the trailing edge (frozen turbulence), i.e., the pressure in the boundary layer is assumed to be unaffected by the edge discontinuity. The difference in unsteady pressure across the airfoil due to the response of the airfoil surface to the incident pressure fluctuations close to the trailing edge region is equivalent to a distribution of dipole sources over the airfoil. Practically, this assumption allows using measurements of the unsteady incident wall pressure spectrum in the boundary layer as an input to Amiet's trailing edge noise model.

Therefore, the fluctuating pressure in the boundary layer of the airfoil close to the trailing edge $\phi_{qq}(\omega)$ is related to the far field noise characteristics $\phi_{pp}(\omega)$, where $\phi(\omega)$ defines the pressure spectrum density. Equation 1.1 shows that Amiet's model requires the spanwise correlation length l_y as a factor that quantifies the coherence between turbulent structures close to the trailing edge. The terms $D(\mathbf{x},\omega)$ and $\mathcal{L}(\omega)$ are, respectively, a dipole type radiation function to the observer location $\mathbf{x}$ and the acoustically weighted airfoil response function that quantifies the unsteady load over the blade.

$$\phi_{pp}(\mathbf{x},\omega) = D(\mathbf{x},\omega)\ |\mathcal{L}(\omega)|^2\ l_y(\omega)\ \phi_{qq}(\omega) \tag{1.1}$$

Roger and Moreau [98, 84] have more recently proposed an extension of Amiet's model for predicting airfoil trailing edge noise. The extended model includes a leading edge back-scattering correction, which takes into account the effect of the finite chord. When the turbulent structures are scattered at the trailing edge, acoustic waves propagate upstream of the flow. Back-scattered waves from the trailing edge are then scattered again at the leading edge of the airfoil. The effect of the back-scattering process can be up to a few dB and is mainly low frequency.

Roger and Moreau also assume that, as suggested by Zhou and Joseph [122], the Kutta condition is applied on the total pressure difference between the airfoil suction and pressure sides, while it is applied only to the scattered pressure in Amiet's model. The resultant pressure difference is zero in the extended model while is equal to half of the incident pressure on one side in the original model. It was also generally found that Amiet's original model consistently under predicts by 6 dB the radiated sound measured during wind tunnel tests while the extended model presents much better agreements.

It is shown in the second part of Roger and Moreau's analysis [84] that the infinite span assumption, i.e, as in Equation 1.1, is only valid for airfoil aspect ratios of at least 3 (errors on the far field pressure smaller than 1 dB). Hence, the simplified expression of the far field noise radiation is generally to be used for comparison with wind tunnel experiments. The full expression is to be considered while dealing with rotating fan and splitting the blades into segments to account for the variation of the chord and of the boundary layer pressure statistics with the blade span.

In this thesis, Amiet's model (see Equation 1.1), which assumes infinite span and does not account for the leading edge back scattering, is used to validate the noise measurements made on an airfoil with aspect ratio equal to 3. The surface pressure spectra are measured close to the trailing edge and used as an input into Amiet's prediction model. Amiet's correction for the incident pressure [8] and for the refraction of the acoustic waves through the shear layer of the open-jet wind tunnel [9] are also applied.

1.2.2 Airfoil trailing noise reduction

Airfoil trailing edge noise reduction has been investigated since the 1970's, mostly through experimental or numerical work, as reviewed in Section 1.2.2.1. Howe [65, 66] proposed a radiation model to predict the noise reduction obtained using sawtooth serrations on an infinite flat plate, as described in Section 1.2.2.2.

1.2.2.1 Biomimetics and the design of novel trailing edges

The study of the phenomena that occur in nature have often led scientists to new ideas and the engineering of new technologies. Biomimetics is defined as the study of the structure and function of biological systems as models for the design and engineering of materials and machines. In the context of this study and of fluid dynamics, the silent flight of the owl was first investigated in 1934 by Graham [53], in the early 1970's by Kroeger [75] as part of a program researching novel designs for quieter aircrafts, Lilley [79] and also more recently by Bachmann [10] and Klan [74]. An in-depth study of the structure of the wing showed that, through millions of years of evolution, the owl has developed wavy comb-type leading edges (or serrations) and fringe type trailing edges that generate noise under 2 kHz, while their preys acute hearing system is typically within the range 2 to 20 kHz. Bachmann [10] provided detailed pictures of the wing structure shown in Figure 1.1 where the leading edge and trailing edge features are highlighted.

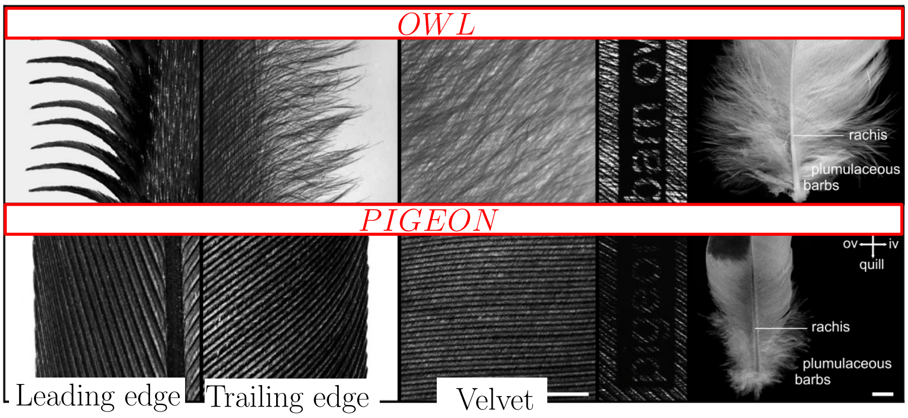

Figure 1.1: Structure of the Owl's wing compared to that of a pigeon of similar size and weight (From Bachmann *et al* [10]).

Kroeger and Lilley also showed that the leading edge serrations on the owl wing completely suppressed the separation of the flow that would normally occur along a steep downwards flight path of 24^o at the low Reynolds number of about 1.5×10^5. Instead, vortices are shed from each serration and the boundary layer remains attached, even when the wing dynamics approach stall, therefore providing noise reductions of up to about 20 dB. When the leading edge comb structure was removed, the flight of the owl became unstable and as noisy as any other bird.

In addition, the fringes at the wing trailing edge provide a smooth mixing of the upper and lower boundary layer and reduce the scattering by the edge discontinuity. Lilley associated a reduction of about 6-7 dB due to the trailing edge fringes only, by comparison with noise measurements performed on a bird of similar size and mass.

Lilley also attributes the very low noise emission at frequencies above 2 kHz to an absorption of the boundary layer energy by the compliant surface covering the upper wing and the paws of the owl, due to a fluffy fibrous material whose fibres are only slightly larger than the Kolmogorov length scales.

Trailing edge serrations

In view of the growing aircraft industry in the early 1990's and of the development of wind farms later, researchers started addressing the airfoil trailing edge noise problem using passive treatments such as serrations, brushes and porous trailing edges.

As presented by, for example, Dassen *et al* [36] in 1996 and Parchen *et al* [92] in 1999, serrated edges have been used as means of reducing trailing edge self noise in airfoil wind tunnel tests and for wind turbine applications, in Oerlemans *et al* [88]. All of these studies have consistently showed noise reductions of up to 5 dB over large frequency bands but an increase of noise at higher frequencies.

Dassen *et al* [36] experimentally investigated airfoil trailing edge noise reductions using serrations. Eight airfoils and six flat plates of 250 mm chord length with different geometries were tested in a wind tunnel. Although no noise spectra were provided, the experiments revealed that the serrated flat plates lead to noise reductions of up to 10 dB from 1 to 6 kHz, while serrated airfoils showed reductions of up to 8 dB. Various implementations of the serrations at the trailing were tested on the flat plates, as shown in Figure 1.2, and no significant effect greater than 2 dB, is reported except for a misalignment of the sawteeth with the flow direction of 15^o where the noise was increased on a flat plate at high frequencies (see flat plate labeled FP 2_15 in Figure 1.2).

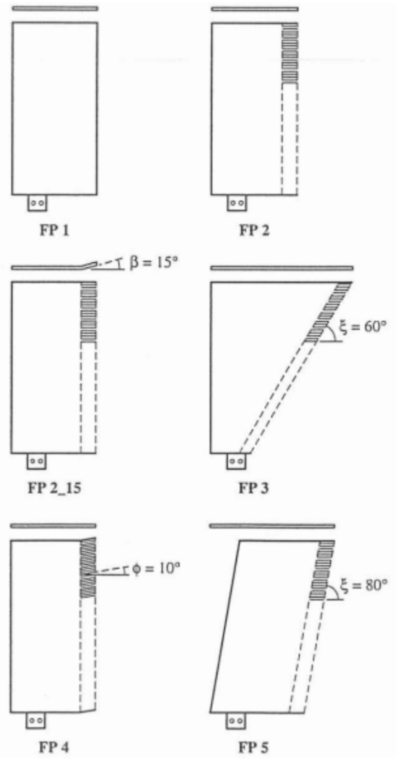

Figure 1.2: Survey of serrated flat plates (From Dassen *et al* [36]).

An extensive detailed study of noise reduction on wind turbines was conducted as part of the project STENO (Serrated Trailing Edge NOise), which aimed at verifying the transfer of the noise reduction performance obtained on a 2D airfoil in a wind tunnel [36] to a 3D, full scale wind turbine. Serrations were applied to the wind turbine blade trailing edge in order to determine the effect of length, position and orientation of the teeth on the noise reductions. This study also included small scale experiments in which it was found that serrations gave an overall reduction of 2 dB at low frequencies while increasing the noise at high frequencies and at high incidence angles of attack. In 1999, Parchen *et al* [92] carried out experiments using serrated trailing edges in order to compare results with Howe's theory [65, 66]. Serrations were applied to both wind tunnel-scale, and full-scale wind turbines. Broadband noise reductions of about 6 dB were achieved. This measurement confirmed that Howe's theoretical model predicted a much larger noise reduction compared to measured values. In addition, it was reported that in the full-scale measurements, noise increases were found for misaligned serrations with respect to the jet direction. However, it will be shown in Chapter 4 that this noise increase occurs at all angles of attack.

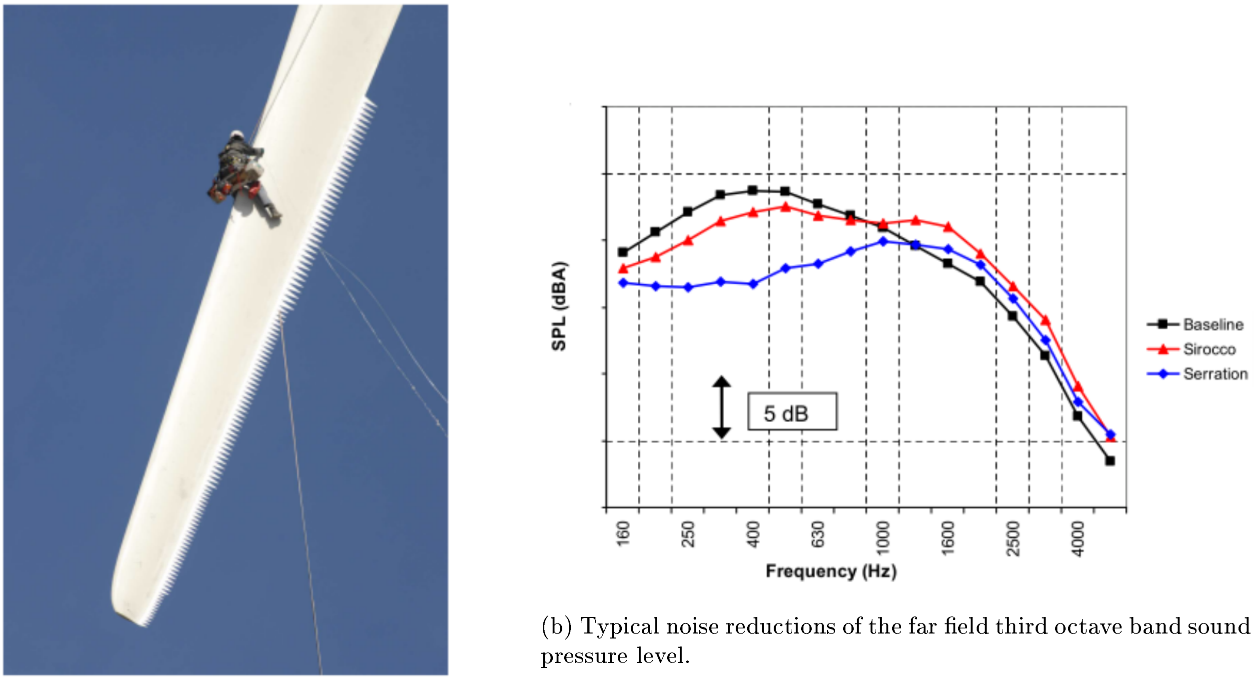

(a) Serrations on the full scale wind turbine.

(b) Typical noise reductions of the far field third octave band sound pressure level.

Figure 1.3: Results of the noise reduction study conducted on a full scale wind turbine using sawtooth serrations (From Oerlemans *et al* [88]).

Oerlemans *et al* [88] investigated the use of serrations and airfoil shape optimization to reduce trailing edge noise. As shown in Figure 1.3a, experiments were conducted on a 94 m diameter, three bladed wind turbine and in an open-jet wind tunnel. A NACA-64418 airfoil model was selected as the reference blade because of its common use in modern wind turbines. One blade was optimized for aerodynamics, one blade for trailing edge noise reduction with serrations along the span, and one blade remained untreated and was used as the reference blade. The optimized airfoil showed an overall trailing edge noise reduction of 3.2 dB and gave a maximum noise reduction of 5 dB up to 1 kHz. Serrations showed further reductions of about 2-3 dB. Despite the noise reduction at low frequencies, a significant high frequency noise increase was also reported and was attributed to a misalignment of the serrations with the flow (see Figure 1.3b).

In 2004, an experimental study into serrated trailing edges on an airfoil was conducted by Herr [60]. She introduced various configurations of brushes at the airfoil trailing edge. Various fibre diameters, separation distance between fibres and lengths of brushes were tested in wind tunnel experiments. Noise reductions of between 2 to 10 dB over large frequency bands occurred, notably due to the suppression of vortex shedding from the blunt baseline trailing edge. The greatest noise reductions were achieved with the thickest trailing edge brush. Herr suggests that this reduction may be caused by viscous damping of unsteady turbulent velocities in the brush region. This trailing edge treatment is similar to the fringes attached to the owl's trailing edge wing, which provide a smooth mixing between the boundary layer pressures from both the pressure and suction sides of the airfoil.

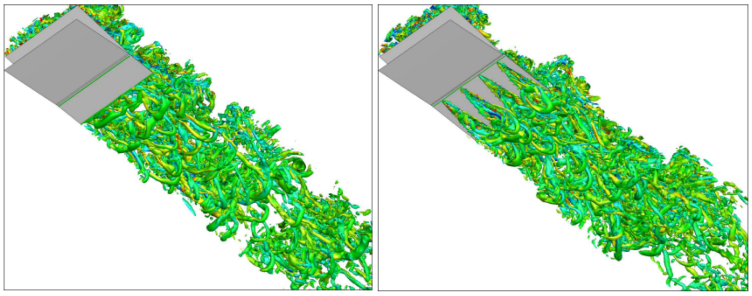

Figure 1.4: Iso-contours of Q = 100 coloured by streamwise vorticity for the straight edge (left) and the long serrated TE (right) (From Jones *et al* [71]).

Herr [59] also reported measurements performed using a single row of fibres and of slit type trailing edges, where two critical parameters were introduced to achieve noise reduction. First, the length of the fibres were required to be at least the boundary thickness or larger. In addition, the fibre diameter and separation distance between fibres is required to be as close as possible to the inner scales in the turbulent boundary layer, typically $< 0.1\,mm$. Finez *et al* [41] also conducted a similar experimental study in ECL's open-jet wind tunnel using a single row of trailing edge brushes. In addition to significant broadband reductions of up to 3 dB, space-time correlation measurements of the velocity in the wake were performed behind the brushes and showed a decrease of up to 25 % of the spanwise correlation length in the trailing edge region.

As shown in Figure 1.4, Jones *et al* [71] performed Direct Numerical Simulations of the flow around a NACA0012 airfoil fitted in turn with a straight edge, a short serration of amplitude similar to the boundary layer thickness δ, and a long serration of amplitude about 2δ, at Reynolds number $Re_c = 50,000$ and $M = 0.4$. Broadband noise reductions of between 6 to 10 dB were obtained, and it was found that the noise reduction was greater for the long serrations and spread over a larger frequency bandwidth. For the shorter serration only, an increase of the noise was observed at high frequencies. The TE noise directivity was not affected by the presence of the serrated TE. The boundary layer properties were found to be little affected by the presence of the serrations and the formation of horse-shoe vortices was reported to occur behind the serrations, promoting a faster mixing of the turbulence in the airfoil wake.

Geiger [47] has investigated the changes in the blade steady loading and in the mean and turbulent wake behind two serrated trailing edges of amplitude $2h = 12.7\,mm$ and $2h = 25.4\,mm$. The steady loading, measured using static pressure taps distributed over the airfoil surface showed differences smaller than 9 % over the whole airfoil body, and almost non existent changes close to the airfoil trailing edge compared to a straight TE. The drag was not investigated in this study. Measurements of the mean and unsteady velocity in the wake were conducted using hot wire anemometry and revealed that:

- The width of the wake is increased in the presence of serrations, and further increased when the amplitude of the sawtooth is increased.

- The maximum velocity deficit at the wake centre-line is decreased as the sawtooth amplitude increases.
- The vorticity in the near wake is increased, resulting in a faster mixing of the turbulence and the levels of turbulent kinetic energy (TKE) are reduced compared to a straight trailing edge when $x/c > 1$, where c is the airfoil chord and $x = 0$ is at the airfoil trailing edge.
- The rate at which the velocity at the wake centre-line decays with downstream distance is faster than with a straight trailing edge behind the tip of the sawtooth but slower behind the root of the sawtooth.
- The spreading of the wake is larger behind the root and smaller behind the tip of the sawtooth, in comparison with a straight trailing edge.
- The production of TKE is dominant behind the tip of the serrations at the trailing edge.

Porous trailing edges

With the objective of reducing airframe noise, Fink *et al* [43] reported noise reductions of up to 2 to 3 dB using porous materials at the trailing edge of a slat and at the trailing edge of a flap. However, no detailed study or optimization of the flow permeability across the trailing edge were performed.

Howe [63] suggested that trailing edge noise attenuation was possible by modifying the impedance properties of the trailing edge, and showed analytically that reductions of 10 dB or more were achievable. Howe also reported that the properties of the material should be of variable porosity so that the impedance of the surface becomes progressively softer as the turbulent eddies approach the edge.

Geyer [48, 49] measured broadband trailing edge noise reductions of up to about 10 dB using porous airfoils on a semi-symmetrical SD7003 profile with a chord length of $0.235\,m$ and a span of $0.4\,m$. Sixteen porous materials with different flow resistivity were used and noise measurements were compared to a non-porous solid airfoil. Noise reductions of about 10 to 20 dB were obtained but it was found that the lift decreased and the drag increased significantly as the flow resistivity was decreased, therefore providing little insight into the noise reduction due to the porous material at identical blade loading. An increase of the noise was also reported at high frequencies and attributed to surface roughness noise.

1.2.2.2 Howe's model for serrated trailing edges

Howe proposed a noise prediction model for an airfoil with a sharp trailing edge [67, 68] and with a serrated trailing edge [65, 66]. His model for serrated trailing edges is used through the thesis, in particular in Chapter 4 to compare the experimental noise reductions obtained using sawtooth serrations, and to understand the mechanisms involved in the change of noise. A brief description

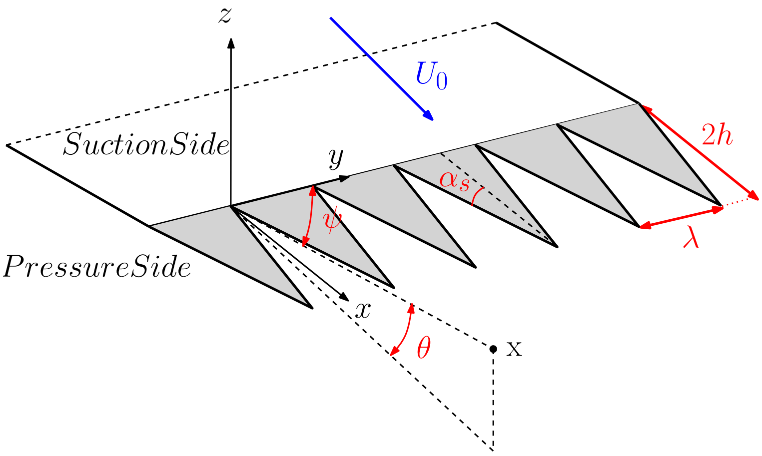

Figure 1.5: Sketch of the trailing edge serrations with geometrical parameters h and λ and definition of the Cartesian coordinate system where $\mathbf{y}$ is the location of acoustic sources and $\mathbf{x}$ is the location of observer.

of the theory and the assumptions made by Howe are given below. Note that in this Section only, δ is used in context as both the Dirac delta function and the boundary layer thickness.

Howe [66] makes the following assumptions:

- Frozen turbulence convected past the trailing edge of a semi-infinite flat plate.
- The model has infinite span.
- The flow is two dimensional and is at low Mach number.
- The Kutta condition is satisfied.
- No other extraneous noise sources are present.

Figure 1.5 shows a sketch of the sawtooth serration at the trailing edge of a flat plate, with the coordinate system used in Howe's derivation. The origin of this coordinate system is defined at the root of the serrations, as presented by Howe [66]. In the rest of the thesis, and for all experimental data, unless mentioned, the origin of the coordinate system is defined at the tip of the serrations, so that $x/c < 0$ defines the boundary layer region and $x/c > 0$ defines the wake region. The sawtooth profile $x = \zeta(y)$ shown in Figure 1.5 is defined in Equation 1.2.

$$x = \zeta(y) = \begin{cases} (4h/\lambda)(y - n\lambda) & n\lambda < y < (n + \frac{1}{2})\lambda \\ -(4h/\lambda)(y - n\lambda) & (n - \frac{1}{2})\lambda < y < n\lambda \end{cases}, \quad n = 0, \pm 1, \pm 2, \pm 3, ... \tag{1.2}$$

where $2h$ is the amplitude of the sawtooth and λ is the spatial periodicity. Using the appropriate Green's function $G(\mathbf{x}, \mathbf{y}, \omega)$ that satisfies the Kutta condition at the trailing edge and whose normal derivative vanishes on the airfoil surface, $d\,G(\mathbf{x}, \mathbf{y}, \omega)/d\,\mathbf{n}\,|_S = 0$, and by means of integration over the surface of the flat plate model (in the region $x \leq 0$), the pressure radiated to the observer's location $p(\mathbf{x},\omega)$ is given by Equation 1.3.

$$p\left(\mathbf{x},\omega\right)=\frac{1}{2}\int\limits_{\mathbf{y}}\int\limits_{\mathbf{k^2}}\gamma\left(\mathbf{k}\right)\,p_{bl}\left(\mathbf{k},\omega\right)\,\mathbf{G}(\mathbf{x},\mathbf{y},\omega)\,e^{i\mathbf{k}.\mathbf{y}}\,d\mathbf{k^2}\,d\mathbf{y}, \tag{1.3}$$

where $\mathbf{k}=(k_x,k_y,0)$ is the boundary layer turbulent wave number vector (k_x in direction of the flow, k_y along the airfoil span), $\gamma\left(\mathbf{k}\right)=\sqrt{k^2-\mathbf{k^2}}$ for $|\mathbf{k}|<k$ or $\gamma\left(\mathbf{k}\right)=i\sqrt{\mathbf{k^2}-k^2}$ for $|\mathbf{k}|>k$, $k=\omega/c_0$ is the acoustic wave number and $p_{bl}(\mathbf{k},\omega)$ is the wave number frequency spectrum of the boundary layer in the absence of the edge.

The acoustic far field pressure spectral density $\phi(\mathbf{x},\omega)$ is given by $\langle p\left(\mathbf{x},\omega\right)p^{\star}\left(\mathbf{x},\omega'\right)\rangle=\phi(\mathbf{x},\omega)\delta(\omega-\omega')$. For a finite section of the airfoil trailing edge of length L wetted by the turbulent flow, the blocked surface wave number frequency spectral density $\phi_{bl}(\mathbf{k},\omega)$ is defined in Equation 1.4

$$\left\langle p\left(\mathbf{k},\omega\right)p^{\star}\left(\mathbf{k}',\omega'\right)\right\rangle\approx\frac{L}{2\pi}\phi_{bl}(\mathbf{k},\omega)\delta(k_x-k_x')\delta(\omega-\omega'), \tag{1.4}$$

where $-L/2<y<L/2$ and $L\gg\delta$. Finally, Howe proposes the use of the wall pressure spectrum $\phi_{bl}(\mathbf{k},\omega)$ of the incident boundary layer pressure due to Chase [26] given in Equation 1.5.

$$\phi_{bl}(\mathbf{k},\omega)=\frac{C_m\rho^2\nu_*^3k_x^2\delta^5}{[(k_x-\omega/U_c)^2(\delta U_c/3\nu_*)^2+(|\mathbf{k}|\,\delta)^2+\epsilon^2]^{5/2}}, \tag{1.5}$$

where δ is the turbulent boundary layer thickness at the trailing edge, $\nu_*\approx0.03U_0$ is the skin friction coefficient, $C_m\approx0.1553$, $\epsilon\approx1.33$ are constants given by Howe [66] and the convection velocity is approximately $U_c=0.7U_0$, where U_0 is the mean flow velocity.

Note that in practice, $\phi_{bl}\left(\mathbf{k},\omega\right)$, the unsteady pressure spectrum on the surface of the airfoil can be measured close to the trailing edge using flush mounted microphones, as described in Chapter 2.

Before investigating the effect on noise by TE serrations, the noise radiation from a straight trailing edge is presented. This is readily achieved by putting $\zeta(y)=0$ in the radiation integral of Equation 1.3. The integration over y in this case is equal to $2\pi\delta(k_y)$, which suggests that in this infinite span limit, only the turbulent wave number contribution $k_y=0$ (i.e. perpendicular to the trailing edge) radiates to the far field. The far field pressure spectral density for a straight trailing edge $\phi_{\mathbf{b}}(\mathbf{x},\omega)$ can be deduced by combining Equations 1.3 and 1.4 and using the appropriate Green's function (see Howe [66]).

$$\phi_{\mathbf{b}}(\mathbf{x},\omega)=\frac{\omega L\sin(\psi)\sin^{\mathbf{2}}(\theta/2)}{2\pi c_0\left|\mathbf{x}\right|^2}\int\limits_{-\infty}^{\infty}\frac{\phi_{bl}(k_x,0,\omega)}{|k_x|}dk_x, \tag{1.6}$$

where the symbol $'\mathbf{b}'$ refers in this thesis to the baseline straight trailing edge. The integration over the streamwise wave number k_x can be simplified by noting from Equation 1.5 that the surface pressure spectral density $\phi_{bl}(\mathbf{x},\omega)$ is dominated by turbulent eddies, which are convected at a speed close to the convection velocity U_c. Therefore, the wave number integral can be replaced with the value of the integrand at $k_x = \omega/U_c$ and $k_y \approx 0$.

To predict the noise generation from a sawtooth serrated trailing edge, the trailing edge profile given in Equation 1.2, i.e., $x = \zeta(y)$, is introduced in the radiation integral of Equation 1.3 and the integration with respect to $\mathbf{y} = (x, y, 0)$ can then be readily evaluated as follows. The spanwise integration over y leads to an expression of the form $\sum \exp(jnk_y\lambda)$, taken over the whole span profile. This term can be re-written using the identity of Equation 1.7 (Poisson sum).

$$\sum_{n=-\infty}^{\infty} e^{jnk_y\lambda} = \frac{2\pi}{\lambda} \sum_{n=-\infty}^{\infty} \delta(k_y - \frac{2\pi n}{\lambda}) \tag{1.7}$$

Equation 1.7 suggests that only the discrete turbulence wave numbers, $k_y = 2\pi n/\lambda$ $(n = 0, \pm 1, \pm 2, \pm 3, ...)$ contribute to the far field noise radiation (compared to $k_y = 0$ for the straight edge). The streamwise integration x has to be treated as a generalized function and is found to be equal to:

$$\int_{-\infty}^{0} \sqrt{|x|}\, e^{jk_x x} dx = -\frac{\sqrt{\pi}}{2} e^{j\pi/4} \left|k_x\right|^{-3/2} \tag{1.8}$$

Finally, the far field noise spectral density $\phi_{\mathbf{s}}(\mathbf{x},\omega)$ for a sawtooth serrated trailing edge is given in Equation 1.9.

$$\phi_{\mathbf{s}}(\mathbf{x},\omega) \approx \frac{2h^2\omega L \sin(\psi)\sin^2(\theta/2)}{\pi c_0 \left|\mathbf{x}\right|^2} \sum_{n=-\infty}^{\infty} \int_{-\infty}^{\infty} \left(1 - \frac{\cos(2k_x h)}{\cos(n\pi)}\right) \times \frac{\left|k_x^2 + (2n\pi/\lambda)^2 - k^2\right|}{(n^2\pi^2 - 4k_x^2h^2)^2 \left|k_x\right|} \phi_{bl}(k_x, 2n\pi/\lambda)\, dk_x, \tag{1.9}$$

where the symbol $'\mathbf{s}'$ refers in this thesis to the serrated trailing edge. The integral over k_x can be evaluated in a similar fashion as mentioned above for a straight edge, by restricting the integrand to $k_x = \omega/U_c$.

Therefore, the trailing edge noise reduction calculation proposed by Howe [66] is formulated as a scattering problem and neglects the direct radiation to the far field due to the quadrupole sources in the boundary layer (low Mach number approximation). Comparison of Equations 1.6 and 1.9, which give the expression of the far field pressure spectrum for a straight edge and a sawtooth serration, respectively, suggest that in the presence of serrations, the integrand oscillates much faster than for a straight edge as the integral is evaluated along the trailing edge. This results in a much smaller prediction of the noise radiation compared to a straight edge, due to cancellation effects between the root and the tip of the serrations. Figure 1.6 shows the non-dimensionalised far field pressure spectrum $\Psi(\omega)$ (see Equation 1.10), where $\phi(\mathbf{x}, \omega)$ is the far field pressure spectrum density radiated in turn from a straight trailing edge (see Equation 1.6) and a sawtooth serration (see Equation 1.9). The parameters of the sawtooth are the sawtooth periodicity along the airfoil span λ and the amplitude of the serrations $2h$. These parameters are chosen to be the same as used in the experimental study in Chapter 4. The details of their geometry are listed in Table 4.1.

$$\Psi(\omega) = \frac{\phi(\mathbf{x}, \omega)}{(\rho\nu_*^2)^2(L/c)(\delta/\left|\mathbf{x}\right|)^2(C_m/\pi)\sin^2(\theta/2)\mathrm{sin}(\psi)} \tag{1.10}$$

The vertical line in Figure 1.6 is the non-dimensionalised frequency $\omega\delta/U_c = 1$. Figure 1.6 shows that noise reduction occurs when $\omega\delta/U_c > 1$ and that when $\omega\delta/U_c \gg 1$ it is controlled by the geometrical parameters λ, h. Under this condition, Howe shows that sawtooth serrations lead to a reduction that asymptotes to $10\log_{10}\left(1 + (4h/\lambda)^2\right)$. These results suggest that most noise reductions occur when the angle between the mean flow and the local tangent to the wetted edge is less than 45^o. In other words, the sharper the serrations, the greater is the noise reduction. Another important feature in Figure 1.6 is the appearance of oscillations due to coherent interference between scattered sound from the root of the serrations and the tip.

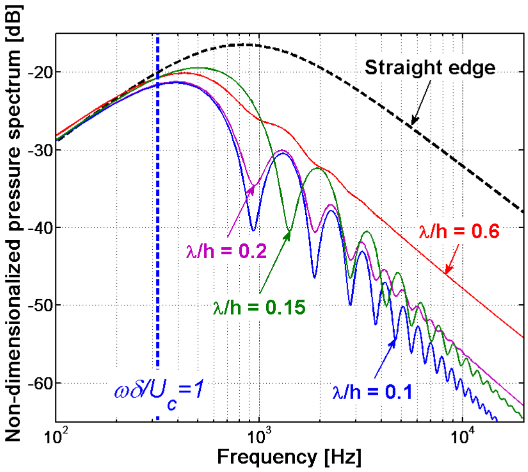

Figure 1.6: Non-dimensional acoustic spectrum $\Psi(\omega)$, defined in Equation 1.10, as in Howe [66] showing a comparison between baseline straight edge and serrations λ/h= 0.1, 0.15, 0.2 and 0.6.

Howe's model therefore provides useful insights into the important parameters that, under the assumptions made to develop his model, determine the noise reduction due to sawtooth trailing edges. Their role in the final formulation of the noise reduction is discussed below.

1. The ratio h/δ, of the sawtooth amplitude to the boundary layer thickness δ, controls the oscillatory behaviour of the far field pressure spectrum due to coherent or incoherent radiation of the noise sources distributed along the wetted edges.

2. The serration geometry, introduced as λ/h, sets the maximum noise reduction level achievable for a given geometry, where the noise reduction increases as $\lambda/h \rightarrow 0$, i.e., the sharper the serration, the greater is the noise reduction.
3. The non-dimensionalised frequency $\omega\delta/U_c$ controls the frequency range over which noise reduction is independent of frequency. More specifically, for $\omega\delta/U_c > 1$ noise reductions are predicted to be independent of frequency while for $\omega\delta/U_c < 1$ noise reductions are insignificant.

The main parameters controlling the levels of noise reduction and frequency range are therefore predicted to be λ/h and $\omega\delta/U_c$, respectively. Howe also predicts that the angle α_s, given in Figure 1.5 as the angle between the flow and the wetted edges of the sawtooth, has to be less than 45^o for the sawtooth to reduce the noise radiation effectively. In this study, all serrated geometries satisfy the condition $\alpha_s < 45^o$ (equivalent to $\lambda/h > 5$ using the notation given in Tables 4.1 and 4.2 below), and therefore this condition has not been tested in this experimental investigation.

1.3 Thesis structure

This thesis describes the results of experimental campaigns performed in the ISVR's open-jet wind tunnel aimed at reducing trailing edge noise using trailing edge geometries, such as sawtooth serrated edges. The reduction of turbulence/leading edge interaction noise is also investigated in Chapter 7 as part of a tandem airfoil study.

Chapter 2 presents a detailed description of the experimental facility and measurement techniques implemented to perform noise and aerodynamics measurements presented in this thesis. The characteristics of the flow around the baseline airfoil are also presented in terms of the steady loading, wake and boundary layer profiles on a straight edge NACA65(12)-10 airfoil.

Chapter 3 describes the trailing edge noise and leading edge noise characteristics of the baseline, no treatment, NACA65(12)-10 airfoil. Experimental data are compared and validated against Amiet's analytical model for both trailing edge self noise [7] and turbulence/leading edge interaction noise [6].

Chapter 4 presents the results of an extensive experimental study, in which the noise performance of thirty six sawtooth trailing edge serrations have been tested in order to optimize and understand the noise reductions obtained with this trailing edge geometry. The experimental noise reductions are compared to Howe's theory for predicting the noise radiation from a sawtooth trailing edge airfoil [66].

Chapter 5 discusses the mechanisms involved in the measured noise reduction and noise increase due to sawtooth trailing edges reported in Chapter 4. The results from an experimental campaign aimed at measuring simultaneously the unsteady surface pressure over a single sawtooth trailing edge and the acoustic radiation are presented. The array of surface pressure sensors is also used to measure and understand the effect of the edge scattering at the trailing edge. Flow visualization and hot wire measurements are also made to relate the changes in the near wake and in the valleys of the sawtooth to the changes in the noise radiation.

Chapter 6 introduces novel trailing edge geometries such as slits, sawtooth with holes, slitted sawtooth and 'random' trailing edges to reduce trailing edge noise. Their noise performances are compared.

Chapter 7 presents an experimental campaign aimed at measuring the noise reduction achievable when using trailing edge serrations and leading edge serrations, using a leading edge design by ONERA [35], simultaneously in a tandem airfoil configuration.

1.4 Original contributions

1. A detailed study of the sound power reduction achievable using sawtooth serrations at the trailing edge was conducted experimentally using thirty six TE geometries in Chapter 4. A thorough comparison with Howe's model [66] is presented and the effects of mean flow velocity, angle of attack and sawtooth geometry on the noise radiation are investigated. Hot wire measurements in the boundary layer over a single sawtooth and in the wake behind a serrated TE airfoil were performed and compared to a straight TE configuration. The critical frequency above which noise is increased due to the sawtooth serrations is identified. This work has been published to the AIAA and ICA conferences (see Gruber *et al* [55, 56, 54]).

2. In Chapter 5, some evidence for the reduction of the scattering due to a serrated TE are identified (as first suggested by Howe [66]). This is conducted using Howe's theory and the results of an experimental campaign aimed at measuring the surface pressure in detail over a single sawtooth in a wall-jet flat plate configuration. The modification of the scattering efficiency, and its interaction with the boundary layer incident pressure over a single sawtooth, is investigated using comparisons with the Brooks model [18]. The presence of a cross flow in the valley of the serrations is also shown to be strongly linked to the increase in the noise radiation at high frequencies.

3. Novel trailing edge geometries that include slits, sawtooth with holes, slitted sawtooth and 'random' TE, are used in Chapter 6 to reduce TE broadband noise. Some of the results on slits have been published at the ICA conference [54]. The slitted serrations have been patented by Rolls Royce as an effective means of reducing TE noise and limiting the high frequency noise increase observed with sawtooth serrations to non significant levels (patent number GB1121753.6).

4. Chapter 7 describes an experimental study aimed at reducing simultaneously broadband TE noise and LE noise using serrations on a pair of tandem airfoils.

Chapter 2

Experimental facility, measurement metrics and flow characterization

This chapter describes the experimental facility and the acoustic and aerodynamic measurement techniques used in this thesis to investigate the reduction of broadband TE and LE noise on a NACA65(12)-10 airfoil. The ISVR's open-jet wind tunnel facility, used to perform acoustics and aerodynamics measurements, is first described. This Chapter also includes a full characterization of the open-jet wind tunnel, which was upgraded to use a centrifugal fan instead of the compressed air tanks originally in place [29]. Flow measurements performed on the baseline straight edge airfoil are also presented.

2.1 Open-jet wind tunnel

The ISVR's open-jet wind tunnel was designed, constructed and tested by Chong *et al* [29] in 2008. It provides a quiet and low-turbulence flow for aerodynamic noise measurements.

Figures 2.1 and 2.2 show the layout of the rig and a picture of the nozzle and test section in-situ in the anechoic chamber of dimensions $8 \, x \, 8 \, x \, 8 \, m$. Note that the hard floor is removed for acoustic tests. Air is supplied from a centrifugal fan driven by a variable speed $110 \, kW$ motor. Noise from the fan is attenuated by a 3-pass lined silencer. Air passes down a vertical duct and is then guided by a 90^o curved diffuser [28] and a second straight silencer tunnel that contains a series of grids, screens and honeycombs to ensure a uniform and low-turbulence flow. Finally, air passes through a 25:1 area contraction ratio nozzle that plays an important role in reducing the lateral velocity fluctuations. The dimension of the nozzle exit are $0.45 \, m$ width by $0.15 \, m$ height. This design results in a jet with a turbulence intensity level of about $0.4 \, \%$ at the nozzle exit. The lower silencer and the nozzle are situated in the ISVR's large anechoic chamber (see Figure 2.1a). The use of side plates mounted flush with the nozzle exit section maintains the flow two dimensionality and helps to support the test model. Mean flow velocity profiles across the exit section at various positions downstream of the nozzle exit are presented in Figure 2.3 and show that the potential core is kept two dimensional, i.e., there are very small variations of the flow velocity in the horizontal and vertical directions.

The main acoustic and aerodynamic characteristics of this facility are summarized below:

- Clean flow: Freestream turbulence intensity is typically 0.4 % in the potential core (see Section 2.4.1 below).
- Working conditions from $10\,m/s$ to $120\,m/s$, i.e., $M = 0.03$ to 0.35.
- Noise due to isolated airfoil is greater than jet background noise by at least 10 dB at all frequencies, as seen in Figure 2.21 below.

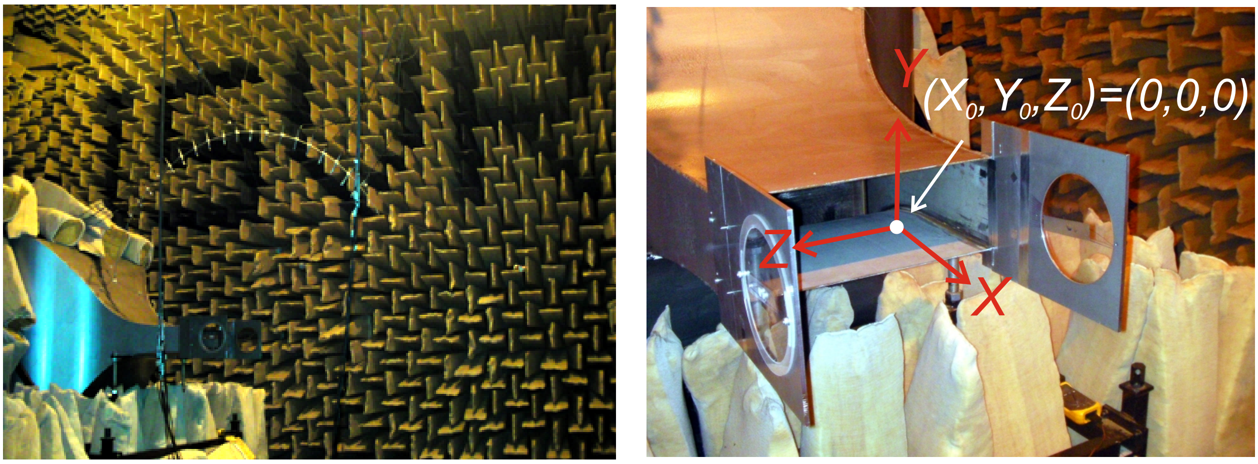

(a) Nozzle exit in the ISVR's large anechoic chamber.

(b) Test section with side plates and airfoil rotating disc.

Figure 2.1: ISVR open-jet wind tunnel.

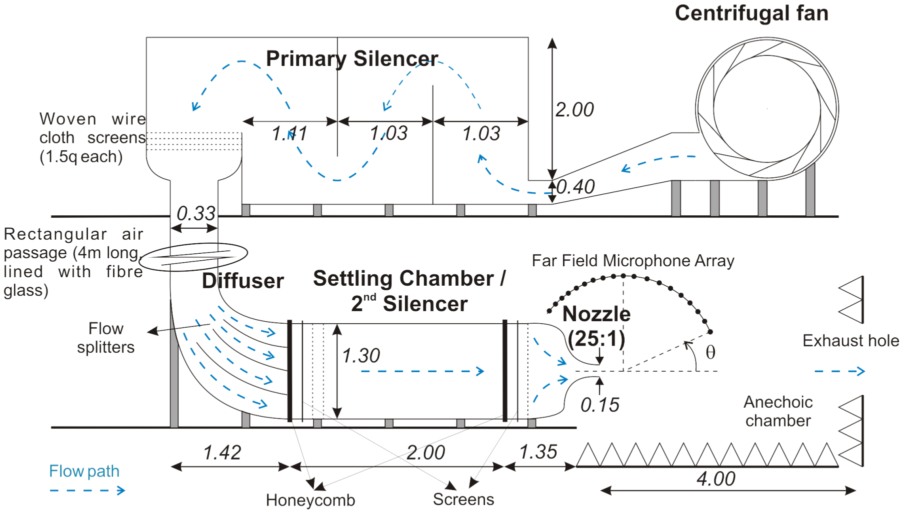

Figure 2.2: Elevation view of the quiet, low turbulence open-jet wind tunnel in ISVR - all units in m (From Chong *et al* [29]).

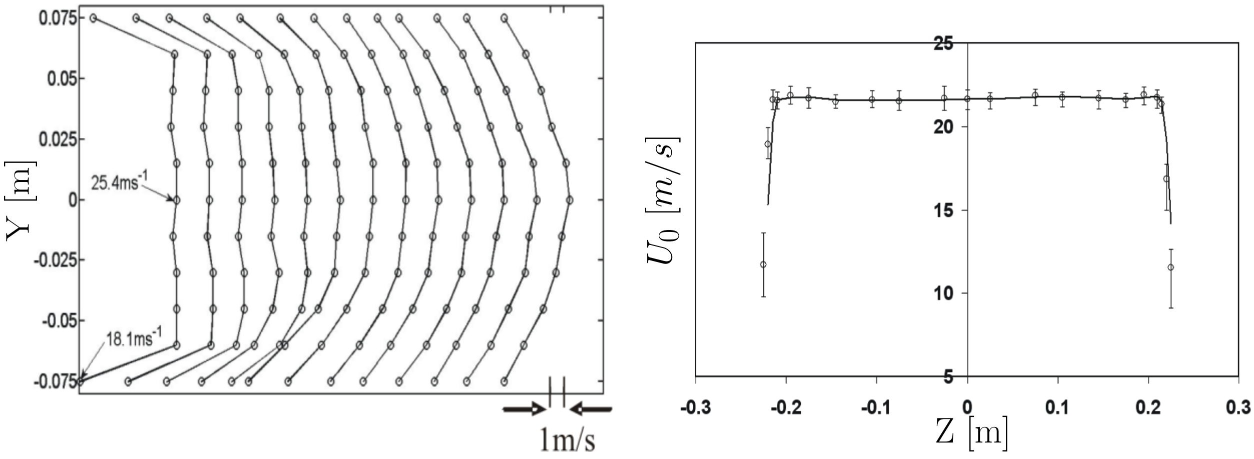

(a) $X-Y$ plane at $Z=0$, measurements are taken from left to right at $X=0.1\,m$ from the nozzle exit to $X=1.3\,m$, with $0.1\,m$ increment.

(b) $X-Z$ plane at $Y=0$ and $X=0.05\,m$ from the nozzle exit, error bars show the maximum and minimum velocity deviations at each location.

Figure 2.3: Mean flow velocity profiles in the $X-Y$ and $X-Z$ planes of the jet (From Chong *et al* [29]).

2.2 Airfoil models investigated

The noise radiation from two airfoils was investigated in this work. Figure 2.4 shows a symmetrical NACA0012 airfoil and a cambered NACA65(12)-10 airfoil (5 % camber, 10 % thickness) installed in the test section of the open-jet wind tunnel. Both airfoils are of dimensions $0.15\,m$ chord and $0.45\,m$ span. The leading edge is located at one chord distance downstream of the nozzle exit in the potential core of the jet. The airfoils are held in the flow using side plates and are fitted onto rotating discs in order to investigate the effect of angle of attack on the noise and aerodynamic performances. The airfoil is held in position onto the disc via a bolt and a dowel pin.

(a) Symmetric NACA0012 airfoil.

(b) Cambered NACA65(12)-10 airfoil.

Figure 2.4: Airfoils fitted onto the rotating discs in the test Section of the open-jet wind tunnel.

2.2.1 Symmetric airfoil: NACA0012

The NACA0012 is a symmetric airfoil and was used for benchmarking purposes only to measure and validate the TE noise measurements (see Chapter 3) against the experimental results from Brooks [18, 19] and the analytical predictions of Amiet [7]. The airfoil was made hollow and pin holes of $0.4\,mm$ diameter were drilled into the surface to allow measurements to be taken of the unsteady surface pressure along the chord in the mid-span plane. Mini microphones from Knowles Electronics (see Section 2.3.4) were mounted flush underneath the airfoil surface.

Note that the unsteady surface pressure spectrum used as an input to Amiet's TE noise model was measured close to the airfoil TE using Remote Microphone Probes (RMP, see Section 2.3.4 below and Perennes *et al* [94]). This airfoil was also used by Chong *et al* to first validate the use of the ISVR open-jet wind tunnel to measure TE noise [29], and to carry out a survey of laminar boundary layer TE noise reduction using serrations [27, 30].

2.2.2 Cambered airfoil: NACA65(12)-10

The NACA65(12)-10 airfoil is used in this thesis to investigate TE noise and LE noise reductions using TE and LE passive treatments on isolated and tandem airfoils. It was chosen by the consortium of the European project FLOCON [1] as a representative airfoil profile of the high lift devices used in, for example, turbomachinery or wind turbine applications. This airfoil profile is also used within FLOCON in ECL's linear cascade facility for noise and aerodynamic measurements.

The test airfoil is shown in Figure 2.5 and is composed of a main steel body of $0.1\,m$ in length and a detachable trailing edge of $0.05\,m$ in length. Two trailing edges were manufactured, a straight sharp one, shown in Figures 2.5 and 2.6b, and a slotted blunt TE shown in Figure 2.7. The slotted blunt TE is used to fit different TE geometries to the airfoil and conduct noise and aerodynamic performance tests. In this thesis, the configuration referred to as the baseline airfoil has a straight LE and straight TE, where the TE is sharp to avoid vortex shedding in the frequency range of interest.

A set of ten pin holes of $1\,mm$ diameter distributed along the chord in the mid-span plane are located on each side of the airfoil (see Figures 2.5 and 2.6a). They are connected to capillary tubes of $1.2\,mm$ internal diameter that are embedded in the main airfoil body and run along the span from the mid-span plane to the airfoil side. The ten pressure side probes are located at the same chordwise positions as the suction side probes shown in Figure 2.6a. Measurements of both static and unsteady pressure can be taken through the capillary tubes to estimate the lift and the boundary layer characteristics for various flow conditions and TE geometries. The steady and unsteady surface pressure probes are connected to the capillary tubes on the side of the airfoil and are described in Sections 2.3.3 and 2.3.4 respectively.

A blunt detachable trailing edge module of thickness $1.2\,mm$ at the edge was also manufactured with a slot cut through the edge along the span (see Figure 2.7). It allows flat plate inserts of

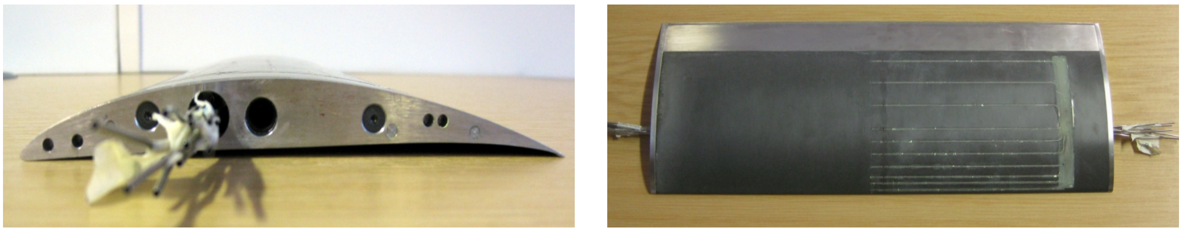

(a) Cross section of the airfoil profile.

(b) View of the capillary tubes running along the span on the suction side.

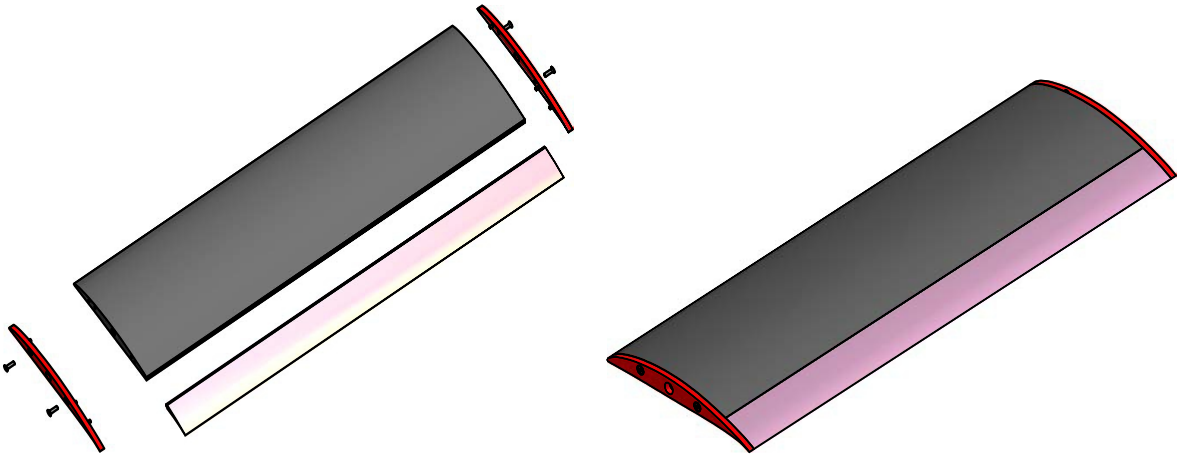

(c) Airfoil CAD exploded view.

(d) Airfoil CAD Assembly view.

Figure 2.5: Cambered NACA65(12)-10 airfoil.

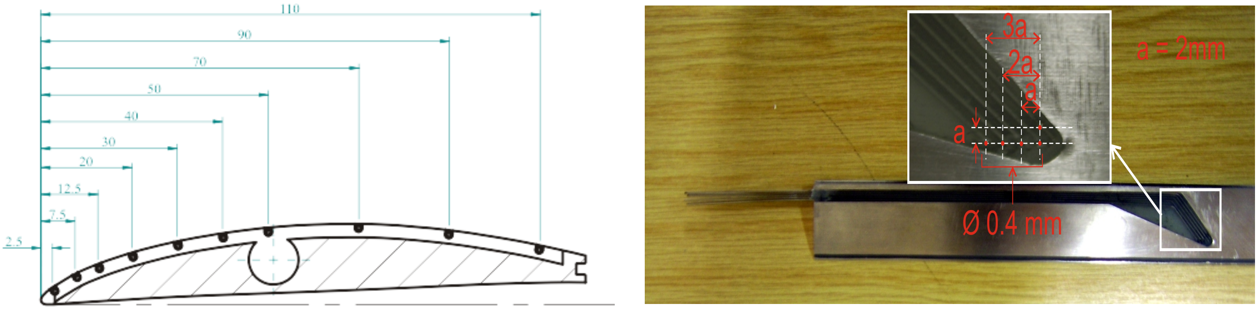

(a) Distribution of the pin holes on the suction side of the airfoil main body.

(b) Capillary tubes embedded in the baseline sharp trailing edge module.

Figure 2.6: Location of the pressure tapping in the main body and in the straight TE module.

$0.8\,mm$ thickness to be fitted to the airfoil. The use of thin flat plate inserts prevents any vortex shedding (due to bluntness at the edges) to occur in the frequency range of interest. In addition, it also allows quick changes from one trailing edge to another while the airfoil is mounted in the test section of the open-jet. This design introduces a small jump of about $0.2\,mm$ on each side of the surface, as pointed in Figure 2.7. However, it is shown in Section 2.4.3 that the far field noise is only slightly affected ($<0.5\,$dB) by this discontinuity and it is shown in Chapters 4 to 7 that the changes in the noise radiation due to the various TE treatments are much greater than that

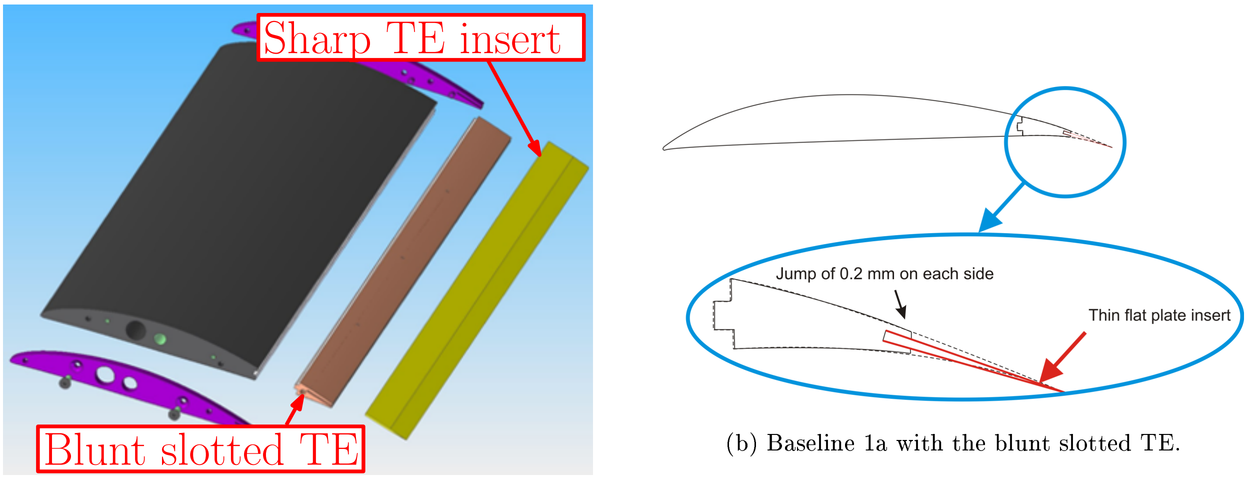

(a) Exploded view of the airfoil fitted with the detachable blunt slotted TE and the flat plate baseline TE insert.

(b) Baseline 1a with the blunt slotted TE.

Figure 2.7: Detachable blunt slotted TE module.

due to the surface jump. Note that the airfoil is tripped near the leading edge and therefore the boundary layer is already turbulent as it passes the surface jump.

There are four different baseline airfoils used in this thesis, as shown in Figure 2.8. The baseline 0 is the reference airfoil; the baseline 1a is the airfoil with the slotted blunt TE and a sharp (no bluntness) insert; the baseline 1b is the airfoil with the slotted blunt TE and a blunt ($0.8\,mm$ thickness) insert; the baseline 2 is the airfoil with the slotted blunt TE and a blunt ($0.8\,mm$ thickness) insert, which length $2h$ can be adjusted to match that of the serrations as described in Chapter 4.

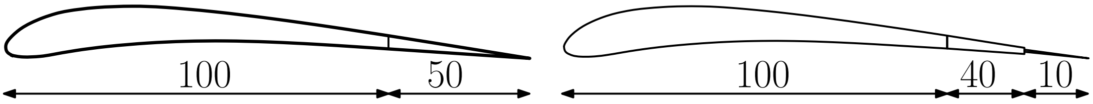

(a) Baseline 0.

(b) Baseline 1a (sharp TE).

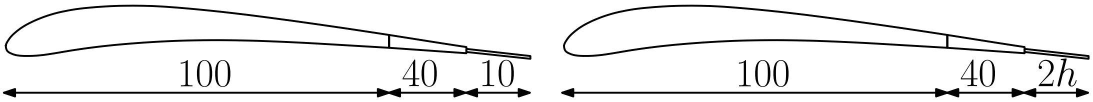

(c) Baseline 1b (blunt TE of $0.8\,mm$ thickness).

(d) Baseline 2 (blunt TE of $0.8\,mm$ thickness with variable amplitude $2h$).

Figure 2.8: Definition of the baseline airfoils - All units in mm.

In order to use Amiet's model to predict TE noise, it is necessary to know the characteristics of the boundary layer in the vicinity of the TE, such as the convection velocity U_c and the spanwise correlation length l_y. Therefore, five additional chordwise and spanwise capillary tubes of $0.6\,mm$ internal diameter are connected to pin holes of $0.4\,mm$ diameter on both sides of the detachable sharp TE fitted to the baseline 0 (see Figure 2.6b). The pin holes are separated by $2\,mm$ along the span and along the chord. Due to the reduced thickness at the airfoil TE, the spanwise pin

x/c	-0.98	-0.95	-0.92	-0.87	-0.80	-0.73	-0.67	-0.53	-0.40	-0.27	-0.08	-0.07

Table 2.1: Chord wise position x/c of the pressure tapping in the airfoil mid-span plane, where $x = 0$ is at the airfoil leading edge, and $x < 0$ is on the airfoil surface.

holes are located at $10\,mm$ ($6.7\,\%$ of the chord) upstream of the edge. Table 2.1 lists the position of the pressure tapping on both sides of the airfoil, where x/c is the chordwise distance of the pin holes from the trailing edge, normalized by the airfoil chord (for the baseline 0).

The trailing edge treatments were first manufactured from metal. Later, serrations were cut in stiff cardboard of $0.8\,mm$ thickness using a laser for ease of manufacture. Various geometries of trailing edges including sawtooth serrations, slits, sawtooth with holes and slitted sawtooth have been manufactured and tested for noise reduction. Their geometries are given with their noise and aerodynamic performances in Chapters 4 and 6.

2.3 Measurement metrics

2.3.1 Far field microphone array

As seen in Figure 2.9, far field pressure is measured by means of a microphone array distributed over a circular arc. Nineteen half inch Brüel & Kjaer Falcon microphones are located at $1.2\,m$ from the airfoil trailing edge. Both pressure spectra and directivity patterns can be studied within an angular range of 90^o on the upper side of the airfoil (from 45^o to 135^o, 0^o being parallel to the direction of propagation of the jet).

Far field microphones are connected to amplifiers, manufactured in-house, and to the National Instruments PXI 1042 chassis. The acquisition system is controlled from a laptop via a NI 8360 Express card. Five NI PXI-4472 Data Acquisition Cards provide a total of 40 channels with an available sampling rate of 102.4 kS/s per channel. Raw time signals are acquired for $20\,s$ with a sampling frequency of 51.2 kHz. Calibration is performed with a conventional Brüel & Kjaer calibrator (94 dB at 1 kHz), and the consistency of the sensitivity over frequency is checked using a Brüel & Kjaer piston phone (giving 124 dB at 250 Hz). Unless mentioned 1024 points are used in the Fast Fourier Transforms to compute all spectra.

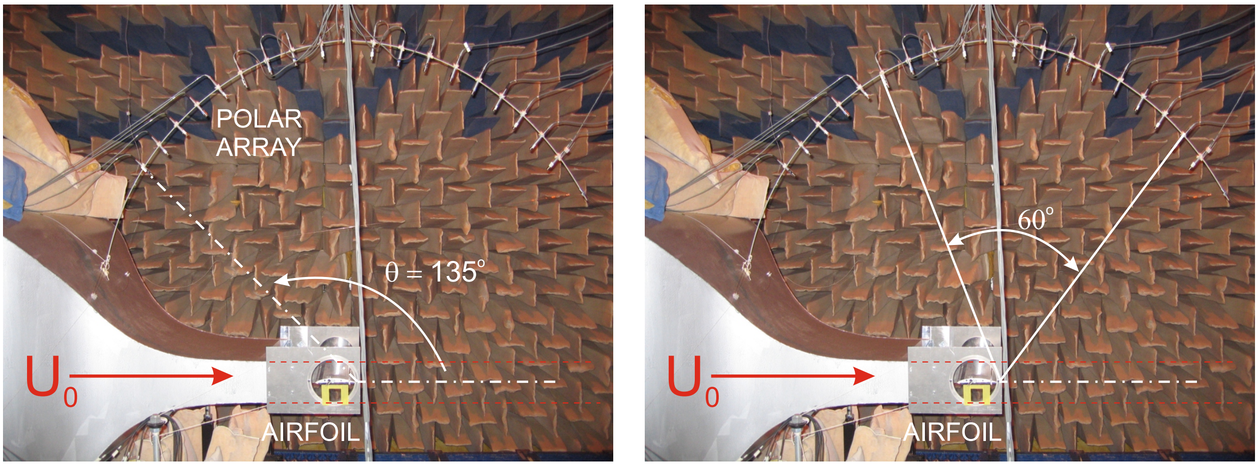

(a) Nozzle, airfoil model and polar array in the large anechoic chamber.

(b) Angle of integration used to estimate the sound power level PWL given in Equation 2.2.

Figure 2.9: ISVR's open-jet wind tunnel.

Noise data were recorded at the four mean flow velocities of 20, 40, 60 and 80 m/s (Re_c=206,500, 413,000, 620,000 and 826,000 respectively) and for the four geometrical angles of attack α_g= 0, 5, 10 and 15^o. A blow-down measurement was also performed during which the noise is measured as the flow velocity is gradually increased from zero to 80 m/s. Note that to ensure fully developed turbulence in the boundary layer, the airfoil was tripped near the leading edge between 10 % and 20 % of the chord using a rough band of tape on both suction and pressure sides.

The noise radiation is investigated in this thesis in terms of Sound Pressure Level spectrum SPL, defined in Equation 2.1 and Sound Power Level spectrum PWL, defined in Equation 2.2.

$$SPL(f) = 10\log_{10}(\phi_{pp}(f)/p_0^2), \tag{2.1}$$

where $\phi_{pp}(f)$ is the far field pressure spectrum density measured at 90^o to the airfoil trailing edge, and $p_0 = 20\mu Pa/\sqrt{Hz}$.

Assuming cylindrical radiation, since the radiation from an airfoil resembles more closely a line source than a point source, the sound power level per unit span PWL, given in Equation 2.2 and measured between radiation angles of 50^o and 110^o(see Figure 2.9b) is also used to assess the noise reduction obtained with the various edge treatments in Chapters 4 to 7.

$$\begin{cases} W(f) = Lr/\rho c_0 \sum\limits_i \phi_{pp}(f,\theta_i).\Delta\theta \\ PWL(f) = 10\log_{10}\left(W(f)/W_0\right) \end{cases}, \quad \begin{matrix} i = 1, ..., N \\ 50^o < \theta < 110^o \end{matrix}, \tag{2.2}$$

where $W(f)$ is the sound power integrated between the radiation angles 50^o to 110^o, $W_0 = 10^{-12} W/Hz$, $\phi_{pp}(f,\theta_i)$ is the pressure spectrum density measured at microphone i, N is the number of microphones, L is the airfoil span, r is the distance between the airfoil trailing edge and the observer, $\Delta\theta = 5^o \times \pi/180$ is the angle between adjacent microphones and c_0 is the speed of sound.

2.3.2 Beamforming array

In order to verify that the dominant sources of noise are located either at the trailing edge or at the leading edge of the airfoil (baseline 0 as in Figure 2.8), a spiral array composed of 49 electret microphones was built, as shown in Figure 2.10. Microphones were phase calibrated following the procedure described in Section 2.3.4.2 in order to use conventional beamforming algorithms. The idea is to visually 'quantify' the contribution of leading edge turbulence interaction noise when trailing edge noise is dominant (with an incoming low turbulent flow) and vice versa (when a grid is inserted in the nozzle and the incoming flow becomes turbulent). The frequency band for using this technique is determined by the total size of the array and the spacing between each microphone. In this case, the array was designed to have the best resolution in the frequency band [2 - 3.5] kHz. The centre of the spiral is situated directly underneath the trailing edge of the airfoil in the mid-span plane. The array is placed at $0.45\,m$ below the airfoil giving a valid low frequency limit for the acoustic far field of approximately 1.2 kHz ($kr >> 1$, where $k = \omega/c_0$).

The beamforming array was designed as part of a student project supervised by the author and lead by Claire Relun [96].

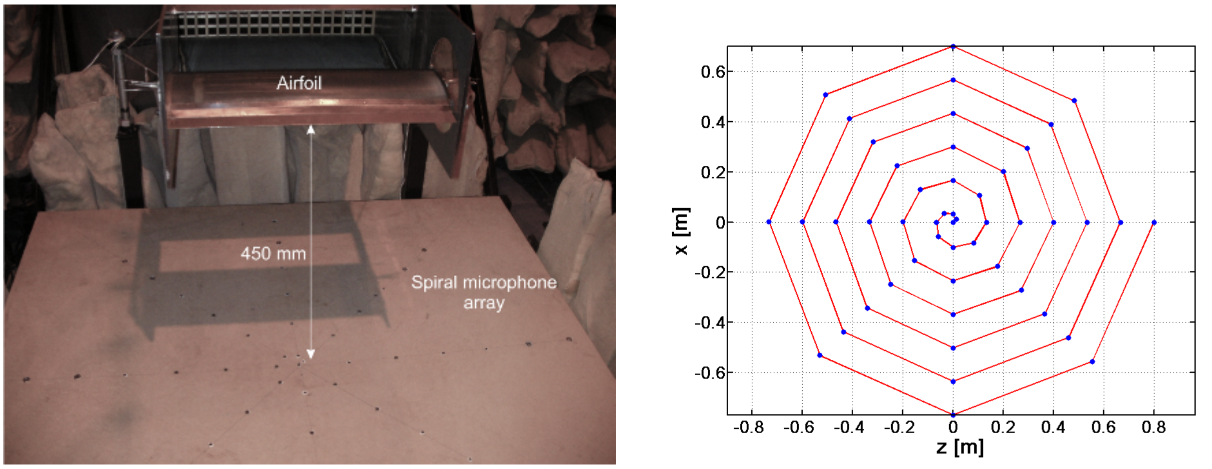

(a) Beamforming array in-situ.

(b) Location of the microphones (reference (x_0,y_0) =(0,0) is centered on the airfoil trailing edge.

Figure 2.10: Spiral microphone array used for beamforming.

2.3.3 Static pressure distribution

The distribution of the static pressure coefficient C_p, given in Equation 2.3, was measured along the airfoil chord to quantify the influence of the various trailing edge treatments on the sectional lift.

$$C_p = \frac{P_i - P_\infty}{\frac{1}{2}\rho U_0^2}, \tag{2.3}$$

where P_i is the static pressure measured at location i along the airfoil chord, P_∞ the atmospheric pressure, ρ the air density and U_0 the freestream mean flow velocity. It was measured on the airfoil main body at the 10 locations listed in Table 2.1 on both pressure and suction sides. A Furness FC014 micro manometer coupled to a scanivalve unit was used, whereby the static pressure at each tube was measured sequentially (see Figure 2.11), allowing a rapid measurement of the static pressure along the chord using a single pressure manometer. The analogue output of the micro-manometer is recorded using the NI PXI-4472 Data Acquisition Card. The incoming flow velocity U_0 is also recorded using a Furness FC012 differential pressure manometer.

The pressure coefficient distribution along the chord is compared to RANS simulations performed by Fluorem as part of FLOCON in Section 2.5.2.

(a) Scanivalve unit. (b) Furness FC014 micro-manometer.

Figure 2.11: Static pressure measurement equipment.

The lift coefficient is also calculated from the measurements of the static pressure distribution C_p on both sides of the airfoil using Equation 2.4.

$$C_L = \int_{x/c=0}^{x/c=1} cos\left(\alpha_g\right)\left(C_{p,lower} - C_{p,upper}\right) d\left(\frac{x}{c}\right) \tag{2.4}$$

where α_g is the geometrical angle of attack in the wind tunnel, c is the airfoil chord, and x is the location of the pin holes along the chord. The lift coefficient C_L is compared to classical aerodynamic theory such as the thin airfoil theory in Section 2.5.2.

2.3.4 Unsteady surface pressure

Flat plate self noise prediction models such as Equation 1.1, suggest that the radiated far field noise can be expressed in terms of the boundary layer pressure spectrum close to the trailing edge. Thus, accurate and reliable data is needed from experiments to ensure the applicability of such prediction models to a specific airfoil profile.

2.3.4.1 Sensors

The sensors selected to measure the unsteady surface pressure are the FG-3329-P07 mini microphones from Knowles Electronics. They have shown to have good reliability in similar measurements performed by for example Garcia Sagrado [103] and Rozenberg [100]. These are omnidirectional electret condenser microphones of 2.5 mm diameter with a circular sensing area of 0.8 mm (Figure 2.12).

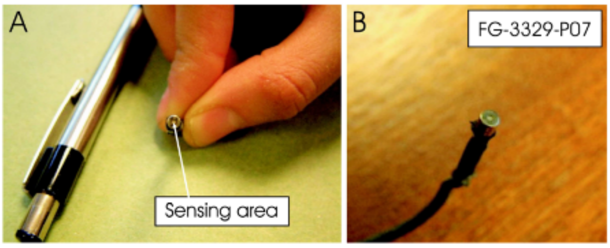

Figure 2.12: FG-3329-P07 microphones from Knowles electronics (Pictures from Sagrado [103]).

Two procedures can be used to obtain accurate measurements of the surface pressure, using either microphones mounted flush below the surface of a hollow airfoil, as on the NACA0012 airfoil of Section 2.2.1, or using Remote Microphone Probes (RMP), as described by Perennes [94]. As mentioned in Section 2.2, capillary tubes embedded in the NACA65(12) airfoil are used to remotely measure the boundary layer pressure using RMPs. Figure 2.13 shows the design of the RMPs manufactured for this experiment.

The principle underlying the RMP is to allow for the pressure fluctuations in the boundary layer of the airfoil to propagate in the capillary tubes, from the surface of the airfoil to the exit of the tube. The measurement of the pressure is taken outside of the airfoil, where the microphones are flush mounted to the capillary tubes. A unique and accurate broadband calibration is needed for each sensor to correct for the time delay, and hence phase delay, and amplitude attenuation due to the propagation of the waves in the capillary tubes. The calibration procedure is performed in-situ and presents many practical difficulties, as described in Section 2.3.4.2.

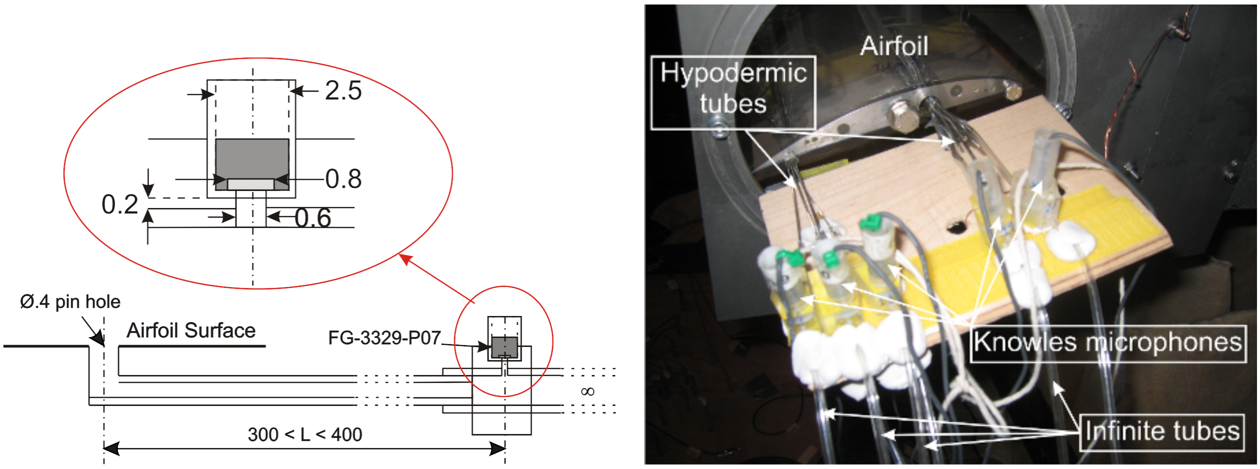

(a) Design of the RMP.

(b) RMPs in-situ on the airfoil.

Figure 2.13: Remote Microphone Probes - All dimensions in mm.

In the current implementation, the distance between the pin hole on the surface of the airfoil and the sensing area of the probe varies significantly from one channel to another. This was done on purpose due to the limit amount of space available to connect the probes on the side of the airfoil. For future studies, the RMPs will be redesigned to improve the handling and mounting of the probes. Ideally, this distance needs to be kept as short as possible to avoid high attenuation of the amplitude at high frequencies.

On the side of the airfoil, flexible tubes of $1.6\,mm$ internal diameter are connected to the airfoil capillary tubes. The internal diameter of the tubes is gradually increased until large enough to connect a FG-3329 microphone. The sensors are glued in a perspex microphone holder (see Figure 2.13), which is tightly fitted into a perspex block. The sensing area of the microphone is connected to the inside of the capillary tube via a $0.6\,mm$ diameter hole. Long plastic tubes of $1.6\,mm$ internal diameter and approximately $3\,m$ long are also connected to the other end to prevent acoustic reflections, since the acoustic energy is naturally dampened through viscous losses in such small tubes. The end of these tubes is sealed to avoid any flow being driven by the pressure difference between the airfoil surface and the ambient air. The weak amplitude of the remaining reflected waves (humps seen in Figure 2.16) can then be corrected from the measurement data by applying the broadband calibration procedure described in Section 2.3.4.2. The quality of the calibrated data is highly sensitive to mounting of the microphones within the perspex blocks and to the accuracy of the calibration itself.

2.3.4.2 Calibration procedure

The broadband two-steps calibration procedure described in Figure 2.14 is performed using an in-duct loudspeaker fed with white noise (see Mish [80]). The sensor to be calibrated is then placed and sealed at the other end of the tube.

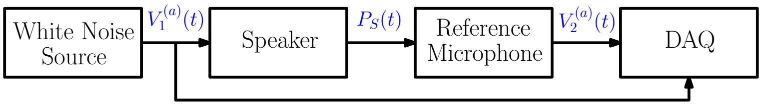

(a) Stage a: Determination of the response of the speaker.

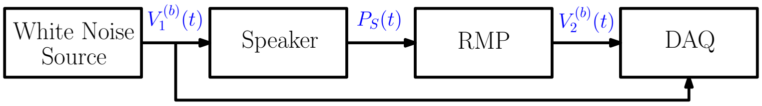

(b) Stage b: Calibration of the unknown microphone probe.

Figure 2.14: Calibration procedure used for the calibration of the Knowles microphones in RMP configurations (from Mish [80]).

First the in-duct calibrator is sealed on a plate where a reference microphone is mounted flush. A 1/4" G.R.A.S microphone with known broadband sensitivity s_{ref} (given flat over frequency by the manufacturer) is used as the reference sensor. The white noise input signal to the speaker $V_1^{(a)}(t)$ and the output signal from the reference microphone $V_2^{(a)}(t)$ are simultaneously recorded. The pressure sensed by the reference microphone is defined as $P_S(t) = V_2^{(a)}(t)/s_{ref}$. The response of the in-duct speaker $H_{Sp}(\omega)$ is then calculated in the frequency domain using Equation 2.5.

$$H_{Sp}(\omega) = \frac{E\left[P_S(\omega)V_1^{(a)*}(\omega)\right]}{E\left[V_1^{(a)}(\omega)V_1^{(a)*}(\omega)\right]} = \frac{G^{(a)}_{V_2V_1}}{G^{(a)}_{V_1V_1}}\frac{1}{s_{ref}}, \tag{2.5}$$

where E is the expectation, $G^{(a)}_{V_2V_1}$ the averaged cross-spectrum between the two signals $V_2^{(a)}$ and $V_1^{(a)}$, and $G^{(a)}_{V_1V_1}$ the auto-spectrum of signal $V_1^{(a)}$.

The second stage of this procedure is to place the in-duct calibrator onto the airfoil surface, as seen in Figure 2.15a. Stage b of Figure 2.14 is carried out and the white noise signal $V_1^{(b)}(t)$ feeding the speaker is simultaneously recorded with the signal from the Knowles microphone $V_2^{(b)}(t)$. The frequency response of the calibrator $H_{Sp}(\omega)$ is known from stage a and the frequency response $RMP(\omega)$ of the RMPs is given in V/Pa in Equations 2.6 and 2.7.

$$H_{Sp}(\omega) \cdot RMP\,(\omega) = \frac{E\left[V_2^{(b)}(\omega) \cdot V_1^{(b)*}(\omega)\right]}{E\left[V_1^{(b)}(\omega) \cdot V_1^{(b)*}(\omega)\right]} = \frac{G^{(b)}_{V_2V_1}}{G^{(b)}_{V_1V_1}} \tag{2.6}$$

$$RMP\,(\omega) = \frac{G^{(b)}_{V_2V_1}}{G^{(b)}_{V_1V_1}}\frac{G^{(a)}_{V_1V_1}}{G^{(a)}_{V_2V_1}}s_{ref} \tag{2.7}$$

Practically, to ensure that the transfer function of the in-duct speaker $H_{Sp}(\omega)$ is consistent and repeatable, the end of the tube is carefully sealed onto the airfoil surface. However, the quality of the in-situ calibration was found to be sensitive to mounting of the in-duct speaker, notably due to the camber of the airfoil.

This calibration is valid only when plane waves propagate in the duct. Duct acoustic theory predicts that plane wave propagation in a hard-walled tube will occur until $ka \simeq 1.84$, where k is the acoustic wave number and a is the radius of the termination of the in-duct speaker. The in-duct broadband calibrator provides an amplitude and phase calibration for each Knowles FG-3329 microphone up to 14,680Hz (the diameter of the tube being 13.6 mm).

This method was first validated using a known sensitivity 1/4” G.R.A.S. microphone as the sensor under calibration. Figure 2.15b shows that the broadband sensitivity obtained after applying the calibration procedure, matches the manufacturer’s sensitivity within 0.5 dB across the whole frequency range. The sensitivity was found to be 4.2 mV/Pa at 1 kHz (against 4.13 mV/Pa provided by the manufacturer).

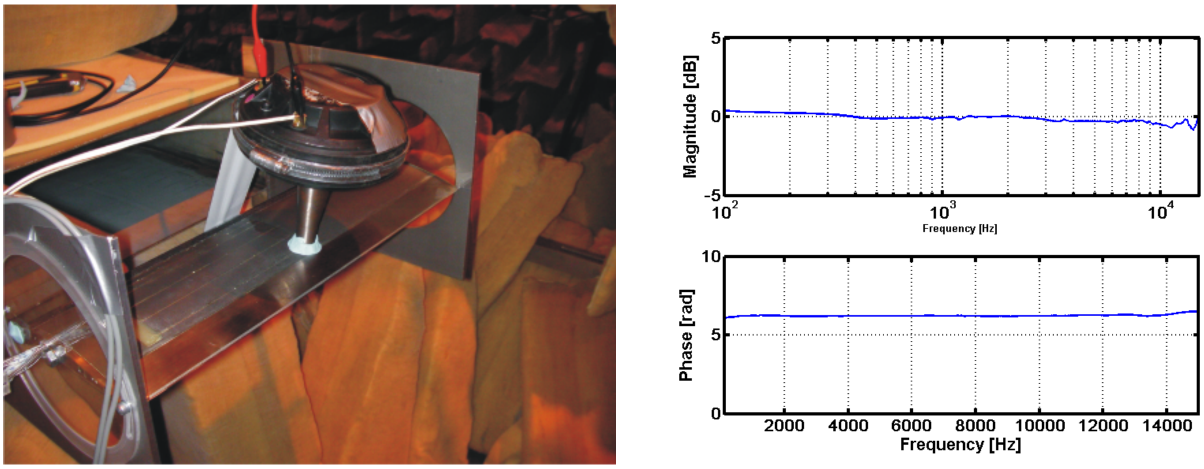

(a) Calibrator in-situ on the suction side of the airfoil.

(b) Deviation of the sensitivity of a 1/4” G.R.A.S. microphone from manufacturer’s specification.

Figure 2.15: Validation of the calibration method.

The calibration of the Knowles microphones was performed in both flush-mounted and RMP configurations. Figure 2.16 shows a typical example of the very good agreement between the flush mounted calibration and the sensitivity specified by Knowles. It also shows the sensitivity function versus frequency for the RMP. The low frequencies are not affected by the capillary tubes, but the quick roll off of the spectrum at high frequencies indicates a strong attenuation of the signal in the capillary tubes.

The coherence function γ^2 defined in Equation 2.8 and the phase spectrum are also used to quantify the reliability of the calibration.

$$\gamma^2(f) = \frac{|G_{V_2V_1}(f)|^2}{G_{V_1V_1}(f)\,G_{V_2V_2}(f)} \tag{2.8}$$

Figure 2.16b illustrates the drop of the coherence of up to about 15 % across the whole frequency range due to the time delay between the white noise signal $V_1(t)$ and the signal measured by the probe $V_2(t)$ in a RMP configuration. However, the coherence γ^2 is always greater than 0.8, which indicates reasonably trustworthy calibration.

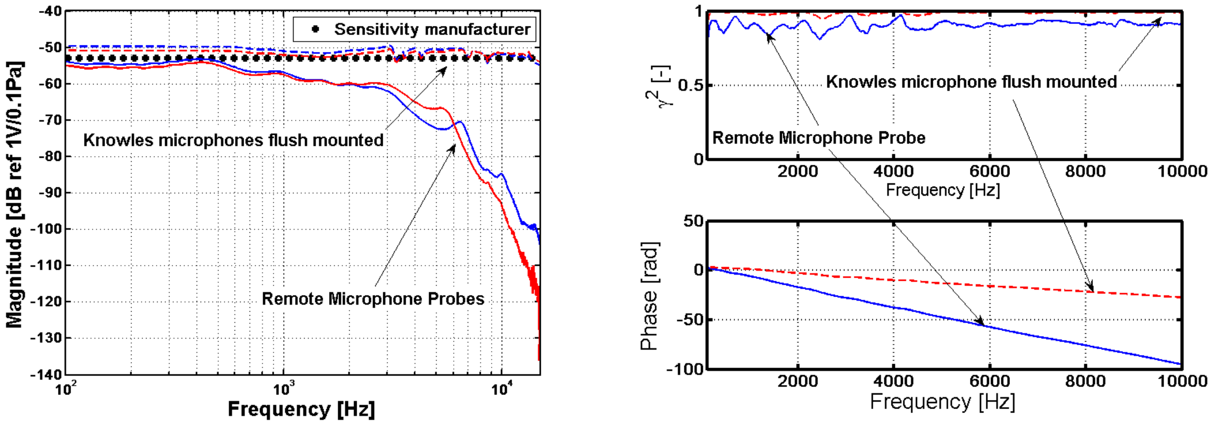

(a) Magnitude.

(b) Calibration coherence function and phase.

Figure 2.16: Typical broadband sensitivity of the Knowles microphone, flush mounted on a flat plate and in RMPs configurations.

2.3.5 Hot Wire Anemometry

Hot wire anemometry was used extensively in this thesis to characterize the mean and turbulent boundary layer and wake shed from the NACA65(12) airfoil, and to estimate the changes in the drag coefficient due to the various geometries used to reduce TE noise. Hot wire anemometry was also used to characterize the flow, with and without the turbulence grid (see Section 2.4).

A TSI single wire, general purpose, probe was used together with a constant temperature anemometer in order to measure the mean and unsteady velocities. The probe is supported by a three axis ISEL traverse unit controlled by stepper motors of precision 0.01 mm shown in Figure 2.17a. Calibration of the wires was performed in the jet using a pitot tube as a reference velocity probe and a temperature probe to correct the data from variation of the temperature in the jet (see Figure 2.17b). Velocity data was then analysed using the Thermal Pro software. Figure 2.17c and d show typical velocity measurements in the wake of the baseline straight edge airfoil and of a sawtooth serrated airfoil, respectively. Measurements of the turbulence in the flow and calibration of the hot wire sensors were performed according to the procedure described by Jorgensen [72].

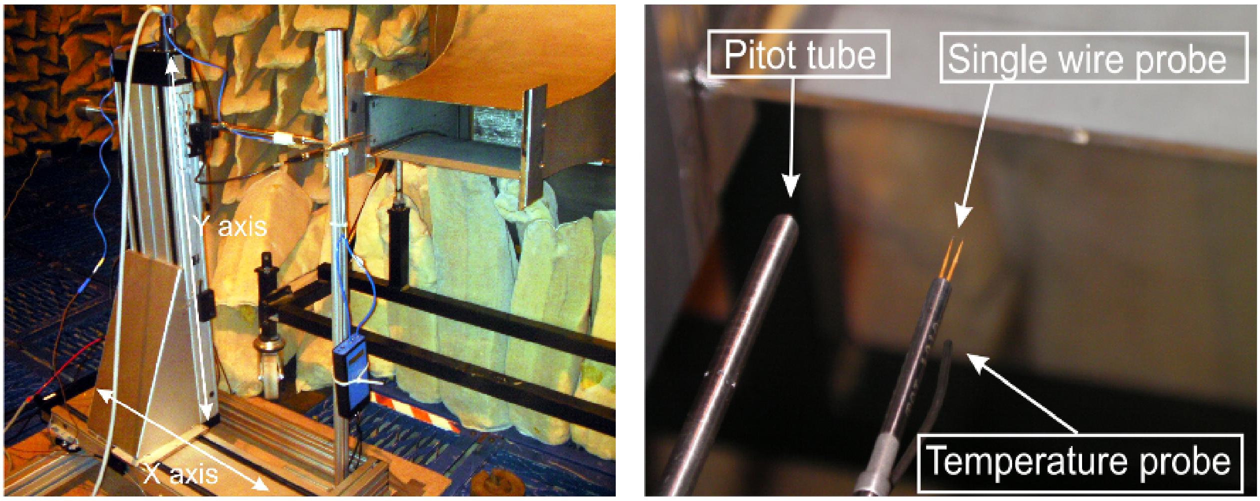

(a) Automated traverse unit.

(b) Single wire probe during calibration procedure.

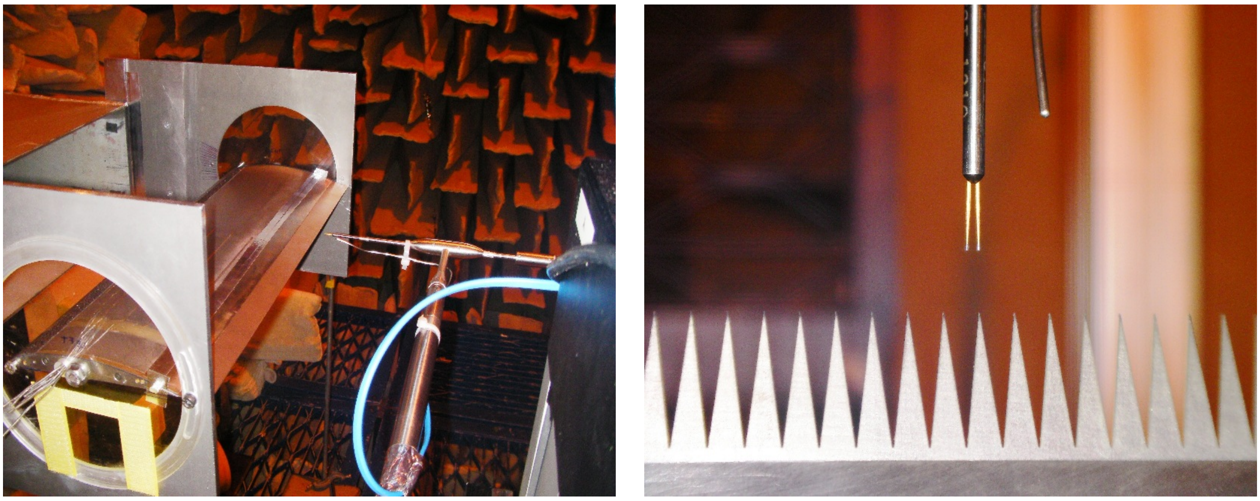

(c) Measurement of the flow in the wake of the baseline airfoil.

(d) Measurement of the flow in the wake of a saw-tooth serrated TE.

Figure 2.17: Flow measurement using hot wire anemometry equipment.

2.4 Measuring airfoil LE and TE noise

2.4.1 Characterization of the jet with turbulence grid

In this thesis, both airfoil TE noise and LE noise are investigated (see Chapter 1). The measurement of LE noise is of interest in this thesis in Chapter 7 when both LE and TE serrations are used in a tandem experiment. TE noise becomes the dominant source when the airfoil is immersed in a low turbulence flow, while LE noise becomes dominant when the incoming flow is turbulent. Controlled homogeneous and isotropic turbulence in the jet is generated using a turbulence grid located in the contraction part of the nozzle (see Figure 2.18). Hot wire anemometry is used to measure and characterize the mean and unsteady flow at the airfoil leading edge cross section, i.e., 145 mm from the nozzle exit.

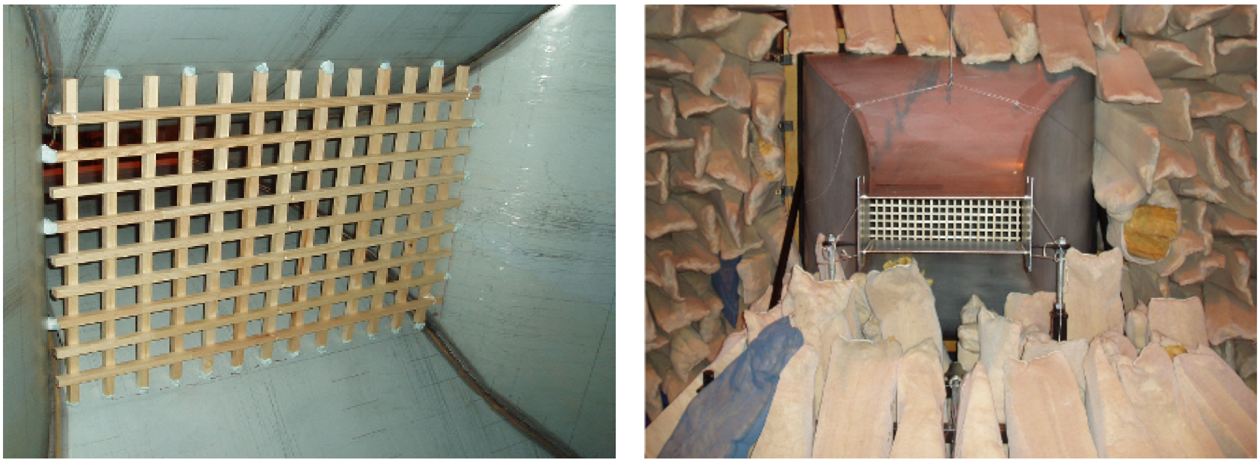

(a) Inside view of the nozzle.

(b) Outside view of the nozzle.

Figure 2.18: Turbulence grid located in the contraction section of the nozzle.

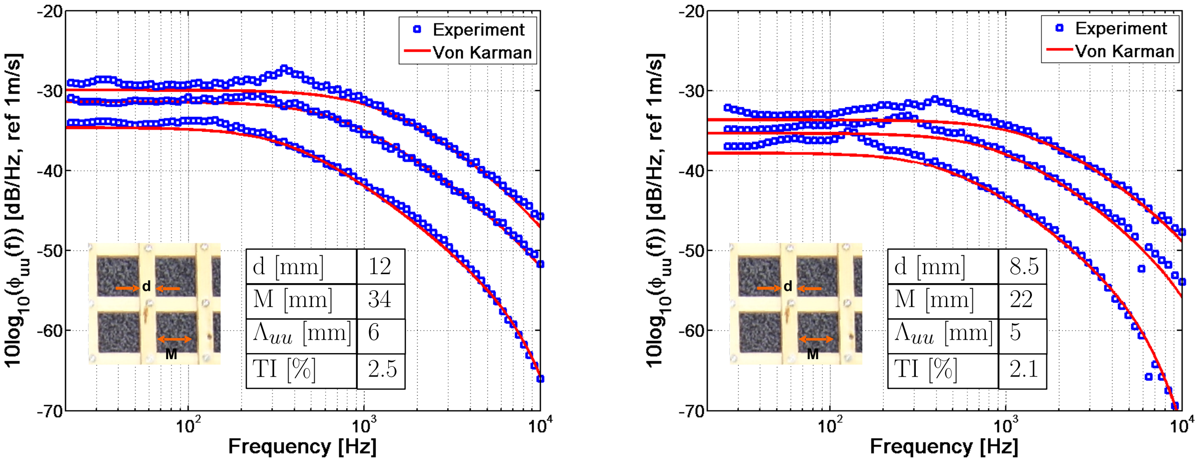

(a) Grid 1.

(b) Grid 2.

Figure 2.19: Comparison of the measured streamwise velocity spectrum ϕ_{uu} against Von Karman model for longitudinal isotropic turbulence, at $U_0 = 20$, 40 and 60 m/s.

Two bi-planar grids made of wooden square bars were used to generate two sets of turbulence intensity level $TI = \sqrt{\overline{u'^2}}/U_0$ and turbulence integral length scale Λ_{uu}. The overall dimensions of the grids are 630 x 690 mm. The dimensions of the grids and the associated values of TI and Λ_{uu} are given in Figure 2.19. The turbulence intensity level TI is calculated from the measured mean square velocity $\overline{u'^2}$ while the integral length scale Λ_{uu} is estimated from data fitting by comparison with the Von Karman spectrum for longitudinal isotropic turbulence given in Equation 2.9 (following Rozenberg [100]).

$$\phi_{uu}^{VK}(\omega) = \frac{\overline{u'^2}\Lambda_{uu}}{\pi U_0} \frac{1}{(1 + (k_x/k_e)^2)^{5/6}}, \tag{2.9}$$

and

$$ke = \frac{\sqrt{\pi}}{\Lambda_{uu}} \frac{\Gamma(5/6)}{\Gamma(1/3)}$$

where $k_x = \omega/U_0$ is the streamwise wavenumber. The Von Karman velocity spectra shown in Figure 2.19 also includes a factor 2 to convert $\phi_{uu}^{VK}(\omega)$ to a single sided spectrum and a factor 2π to convert to frequency in Hz. The high frequency attenuation due to the Kolmogorov scales is also included in the form and the exponential function $\phi_{uu}^{VK}(\omega) \times e^{-9/4(k_x/C_{kol})}$ where C_{kol} is a constant that controls the gradient of the roll off at high frequencies (see Rozenberg [100]). The isotropy of the grid generated turbulence is therefore also verified in Figure 2.19 by comparing the Von Karman spectrum for isotropic turbulence to the measured velocity spectrum density ϕ_{uu}. This comparison is presented for the two grids and for the three mean flow velocities U_0 =20, 40 and 60 m/s. Experiments and theory show excellent agreement, hence confirming that the turbulence generated in the rig is isotropic to a very high degree. The average turbulence intensity level for the two grids are 2.5 % and 2.1 % and the integral length scales are respectively 6 and 5 mm. These parameters are independent of jet speed.

It is worth mentioning that the main difficulty arising from the use of grids to generate turbulence for airfoil LE noise measurements is the position of the grid in the contraction section of the nozzle, which was found to be critical. The balance between the self-noise of the grid and the required turbulence intensity level to make the LE noise source dominant is delicate. These results are not shown here for brevity.

The normalized mean and turbulent velocity profiles in the $X - Z$ and $X - Y$ planes (see Figure 2.1) are shown in Figure 2.20 at the airfoil leading edge with and without the turbulence grid. Both mean and turbulent flow velocity profiles show reasonable uniformity across the test section. The turbulence intensity level in the clean jet is about 0.4 % and the grid generates about 2 % turbulence intensity which, as shown below in Figure 2.21, is sufficient to make the LE noise source dominant over TE noise across the whole frequency band [0.1 - 20] kHz.

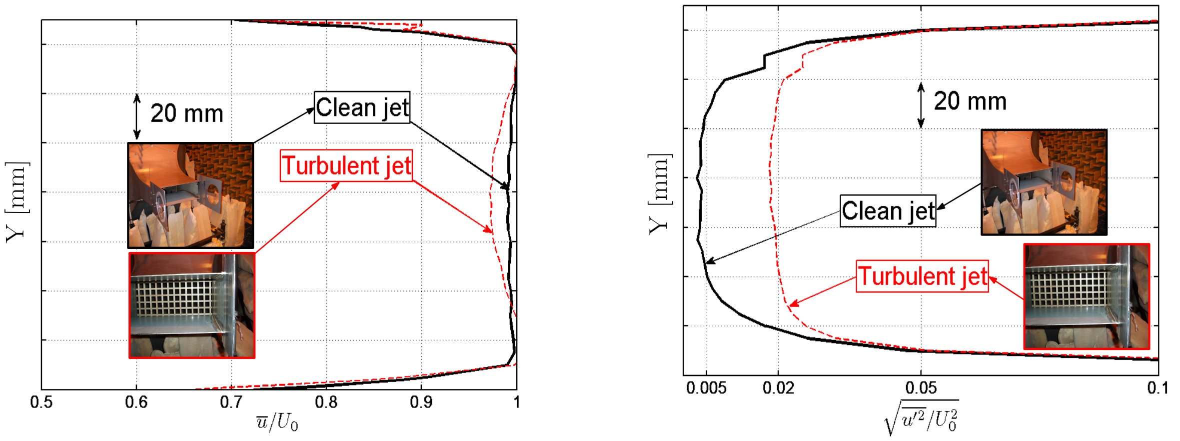

(a) Mean velocity profile U/U_0 in the $X-Z$ plane.

(b) Unsteady velocity profile TI in the $X-Z$ plane.

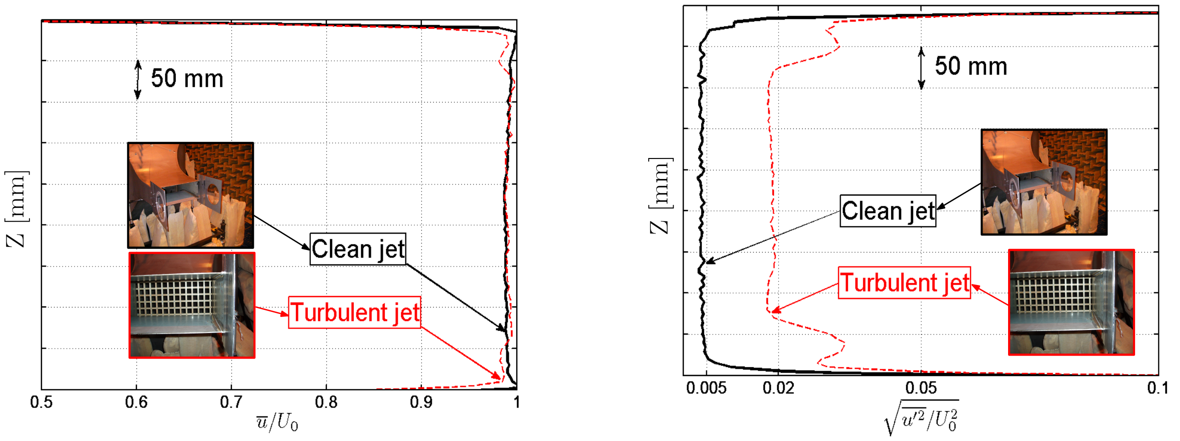

(c) Mean velocity profile U/U_0 in the $X-Y$ plane.

(d) Unsteady velocity profile TI in the $X-Y$ plane.

Figure 2.20: Normalized mean and unsteady velocity profiles with and without turbulence grid, measured at the airfoil leading edge cross section.

2.4.2 Measuring TE noise and LE noise

This Section presents typical measurements of airfoil TE noise and LE noise, taken for the baseline 0 as shown in Figure 2.8. It is shown that TE noise naturally dominates due to the low-turbulence characteristics of the jet and therefore turbulence grids are used to generate LE noise, as described in Section 2.4.1. Figure 2.21a shows the sound pressure level spectrum $SPL(f)$, defined in Equation 2.1, measured at $U_0 = 40\,m/s$. Figure 2.21b shows the sound power level spectrum $PWL(f)$ calculated using Equation 2.2. It is striking that the LE noise dominates the TE noise radiation up to about 10 kHz (up to 20 dB at 1 kHz, at the peak of LE noise). At high frequencies, TE noise appears to become dominant due to the fast roll off of the LE noise spectrum. The background jet noise is at least 10 dB lower than the noise generated by the interaction of the flow with the airfoil, even in the presence of the turbulence grid.

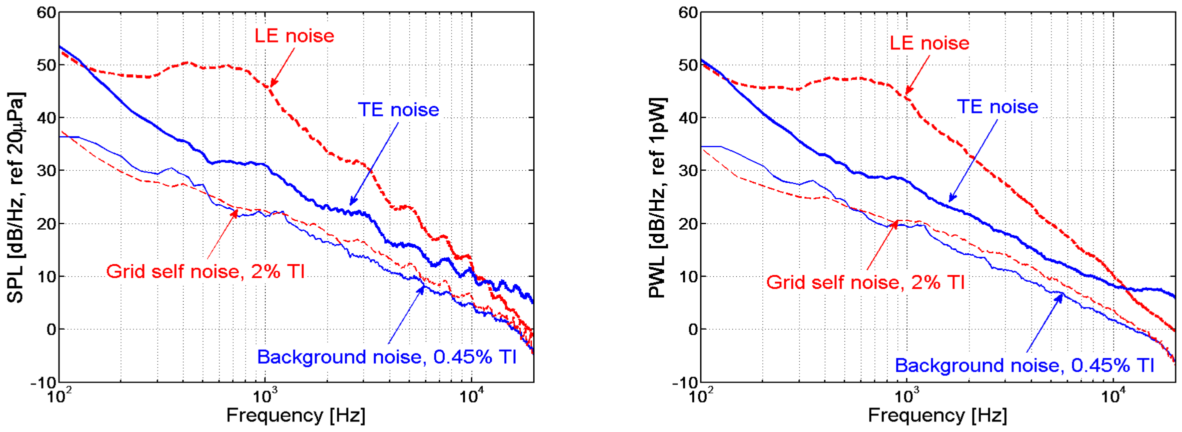

(a) Sound pressure level SPL at 90^o. (b) Sound Power Level PWL.

Figure 2.21: Typical far field LE interaction noise and TE noise measured on the isolated NACA65(12) airfoil, at $U_0 = 40\,m/s$ and 0^o AoA.

The beamforming array presented in Section 2.3.2 is now used to verify the location of the dominant sources on the airfoil, with and without the turbulence grid fitted in the nozzle. Figure 2.22 shows a typical acoustic source map on the airfoil at 2 kHz, where the sound pressure level is normalized by its maximum value over the region scanned by the beamformer. The distribution of the dominant acoustic sources is clearly shifted from the trailing to the leading edge once a turbulence grid is introduced into the contraction section of the nozzle. The absence of 'sources' near the ends of the airfoil is due to the size of the main lobe of the beamformer.

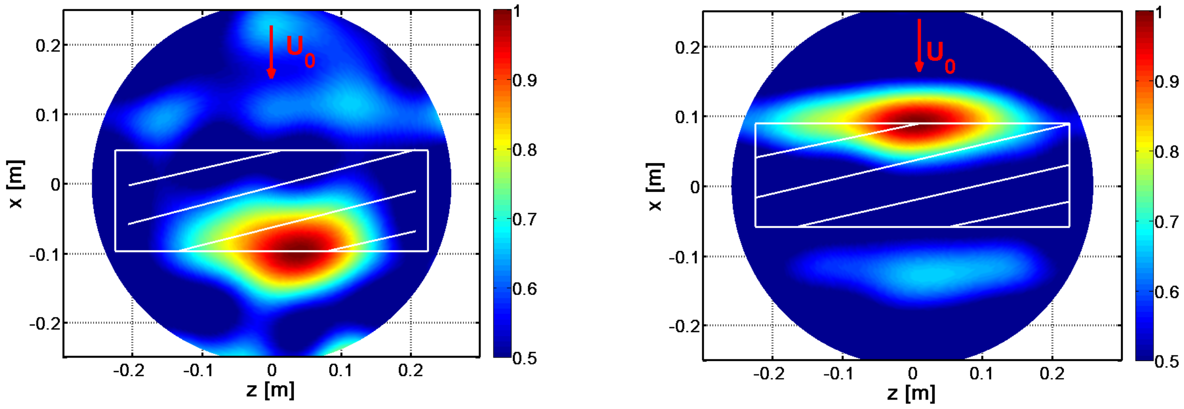

(a) Trailing edge noise. (b) Leading edge noise.

Figure 2.22: Typical acoustic map at 2 kHz.

2.4.3 Influence of the surface discontinuity at the TE on the sound power level

The detachable blunt TE used to fit flat plate TE inserts onto the airfoil is described in Section 2.2 and contains a small step of $0.2\,mm$ on both sides of the airfoil close to the TE. This Section aims at assessing the effect of this step on TE noise. This test is performed by direct comparison of the TE noise measured for the baseline 0 and for the baseline 1a (as seen in Figure 2.8). In order to do so, a flat plate insert with a sharp edge was manufactured (baseline 1a). The noise radiated from the original baseline airfoil with no step (baseline 0) and with the step was measured and compared in Figure 2.23 at the three mean flow velocities of $U_0 = 20$, 40 and $60\,m/s$. Figure 2.23a shows a comparison of the Sound Pressure Level spectrum $SPL(f)$ at 90^o and Figure 2.23b shows a comparison of the sound power level spectrum $PWL(f)$. The airfoil is tripped in both cases, as described in Section 2.2. Overall, the changes in the noise spectra due to the step are smaller than 1 dB across the whole frequency range at $U_0 = 20$ and $40\,m/s$. At $60\,m/s$, a reduction of up to 2 dB is measured after 3 kHz. Therefore, the step associated with the blunt detachable TE is also included in all the baseline straight edge measurements performed in this thesis. On this basis, a noise and aerodynamic study was performed for several geometries of trailing edge inserts as detailed in Chapters 3 to 7.

It is worth mentioning that the high frequency peaks observed at $U_0 = 20\,m/s$ in Figure 2.23 and throughout this thesis, are due to background noise. Therefore, these are restricted to low velocities and high frequencies since this corresponds to the lowest sound levels.

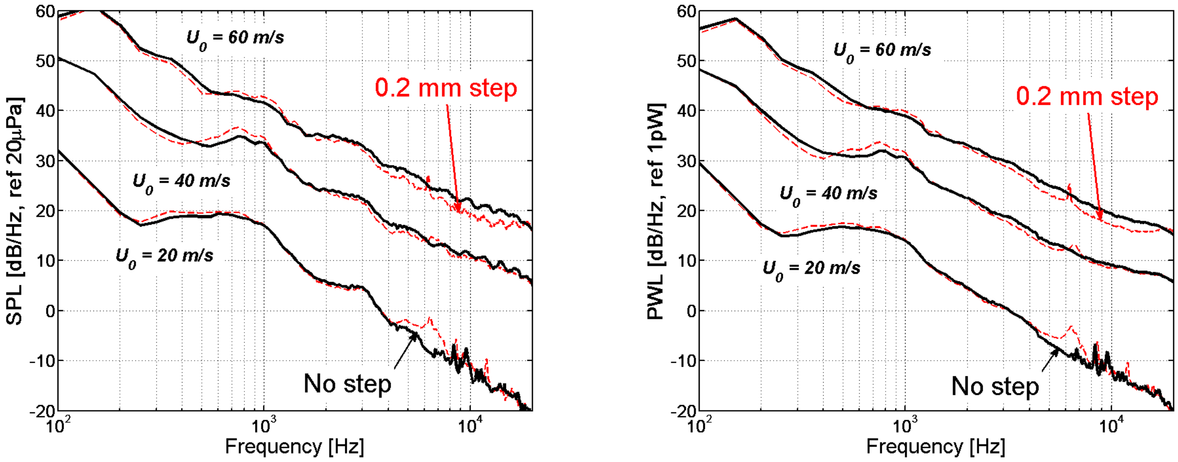

(a) Sound pressure level SPL at 90^o.

(b) Sound Power Level PWL.

Figure 2.23: TE noise spectra showing the effect of the step on the surface of the blunt detachable TE (see Figure 2.7).

2.4.4 Influence of the TE material on the sound power level

The TE flat plate inserts are used in this study to allow quick change of the TE geometry. As described in Section 2.2, these flat plate inserts of $0.8\,mm$ thickness were first made from metal

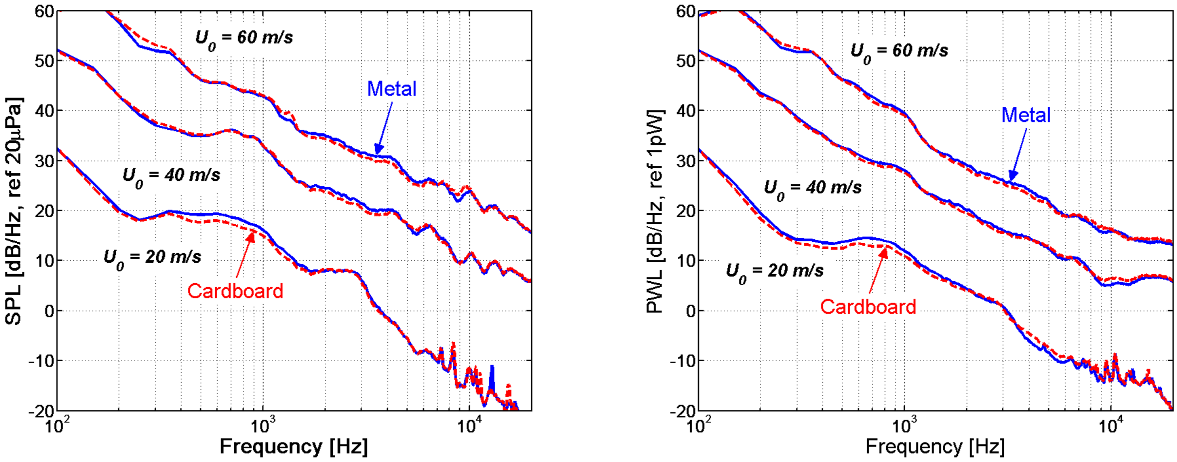

(a) Sound pressure level SPL at 90^o.

(b) Sound Power Level PWL.

Figure 2.24: TE noise spectra showing the effect of the trailing edge material, i.e. metal or rigid cardboard.

and then from a stiff rigid cardboard for ease of manufacturing. This Section aims at assessing the effect of the material (whether metal or cardboard) on TE noise. The baseline 1b airfoil seen in Figure 2.8 is used for this comparison. In order to do so, an identical flat plate insert with a sharp edge was manufactured from both material and fitted in turn onto the airfoil. The noise spectra are shown in Figure 2.24 in terms of the Sound Pressure Level spectrum $SPL(f)$ at 90^o and the Sound Power Level spectrum $PWL(f)$ at the three mean flow velocities of $U_0 = 20$, 40 and 60 m/s. The airfoil is tripped in both cases, as described in Section 2.2. Overall, the changes in the noise spectra due to the nature of the material are smaller than 1 dB across the whole frequency range at all mean flow velocities. The small noise reduction obtained using cardboard is believed to be mainly due to a small decrease in the total lift. However, the investigation of TE noise reduction in Chapters 3 to 7 is carried out relative to a baseline airfoil fitted with a cardboard straight edge and therefore no significant differences are expected to occur due to the material of the trailing edge.

2.5 Angle of attack correction

2.5.1 Zero-camber angle of attack correction

As pointed out by Brooks *et al* [19], in the presence of an airfoil, the flow from the open-jet wind tunnel is deflected downwards. As this deviation does not occur in free air, it is important to correct for it in order to determine the effective angle of attack α_e in free air. This correction only applies for 2D wind tunnel deviation and although it does not take into account the camber line of the airfoil, it is used in the current study to estimate the angle of attack in free air. Equation 2.10 indicates that the geometrical angle of attack α_g is corrected by the geometrical factor ζ to obtain the equivalent angle in free air α_e for an equivalent lift force. The geometrical angle of attack α_g in the rig is defined as the angle between the flow and the chord line.

$$\alpha_e = \alpha_g/\zeta \quad , \quad \begin{cases} \zeta = (1+2\sigma)^2 + \sqrt{12\sigma} \\ \sigma = \frac{\pi^2}{48}(\frac{c}{H})^2 \end{cases} , \tag{2.10}$$

where c and H are the airfoil chord and the height of the jet, respectively, for a horizontally aligned airfoil (with $c = H = 0.15\,mm$ in this study). The actual tunnel angles of attack investigated for noise reduction are listed with their free air equivalent values in Table 2.1. While these corrections are accurate for a symmetrical NACA0012 airfoil, it is less accurate for the non-symmetrical NACA65(12)-10 airfoil. The correction for the case 0^o angle of attack is not accurate because for a cambered airfoil, the 0^o geometrical angle of attack generates a positive lift. Therefore, a lift comparison is also made with RANS simulations performed by Rolls Royce and Fluorem (as part of FLOCON) and presented in the next Section. For convenience, in this report, unless mentioned, angles of attack are geometrical, this is without the correction described in this Section.

α_g $[^o]$	0	5	10	15
α_e $[^o]$	0	1.40	2.81	4.21

Table 2.2: Angle of attack correction due to the flow deviation by the airfoil.

2.5.2 Static pressure distribution coefficient C_P

The static pressure coefficient has been calculated from experimental data using Equation 2.3. Its distribution along the chord of the airfoil is shown in Figure 2.25 at zero angle of attack and $U_0 = 60\,m/s$. In addition, RANS simulations are included in Figure 2.25 for comparisons with the experimental data taken on the baseline 0 (see Figure 2.8). These were performed by Rolls Royce and Fluorem, as part of the European project FLOCON and include the jet deviation due to the presence of the airfoil in an open-jet flow, as shown in Figure 2.25a. The hump in the pressure side experimental C_p is due to a flow separation near the airfoil leading edge. Generally, the static pressure coefficient distribution along the chord shows reasonable agreement with the experimental data (see Figure 2.25b).

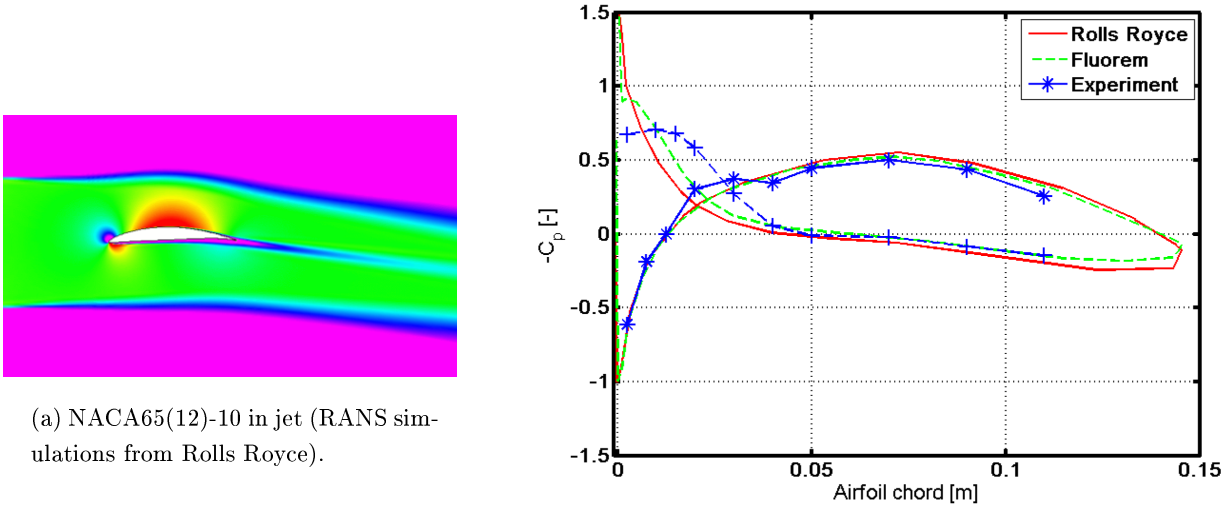

(a) NACA65(12)-10 in jet (RANS simulations from Rolls Royce).

(b) Typical C_p distribution at 0^o AoA and $60\,m/s$.

Figure 2.25: Validation of the measurements of the airfoil loading against RANS simulations provided by Rolls Royce and Fluorem.

A complete characterization of the baseline airfoil loading was conducted with a range of angles of attack α_g from -6^o to 18^o. The lift coefficient was then estimated using Equation 2.4 from experimental data with and without boundary layer tripping. Figure 2.26 shows a comparison with the thin airfoil theory for a non-symmetrical airfoil [12] (where $C_L = 2\pi\alpha + C_{L0}$), versus effective angle of attack α_e (applying the angle of attack correction from Equation 2.10 to the experimental data). It assumes a two dimensional flow around a thin airfoil of infinite span.

The value of C_{L0} is chosen as 0.1 at 0^o angle of attack to match the experimental data and account for the camber line of the airfoil. Zero lift is generated at -1.4^o effective angle of attack. Finally, Figure 2.26 also shows that the tripping band applied to trigger the turbulent boundary layer on both sides of the airfoil (see Section 2.6) does not significantly affect the lift coefficient.

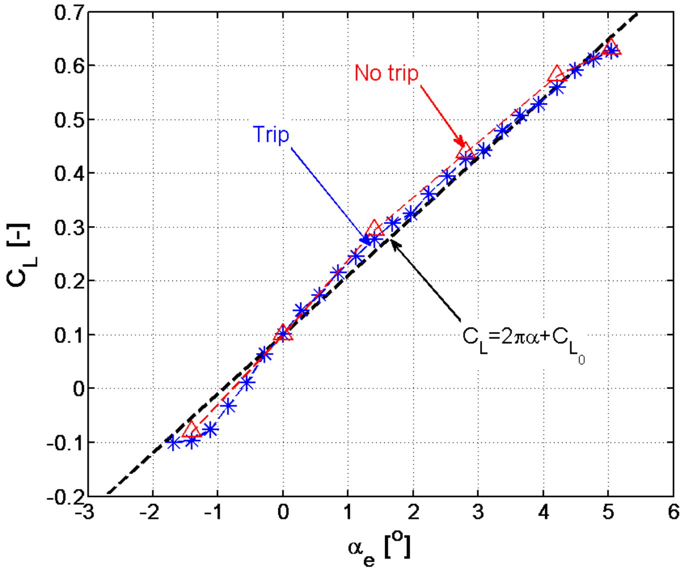

Figure 2.26: Comparison of the lift coefficient C_L against Thin airfoil theory $C_L = 2\pi\alpha + C_{L_0}$ and effective AoA α_e.

2.6 Flow around the airfoil

Presented in this Section are measurements and visualizations of the flow, performed on the baseline airfoil (baseline 0 as in Figure 2.8) with no grid in the nozzle of the open-jet. All flow measurements presented in this Section are performed using the baseline 1b (see Figure 2.8).

2.6.1 Flow visualization

Oil and dye flow visualization was performed on the baseline airfoil in order to qualitatively assess the structure of the boundary layer with and without tripping band. This experiment was conducted at $U_0 = 50\,m/s$ with the airfoil at 0 and 10^o angles of attack in the jet.

As shown in Figure 2.27, the trip used to trigger a turbulent boundary layer is a rough band of about $0.8\,mm$ thickness. It is attached on each surface of the airfoil near the leading edge from 10 % to 20 % of the chord and ensures that the boundary layer is fully turbulent at 20 % of the chord.

Figure 2.27 also shows the oil and dye flow visualization performed on the suction side of the tripped airfoil. A thin layer of the mixture is applied with a brush onto the airfoil surface and air is blown until the oil evaporates and the paint dries out leaving a snapshot of the boundary layer flow. The flow visualization shows that there is no separation of the flow in the boundary layer on the suction side at 0^o angle of attack.

Figure 2.28 shows that the imprint of the boundary layer structure at $U_0 = 50\,m/s$ and 10^o angle of attack, for an airfoil with and without trip. In the absence of the trip, the flow in the boundary layer separates at about 65 % of the chord while it remains attached in the presence of a tripping band.

Unless mentioned, the noise and aerodynamic data presented in this thesis were measured on an airfoil with the tripping shown in Figure 2.27, so that the boundary layer is fully turbulent from 20 % of the chord on both suction and pressure sides.

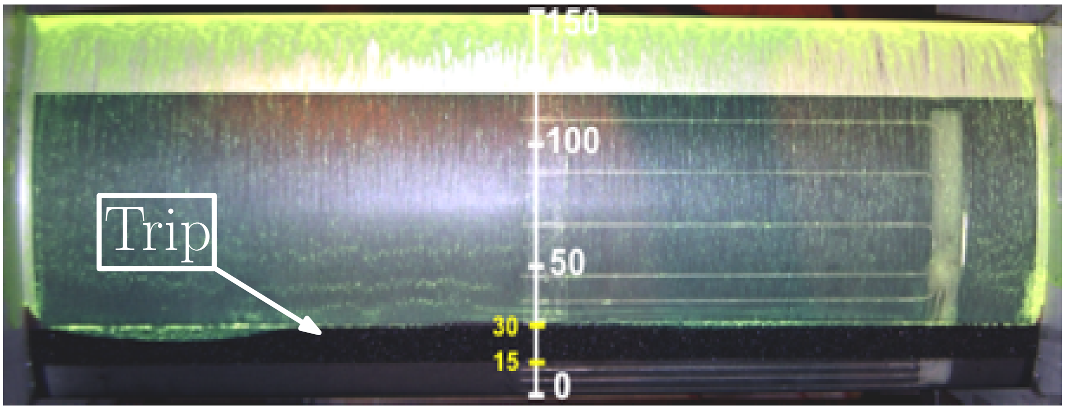

Figure 2.27: Flow visualization on suction side, 0^o AoA with trip at $U_0 = 50\,m/s$ ($x = 0$ is the airfoil leading edge).

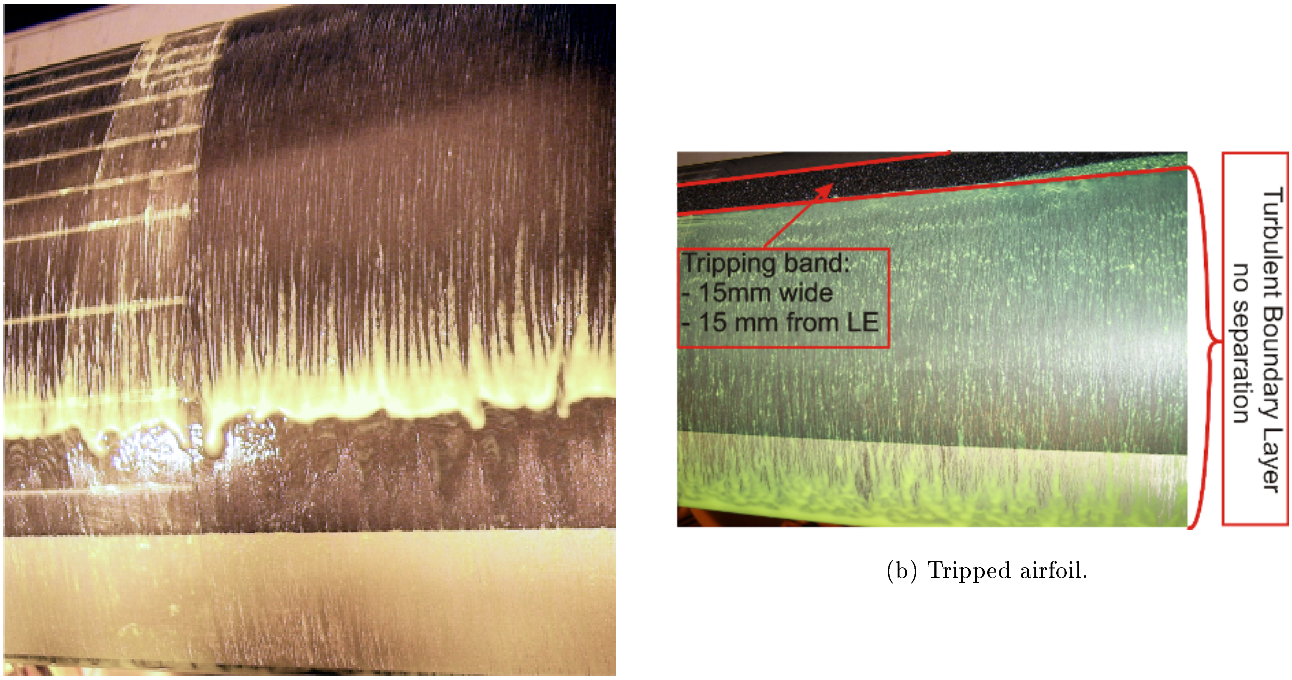

(b) Tripped airfoil.

(a) Untripped airfoil.

Figure 2.28: Flow visualization on suction side, at $U_0 = 50\,m/s$ and 10^o AoA.

2.6.2 Flow measurements

Unsteady velocity flow measurements have been performed in the wake and in the boundary layer of the baseline NACA65(12)-10 airfoil using hot wire anemometry. These results are used in Chapters 4 and 5 as a reference for comparison with the measurements of the unsteady flow performed in the boundary layer and in the wake of sawtooth serrated trailing edge airfoils.

2.6.2.1 Wake profiles

Figure 2.29 shows the spreading of the mean wake profile normalized by the freestream velocity U_0. Measurements were taken at the two mean flow velocities of $U_0 = 20$ and $40\,m/s$, and at the three downstream distances of $x/c = 0.03$, 0.15 and 0.6 behind the baseline trailing edge, where $x = 0$ is located at the airfoil trailing edge. The airfoil is at 0^o angle of attack and the deviation of the jet shown in Figure 2.29 is due to the airfoil camber line only. The measured normalized mean velocity profiles in the wake also show reasonable agreement with the mean wake profiles obtained from RANS simulations provided by Rolls Royce, also shown in Figure 2.29. The mean flow velocity has no significant effect on the wake profiles and on the normalized maximum wake deficit located at the wake centre-line.

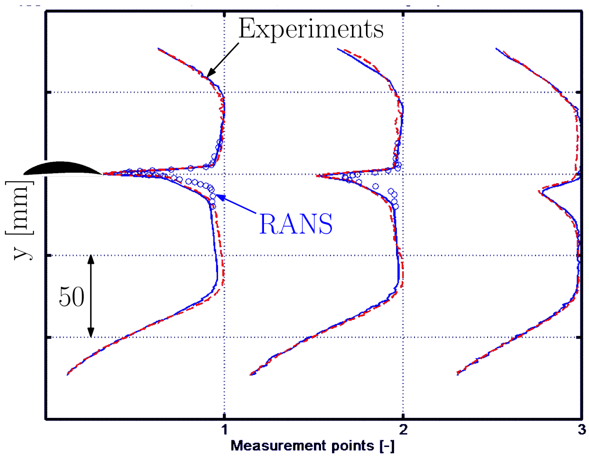

Figure 2.29: Trajectory of the normalized wake deficit behind the baseline airfoil at 0^o AoA, RANS simulations from Rolls Royce.

Figure 2.30 shows the variation of the mean wake deficit and of the unsteady wake velocity with airfoil angle of attack. At 0^o angle of attack, the wake width is larger than at higher angles. This is due to a local separation of the flow near the leading edge on the pressure side of the airfoil, shown in Figure 2.31 from the RANS computations provided by Fluorem [44] using the code Turb'Opty. The separation bubble near the airfoil leading edge results in the boundary layer growing bigger on the pressure side at 0^o angle of attack. However, as the angle of attack increases the flow remains attached on the pressure side and the boundary layer becomes thinner on the pressure side (see Table 2.3).

The mean velocity profiles in the wake are also used to estimate the drag coefficient in Chapter 4 to assess the aerodynamic performances introduced by the trailing edge treatments.

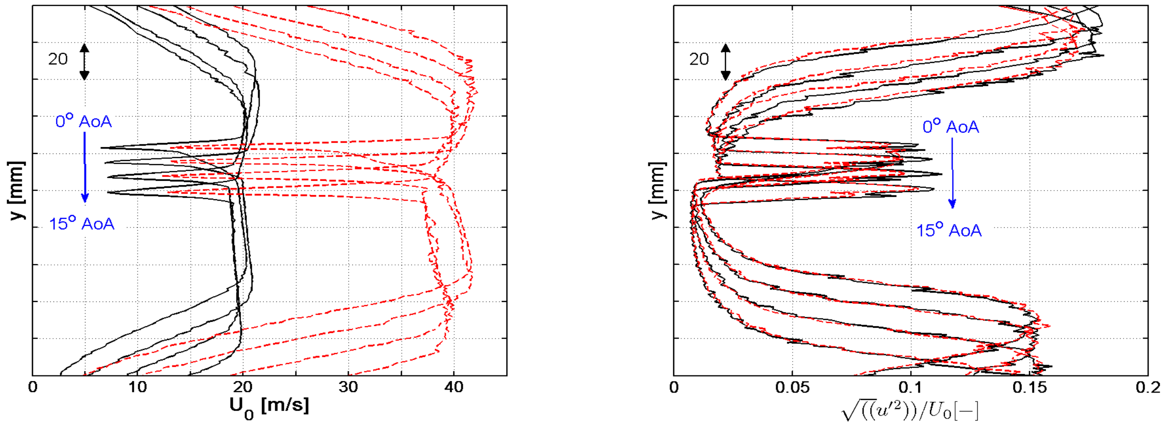

(a) Mean velocity profiles.

(b) Normalized unsteady velocity profiles.

Figure 2.30: Wake velocity profiles, measured at 0, 5, 10 and 15^o AoA and at $5\,mm$ downstream of the TE, at $U_0 = 20$ and $40\,m/s$.

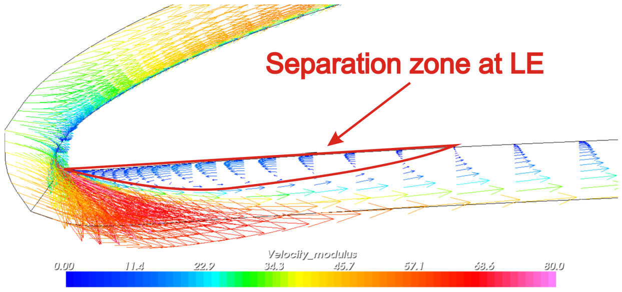

Figure 2.31: Separation of the flow on the pressure side at 0^o AoA (RANS simulation provided by Fluorem [44]).

2.6.2.2 Boundary layer profiles

The boundary layer thickness δ_{99} can be estimated as the thickness for which the local mean velocity in the boundary layer is equal to $99\,\%$ of the freestream velocity. Boundary layer profiles have been measured on both the pressure and suction sides of the baseline airfoil using a general purpose TSI 1.5 single hot wire probe. The airfoil surface was approached within about $0.5\,mm$. In order to validate the estimation of the boundary layer thickness, and with the lack of a boundary layer probe, the mean velocity profiles were measured in the boundary layer $1\,mm$ upstream of the trailing edge and in the wake $1\,mm$ downstream of the trailing edge. It is also assumed that over the small distance of $2\,mm$, the boundary layer flow is frozen.

Figure 2.32 shows a superposition of the mean velocity profiles measured $1\,mm$ upstream and $1\,mm$ downstream of the TE, at the four angles of attack 0, 5, 10 and 15^o. The close matching of the velocity profiles allows a more accurate estimation of the boundary layer thickness at the airfoil trailing edge.

Table 2.3 summarizes the boundary layer thicknesses δ_{99} on both sides of the airfoil and at the four angles of attack 0, 5, 10 and 15^o. As expected from the wake profiles shown in the previous Section, the boundary layer becomes thinner on the pressure side and thicker on the suction side with increasing angle of attack.

Finally, Figure 2.33 shows the growth of the boundary layer along the suction side of the airfoil. Note that since part of the velocity profile close to the surface was missed by the probe, this plot only provides qualitative information on the development of the boundary layer along the chord, and the velocity profiles were oriented manually.

AoA	Pressure Side	Suction Side
0^o	17	7.2
5^o	6.6	7.1
10^o	5.5	7.3
15^o	4.6	9.4

Table 2.3: Boundary layer thickness δ_{99} at the airfoil trailing edge - all units in mm.

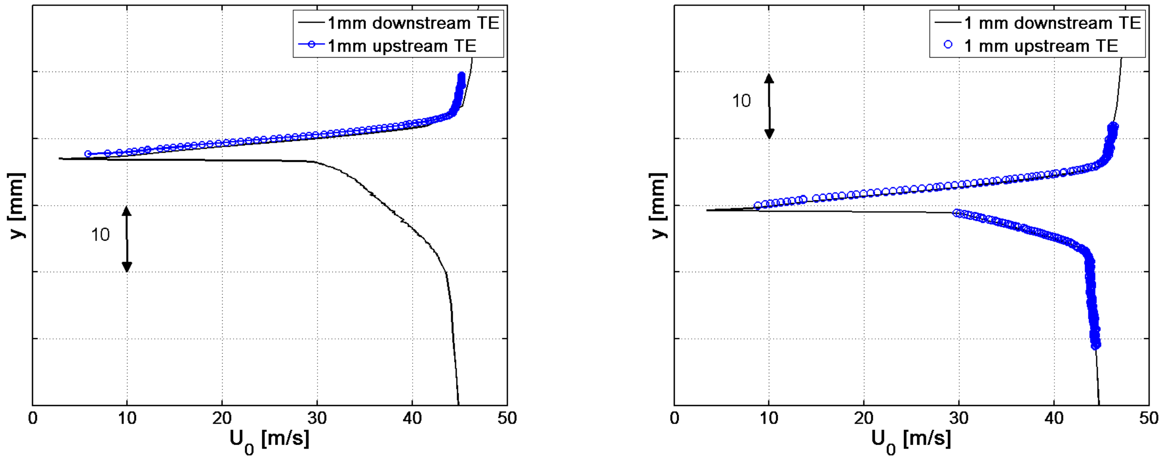

(a) 0^o AoA. (b) 5^o AoA.

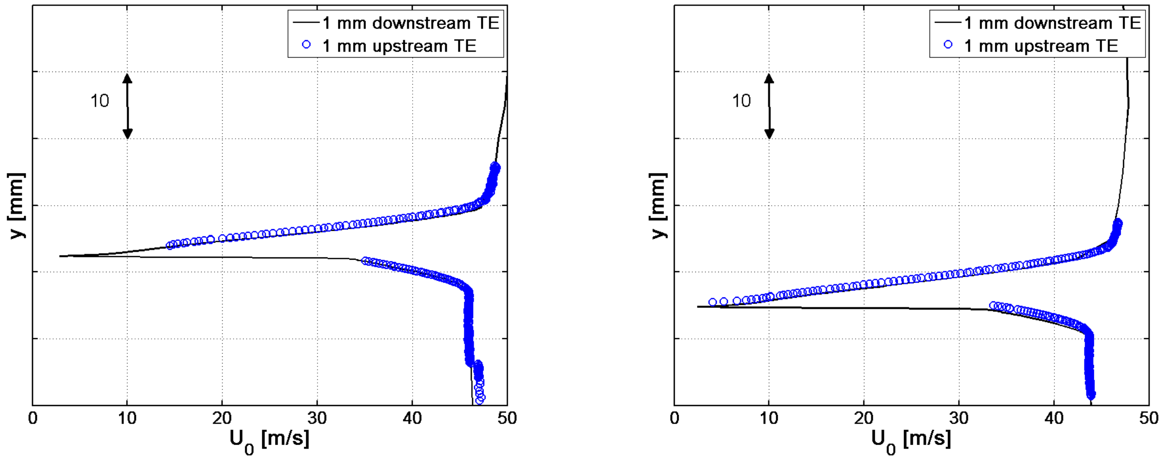

(c) 10^o AoA. (d) 15^o AoA.

Figure 2.32: Mean velocity profile in the boundary layer and in the wake at the airfoil TE.

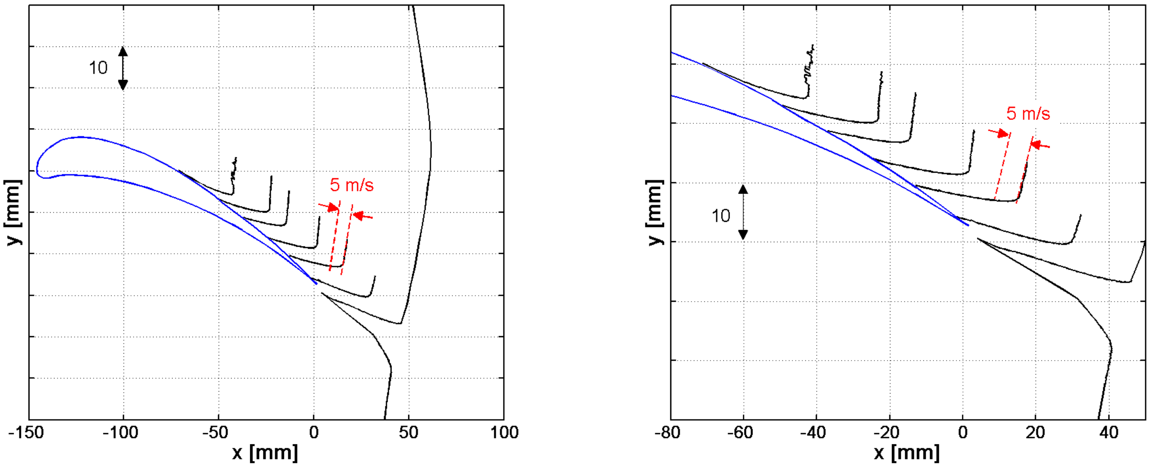

(a) Mean velocity profiles in the boundary layer.

(b) TE view.

Figure 2.33: Growth of the boundary layer mean velocity profile along the airfoil chord on the suction side at $U_0 = 40\, m/s$.

2.6.3 Estimation of the boundary layer parameters using Xfoil

As suggested in Howe's theory [66], the boundary layer thickness δ at the airfoil trailing edge is an important parameter that controls the noise performance of trailing edge serrations. To estimate the boundary layer thickness, the turbulent boundary layer profile was measured experimentally at various locations along the baseline airfoil chord, at $U_0 = 40\, m/s$ and 5^o AoA, using a single hot wire probe (see Sections 2.6.2.1 and 2.6.2.2). In order to compare Howe's predictions to the experimental results obtained using sawtooth serrations in Chapter 4, it is necessary to be able to estimate the boundary layer thickness at the airfoil trailing edge for a range of airfoil chords, mean flow velocities and angles of attack. Therefore, due to the limited number of cases available from RANS data, and because of the large number of cases in this study, the panel method code Xfoil [38] was used to estimate the required boundary layer parameters.

In order to relate Xfoil with the experiment, the deflection of the flow due to the high camber of the airfoil and the geometrical angle of attack in the rig was taken into account. This was done by adjusting the angle of attack predicted by Xfoil so that the static pressure distribution along the airfoil chord, on the suction side, matches the RANS calculation provided by Fluorem (using the Turb'opty code) and the experimental data (Figures 2.34a to c).

Figure 2.34d shows a good accuracy in the boundary layer displacement thickness δ^* predicted by Xfoil, when compared with experimental data, at 99 % of the chord on the suction side. Therefore, by matching the static pressure distribution, Xfoil [38] was used to estimate the boundary layer displacement thickness data in this study for all experimental cases, including various chord lengths, angles of attack and flow speeds. The boundary layer thickness was then calculated for each case using a constant ratio of δ/δ^* given by the CFD data from Fluorem and Rolls Royce.

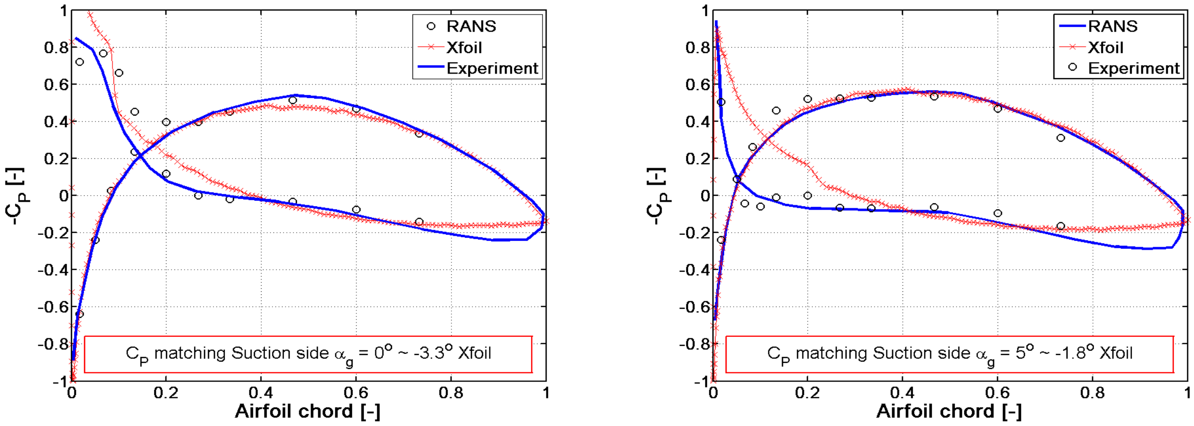

(a) $\alpha_g = 0^o$ in the wind tunnel, -3.3^o in Xfoil.

(b) $\alpha_g = 5^o$ in the wind tunnel, -1.8^o in Xfoil.

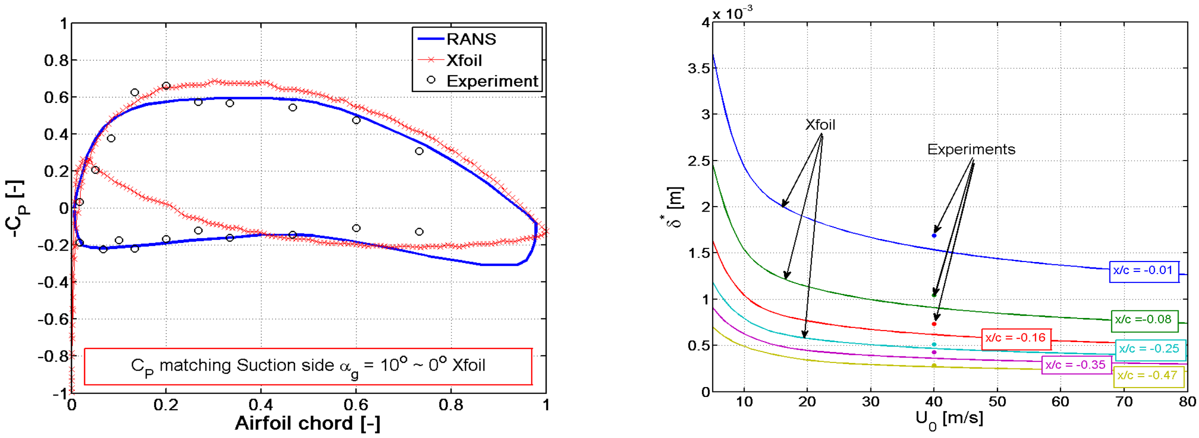

(c) $\alpha_g = 10^o$ in the wind tunnel, 0^o in Xfoil.

(d) Estimation of δ^* as a function of mean flow velocity at various positions along the airfoil chord using Xfoil [38].

Figure 2.34: Predicting the boundary layer parameters C_p and δ^* using Xfoil [38].

Chapter 3

Baseline airfoil characterization

This chapter is dedicated to the experimental characterization of trailing edge noise and leading edge interaction noise of the NACA0012 and NACA65(12)-10 airfoils. These trailing edge noise measurements are compared to the semi-empirical flat plate models of Amiet [7] and Brooks [19]. The unsteady surface pressure is also measured in the vicinity of the airfoil trailing edge and is used as an input into Amiet's trailing edge noise model. Useful parameters such as the convection velocity U_c of the turbulent eddies in the boundary layer near the trailing edge and the spanwise correlation length l_y are also estimated from the measured data. Leading edge interaction noise measurements are also compared to Amiet's model [6] using measured turbulent velocity spectra in the jet (see Chapter 2) as input data. All measurements presented in this Section are performed using the baseline 0 (see Figure 2.8).

3.1 Baseline airfoil trailing edge noise

3.1.1 Benchmark of the rig using a symmetric airfoil

The NACA0012 airfoil described in Chapter 2 was designed and tested as part of the validation procedure of the acoustic performances of the open-jet wind tunnel [29]. Due to its symmetric geometry it is commonly used as a reference airfoil for benchmarking purposes.

This Section verifies the use of unsteady surface pressure measurements as an input into Amiet's flat plate model to predict TE noise. The advantage of this airfoil model resides in being able to mount the pressure sensors flush underneath the surface without the use of RMPs described in Chapter 2. The wall pressure spectra ϕ_{qq_S} and ϕ_{qq_P}, are measured at $x/c = -0.36$ on the airfoil suction side and pressure side, respectively. To account for the radiation from both sides, the wall pressure spectrum input into Amiet's model [7] is therefore the sum of the surface pressure spectra near the TE on the suction and pressure sides, i.e., $\phi_{qq} = \phi_{qq_S} + \phi_{qq_P}$. Following previous studies [7, 18, 97, 100, 31], the convection speed U_c of the turbulence in the boundary layer, defined below in Equation 3.2, and the Corcos constant b_c were chosen as $U_c = 0.7U_0$ and $b_c = 1.6$. The procedure to determine these parameters experimentally is shown in the next Section from the wall pressure measurements performed on the NACA65(12)-10 airfoil and follows that of these previous studies. Note that Amiet's model is also corrected for the refraction of the acoustic waves through the shear layer of the open-jet [9].

Figure 3.1 shows the Sound Pressure Level spectra $SPL(f)$ given in Equation 2.1 at 90^o of the airfoil trailing edge, measured for the two mean flow velocities of U_0 =20 and $40\,m/s$ at 0^o angle of attack. Predictions from the Amiet [7] and Brooks [19] semi-empirical models, based on measurements on a NACA0012 airfoil, are also shown for comparison. The nearly identical matching of the measured wall pressure spectra ϕ_{qqS} and ϕ_{qqP} measured on either sides of the airfoil shows that at 0^o angle of attack the airfoil is at near zero loading. These measurements are in good agreement with Amiet and Brooks models and therefore validate the experimental procedure to measure and predict airfoil trailing edge noise in ISVR's open-jet wind tunnel.

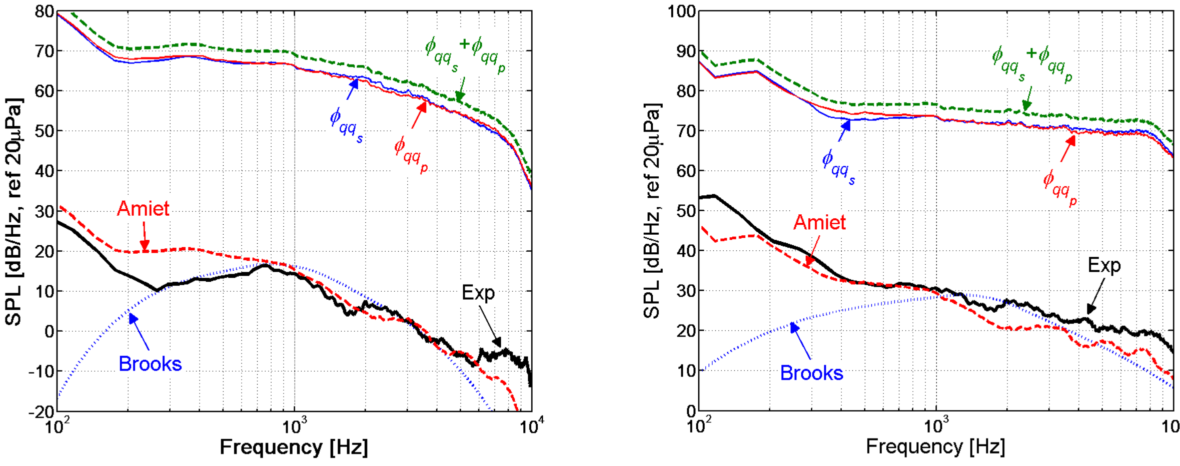

(a) At $U_0 = 20m/s$. (b) At $U_0 = 40m/s$.

Figure 3.1: Validation of the trailing edge noise measurements on the tripped baseline NACA0012 airfoil at 0^o AoA.

3.1.2 Airfoil self noise measurements on a cambered airfoil

3.1.2.1 Unsteady wall pressure measurements

The wall pressure spectrum (WPS) close to the airfoil trailing edge is of main importance in predicting the noise radiation using, for example, Amiet's TE noise model [7]. Therefore, a detailed study of the behaviour of the boundary layer spectrum is discussed in this Section, with the airfoil at 5^o angle of attack and at $U_0 = 20\,m/s$.

The wall pressure spectrum was measured using RMPs (see Chapter 2) along the chord of the NACA65(12)-10 airfoil on both the suction and pressure sides. Figure 3.2 shows the variation of the WPS along the chord, from $x/c = -0.53$ to -0.07. As the boundary layer develops and grows along the airfoil chord, on both sides, the level of the low frequency content of the spectrum increases while the high frequency decreases. This behaviour is also described by Sagrado [103] who performed detailed measurements of the WPS on a NACA0012 airfoil. Under the assumption of frozen turbulence, the pressure spectra of the turbulence measured along the span at $x/c = -0.07$ are verified to be nearly identical on the suction side and on the pressure side in the region of the airfoil trailing edge (see Figure 3.3). Figure 3.4 shows that as the airfoil angle of attack increases from -5^o to 15^o, and therefore as the boundary layer thickens, the WPS on the suction side increases at low frequencies and decreases at high frequencies, for all locations along the airfoil chord. The opposite behaviour occurs on the pressure side, i.e., when the airfoil angle of attack increases, the boundary layer thickness decreases. This is consistent with the observations made by Sagrado on the NACA0012 airfoil.

Figure 3.5 presents a comparison of the WPS measured in the current study with similar measurements performed by Winkler *et al* [121] at $x/c = -0.05$ at $U_0 = 22\,m/s$ on a NACA65(12)-63 airfoil. The results are shown non-normalized (Figure 3.5a), normalized on the outer scales δ^* and U_0 (Figure 3.5b) and normalized on the inner scales ν and u_τ (Figure 3.5c), where ν is the kinematic viscosity and $q_0 = 0.5\rho U_0^2$ is the dynamic pressure. These boundary layer parameters are estimated using Xfoil, as described in Chapter 2. The wall friction velocity u_τ is defined as $u_\tau = \sqrt{\tau_\omega/\rho}$, where τ_ω is the wall pressure shear stress and ρ is the density of air. The boundary layer parameters δ^* and τ_ω are determined using Xfoil (see Chapter 2). The normalization based on the outer scales shows that all the WPS measured at the four angles of attack 0, 5, 10 and 15^o and at the two flow speeds of $U_0 = 20$ and $40\,m/s$ collapse within 5 dB up to about $\omega\delta^*/U_0 = 0.7$. The high frequencies, i.e., when $\omega\nu/u_\tau > 0.2$, appear to collapse within 5 dB when normalized on inner scales. This is consistent with a similar study conducted by Sagrado [103]. Overall, the comparisons of the experimental data matches less well the measurement performed on the NACA65 profile by Winkler, within about 5 dB. These discrepancies are believed to be due to uncertainties about the values of the internal and external variables associated with Winkler's data.

Note that although various models exist to predict the WPS, including for example Goody [52], Rozenberg [100], Chase [26], Glegg-Jochault [51] or Willmarth-Roos [118], these were not computed in this study due to the large discrepancies between these models (see Blandeau [13]).

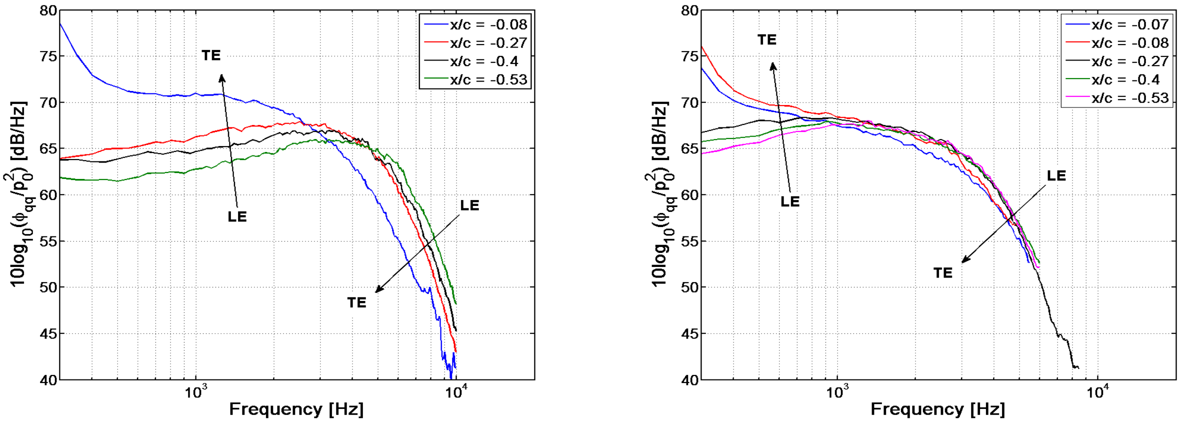

(a) Suction Side. (b) Pressure Side.

Figure 3.2: Wall pressure spectra at 5^oAoA and $U_0 = 20\,m/s$ ($p_0 = 20\mu Pa$).

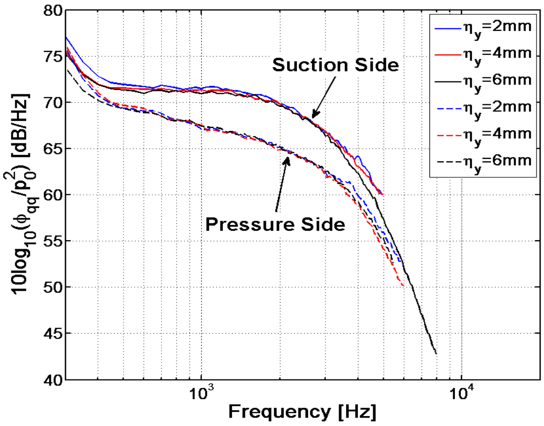

Figure 3.3: Uniformity of the wall pressure spectra along the airfoil span at $x/c = -0.07$, where $x = 0$ is at the LE - 5^o AoA and $U_0 = 20\,m/s$ ($p_0 = 20\mu Pa$), η_y is the separation distance between spanwise distributed sensors.

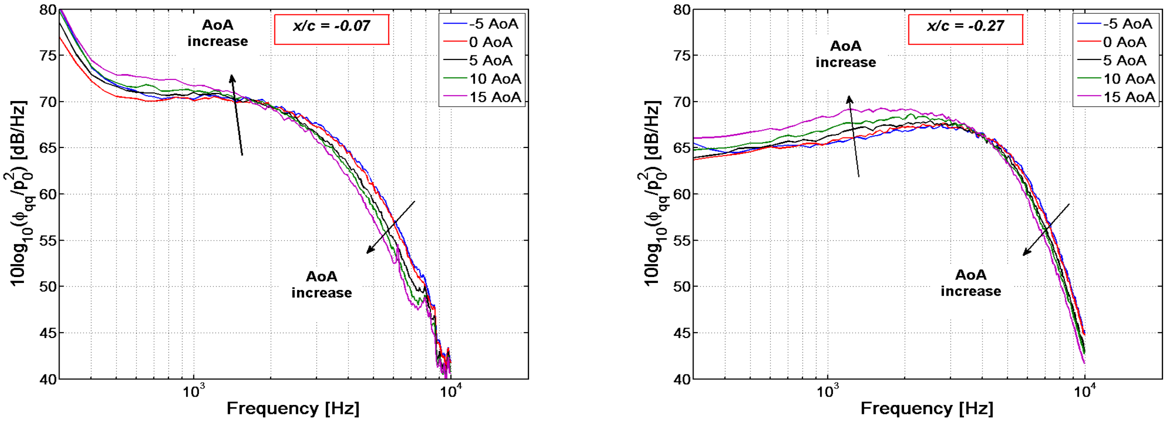

(a) Suction side $x/c = -0.07$.

(b) Suction side $x/c = -0.27$.

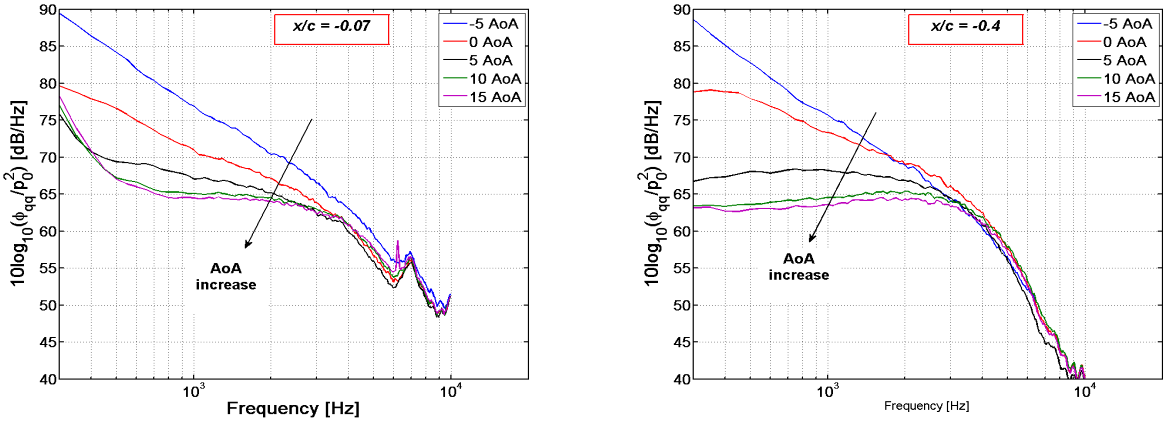

(c) Pressure side $x/c = -0.07$.

(d) Pressure side $x/c = -0.4$.

Figure 3.4: Variation of surface pressure spectrum with AoA at $U_0 = 20\,m/s$.

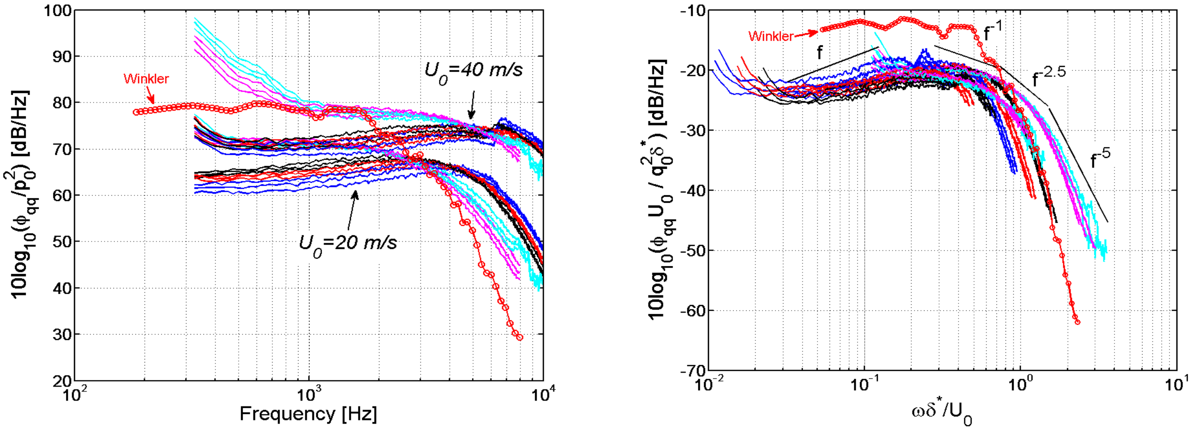

(a) Not normalized.

(b) Normalized with outer scales.

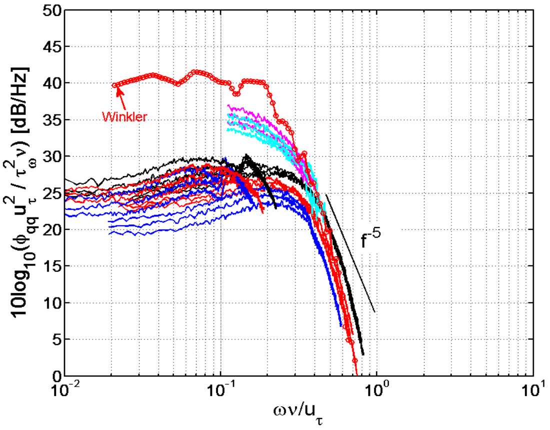

(c) Normalized with inner scales.

Figure 3.5: Surface pressure spectra normalization at $U_0 = 20\,m/s$ and $U_0 = 40\,m/s$, for all AoA and all x/c.

3.1.2.2 Flat plate theory input parameters

The trailing edge noise radiation model proposed by Amiet [7] and used in this thesis to compare to the experimental data, uses the pressure spectrum in the boundary layer ϕ_{qq} close to the trailing edge as input data. Equation 3.1 expresses the far field radiation as proposed by Amiet.

$$\phi_{pp}(\mathbf{x}, \omega) = D(\mathbf{x}, \omega)\ |\mathcal{L}(\omega)|^2\ l_y\,(\omega)\ \phi_{qq}(\omega), \tag{3.1}$$

where $D\,(\mathbf{x}, \omega)$ is a dipole type radiation function to the observer location $\mathbf{x}$, $\mathcal{L}\,(\omega)$ the acoustically weighted airfoil response function and $l_y(\omega)$ the spanwise correlation length. In order to predict the trailing edge noise radiation from the NACA65(12)-10 airfoil, the spanwise correlation length l_y and the WPS ϕ_{qq} near the trailing edge must be estimated from experimental data. This Section aims at estimating l_y close to the trailing edge from the measurements of the unsteady surface pressure presented in the previous Section. First, the convection velocity is calculated from the streamwise phase spectrum between pairs of sensors.

Convection velocity

The convection speed $U_c(f)$ is the speed at which each Fourier component of the turbulence wave number in the boundary layer is convected on the airfoil surface. It assumes frozen turbulence and it is determined from the gradient of the phase spectrum $d\phi_{ij}/df$ between streamwise pairs of sensors i and j separated by a distance $\eta_x = x_i - x_j$ (see Equation 3.2).

$$U_c(f) = \frac{2\pi\eta_x}{d\phi_{ij}(f)/df} \tag{3.2}$$

Figure 3.6 shows typical phase spectra between pairs of sensors separated by η_x=2 mm and η_x=20 mm. Table 3.1 summarizes the values of the convection velocities estimated for the two flow velocities $U_0 = 20$ and $40\,m/s$, and for various sensor separation distances with the reference sensor located in the mid-span plane at $10\,mm$ upstream of the trailing edge. Figure 3.6 and Table 3.1 emphasize the non uniqueness of the convection velocity, which can vary by up to about 20 % depending on frequency, mean flow velocity and sensor separation distance. Unless mentioned, a value of $U_c/U_0 = 0.7$ is used in the rest of this study, which is consistent with past studies [7, 18, 31, 97, 100, 103]. Rozenberg [100] also estimated that a relative error of 30 % in the estimation of the convection velocity only impaired the far field noise prediction by 1.4 dB using Amiet's semi-empirical model.

	Suction Side			Pressure Side		
η_x [mm]	2	30	50	2	30	50
$U_{c_{20}}/U_0$	0.6	0.8	0.9	0.9	0.8	0.75
$U_{c_{40}}/U_0$	0.77	0.7	0.9	-	-	-

Table 3.1: Estimation of the convection velocity U_c for $\eta_x = 2$, 30 and $50\,mm$, at 5^o AoA, where $U_{c_{20}}$ is measured at $U_0 = 20\,m/s$ and $U_{c_{40}}$ at $U_0 = 40\,m/s$.

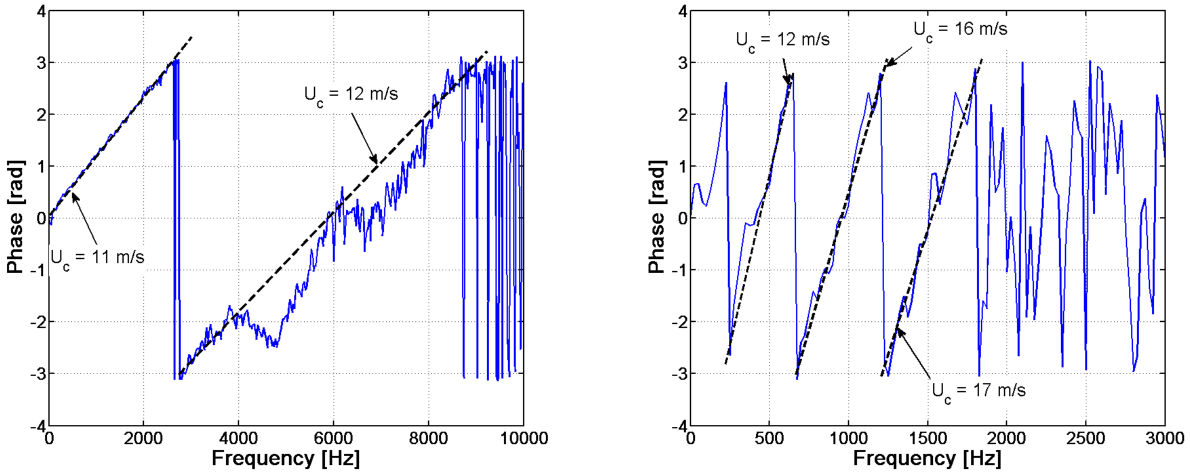

(a) $U_0 = 20\,m/s$, $\eta_x = 2\,mm$.

(b) $U_0 = 20\,m/s$, $\eta_x = 20\,mm$.

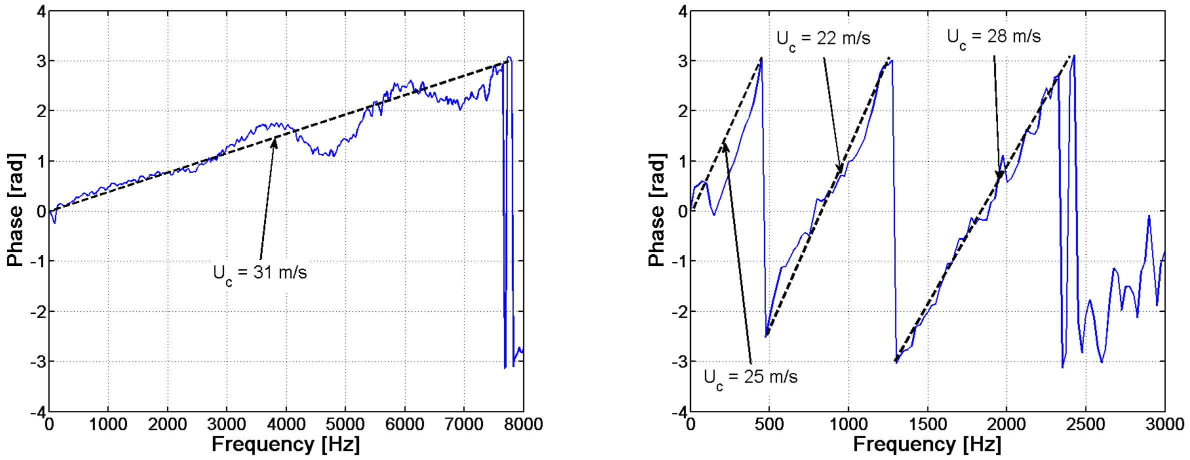

(c) $U_0 = 40\,m/s$, $\eta_x = 2\,mm$.

(d) $U_0 = 40\,m/s$, $\eta_x = 20\,mm$.

Figure 3.6: Convection velocity estimated from the phase spectrum ϕ_{ij} at 5^{o}AoA on the airfoil suction side.

Spanwise correlation length

The spanwise correlation length l_y is defined as the integral of the coherence function γ^2 over the span of the airfoil. For an airfoil with infinite span, it is defined as:

$$l_y(f) = \int_0^{\infty} \sqrt{\gamma^2(\eta_y, f)}\, d\eta_y, \tag{3.3}$$

where η_y is the spanwise separation distance between two sensors.

Due to the reduced number of sensors distributed along the span the correlation length cannot be estimated accurately using Equation 3.3 and therefore the model for the spanwise correlation length $l_y(f)$ given by Corcos [31] is used instead:

$$l_y\left(f\right) = \frac{b_c U_c}{f}, \tag{3.4}$$

where b_c is the Corcos constant, determined from data fitting to a measured coherence function. Brooks [18] proposed to model the coherence between two sensors as an exponential decaying as $1/l_y$ (Equation 3.5).

$$\gamma^2\left(f\right) = \exp\left(-C\frac{2\pi f}{U_c(f)}\eta_y\right), \tag{3.5}$$

where C is a constant. The correlation length of the turbulence along the airfoil span can therefore be estimated by data fitting of the measured coherence γ^2, defined in Equation 2.8, between pairs of sensors using Equations 3.4 and 3.5, where $\gamma^2(f) = exp(-\eta_y/l_y(f))$ and $b_c = \frac{1}{C}$.

Figure 3.7 shows the measured coherence γ^2 for the three spanwise sensor separation distances on the suction side, $\eta_y = 2$, 4 and $6\,mm$, at $\alpha = 5^o$ angle of attack and $U_0 = 20\,m/s$. The experimental data matches reasonably well with the exponential decay function given by Equation 3.5 when the value of b_c and hence l_y is chosen appropriately, i.e., $b_c = 0.66$ and $U_c = 0.7U_0$.

Table 3.2 summarizes the values of b_c obtained for the five angles of attack -5^o, 0^o, 5^o, 10^o and 15^o and the two mean flow velocities U_0 =20 and $60\,m/s$. The Corcos constant b_c varies between 0.6 to 0.8 and therefore does not significantly change with angle of attack and mean flow velocity, with a mean value of $b_c = 0.69$. Past studies [18, 97, 31] have generally shown higher values of b_c, between 1.4 and 1.7 for a similar range of velocities, flow conditions and on symmetrical and non-symmetrical airfoils. Although the Corcos constant b_c is lower than that reported by other researchers, the next Section shows that the value of b_c is consistent with the predictions of the far field pressure obtained using Amiet's model, i.e., typically within less than 5 dB.

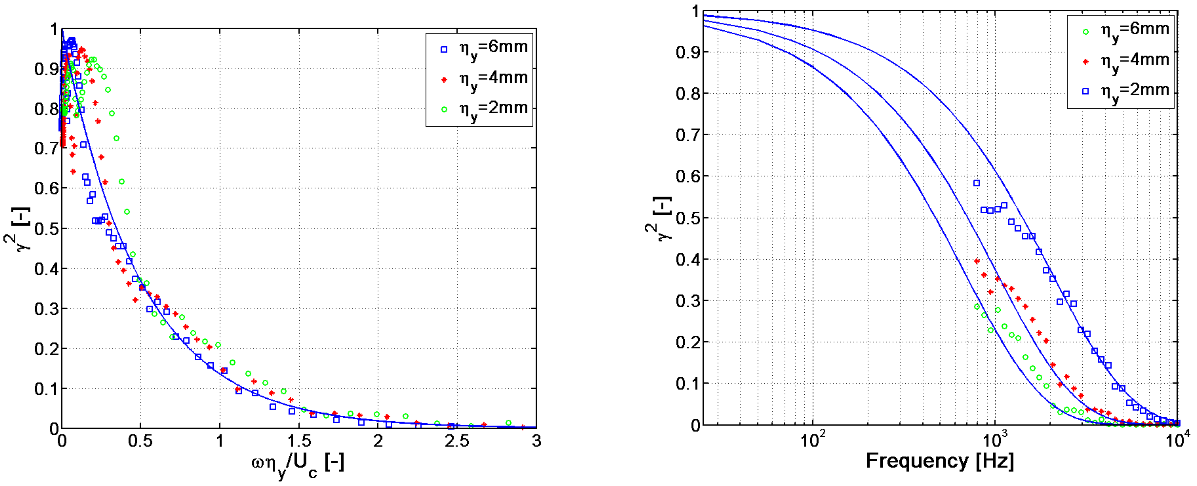

(a) Over non-dimensional frequency $\omega\eta_y/U_c$.

(b) Over frequency f.

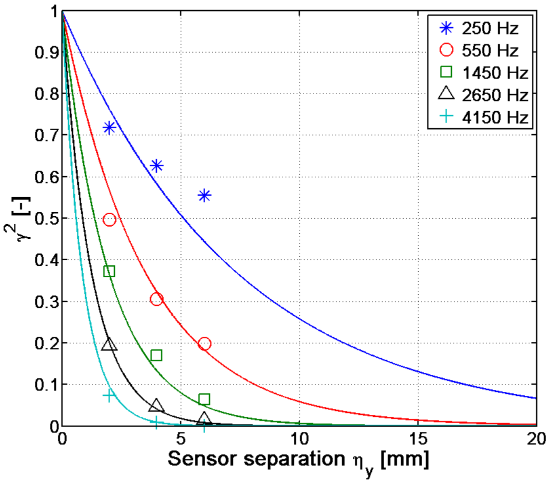

(c) Over separation distance η_y.

Figure 3.7: Data fitting of the coherence γ^2 given in Equation 2.8 with the Corcos model $\gamma^2 = exp(-\eta_y/l_y)$ at 5^o AoA and $U_0 = 20\,m/s$, with $b_c = 0.66$ and $U_c = 0.7U_0$.

AoA	-5^o		0^o		5^o		10^o		15^o	
U_0	20	40	20	40	20	40	20	40	20	40
b_c	0.73	0.65	0.69	0.59	0.66	0.61	0.82	0.75	0.72	0.67

Table 3.2: Estimation of the Corcos constant b_c with varying AoA and mean flow velocity U_0, with $U_c = 0.7U_0$.

3.1.2.3 Airfoil trailing edge noise: Experimental and analytical results.

Figures 3.8 to 3.11 show a comparison of the measured Sound Pressure Level spectra $SPL(f)$ (see Equation 2.1) spectra with Amiet's [7] prediction, for the four angles of attack 0^o, 5^o, 10^o and 15^o

and the two mean flow velocities $U_0 = 20$ and $40\,m/s$ with the WPS used as an input. The WPS measured at $x/c = -0.07$ close to the trailing edge on both sides of the airfoil are also shown and the sum $\phi_{qq_S} + \phi_{qq_P}$ is used as input into the Amiet's model. As discussed in the previous Section, the convection velocity is taken from experimental data as $U_c = 0.7U_0$ and the Corcos constant $b_c = 0.69$. The Sound Power Level spectrum $PWL(f)$ defined in Equation 2.2 is also shown at $U_0 = 20\,m/s$ in Figure 3.8 for comparison, where Amiet's model is predicted at the microphone locations and integrated over the radiation angle 50^o to 110^o using Equation 2.2. Amiet's trailing edge model is corrected for the refraction of the acoustic wave through the shear layers of the open-jet [9].

It can clearly be seen that, as for the NACA0012 airfoil (see Section 3.1), the general shape of the experimental far field noise spectra is strongly related to the wall pressure spectra, which indicates that the dominant acoustic sources are located close to the trailing edge of the airfoil. Generally, good agreement in level and shape, within about 3 dB, is obtained for $f > 300$ Hz. At lower frequencies, the level of the WPS is up to 20 dB higher, which explains the over prediction of the noise radiation by Amiet's model at these low frequencies, although the reason for this low frequency increase is currently not known. The oscillations in the spectrum are also reasonably well predicted.

Note that the WPS is not plotted above 6 kHz due to a poor calibration at higher frequencies, which is due to difficulties in correctly sealing the surface of contact between the in-duct calibrator and the cambered surface of the airfoil (see Chapter 2). The high frequency narrowband peak observed in the noise radiation at low Reynolds numbers and at the high angles of attack 10^o and 15^o only (see Figures 3.10b and 3.11 respectively) is most likely due to flow separation and instabilities developing in the boundary layer.

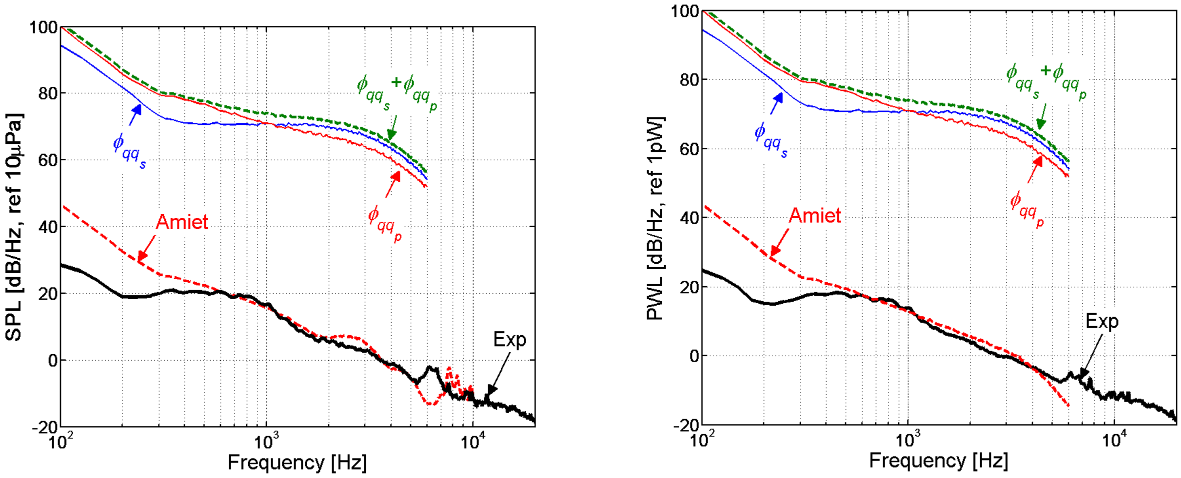

(a) SPL at 90^o.

(b) PWL.

Figure 3.8: Using the measured WPS into Amiet's model [7] to predict the measured TE noise at 0^o AoA and $U_0 = 20\,m/s$.

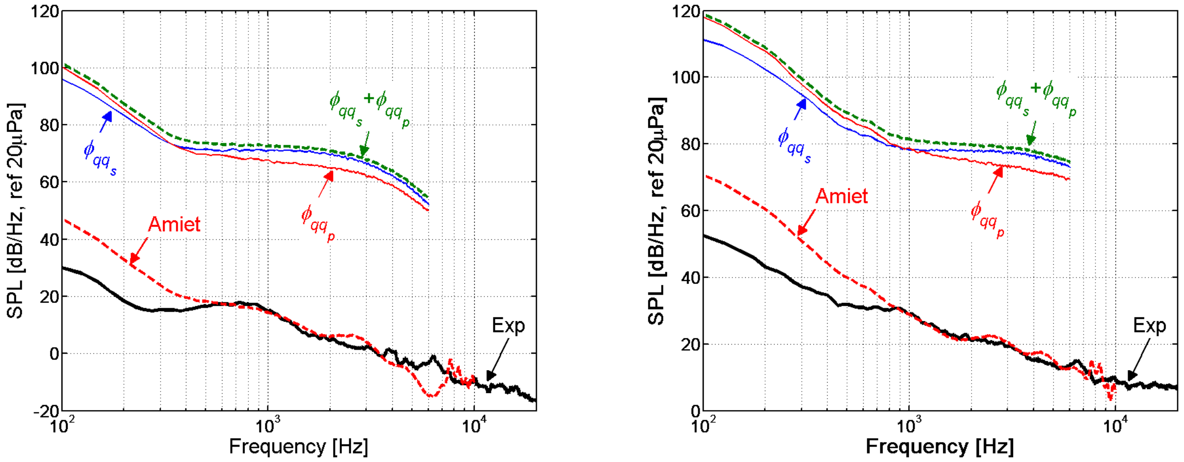

(a) $U_0 = 20\,m/s$.

(b) $U_0 = 40\,m/s$.

Figure 3.9: Using the measured WPS into Amiet's model [7] to predict the measured SPL TE noise at 90^o and at 5^o AoA.

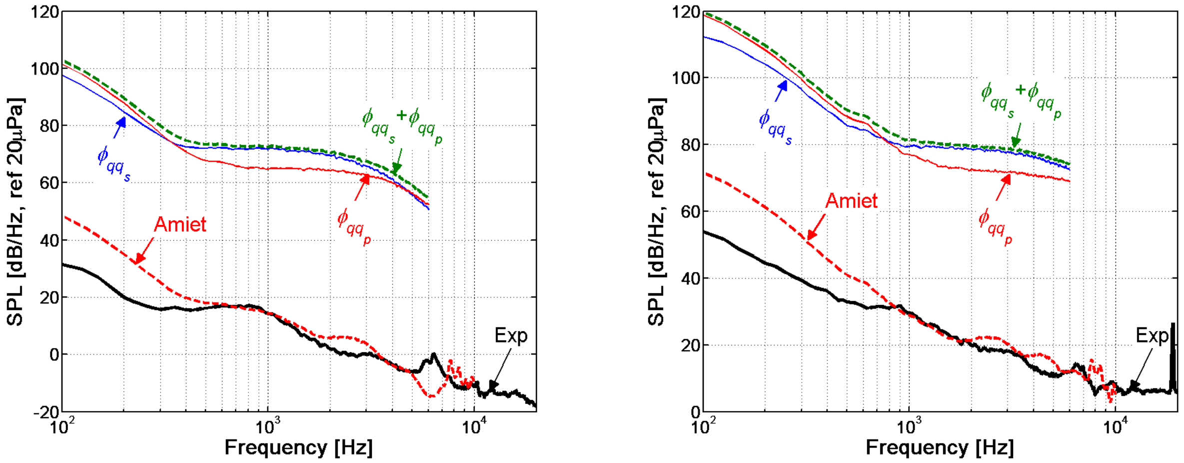

(a) $U_0 = 20\,m/s$.

(b) $U_0 = 40\,m/s$.

Figure 3.10: Using the measured WPS into Amiet's model [7] to predict the measured SPL TE noise at 90^o and at 10^o AoA.

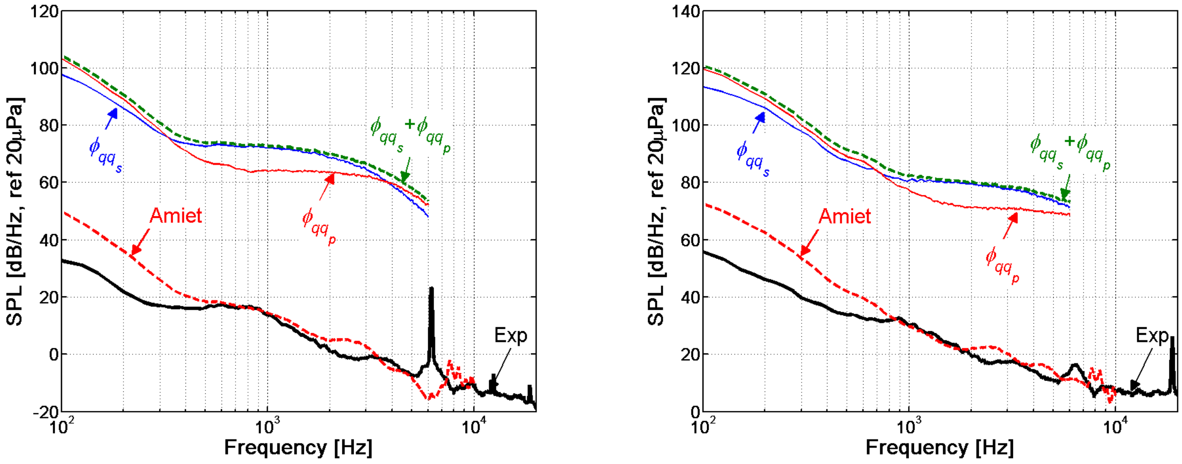

(a) $U_0 = 20\,m/s$.

(b) $U_0 = 40\,m/s$.

Figure 3.11: Using the measured WPS into Amiet's model [7] to predict the measured SPL TE noise at 90^o and at 15^o AoA.

3.1.2.4 Airfoil trailing edge noise: Directivity.

Figure 3.12 shows a comparison of the measured far field noise directivity using the circular microphone arc (see Chapter 2) at $U_0 = 20\,m/s$ with Amiet's noise prediction [7] computed using measured WPS, as discussed in the previous Sections, and corrected for the shear layer effects [9]. Results are presented for an angular range of 45^o to 115^o at the four discrete frequencies f = 400, 1350Hz, 2100 and 4000 Hz. The radiation pattern is similar to a single compact dipole at low frequencies, while with increasing frequency, the acoustic source becomes a distribution of elementary acoustic sources, which results in a directivity pattern with numerous side lobes. The trailing edge noise is also shown to radiate upstream, i.e., towards the leading edge of the airfoil.

In general the agreement in shape between experimental data and noise predictions is good but with the experimental results shifted down by about 10^o. This could partly be due to installation effects caused by the presence of the nozzle close to the microphone array. Moreau *et al* [87], reported that the presence of the nozzle affects the free field radiation condition that normally occurs in the anechoic chamber. Therefore, diffraction effects from the rig have to be taken into account for experimental data fitting with noise prediction models, as seen in Figure 3.13, where a shift in the main radiation lobe can be seen. However, this was not further investigated in this thesis as the main goal of this project was to investigate trailing edge and leading edge noise reduction treatments (see Chapters 4 to 7).

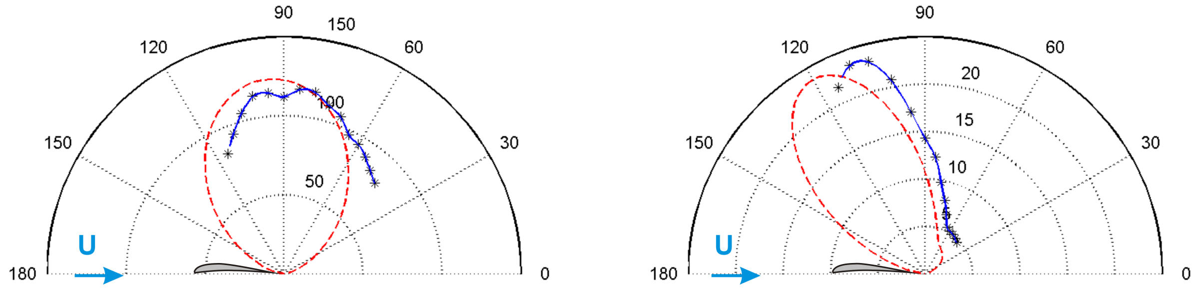

(a) $f = 400\,\text{Hz}$.

(b) $f = 1350\,\text{Hz}$.

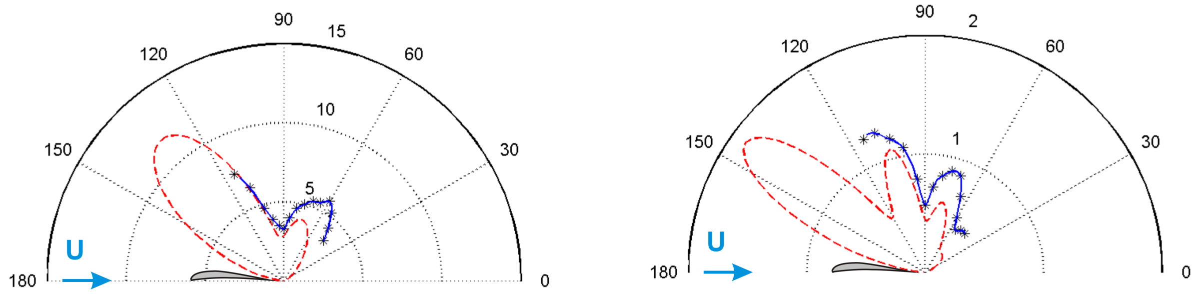

(c) $f = 2100\,\text{Hz}$.

(d) $f = 4000\,\text{Hz}$.

Figure 3.12: Polar directivity in Pa^2/Hz (normalized by p_0=20μPa), at $U_0 = 20\,m/s$, (–) Amiet, (*) Experiments.

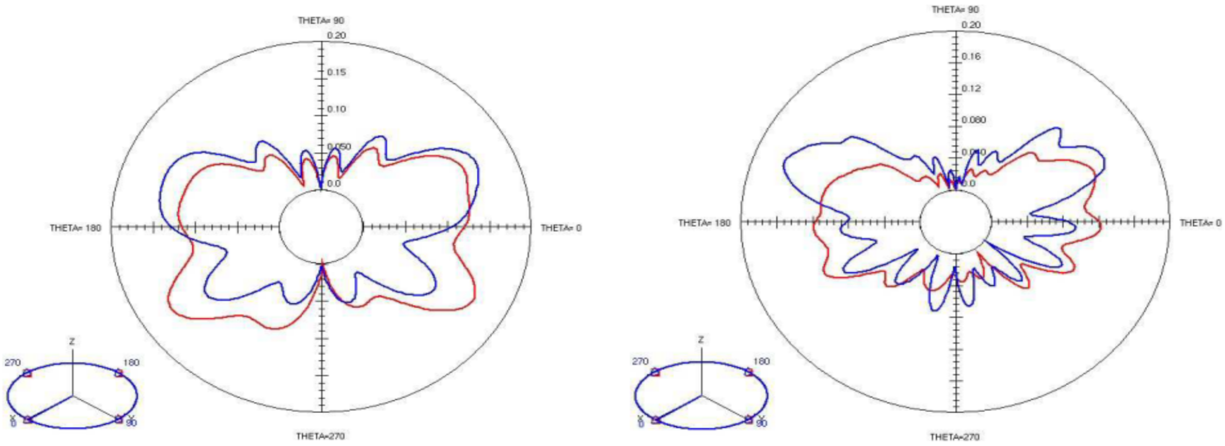

(a) 1 kHz. Red: unit dipole at the TE; blue: dipole distribution according to Amiet's theory.

(b) 2 kHz. Red: unit dipole at the TE; blue: dipole distribution according to Amiet's theory.

Figure 3.13: Broadband diffraction effects on TE noise in ECL's open-jet facility (taken from Moreau *et al* [87]), where Amiet's distribution includes the actual experimental set-up with a simplified model of the nozzle and side plates, at 8^o AoA.

3.2 Baseline airfoil turbulence / leading edge interaction noise

This chapter describes measurements of leading edge turbulence interaction noise on the baseline NACA65(12)-10 airfoil, using turbulence grids located in the nozzle of the open-jet, as described in Chapter 2. This measurement will be useful in Chapter 7 where interaction noise is measured and reduced in a tandem airfoil configuration.

3.2.1 Airfoil leading edge noise: Experimental and analytical results

Turbulence in the flow is generated by introducing a wooden bi-planar grid in the contraction section of the nozzle, as described in Chapter 2. Two grids with streamwise turbulence intensity TI (2.5 and 2.1 % respectively) and integral length scale Λ_{uu} (6 and 5 mm respectively) were used in turn to generate controlled turbulence for the investigation of leading edge turbulence interaction noise.

Figure 3.14 shows the Sound Power Level spectrum $PWL(f)$ defined in Equation 2.2, measured with the airfoil at 0^o angle of attack and for the two flow velocities of $U_0 = 20$ and $60\,m/s$. It is presented with both grids used in turn to generate turbulence in the jet. Details of the turbulence grids and their turbulence characteristics are presented in Section 2.4.1. Amiet's interaction noise model [6] was also implemented to predict the sound power level spectrum with both incoming turbulence characteristics. Reasonably good agreement is shown between experimental and theoretical data except at the lower frequencies, where the jet noise dominates. The change from turbulence grid 1 ($TI = 2.5\,\%$ and $\Lambda_{uu} = 6\,mm$) to grid 2 ($TI = 2.1\,\%$ and

$\Lambda_{uu} = 5\,mm$) introduces a reduction of the measured Sound Power Level spectrum $PWL(f)$ of up to about 4 dB in the frequency ranges [0.1 - 0.8] kHz and [0.3 - 2] kHz, at U_0 =20 and 60 m/s respectively. Amiet's model also predicts a similar change in the Sound Pressure Level, but over a broader frequency range, as shown in Figure 3.14. Overall, Figure 3.14 shows that the use of grids allows the generation of controlled turbulence to measure airfoil interaction noise in the open-jet wind tunnel. The change in the turbulence intensity TI and integral length scale Λ_{uu}, measured at the airfoil leading edge in the incoming flow, does not appear to affect frequencies higher than 2 kHz.

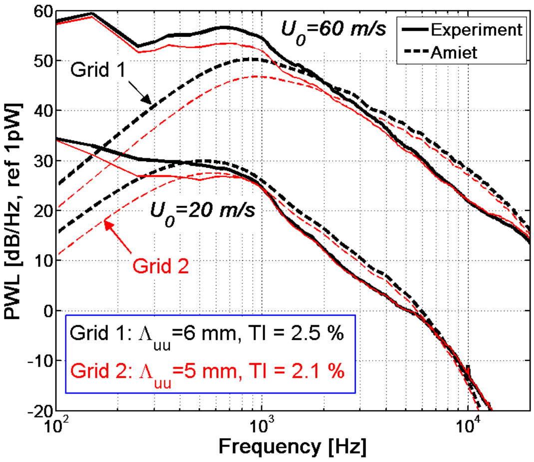

Figure 3.14: Typical leading edge turbulence interaction noise spectrum $PWL(f)$ at 0^o AoA, measured for both grids, and compared to Amiet's model [6].

3.2.2 Variation of LE noise with airfoil angle of attack

Figure 3.15 shows the variation of the Sound Pressure Level spectrum $SPL(f)$ at U_0 =20 and 60 m/s, for the four angles of attack 0^o, 5^o, 10^o and 15^o. At U_0 =20 m/s, the sound pressure level reduces by up to 4 dB below 10 kHz with increasing angle of attack, at a rate of approximately 1 dB for each 5^o increase of the geometrical angle of attack. At $U_0 = 60\,m/s$ this reduction is limited to 2 dB up to 2 kHz, with a rate of about 0.5 dB for each 5^o increase. However, experimental studies by others, where grid generated turbulence was used, for example, Paterson *et al* [93], Oerlemans *et al* [89], Moreau *et al* [85], Devenport *et al* [37] and Hutcheson *et al* [69] showed either no significant effect or a small increase of less than 3 dB of the interaction noise when increasing the airfoil angle of attack. In particular, Hutcheson *et al* [69] emphasized that the interaction noise spectrum was strongly dependent on angle of attack when the turbulence longitudinal integral length scale to chord ratio $\Lambda_{uu}/c > 1$ (about 2 dB for each 5^o increase), and that this dependency decreased when $\Lambda_{uu}/c < 1$. Moreau *et al* [85] also emphasized that the LE noise is considerably reduced when the leading thickness becomes larger than the integral length scale of the turbulence.

In the current study, $\Lambda_{uu}/c = 0.04$ for Grid 1 and 0.03 for Grid 2. Therefore, although the ratio of the turbulence streamwise integral length scale Λ_{uu}/c is small, the conclusions from previous studies indicate that the variations measured in the LE noise spectra when increasing angle of attack may be due to some non-homogeneity of the turbulence statistics across the test section. Due to the location of the grid in the contraction part of the nozzle, distortion of the turbulence is likely to occur at the airfoil test section, causing the local integral length scale to vary slightly as the leading edge is moved upwards from 0^o to 15^o angle of attack. However, generating perfectly homogenous and isotropic turbulence with no noise contamination due to grid self noise proved difficult in the current study and in previous work [93, 89, 85, 37, 69].

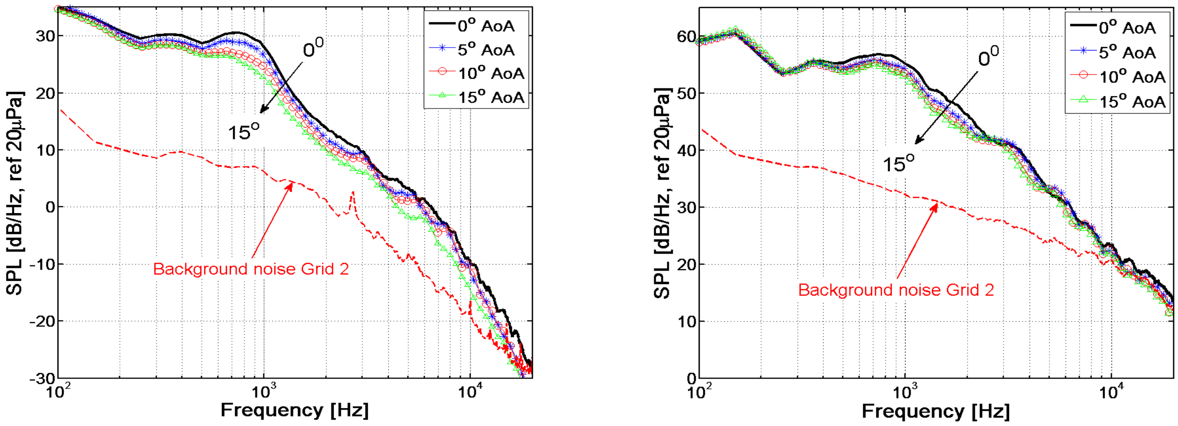

(a) $U_0 = 20m/s$.

(b) $U_0 = 60m/s$.

Figure 3.15: Variation of LE noise with increasing angle of attack.

Chapter 4

Airfoil trailing edge noise reduction using sawtooth serrations

The main aim of this Chapter is to investigate in detail the trailing edge noise reduction performance of sawtooth serrations. The reduction of the turbulence in their wake will also be investigated. The results of an extensive experimental campaign are reported, in which thirty seven trailing edge serration geometries were designed, manufactured and tested on the NACA65(12)-10 airfoil. The noise reductions were measured in the ISVR's open-jet facility and are presented as a function of frequency, mean flow velocity ($U_0 = 20$, 40, 60 and $80\,m/s$), serration geometry and airfoil angles of attack ($\alpha_g = 0^o$, 5^o, 10^o and 15^o). The results of a blow-down test are also reported, in which the noise is continuously recorded while the mean flow velocity is slowly but steadily increased.

The static pressure distribution along the airfoil was also measured in order to assess the effect of the trailing edge serrations on the lift. Hot wire measurements were performed in the boundary layer and in the wake of some representative serrated trailing edges to estimate the changes in turbulence, length scales and wake spreading. The drag was estimated by integration of the mean flow velocity profiles over the wake width.

A further objective of this Chapter is to compare the noise reduction against the theory proposed by Howe [66] for predicting the noise from serrated trailing edge airfoils. The assumptions made by Howe and the main steps of the derivation are detailed in Chapter 1.

Unless mentioned, the experimental data shown, are for the angle of attack $\alpha_g = 5^o$ and the mean flow velocity $U_0 = 40\,m/s$. The mechanisms of the change in the noise radiation due to serrated trailing edges are further discussed in Chapter 5. From hereon, all measurements presented in this thesis are performed using the baseline 2 (see Figure 2.8), where the amplitude $2h$ can be adjusted to that of the treated airfoil, as explained in Section 4.1.

4.1 Geometry of the serrations

Two geometrical parameters define the sawtooth serration, the serration periodicity λ and the serration amplitude $2h$, as shown in Figure 4.1 inserted into the NACA65(12)-10 airfoil trailing edge.

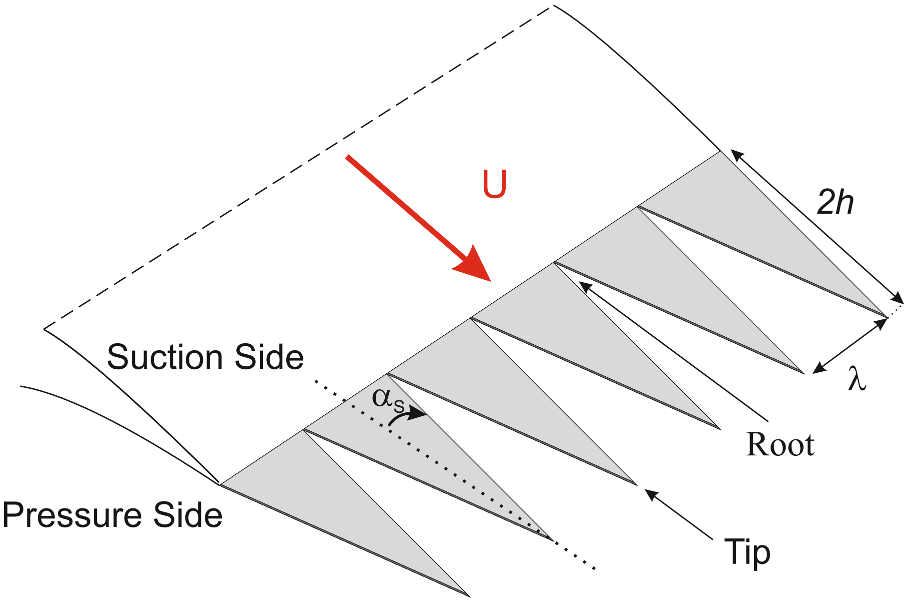

Figure 4.1: Sketch of the flat plate insert trailing edge serration with geometrical parameters λ and $2h$.

In order to experimentally investigate the noise and aerodynamic performances of the serrations with variations of λ and h, thirty seven serrations were designed and tested in the ISVR's wind tunnel. The spanwise periodicity λ was varied from $1.5\,mm$ to $12.5\,mm$, while the amplitude of the serrations $2h$ was varied from $1\,mm$ to $40\,mm$. For each trailing edge serration, a straight trailing edge was tested at the same flow conditions to allow comparisons of the noise data. In order to minimize the influence of the different serrated edges on the total lift of the airfoil, the baseline straight edge airfoil was designed to have the same surface area as the corresponding serrated trailing edge.

The trailing edge treatments were cut from stiff card of thickness $0.8\,mm$, using a laser, and inserted in the blunt slotted trailing edge of the airfoil (see Chapter 2). This technique also allowed fast and consistent mounting of all trailing edge serrations. Comparisons of the noise radiated from a metal trailing edge insert with an identical thickness of $0.8\,mm$ and a cardboard trailing edge insert showed almost identical noise spectra (see Chapter 2).

The serrated trailing edges were split into two sets, as shown in Figure 4.2 and as listed in Tables 4.1 and 4.2.

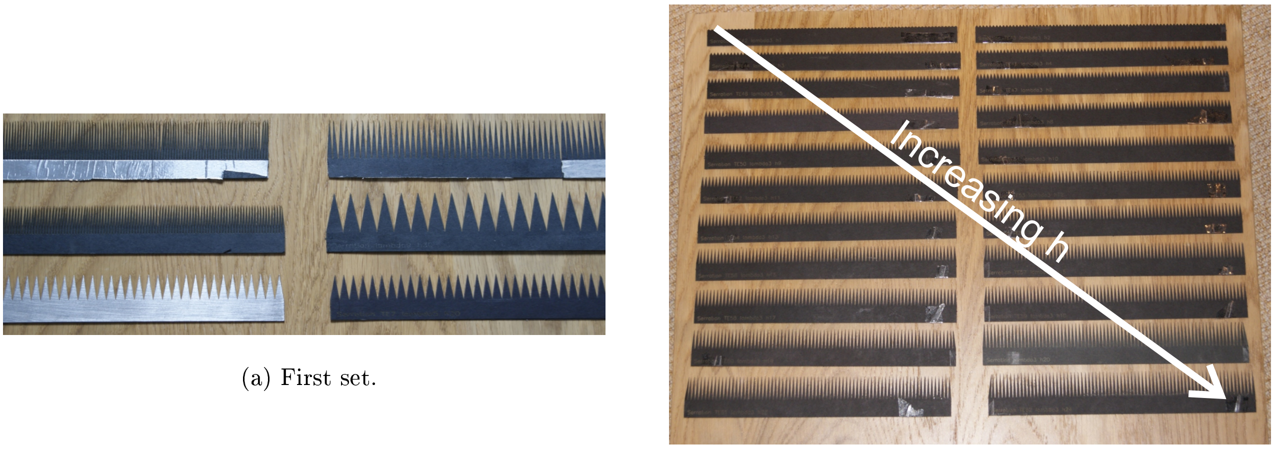

(a) First set.

(b) Second set.

Figure 4.2: Picture of some serrated trailing edge inserts.

In the first set of serrations tested, listed in Table 4.1, the noise impact of varying the non dimensional parameter λ/h, which quantifies the angle of the edges of a given serration to the flow direction ($\cos(\alpha_S) = \lambda/h$ in Figure 4.1) was investigated. Note that the dimensions of the smaller (sharper) serrations were not optimized for noise reductions but were limited by the accuracy of the laser beam, which is $0.25\,mm$. It is worth mentioning that the serration $\lambda/h = 0.3$ ($\lambda = 3\,mm$ and $2h = 20\,mm$) was selected as the best serrated treatment within the FP7 European project FLOCON [1], for giving the best noise reductions with minimum effect on the aerodynamic performances.

	$2h$	λ	λ/h	α_S [^{o}]	Material
1	30	1.5	0.1	1.43	Cardboard
2	20	1.5	0.15	2.15	Cardboard
3	30	3	0.20	2.86	Cardboard
4	20	3	0.30	4.29	Cardboard
5	30	7	0.47	6.65	Metal
6	20	5	0.50	7.13	Metal
7	30	9	0.60	8.53	Cardboard
8	30	12.5	0.83	11.77	Metal
9	20	8.5	0.85	12.00	Metal
10	20	19	1.90	25.41	Metal

Table 4.1: Geometrical parameters of the first set of trailing edge serration inserts as depicted in Figure 4.1 - All units in mm.

The second set of trailing edge serrations, listed in Table 4.2, was designed to investigate, more systematically, the variation in noise reduction with the amplitude of the serrations. Therefore, while keeping the periodicity λ constant, the amplitude $2h$ of the serrations was gradually increased from $1\,mm$ to $40\,mm$ to determine if, as concluded by Howe, the noise reduction increases as α_S reduces. The periodicity was chosen as $\lambda = 3\,mm$.

	$2h$	λ	λ/h	$\alpha_S\,[^o]$
11	1	3	6	56.31
12	2	3	3	36.87
13	3	3	2	26.57
14	4	3	1.50	20.56
15	5	3	1.20	16.70
16	6	3	1	14.04
17	7	3	0.86	12.09
18	8	3	0.75	10.62
19	9	3	0.67	9.46
20	10	3	0.60	8.53
21	11	3	0.55	7.77
22	12	3	0.50	7.13
23	13	3	0.46	6.58
24	14	3	0.43	6.12
25	15	3	0.40	5.71
26	16	3	0.38	5.36
27	17	3	0.35	5.04
28	18	3	0.33	4.76
29	19	3	0.32	4.51
30	20	3	0.3	4.29
31	22	3	0.27	3.90
32	24	3	0.25	3.58
33	26	3	0.23	3.30
34	28	3	0.21	3.07
35	30	3	0.20	2.86
36	35	3	0.17	2.45
37	40	3	0.15	2.15
-	-	-	-	-

Table 4.2: Geometrical parameters of the second set of trailing edge serration inserts as depicted in Figure 4.1 - All units in mm, all inserts made of cardboard of thickness $0.8\,mm$.

4.2 Noise radiation from a sawtooth serrated trailing edge

This section describes the measured noise and aerodynamic performances of the sawtooth serrated geometries, listed in Tables 4.1 and 4.2, measured in the ISVR open-jet wind tunnel. Note that the convection velocity, measured to be about $U_c = 0.7U_0$ (see Chapter 3) on this airfoil, is used in Howe's model to predict the theoretical noise reductions.

In this thesis, the boundary layer thickness δ is used as a normalization parameter for the noise reduction, as suggested by Howe. For each mean flow velocity, airfoil angle of attack and chord length (depending on the serration amplitude $2h$), the boundary layer thickness was estimated at $x/c = -0.01$, using the panel method code Xfoil [38], as described in Section 2.6.3. Although less accurate than CFD calculations, this prediction tool was used for rapid calculation due to the large number of cases tested, i.e., 432 in total (4 flow velocities, 4 angles of attack and 27 chord lengths). As explained in Chapter 2, the angles of attack input to Xfoil were corrected so that the jet deflection due to the airfoil, present in the experiments, is taken into account. As seen in Chapter 2, a reasonable match of the static pressure coefficient distribution with experimental data was obtained. In order to allow for the use of Xfoil to predict the boundary layer thickness δ, it is assumed that it remains unchanged by the presence of the sawtooth.

4.2.1 Variation of sound power level with varying λ

4.2.1.1 Experimental results

This Section investigates the variation of the sound power level radiated between 50^o and 110^o to the trailing edge with varying sawtooth periodicity λ and for two given serration amplitudes $2h$, as listed in Table 4.1 (first set of serration geometries). Figure 4.3 shows a comparison of the sound power level spectrum $PWL(f)$, defined by Equation 2.2, for the nine serrations given in Table 4.1 relative to that of a straight edge of identical wetted surface area. Data are presented over the low and mid frequency bandwidth 300 Hz to 7 kHz (Figure 4.3a and c), and over the high frequency bandwidth 7 kHz to 20 kHz (Figure 4.3b and d).

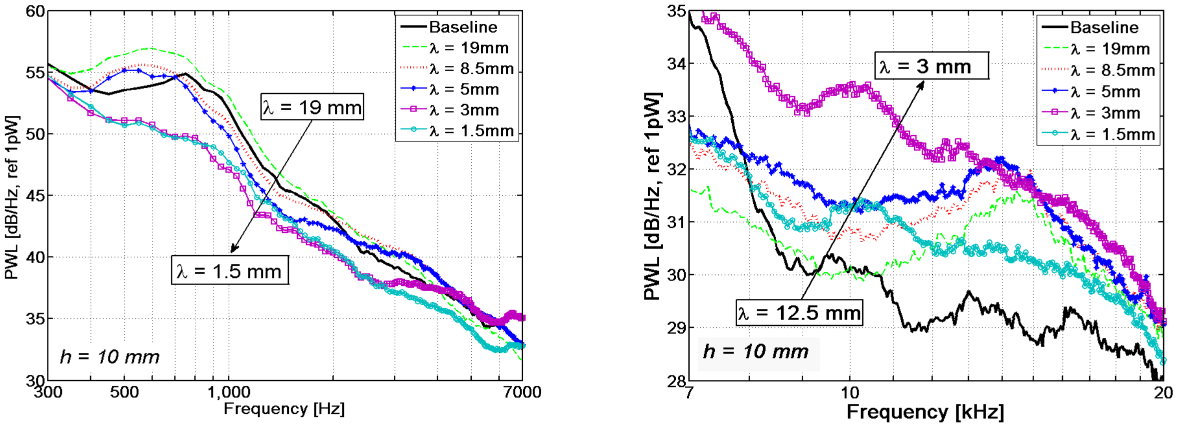

(a) $h = 10\,mm$ from 300 Hz to 7 kHz.

(b) $h = 10\,mm$ from 7 kHz to 20 kHz.

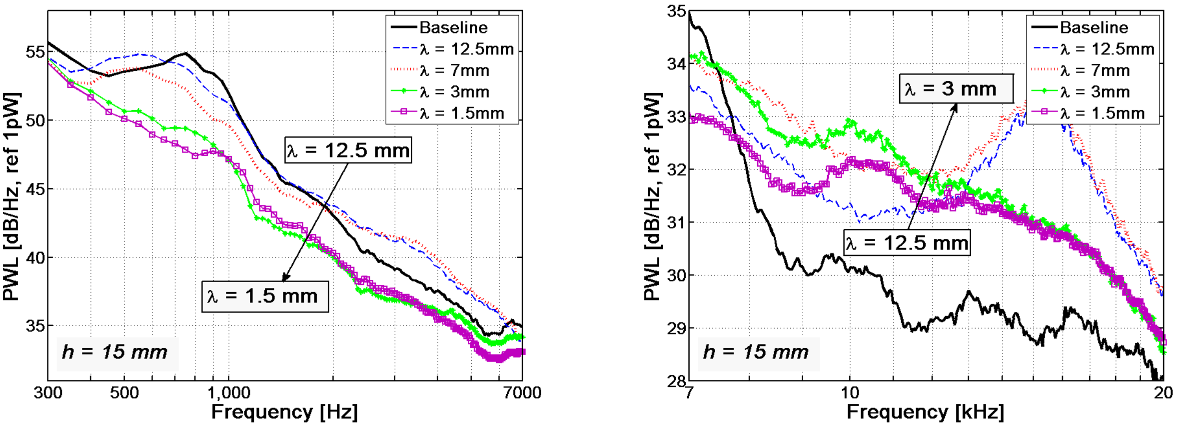

(c) $h = 15\,mm$ from 300 Hz to 7 kHz.

(d) $h = 15\,mm$ from 7 kHz to 20 kHz.

Figure 4.3: Measured far field power spectra showing a comparison between baseline straight edge and serrated edges for various values of λ and two values of h. The airfoil is at 5^o AoA and $U_0 = 40\,m/s$.

Figure 4.3a shows that at lower frequencies, below 400 Hz, noise reductions are limited to 1 dB due to the dominance of jet noise. For $\lambda = 1.5\,mm$ and $\lambda = 3\,mm$, a maximum noise reduction of about 5 dB is obtained in the mid frequency range. Generally, the noise reduction is increased as λ is reduced. As shown in Figure 4.3c, a similar behaviour is observed for a larger amplitude of $h = 15\,mm$, with a larger maximum reduction of 7 dB for $\lambda = 1.5\,mm$. Figures 4.3b and d show an increase in the sound power level spectrum $PWL(f)$ at high frequencies, for all values of λ, which increases with decreasing λ. The power increases by a maximum of about 3 dB for all cases.

Figure 4.3 shows that, given the flow conditions of this study, sawtooth serrations are most effective at reducing the radiation efficiency in the mid frequency range, while for higher frequencies, the sound power increases with decreasing λ. This increase in the noise radiation using serrations at the airfoil trailing edge was reported in other studies, as mentioned previously. Oerlemans [88] observed that a misalignment of the serrations with the flow direction causes this increase in noise. Note that the highest measured noise reduction is achieved for the serrations λ/h=0.15.

4.2.1.2 Comparison with Howe's theory

Figure 4.4 shows a comparison of the narrow band noise reduction $\Delta SPL = 10\log_{10}(\phi_{pp_\mathrm{b}}(f)/\phi_{pp_\mathrm{s}}(f))$, where $\phi_{pp_\mathrm{b}}(f)$ and $\phi_{pp_\mathrm{s}}(f)$ are the acoustic spectra measured over the straight trailing edge airfoil and over the serrated trailing edge airfoils, respectively. Experimental data are compared to Howe's prediction for the two serrations λ/h= 0.1 and 0.6 . The predicted noise reduction is approximately 15 to 30 dB higher than the measured reduction. Furthermore, the predicted noise reduction tends to increase with frequency while the measured reduction decreases with frequency. The strong oscillations in the theoretical noise reduction presented in Figure 4.4 for the case $\lambda/h = 0.1$ are due to interferences between the root and the tip of the serrations, which are not observed in the experimental data. These oscillations in noise reduction are predicted not to occur for $\lambda/h = 0.6$. Small oscillations (within 1 dB) are observed in the experimental noise reductions shown in Figure 4.4. However, these oscillations are of comparable amplitudes for both serrations $\lambda/h = 0.1$ and $\lambda/h = 0.6$ and are therefore not to be compared with the edge interferences mentioned above and described by Howe.

The increase in noise at high frequencies in the experimental data suggests that additional noise sources are present due to the introduction of serrations. This issue will be discussed in detail in Chapter 5. Other studies by Oerlemans [88], Parchen [92], Dassen [36] and Finez [42] for example, have found identical trends where the noise radiated over a serrated trailing edge is increased at high frequency.

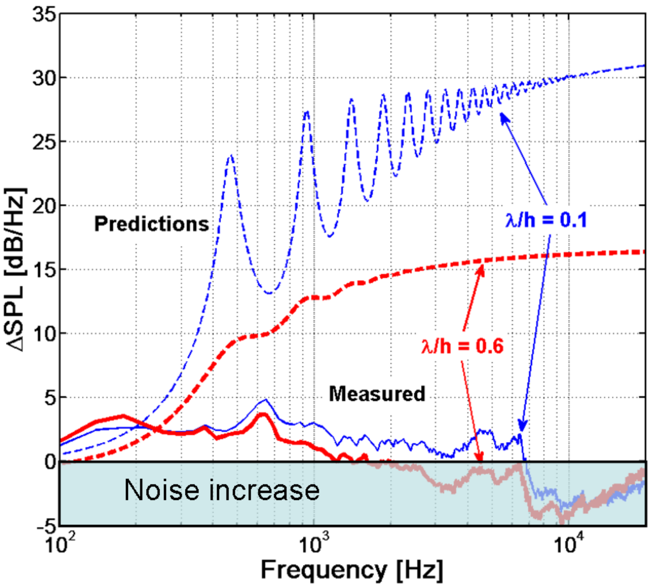

Figure 4.4: Narrow band noise reduction predicted by Howe (Dashed) and measured experimentally (Solid) for serration profiles $\lambda/h=0.6$ and $\lambda/h=0.1$ - Experimental data at 90^o with airfoil at 5^oAoA and $U_0 = 40\,m/s$.

Equation 4.1 defines the difference in the frequency-averaged sound power level $\Delta OAPWL$ between 50^o and 110^o, between a sawtooth trailing edge and a straight trailing edge airfoil.

$$\Delta OAPWL = 10\log_{10}\left(\frac{\sum\limits_j\sum\limits_i^N \phi_{pp}(f_j,\theta_i)|_{\mathbf{s}}}{\sum\limits_j\sum\limits_i^N \phi_{pp}(f_j,\theta_i)|_{\mathbf{b}}}\right), \qquad \begin{array}{c} i=1,...,13 \\ f_1 < f < f_2 \\ 50^o < \theta < 110^o \end{array}, \qquad (4.1)$$

where $\phi_{pp}(f,\theta_i)|_{\mathbf{s}}$ is the pressure spectral density measured at microphone i for a serrated trailing edge, $\phi_{pp}(f,\theta_i)|_{\mathbf{b}}$ is the pressure spectral density measured at microphone i for the straight edge baseline airfoil, and $N=13$ is the number of microphones.

Figures 4.5a and b show $\Delta OAPWL$, as given in Equation 4.1, against λ/δ, averaged over the low frequency bandwidth 1 kHz to 2 kHz, and over the high frequency bandwidth 10 kHz to 12 kHz, respectively. The results are shown together for the angles of attack 0^o, 5^o and 10^o, the mean flow velocities U_0 =20, 40 and 60 m/s and for $h=10\,mm$ (square) and $h=15\,mm$ (circle). Note that λ is non-dimensionalised by the boundary layer thickness δ, as suggested by Howe, in order to compare the data from both sawtooth amplitudes $h=10\,mm$ and $h=15\,mm$, presented in Figure 4.3.

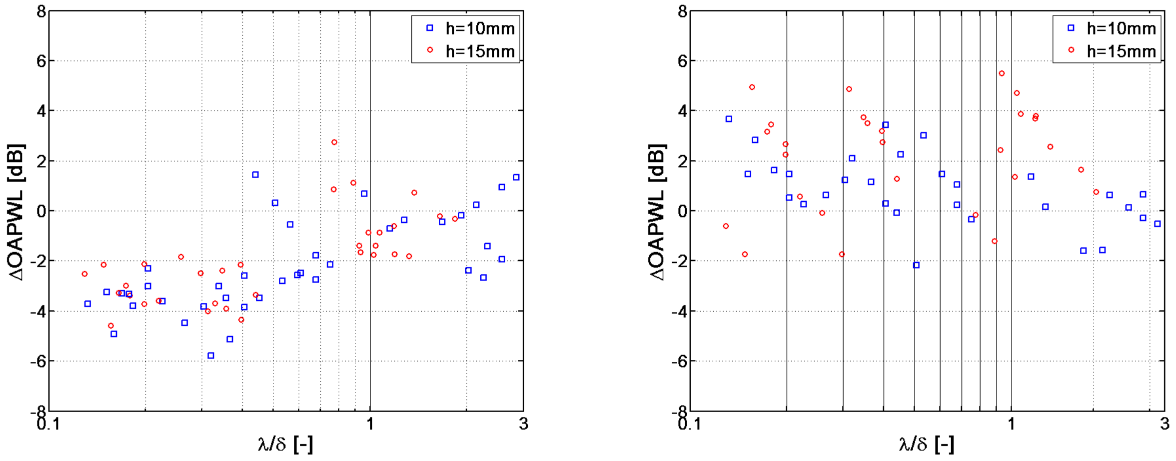

(a) $\Delta OAPWL$ averaged between 1 and 2 kHz. (b) $\Delta OAPWL$ averaged between 10 and 12 kHz.

Figure 4.5: Scattering of measured $\Delta OAPWL$ as a function of λ/δ. The data include variation over mean flow velocity (U_0 = 20, 40, 60 m/s), AoA (0^o, 5^o and 10^o) for two amplitude serrations $h = 10\,mm$ (square) and $h = 15\,mm$ (circle).

Figure 4.5a shows that in general the sound power reductions increase as λ/δ decreases. A different behaviour is observed at high frequencies. Figure 4.5b shows that in the high frequency range, the radiated power increases by up to 6 dB as λ/δ decreases. Figures 4.5a and b confirm that decreasing λ generally causes an increase of noise reduction at low to mid frequencies and an increase in noise at higher frequencies. Figures 4.5a and b exhibit a significant amount of scatter and no obvious relationship can be seen between noise reduction and angle of attack, mean flow velocity or sawtooth amplitude h. A more detailed investigation of the effect of h on noise reduction is presented in Section 4.2.3 below.

Figures 4.6a and b are plots of the pressure level difference $\Delta OASPL$ predicted by Howe's model, over the low frequency bandwidth 1 kHz to 2 kHz (corresponding to $1.4 < \omega\delta/U_c < 7.82$), and over the high frequency bandwidth 10 kHz to 12 kHz (corresponding to $10.9 < \omega\delta/U_c < 62.6$), respectively. It is presented as a function of λ/δ, with flow conditions and sawtooth geometries identical to that of Figure 4.5. The experimental data from Figure 4.5 are also overlaid. Note that the theoretical predictions by Howe are given in terms of sound pressure level $\Delta OASPL$, hence exact comparisons of the noise reduction with experimental data (which are given in terms of sound power) is not possible. However, the differences between measurements and predictions are sufficiently large (>10 dB) to suggest that Howe's model provides poor predictions of the noise reduction due to trailing edge serrations. However, in this low frequency range it is clear that the general trend with λ/h is reasonably well captured by Howe's model even though the high sensitivity to U_0 predicted by Howe is not observed.

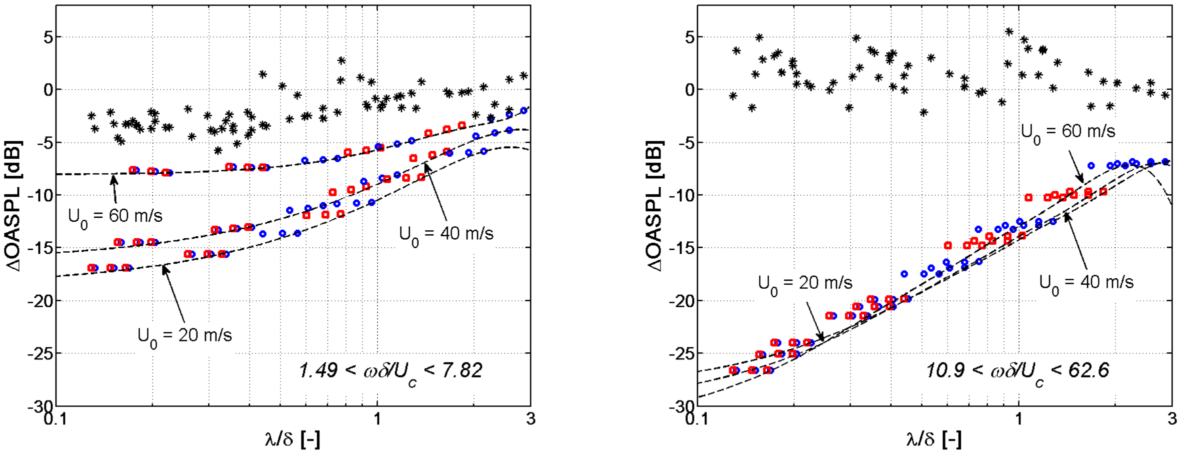

(a) $\Delta OASPL$ averaged between 1 and 2 kHz. (b) $\Delta OASPL$ averaged between 10 and 12 kHz.

Figure 4.6: Variation of sound pressure difference $\Delta OASPL = 10\log_{10}\left(\phi_{pp}|_{\mathbf{s}} / \phi_{pp}|_{\mathbf{b}}\right)$ predicted using Howe's formulation as a function of λ/δ - The data include variation over mean flow velocity ($U_0 = 20,\ 40,\ 60\,m/s$) and boundary layer thickness δ, for two amplitude serrations $h = 10\,mm$ (square) and $h = 15mm$ (circle), (*) Experimental data $\Delta OAPWL$ of Figure4.5.

In the frequency range between 10 and 12 kHz, comparison of the experimental and theoretical data of Figure 4.6a shows that the theoretical noise reduction increases with decreasing λ, at a much higher rate than the measured noise reductions, giving a maximum noise reduction of 18 dB at $U_0 = 20\,m/s$ and of 8 dB at $U_0 = 60\,m/s$. As δ is only used as a normalisation parameter on λ in Figure 4.6, the change in rate with which noise reduction is increased can be directly related to the parameter $\omega\delta/U_c$, introduced by Howe [66], through a measured value of convection speed $U_c = 0.7U_0$. Figures 4.6a and b illustrate Howe's findings that the condition $\omega\delta/U_c > 1$ needs to be satisfied to obtain theoretical noise reduction. Figure 4.6b also shows that for sufficiently high values of $\omega\delta/U_c$, the predicted noise reduction is only dependent on serration geometry. Finally, Figure 4.6b also shows that the experimental noise increase observed in Figures 4.3 to 4.6, and reported in various other studies [88, 92, 36, 42] is not predicted by Howe's model.

Whilst absolute reductions are poorly predicted by Howe, the experimental data set confirms Howe's prediction that for a given amplitude $2h$ the level of noise reduction increases as λ reduces.

4.2.2 Variation of sound power level with mean flow velocity U_0

4.2.2.1 Experimental results

This section describes the changes in sound power radiation with varying mean flow velocity U_0 using the blow-down technique, in which the far field acoustic pressure along the polar array is measured as the mean flow velocity is gradually increased (see Chapter 2). Note that below $U_0 = 10\,m/s$ airfoil noise falls below the background noise.

$$\Delta PWL(f) = 10\log_{10}\left(\sum_i \frac{\phi_{pp}(f,\theta_i)|_{\mathbf{s}}}{\phi_{pp}(f,\theta_i)|_{\mathbf{b}}}\right), \qquad \begin{array}{c} i = 1,...,13 \\ 50^o < \theta < 110^o \end{array}, \tag{4.2}$$

Figure 4.7 shows the typical behaviour of the sound power level reduction ΔPWL, defined in Equation 4.2, for $\lambda/h = 0.2$ and 0.6 and for the two angles of attack 0^o and 5^o, as a function of frequency and mean flow velocity U_0. Note that the limits of $\pm 2\,$dB in this Figure are set to emphasize the behaviour of the transition frequency between power reduction and power increase and do not refer to maximum and minimum changes in power. A noise reduction larger than 2 dB, as shown in Figures 4.3a and c is observed at low to mid-frequencies. A noise increase, consistent with Figures 4.3b and d, and greater than 2 dB, is shown at higher frequencies. By inspection of these 'maps', the frequency f_δ that delimits noise reductions and noise increases appears to closely follow a constant Strouhal number dependency, defined in Equation 4.3, where $St_\delta \sim 1$ is plotted as a dashed curve chosen in each case to give best fit to the data in Figure 4.7.

$$St_\delta = \frac{f_\delta \delta}{U_0}, \tag{4.3}$$

where f_δ is the frequency above which noise is increased and δ is the turbulent boundary layer thickness estimated at $x/c = -0.01$ of the appropriate reference airfoil with a straight trailing edge, using Xfoil (see Chapter 2). Note that for simplicity, St_δ is calculated using the value of the boundary layer thickness δ, estimated using Xfoil (see Chapter 2), taken at $U_0 = 40\,m/s$. It is shown in Chapter 2, using Xfoil, that doing so induces an error of less than 5 % on the estimation of the boundary layer thickness δ for $U_0 > 40\,m/s$.

In order to identify the relationship between St_δ and λ/h, Figure 4.8 shows St_δ plotted against λ/h, for the angles of attack 0^o, 5^o and 10^o and for twenty eight of the serrated edges listed in Tables 4.1 and 4.2 where f_δ is chosen by eye to fit the transition between noise increase and reduction. Figure 4.8 indicates that the values of St_δ are included within the range [0.7 - 1]. Larger deviations from 0.5 to 1.3 were found for few serrations. Overall, $St_\delta = 1$ provides a good estimate of the frequency f_δ above which the noise is increased, for a wide range of serrated trailing edges and airfoil angles of attack. Greatest deviation of St_δ is no more than 30 % outside of the range [0.7 - 1] and mainly occurs for the small angle serrations for which $\lambda/h < 0.3$. No clear trend could be drawn indicating the dependency of St_δ on mean flow velocities and airfoil angles of attack. The variation of St_δ, observed in Figure 4.8, from 0.7 to 1, is most likely due to the lack of accuracy of Xfoil [38] to predict the boundary layer thicknesses at the trailing edge with changing flow conditions, i.e., angles of attack and tripping of the airfoil, and trailing edge geometry. Therefore, it is worth mentioning that the variation of St_δ by up to $\pm 30\,\%$ is most likely due to the fact that the boundary layer thickness is only estimated and the value of the critical Strouhal number is an order of magnitude only. In addition, it is shown below in Section 4.5.2 that the boundary layer velocity profiles change by up to 12 % between a straight edge and a serrated edge, close to the tip of the sawtooth.

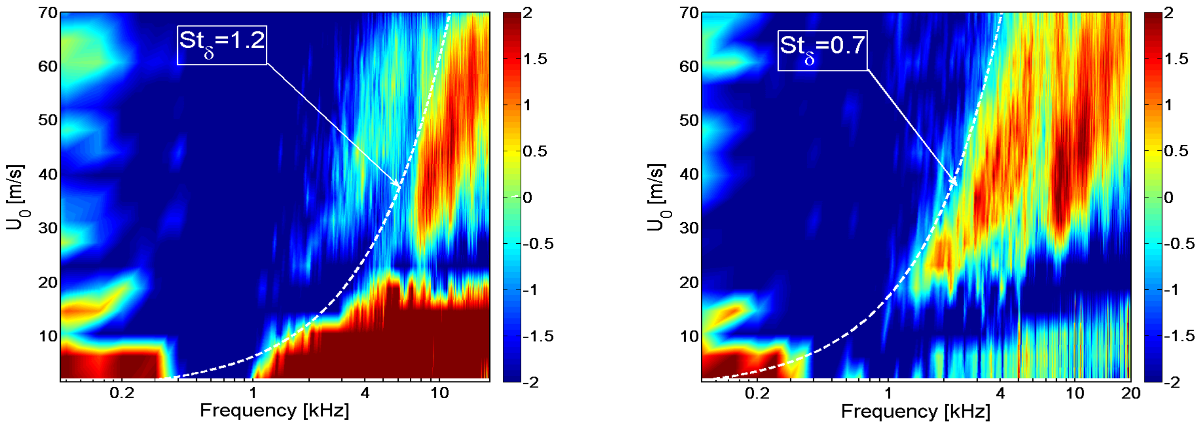

(a) Serration $\lambda/h = 0.6$ - 0^o AoA.

(b) Serration $\lambda/h = 0.6$ - 5^o AoA.

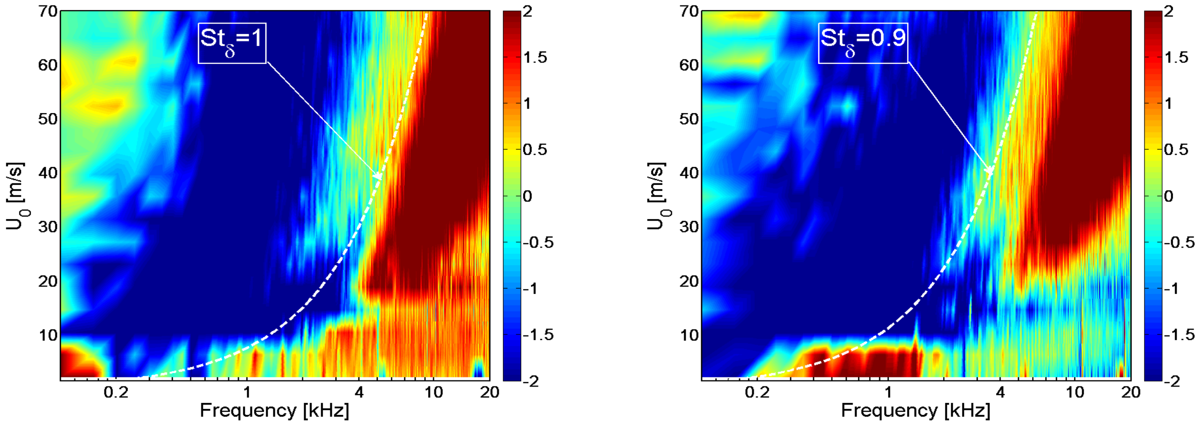

(c) Serration $\lambda/h = 0.2$ - 0^o AoA.

(d) Serration $\lambda/h = 0.2$ - 5^o AoA.

Figure 4.7: Sound power level change ΔPWL as a function of frequency and mean flow velocity U_0.

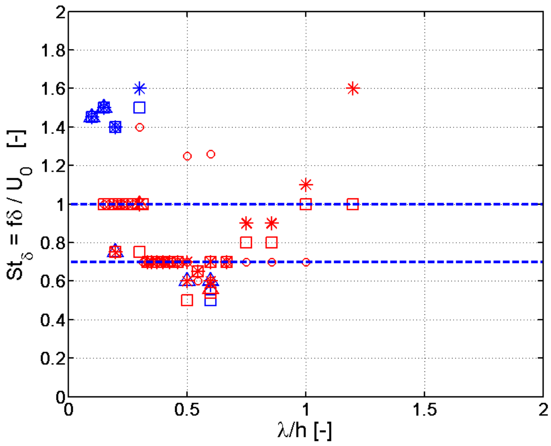

Figure 4.8: Variation of Strouhal number St_δ defined in Equation 4.3 with λ/h, (o) $U_0 = 20\,m/s$, ($\square$) $U_0 = 40\,m/s$, ($*$) $U_0 = 60\,m/s$, ($\triangle$) $U_0 = 80\,m/s$ - (Blue) 0^o AoA, (Red) 5^o AoA.

The mechanism for this noise increase is investigated in detail in Chapter 5.

4.2.2.2 Comparison with Howe's theory

Figure 4.9 shows the predicted noise reduction maps, for comparison with that of Figure 4.7, computed using Howe's theory for predicting the noise reduction from serrated trailing edges [66]. It is given as a function of frequency and mean flow velocity U_0 for the sharp serration $\lambda/h = 0.1$ and the larger base serration $\lambda/h = 0.6$. The predicted noise reduction increases with frequency and exhibits an oscillatory behaviour due to constructive and destructive interferences between the noise sources distributed along the edges, as discussed in Section 1.2.2.2. The model also predicts that the noise reduction increases with decreasing λ/h, i.e., the sharper the serration, the greater is the noise reduction. The increase in noise measured at high frequencies is not predicted by Howe's theory.

Comparison of the predictions in Figure 4.9 with the experimental results of Figure 4.7 shows conclusively that Howe's model does not fully capture the complexity of the noise reduction mechanism although some general trends are correctly predicted.

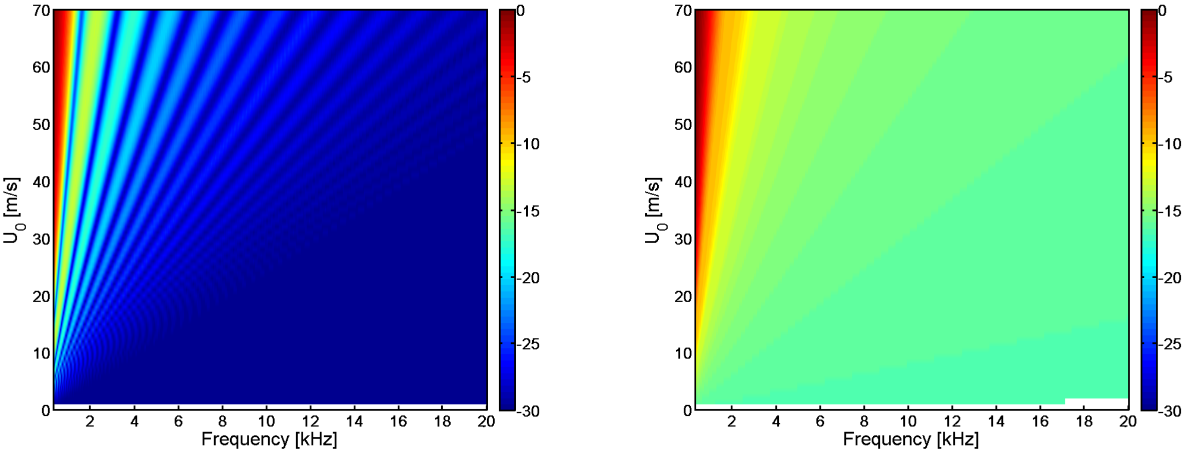

(a) Serration λ/h= 0.1. (b) Serration λ/h= 0.6.

Figure 4.9: Noise reduction as a function of frequency and mean flow velocity U_0 from Howe's theory [66].

4.2.3 Variation of $PWL(f)$ with sawtooth amplitude $2h$

4.2.3.1 Experimental results

In this section, the sensitivity of the noise reduction to the serration amplitude $2h$ is investigated. This was undertaken using the second set of twenty eight sawtooth inserts, listed in Table 4.2, in which the amplitude was gradually increased from $1\,mm$ to $40\,mm$, while keeping the periodicity λ fixed equal to $3\,mm$.

Figures 4.10 and 4.11 show the difference in sound power level ΔPWL, defined in Equation 4.2 (between 50^o and 110^o), in narrow bands at 0^0 and 5^o angles of attack, respectively. The power change ΔPWL is shown as a colour map as a function of Strouhal number $f\delta/U_0$, h/δ, and h/λ. Data is given for the four velocities of U_0 =$20\,m/s$, $40\,m/s$, $60\,m/s$ and $80\,m/s$. Note that the limits of ± 2 dB are set to emphasize the behaviour of the transition frequency between power reduction and power increase and do not refer to maximum and minimum changes in power.

These Figures clearly show that for both angles of attack and all flow velocities, noise reductions occur only in the low frequency range for $f\delta/U_0 < St_\delta$, where $St_\delta \sim 1$ and noise increase occurs when $f\delta/U_0 > St_\delta$. As mentioned in Section 4.2.2, St_δ, shown by the vertical dashed line, varies by no more than 30 % depending upon serration geometry and angle of attack.

The other striking feature of Figures 4.10 and 4.11 is that negligible noise reductions are obtained when the root to tip distance $2h$ is less than half the boundary layer thickness, i.e, $h/\delta < 0.25$, as indicated by the horizontal dashed line. Both Figures 4.10 and 4.11 reveal a critical value of either $h/\delta \sim 0.25$ or $h/\lambda \sim 0.5$, above which significant noise reductions occur. In conclusion, therefore, noise reductions are limited to the upper left quadrant of the Figures, in which $h/\delta > 0.25$ and $f\delta/U_0 < 1$. The existence of a critical value of $h/\delta \sim 0.25$, suggests that when the eddys are too large to be influenced by the amplitude $2h$ of the serration, no noise reduction occurs. Generally, the parameter h/λ seems to be strongly linked to h/δ, in contrast with Howe's theory. Further discussions about the relative importance of h/δ and h/λ are presented in Chapter 5.

Negligible differences are observed between the two angles of attack 0^o and 5^o, shown in Figures 4.10 and 4.11 respectively. In addition, the changes in noise (reductions and increases) become less important with increasing flow speed.

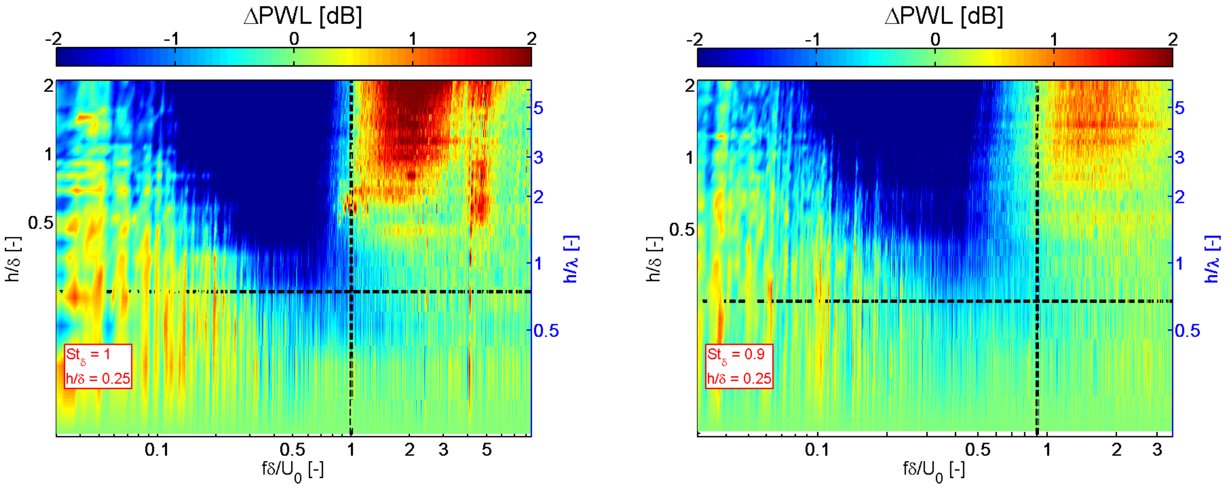

(a) $U_0 = 20\,m/s$. (b) $U_0 = 40\,m/s$.

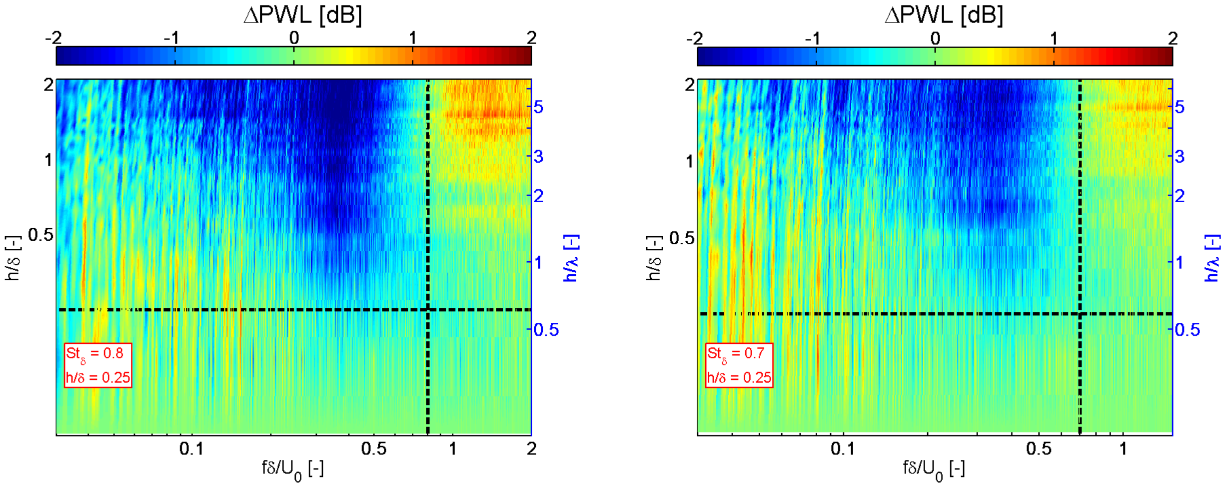

(c) $U_0 = 60\,m/s$. (d) $U_0 = 80\,m/s$.

Figure 4.10: Sound power level difference ΔPWL as a function of $f\delta/U_0$, h/δ and h/λ at 0^o AoA.

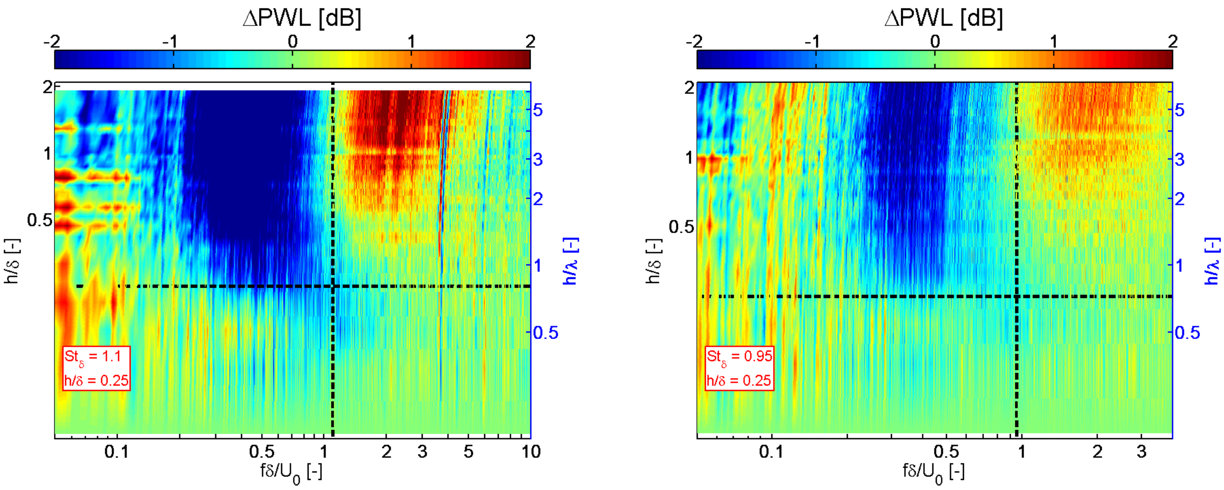

(a) $U_0 = 20\,m/s$.

(b) $U_0 = 40\,m/s$.

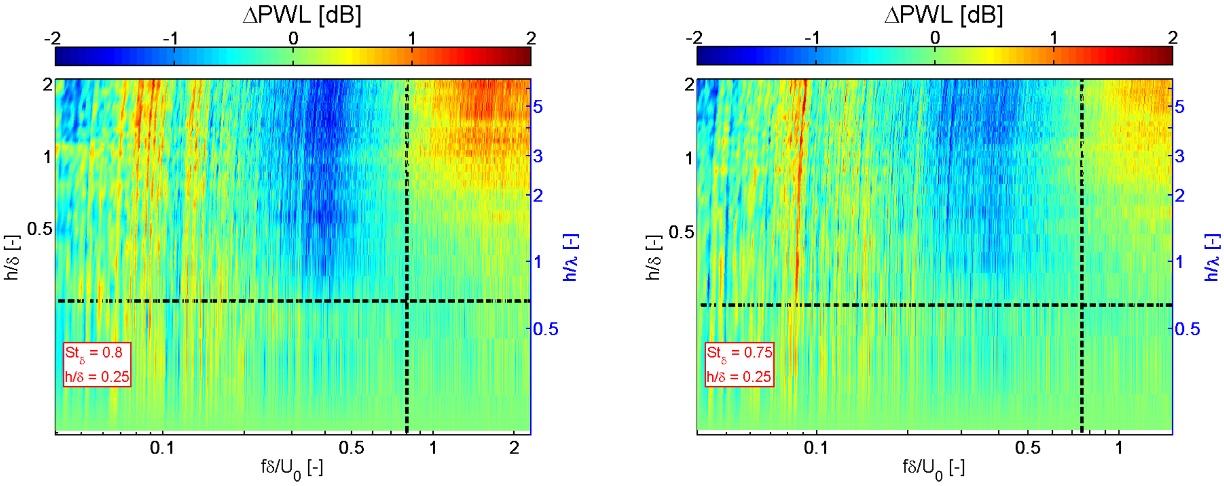

(c) $U_0 = 60\,m/s$.

(d) $U_0 = 80\,m/s$.

Figure 4.11: Sound power level difference ΔPWL as a function of $f\delta/U_0$, h/δ and h/λ at 5^o AoA.

This work now focuses on the sound power reduction obtained when varying the serration amplitude $2h$. Figure 4.12 is a plot of ΔPWL, where each curve is a vertical 'slice' of the data plotted in Figure 4.10b, taken at the four Strouhal numbers of St =0.17, 0.45, 0.9 and 1.4. Dashed lines are used to emphasize the frequencies where noise reductions occur, i.e., $St_\delta < 1$, while solid lines show the increase in noise, i.e., $St_\delta > 1$. Figure 4.12 illustrates that when $St_\delta < 1$, the noise reduction increases with increasing values of h/δ and h/λ, to a measured maximum of 4.5 dB at $h/\delta = 2.7$ or $h/\lambda = 6.7$. When $St_\delta \sim 1$, the noise reduction appears to plateau as h/δ and h/λ increase. When $St_\delta > 1$, the noise increase increases as h/δ and h/λ increase. The trend in the data shown in Figure 4.12 for $St_\delta \ll 1$ suggests that the noise reduction would continue to increase for even sharper serrated geometries than the ones used in this study, i.e., $h/\lambda > 6.5$. Therefore, it is reasonable to assume that when $St_\delta \ll 1$, although the levels of noise reduction are largely over predicted by Howe, his model is accurate in predicting the important trend that noise reductions increase as the serration is made sharper.

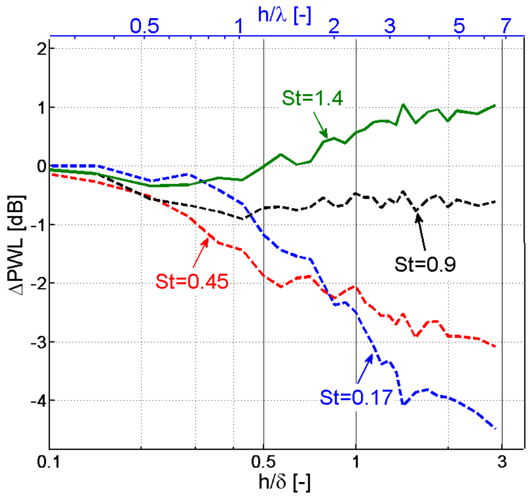

Figure 4.12: Sound power level difference ΔPWL as a function of h/δ and h/λ at 0^o AoA - (Solid) $f\delta/U_0 > 1$, (Dashed) $f\delta/U_0 \leq 1$.

4.2.3.2 Comparison of the measured noise reduction with Howe's theory

Figure 4.13a presents the predicted difference in sound pressure level ΔSPL using Howe's model for sawtooth trailing edges. The data is shown as a function of Strouhal number $f\delta/U_0$, h/δ, and h/λ, for $U_0 = 40\,m/s$ and 0^o angle of attack. This prediction is compared to the experimental data of Figure 4.13b (also shown in Figure 4.10b). As Howe's model does not predict the increase in noise for $f\delta/U_0 > 1$, both Figures 4.13a and b are only presented for $f\delta/U_0 \leq 1$. Direct comparison shows that the decrease in radiation with increasing h/δ, shown in the measured data, begins in Howe's theory for $f\delta/U_0 > 0.2$. The important condition for a decrease in noise radiation shown experimentally, $h/\delta > 0.25$, does not appear in Howe's model. Generally, the condition $h/\delta = 0.25$ does not appear to be a critical value in Howe's model.

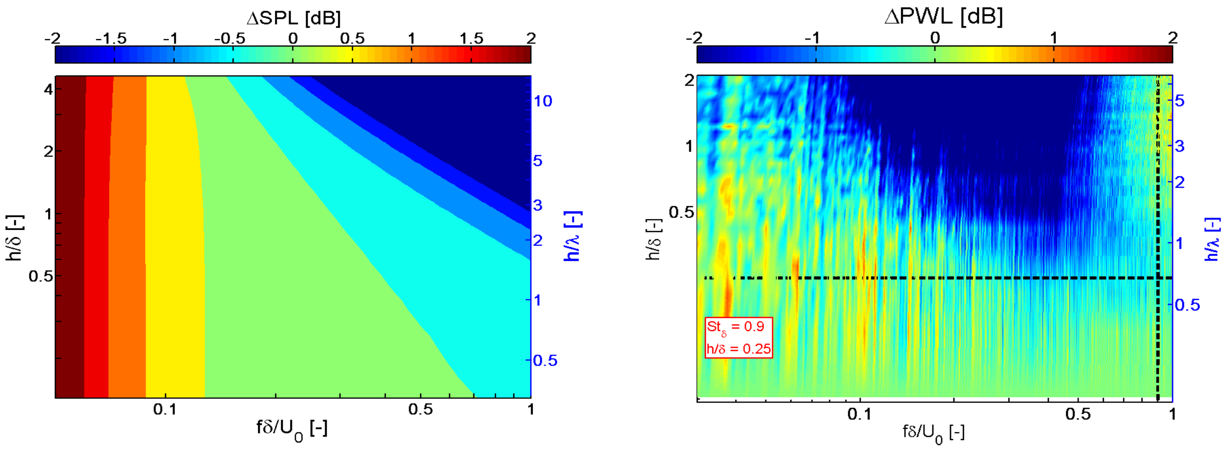

(a) Sound pressure level difference from Howe's theory.

(b) from measured data as a function of $f\delta/U_0$ and h/δ at $U_0 = 40\,m/s$ and δ for 0^o AoA.

Figure 4.13: Comparison between Howe's prediction and experimental noise reductions.

Whilst Howe's model predicts some important general trends in the noise data, absolute reduction and some important features are not accurately predicted. Howe's model will not be considered further here. However, the reason why Howe's model is not accurate will be discussed in Chapter 5.

4.2.4 Noise reduction as a function of angle of attack α_g

Figure 4.14 presents the variation of the sound power change ΔPWL, defined in Equation 4.2, with frequency and geometrical angle of attack $\alpha_g = 0$, 5, 10 and 15^o, at $U_0 = 40\,m/s$ and $U_0 = 60\,m/s$ for the two serrations $\lambda/h = 0.1$ and 0.6. The noise reduction is shown with a solid line while the noise increase is shown with a dashed line. Figure 4.14 shows that the peak of noise reduction varies little in levels ($< 2\,$dB) and frequency, when varying the airfoil angle of attack. Conversely, the amplitude of the peak of noise increase varies by up to 4 dB when varying the airfoil angle of attack. At low frequencies, jet noise masks any noise reduction by the serrated trailing edges. The interest below is focused on the frequency range where the noise is increased.

At high frequencies, as mentioned in the previous Sections, the noise is consistently increased by the serrations. Figure 4.14 shows that this increase in noise is amplified with increasing airfoil angle of attack, from 0^o to 15^o, by up to 4 dB for the serration $\lambda/h = 0.6$ and up to 3 dB for the serration $\lambda/h = 0.1$. The peak of noise increase is measured to be 7 dB for the sharper serration $\lambda/h = 0.1$ while only 4 dB for the serration $\lambda/h = 0.6$. Thus, the geometry of the serration has a strong effect on the absolute level of noise increase. These findings are consistent with the hypothesis introduced in Chapter 5 that the high frequency noise amplification is due to small micro jets in the valleys of the sawteeth, caused by the pressure difference around the trailing edge. As the angle of attack increases, the pressure difference at the airfoil TE increases and so does the intensity of the micro jets through the valleys of the serrations. Also, because it only occurs for $f\delta/U_0 > 1$, they are associated with small eddies. The mechanisms responsible for the noise increase at high frequency are further discussed in Chapter 5.

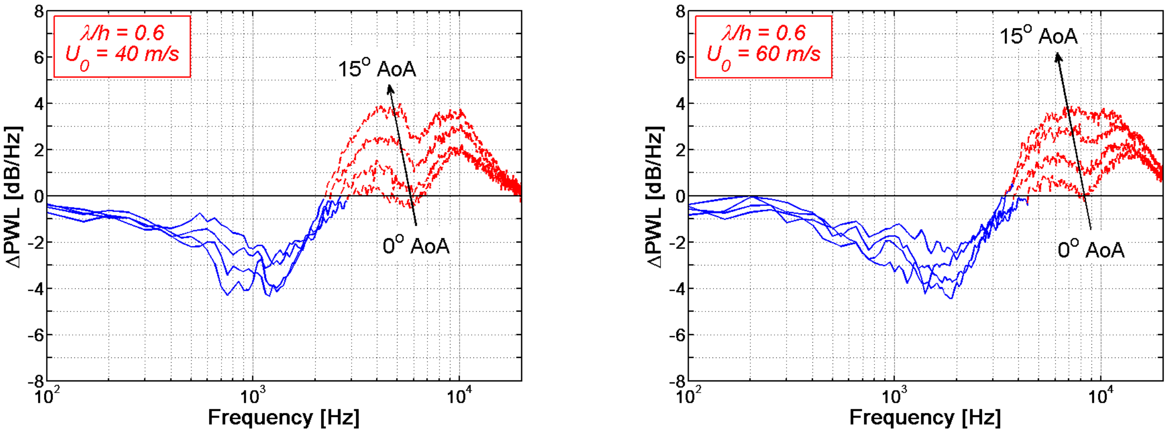

(a) $\lambda/h = 0.6$ and $U_0 = 40\,m/s$.

(b) $\lambda/h = 0.6$ and $U_0 = 60\,m/s$.

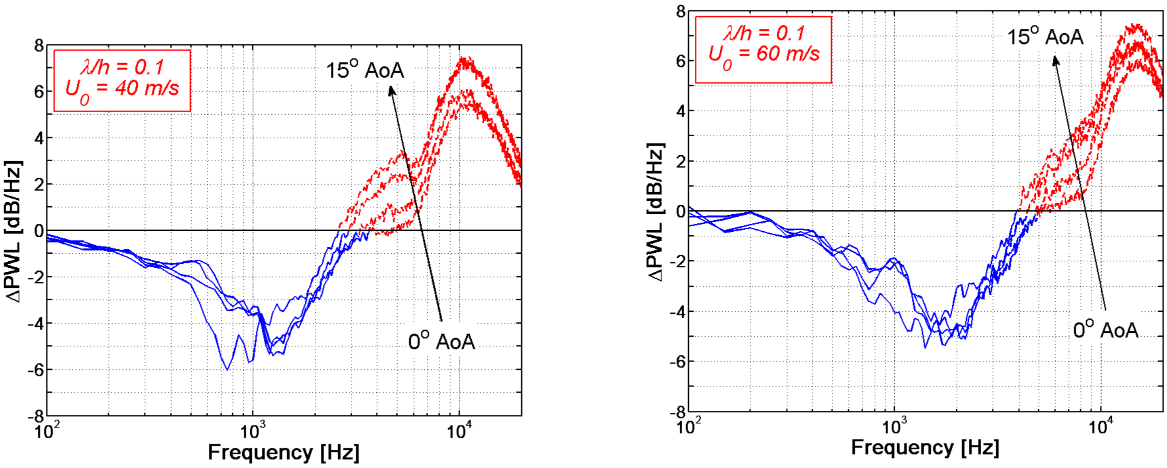

(c) $\lambda/h = 0.1$ and $U_0 = 40\,m/s$.

(d) $\lambda/h = 0.1$ and $U_0 = 60\,m/s$.

Figure 4.14: Change in ΔPWL, presented as a function of frequency and angle of attack α_g.

4.3 Narrow band polar directivity

This Section assesses the changes in the narrow band directivity features measured on a baseline straight edge airfoil and an airfoil with the serration $\lambda/h = 0.5$. Figure 4.15 shows the polar radiation measured for both the baseline and treated airfoils, at the three frequencies 1350Hz, 2100 Hz and 4000Hz. The predicted directivity from Amiet's flat plate theory [7] is also included for comparison with the baseline case, which includes the effect of jet refraction [9]. The radiation pattern measured over the baseline airfoil shows a reasonable agreement with Amiet's prediction. Figure 4.15a shows a change in the orientation of the main radiation lobe by about 15^o. For higher frequencies, Figure 4.15b and c show that the radiation angle of the upstream lobe appear not to be affected by the presence of the serrations. Although the amplitude of the pressure of the downstream lobe is reduced by the serrations, the radiation angle remains relatively unchanged.

As observed in the previous Sections of this Chapter, the radiated pressure measured at all microphone positions is reduced by the presence of the serrated trailing edge. In addition, the radiation angle of the main upstream lobe appears to be tilted further forward by up to 15^o. The radiation angle of the downstream lobe is less affected by the serration at the trailing edge, and differences no larger than 3^o were measured, which can be attributed to measurement error.

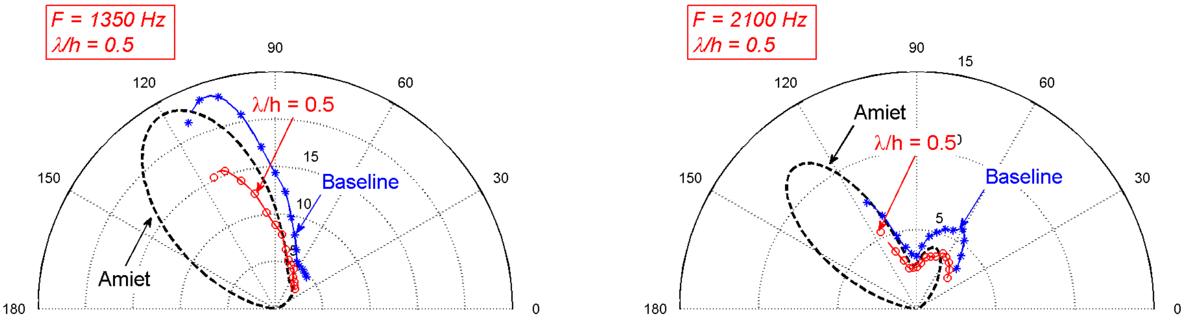

(a) $F_c = 1350\,Hz$. (b) $F_c = 2100\,Hz$.

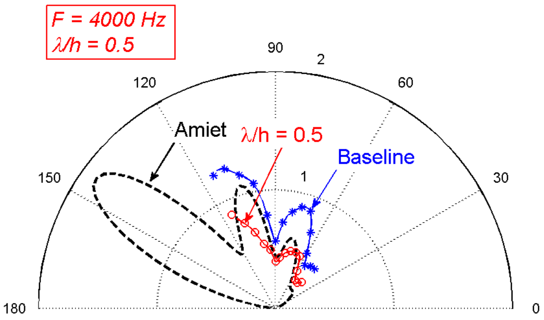

(c) $F_c = 4000\,Hz$.

Figure 4.15: Changes in polar directivity using trailing edge serration λ/h=0.5, in Pa^2/Hz (normalized by $p_0 = 20\mu Pa$) at $U_0 = 20\,m/s$.

4.4 Critique of Howe's theory

The results presented in this Chapter and various other experimental and numerical studies listed in Chapter 1 have used sawtooth serrations as a means of reducing the trailing edge noise from airfoils. Howe investigated analytically the mechanisms responsible for the noise reduction. The results previously presented in this Chapter suggest that the noise reduction mechanisms are more complex than anticipated by Howe. As presented in Section 1.2.2.2, Howe introduces three parameters that control the predicted noise reduction, i.e., $\omega\delta/U_c$, h/δ and h/λ. To allow direct comparison with Howe's predictions and further discussions of the mechanisms of noise reduction in Chapter 5, the effect of these three parameters are assessed below.

4.4.0.1 Non-dimensional frequency, $\omega\delta/U_c$

In the current experimental study the Strouhal number defined with respect to δ has been shown to be a more critical parameter than predicted by Howe. One of the most striking features arising from this experimental investigation is a clear increase in noise at frequencies, $f\delta/U_0 > St_\delta$ and $St_\delta \sim 1$. As presented below, in Chapter 5, this behaviour was not observed in the difference of the turbulence spectra measured in the boundary layers between a straight edge and a serrated edge, suggesting that the cause of this high frequency increase is the presence of small jets due to a cross-flow through the valleys of the sawtooth. At lower frequencies, $f\delta/U_0 < St_\delta$, noise reductions are observed whose level depends on h/λ and h/δ.

4.4.0.2 Non-dimensional amplitude, h/δ

The other important observation resulting from this investigation, in addition to the dependence on $f\delta/U_0$ discussed above, is that insignificant noise reductions were obtained across the entire frequency range for $h/\delta < 0.25$. In this case, eddys pass over the serration and are scattered into sound with an efficiency similar to that of a straight edge. It is also noteworthy that the oscillations in the spectrum predicted by Howe for $h/\delta \approx 1$ arising from coherent interference between the radiation from the root and the tip are not present in the measurements. This suggests that the turbulence at the root and at the tip is largely uncorrelated owing to the fast decay time of the eddys compared to the time taken for the eddys to pass over the serration.

4.4.0.3 Serration angle, h/λ

In this experimental investigation, noise reductions from the trailing edge serration were found to improve as h/λ increases, as predicted by Howe. Nevertheless, experimental reductions were substantially smaller than that predicted. However, it was observed that noise reductions are considerably more sensitive to h, through the ratio h/δ, than Howe predicted. For a given h, the noise reduction is equally sensitive to λ as h is for a given value of λ. At the present it is unclear whether h/λ is the independent parameter determining the level of noise reduction, i.e., the angle α_S of the flow relative to the edge, as predicted by Howe, or whether it is λ and h individually.

Howe also predicts that for reduced frequencies $\omega h/U \gg 1$, the noise reduction in its asymptotic form can be approximated by $10.log_{10}\left(1+(4h/\lambda)^2\right)$. This was found to be incorrect and an increase of noise measured at high frequencies, when $f\delta/U_0 > 1$, was observed.

4.5 Aerodynamic data

This Section investigates the effects on the flow due to the presence of trailing edge serrations, by analyzing steady and unsteady aerodynamic data over the airfoil surface and in the wake. The static pressure distribution along the airfoil and the drag behind the airfoil were measured in order to investigate the effects on steady lift and drag. Mean and unsteady wake and boundary layer velocity profiles, around a straight edge and a serrated edge, were measured using a single hot wire probe. Finally, a detailed analysis of the turbulence intensities, spectra and length scales close to the airfoil trailing edge was carried out in order to provide more insight into the mechanisms involved in the noise reduction / noise increase further discussed in Chapter 5.

4.5.1 Steady aerodynamics

Figure 4.16 shows a comparison of the static pressure coefficient distribution C_p, defined in Equation 2.3, along the airfoil chord measured over the sharp edge airfoil, and the three sawtooth serrations $\lambda/h = 0.1$, 0.2 and 0.6. Corresponding predictions computed from the RANS code provided by the company Fluorem [44], as given in Chapter 2, are also shown for the baseline airfoil. Measurements are performed as detailed in Chapter 2. The airfoil is set at the two angles of attack $\alpha_g = 0^o$ and $\alpha_g = 10^o$. Reasonable agreement is observed between measurement and predictions, with the largest discrepancies occurring near the leading edge on the suction side.

Note that as the airfoil is fitted with a detachable trailing edge, there is no static pressure sensors close to the trailing edge. Thus the effect of the serrated edges in this trailing edge region could not be estimated. However, as most of the lift is generated on the upstream part of the airfoil, it is reasonable to assume that the introduction of trailing edge serrations has no significant effect on the lift. No significant influence of the serrations on the steady loading on the airfoil can be seen upstream of the trailing edge. These results are consistent with the observations made by Dassen [36], where the lift and drag forces were measured using an external balance on several airfoil profiles and no influence on the performance, due to the trailing edge serrations, was established. Geiger [47] also measured detailed comparisons of the blade loading around a straight edge airfoil and around two different serrated edges of amplitude $2h = 12.7\,mm$ and $2h = 25.4\,mm$. Figure 5-1 and Table 5-1 of Geiger's thesis [47] show differences smaller than 9 % over the whole airfoil body, and almost nonexistent close to the airfoil trailing edge. It is also reported that the largest variations of C_p were found when the serrated edge is drooped, i.e., when its alignment to the mean flow is changed, which is not the case in the present study.

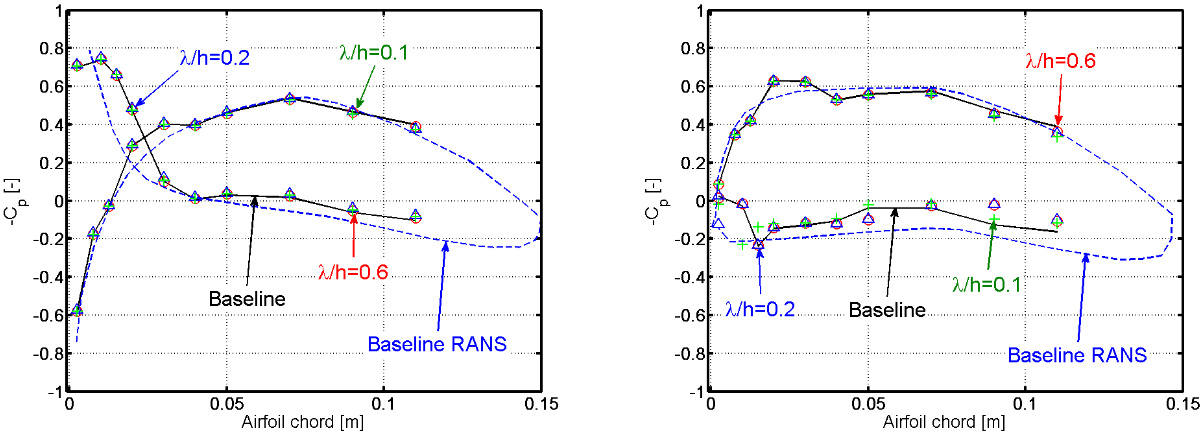

(a) 0^o angle of attack.

(b) 10^o angle of attack.

Figure 4.16: Comparison of the static pressure distribution coefficient C_p between measurements on the baseline and the serrated trailing edges λ/h= 0.1, 0.2 and 0.6, and with RANS data on the baseline (Turb'Flow by Fluorem [44]).

Figure 4.17 shows the variation of the drag coefficient measured from wake data, for the baseline and sawtooth trailing edges λ/h=0.1, 0.2, 0.5 and 0.6 at $x/c = 0.63$, where $x = 0$ is located at the airfoil trailing edge. The data is divided between the $h = 10\,mm$ and $h = 15\,mm$ serration geometries. Equation 4.4 is used to calculate C_d from the measurements of the wake velocity behind the airfoil [12], which are described below in this Chapter.

$$C_d = \frac{2}{c}\int_{z_1}^{z_2} \frac{U_i(z)}{U_0}\left(1 - \frac{U_i(z)}{U_0}\right) dz, \tag{4.4}$$

where U_i is the measured mean streamwise velocity in the wake, U_0 is the freestream mean velocity, and $L_w = z_2 - z_1$ is the width of the wake.

Figure 4.17 shows that the introduction of serrations at the trailing edge of the airfoil increases the drag coefficient by up to 10 % for the sharper serrations but only by up to 2 % for the large base serrations. This estimation of the drag coefficient is consistent with measurements subsequently made on cascade airfoils fitted with trailing edge serrations, by Finez *et al* [42]. An increase of 14 % of the drag coefficient was reported in his experiment for the serration $\lambda/h = 0.3$. Geiger [47] did not estimate the changes in the drag in his study but performed detailed measurements of the steady and unsteady flow in the wake of two serrations. The results reported in his thesis are referred to in the next Section in comparison to the present work.

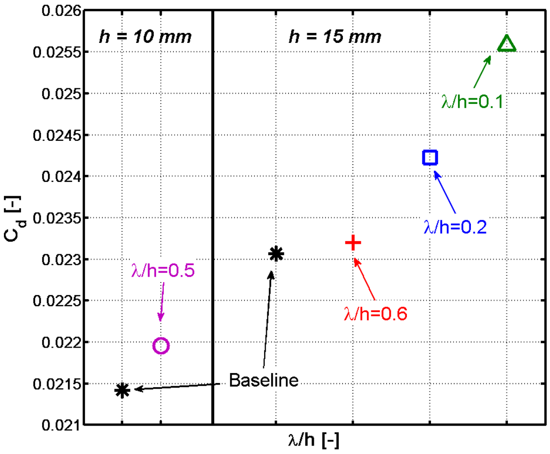

Figure 4.17: Comparison of the drag coefficient C_d between the two baseline $h = 10\,mm$ and $h = 15\,mm$ and the sawtooth serrations λ/h=0.1, 0.2, 0.5 and 0.6, at $x/c = 0.63$, along the tip of a single tooth.

4.5.2 Boundary layer profiles

This Section assesses whether the boundary layer close to the trailing edge remains unaffected by the presence of serrations as assumed by Howe [66]. In order to assess this, detailed measurements of the boundary layer profiles over a single tooth of a serrated edge and over a straight trailing edge were performed. This measurement also assists in the understanding of the noise reduction mechanisms discussed in Chapter 5.

Using the hot wire measurement system and a single sensor wire probe, as detailed in Chapter 2, boundary layer measurements were performed at 5^o angle of attack and $U_0 = 40\,m/s$. The boundary layer mean and unsteady streamwise velocity profiles, on the suction side of the airfoil, were measured over a straight edge and over the serration $\lambda/h = 0.5$, at the seven spanwise and chordwise locations shown in Figure 4.18. The data taken on a single tooth were compared to the data taken at the same locations on the straight edge. Due to the size of the probe relative to that of the sawtooth geometries available, measurements were only performed on the serration $\lambda/h =$ 0.5. Note that the tip of the serrations corresponds to the same chord length as the straight edge for this measurement.

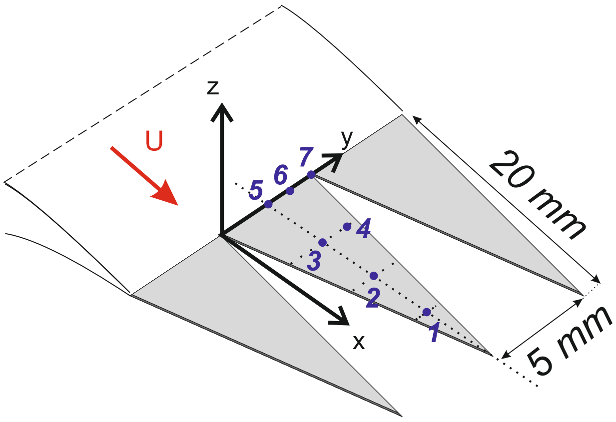

Point	x [mm]	y [mm]
1	15	2.5
2	10	2.5
3	5	2.5
4	5	3.75
5	0	2.5
6	0	3.75
7	0	5

Figure 4.18: Location of the boundary layer measurements over the sawtooth $\lambda/h = 0.5$, where $\lambda = 5\,mm$ and $2h = 20\,mm$.

The streamwise mean velocity profiles and the turbulent unsteady velocity profiles are shown in Figures 4.19 and 4.20, respectively, at the seven positions depicted in Figure 4.18. Note that the symbols represent the spanwise distributed locations of Figure 4.18.

The mean velocity profiles, in Figure 4.19, measured close to the root of the serration are nearly identical to the straight trailing edge. However, the boundary layer profiles on the serrated edge and the straight edge increasingly differ as the measurement moves towards the tip of the serration. The boundary layer thickness δ is increased from $7.1\,mm$ to $8\,mm$ at location 1, i.e., the tip of the sawtooth, in the presence of serrations. The gradient of the mean velocity profiles $\partial u/\partial z$ are also steeper close to the airfoil surface, suggesting greater turbulence generation in this region.

Figure 4.20 is a plot of the unsteady velocity boundary layer profiles and shows that the peak of turbulence in the boundary layer is gradually shifted away from the airfoil surface as the tip is approached. However, the maximum turbulence intensity increases by about 30 % at the root of the serrated trailing edge. Subsequently, Finez [42] carried out PIV measurements on cascade airfoils fitted with sawtooth serrations and also reported that the peak of turbulence was moved away from the surface in the presence of serrations. It is therefore likely that the surface hydrodynamic pressure due to the turbulent boundary layer is reduced as a result. However, as shown in Chapter 5, the surface pressure near the tip increases by about 5 dB compared to a straight edge, which has been attributed to back-scattered pressure by the edge.

No variation of the velocity profiles were measured along the span of the serrations. The serrations have little effect on the mean velocity gradients close to the root of the serrations.

Howe's assumption that the boundary layer remains unchanged by the presence of a serrated edge is therefore to be reconsidered. The peak of turbulence is gradually moved away from the wetted edges as the measurement position is shifted to the tip of the sawtooth. Figure 4.20 therefore suggests that another mechanism by which noise is reduced by pushing away the turbulence from the surface could also occur. Chapter 5 further discusses the implications of this observation on the noise reduction but shows that it is not likely to be the dominant mechanism.

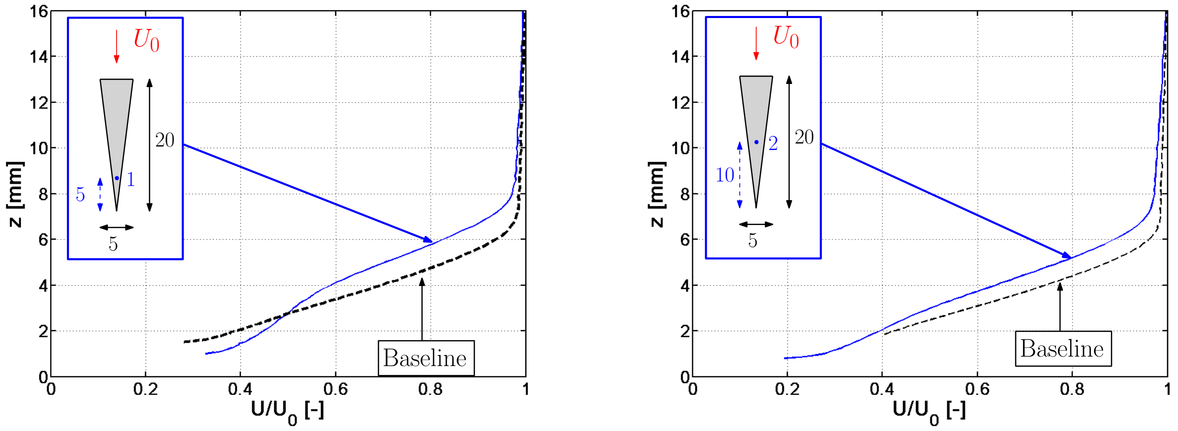

(a) At 5 *mm* from the tip.

(b) At 10 *mm* from the tip.

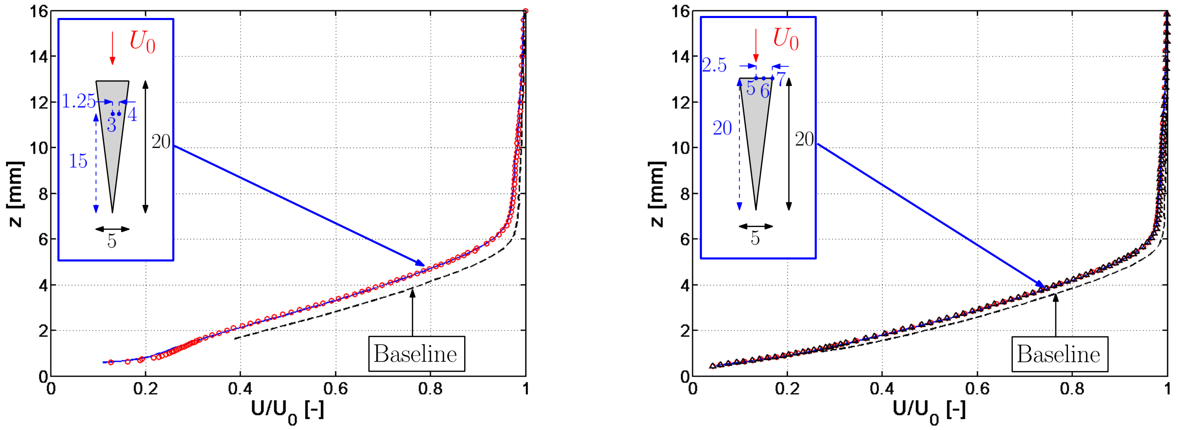

(c) At 15 *mm* from the tip.

(d) At the root of the serration.

Figure 4.19: Normalized mean velocity profiles measured in the boundary layer over one single tooth of the serration $\lambda/h = 0.5$; the blue dot represents the measurement locations; Measurements performed at $U_0 = 40\,m/s$ and 5^o angle of attack.

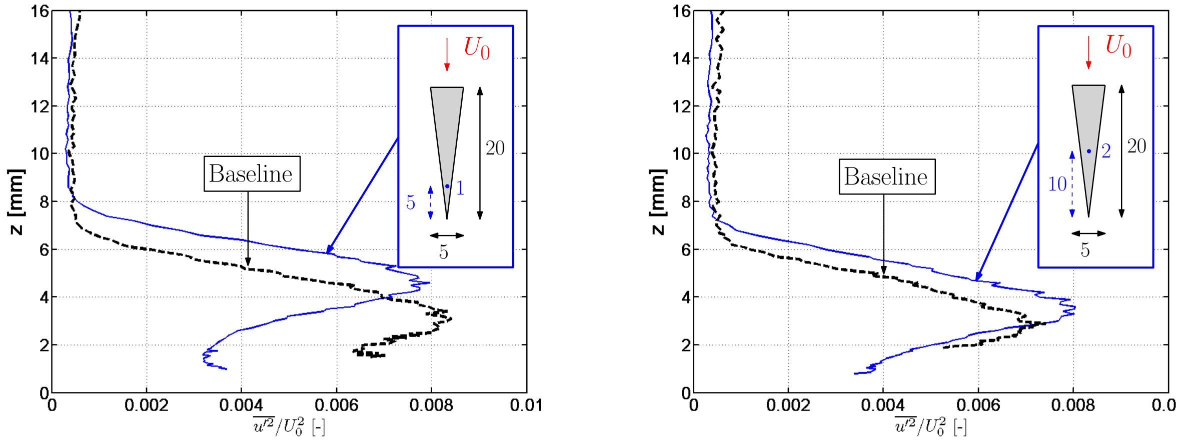

(a) At 5 mm from the tip.

(b) At 10 mm from the tip.

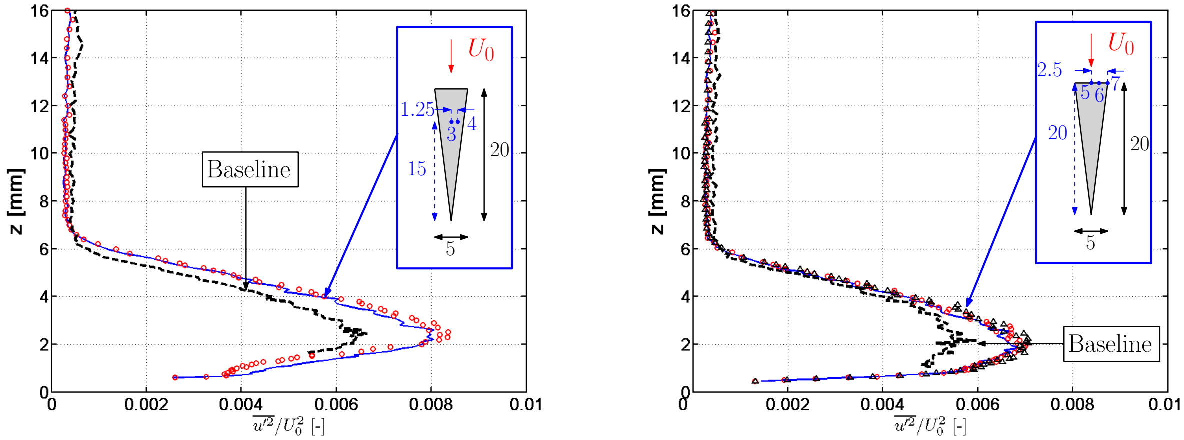

(c) At 15 mm from the tip.

(d) At the root of the serration.

Figure 4.20: Normalized unsteady velocity profiles measured in the boundary layer over one single tooth of the serration λ/h= 0.5; the blue dot represents the measurement locations; Measurements performed at $U_0 = 40\,m/s$ and 5^o angle of attack.

4.5.3 Variation of wake parameters with downstream distance

General airfoil noise theory, such as Amiet's [6], and the experimental tandem airfoil study presented in Chapter 7, suggests that leading edge turbulence interaction noise and its reduction are affected by the characteristics of the incoming turbulent flow. In the tandem airfoil experiment of Chapter 7, trailing edge serrations are used to alter the turbulence intensities and length scales in the wake of the upstream airfoil, to reduce the interaction noise generated at the downstream airfoil.

Therefore, this Section investigates the changes in turbulence intensity, length scales and velocity spectra behind the serrated trailing edges $\lambda/h = 0.1$, $\lambda/h = 0.2$, $\lambda/h = 0.5$ and $\lambda/h = 0.6$.

4.5.3.1 Mean velocity and trajectory of the wake

Figure 4.21 shows the variation of the wake profile with downstream distance x, where $x = 0$ is at the airfoil trailing edge (at the tip of the sawtooth for the serrated trailing edges), measured at the locations $x/c =$ 0.03, 0.13, 0.26, 0.4, 0.53 and 0.66 in the wake of the straight trailing edge and the two serrations $\lambda/h=$ 0.1 and 0.6 of amplitude $2h = 30\,mm$. The maximum mean wake deficit is smaller by up to 20 % for the serration $\lambda/h = 0.6$ and similar to that of the straight edge for the serration $\lambda/h = 0.1$. However, the width of the wake is larger behind a serrated trailing edge, resulting in an increase in the drag as shown in Section 4.5.1. In addition, it appears that for a given value of h, reducing the sawtooth periodicity λ further increases the maximum wake deficit and reduces the wake width.

The effect of the sawtooth amplitude on the mean wake trajectory was not investigated in this project but Geiger [47] reported that the width of the wake is increased in the presence of serrations, and further increased when the amplitude of the sawtooth is increased. In addition, he observed that the value of the maximum velocity deficit in the wake is decreased as the sawtooth amplitude increases.

Figure 4.21 also shows that the flow deflection by the airfoil is weaker behind the serrations due to the early mixing of the turbulence in the wake promoted by the sawtooth edges. While the mixing of the turbulence starts uniformly along the span behind the straight trailing edge, the sawtooth serrations provide an early mixing which starts at the root of the sawtooth. Consequently, for both serrated trailing edges presented in Figure 4.21, the mixing of the turbulence starts at $x/c = -0.1$, thus promoting a weaker deflection of the flow relative to the baseline airfoil.

Geiger also reported that the rate at which the centre-line maximum deficit velocity decays with downstream distance is faster than the baseline behind the tip of the sawtooth but slower than the straight edge behind the root of the sawtooth. He also reports that the spreading of the wake is larger behind the root and smaller behind the tip of the sawtooth, in comparison with a straight trailing edge.

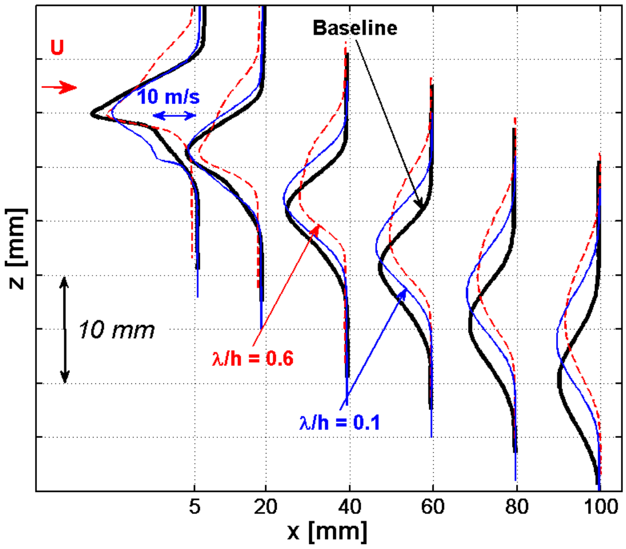

Figure 4.21: Variation of the mean wake velocity profile with downstream distance for the baseline trailing edge and the serrations λ/h=0.1 and 0.6

Figure 4.22 shows the mean velocity in the near wake, measured at $x/c = 0.03$, along the span across two sawteeth of the serration $\lambda/h = 0.5$. The imprint of the serration geometry is clearly seen and suggests that the wake spreading is non uniform across the span of the serration. The variation of the turbulence across the span is studied below in the next Section.

Measurements of the mean wake velocity across the span of two serrated edges performed by Geiger also showed a similar wavy pattern. However, this pattern was only observed on the large serration ($2h = 25.4\,mm$) at a downstream distance of $x/c = 0.61$, where $x = 0$ is located at the airfoil trailing edge. This non-uniformity in the mean wake was shown to disappear further downstream. It is suspected that the wavy pattern also occurs behind the shorter serrations ($2h = 12.7\,mm$) in Geiger's work but has already disappeared at $x/c = 0.61$, because a reduced serration amplitude would cause smaller perturbations of the flow at the trailing edge. In the next Section, it is also shown that the wake becomes more and more uniform as it convects downstream. Differences with Geiger's work are believed to be mainly due to the large differences in the airfoil aspect ratio, i.e., $AR = 51$ in Geiger's thesis and $AR = 3$ in this project and to possible discrepancies in the periodicity of sawtooth (which, to the author's knowledge, remains unknown in Geiger's work).

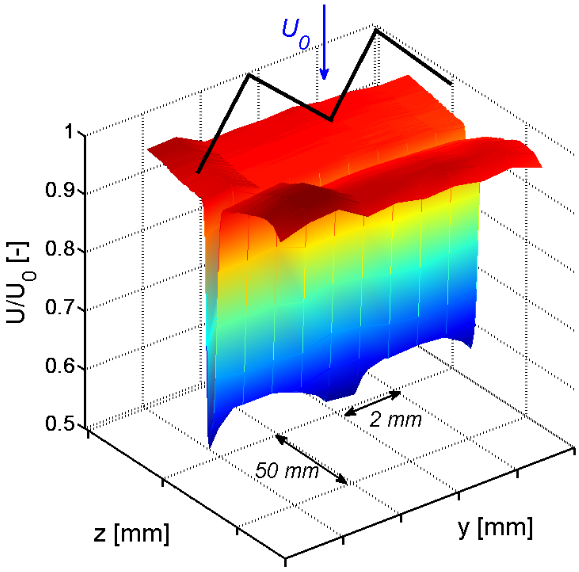

Figure 4.22: Mean wake deficit along the span of the serration $\lambda/h = 0.5$, measured in the near wake at $x/c = 0.03$ (where $x = 0$ is at the airfoil trailing edge).

4.5.3.2 Turbulence in the wake

For applications such as rotor - stator interaction, where the turbulent wakes of the upstream rotor impinge on the downstream stator vanes, which then radiate broadband noise, the introduction of trailing edge serrations to reduce wake turbulence therefore provides a strategy for reducing rotor / stator interaction noise.

The variation of the streamwise turbulence intensity in the wake of the four serrated trailing edges $\lambda/h = 0.1$, 0.2, 0.5 and 0.6, are investigated at the positions $x/c = 0.03$, 0.13, 0.4 and 0.66 (where $x = 0$ is at the airfoil trailing edge), as shown in Figure 4.23. For each trailing edge serration, data is measured behind the tip of one sawtooth. The turbulent profiles in this Figure have been corrected for the trajectory behind each trailing edge, so that the centre-lines are aligned. Two peaks of turbulence, on each side of the centre-line are observed and are a result of the boundary layer profiles leaving the airfoil at the trailing edge on either side.

In the very near wake, at $x/c = 0.03$ and $x/c = 0.13$ (see Figures 4.23a and b) the turbulence is asymmetric around the centre-line, and differs largely in shape and magnitude between serrations and straight edge, due to the early mixing in the presence of the serration, as mentioned previously. Further downstream at $x/c = 0.4$ and $x/c = 0.66$ (see Figures 4.23c and d), the turbulence distribution becomes more uniform and gradually follows the same profile behind the straight edge and the serrated edges, as the turbulence mixes. The width of the wake also increases behind all serrated trailing edges, which is further investigated through the variation of turbulence length scales in Section 4.5.3.3 below.

Another striking feature, consistent with the the fact that the turbulence is pushed away from the surface near the tip of the sawtooth (see Figure 4.20), is that in the near wake, at $x/c = 0.03$ and $x/c = 0.13$, the peaks of turbulence are pushed away from the centre-line. Further downstream at $x/c = 0.66$, the turbulence profile differs little from the straight edge. The general trend in Figure 4.23 is that the turbulence profile in the wake is less affected by short serrations ($2h = 20\,mm$ here) than by long serrations ($2h = 30\,mm$). This was also reported by Geiger [47] who identified non-symmetrical features in the mean flow for the larger sawtooth amplitude but not for the smaller sawtooth amplitude. Note also that the two baseline airfoils associated with the two amplitudes of serrations showed almost identical turbulence characteristics in the wake region of interest. Therefore, only the results from the airfoil with the shortest chord, i.e., $c = 0.15\,m$ are shown in this Section.

Figure 4.23 also indicates that a small sawtooth periodicity, i.e., $\lambda/h = 0.1$ ($\lambda = 1.5\,mm$), generates higher levels of turbulence in the near wake and further downstream, than a larger sawtooth periodicity, i.e., $\lambda/h = 0.6$ ($\lambda = 9\,mm$).

Finally, Figure 4.23 shows that as the turbulence increases on either side of the centre-line due to the serrations, it decreases by up to 18 % at the centre-line. This indicates a different behaviour at the centre-line and in the rest of the wake and is therefore investigated below.

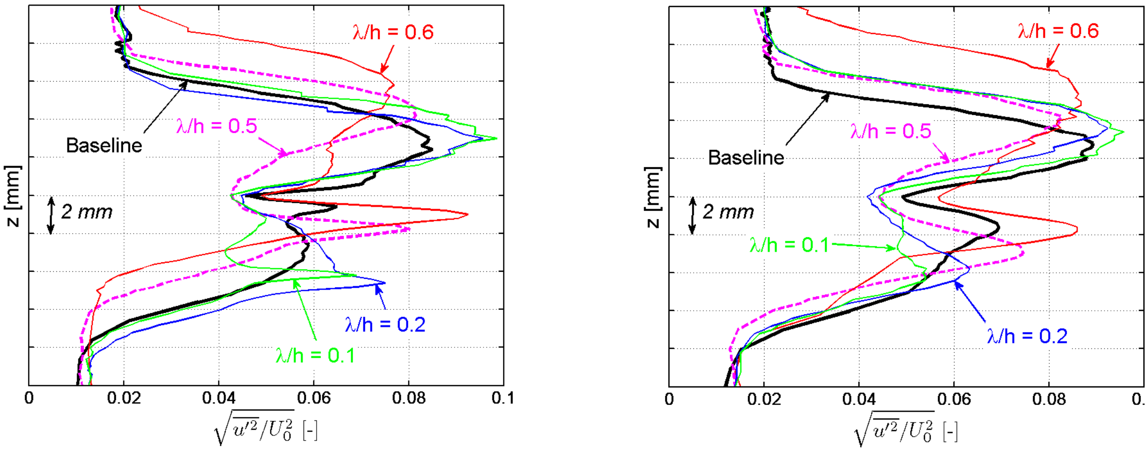

(a) $x/c = 0.03$.

(b) $x/c = 0.13$.

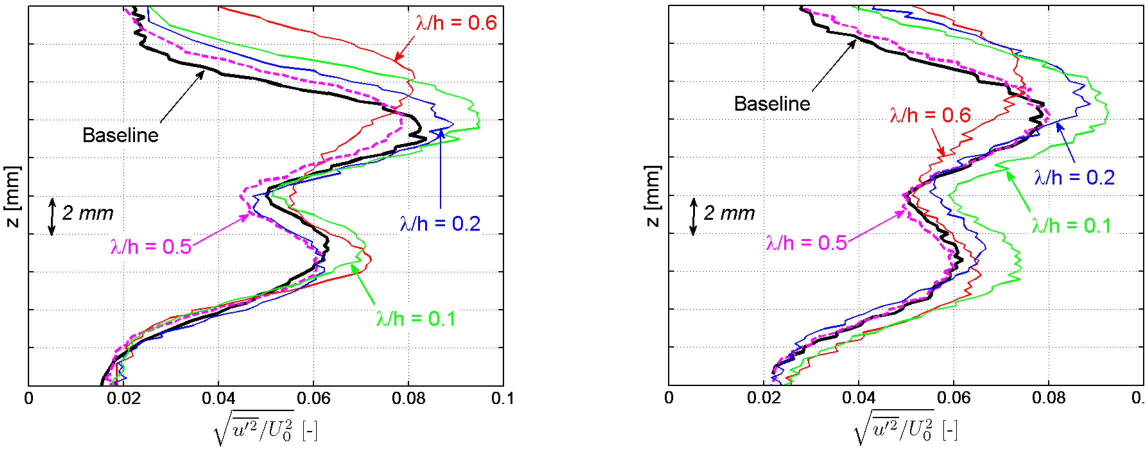

(c) $x/c = 0.40$.

(d) $x/c = 0.66$ ($x = 0$ is at the airfoil trailing edge).

Figure 4.23: Variation of the turbulence in the wake measured behind a straight edge and the four serrated edge $\lambda/h = 0.1$, $\lambda/h = 0.2$, $\lambda/h = 0.5$ and $\lambda/h = 0.6$.

In order to compare the behaviour of the streamwise turbulence at the centre-line and in the rest of the wake, the average wake turbulence was calculated by integrating the rms velocity over the wake width, for each position $x/c = 0.03$ to $x/c = 0.66$, and for each serration geometry. Figure 4.24a and b respectively show the variation of the unsteady velocity, normalized by U_0, integrated over the wake width and integrated over $\pm 2\,mm$ around the centre-line. Data is presented as a function of downstream distance and for the baseline trailing edge and the four serrations discussed above.

While the trends of the integrated turbulence and of the turbulence at the centre-line differ significantly in the very near wake ($x/c < 0.4$), Figures 4.24a and b show reasonably similar results at $x/c = 0.66$. The general trends discussed below can be seen in both Figures.

A difference can be observed between the serrations with amplitude $2h = 30\,mm$, i.e., $\lambda/h = 0.1$, $\lambda/h = 0.2$ and $\lambda/h = 0.6$, and the short serration with amplitude $2h = 20\,mm$, i.e. $\lambda/h = 0.5$ (shown by the dotted line). The turbulence increases in the presence of the longer serrations ($2h = 30\,mm$) and decreases by up to $10\,\%$ in the presence of the shorter serrations ($2h = 20\,mm$). This was also reported by Geiger who found the Turbulent Kinetic Energy (TKE) being larger behind a long serration.

Figure 4.24a shows that the small overall decay of the average turbulence velocity can be observed for the baseline case, and for the two serrations $\lambda/h = 0.5$ and $\lambda/h = 0.6$ only. This is mainly due to the fact that the turbulence is integrated over the whole wake width. The decay of the turbulence along the centre-line is faster, as seen in Figure 4.24b, although this is only seen for the straight edge and the serration $\lambda/h = 0.6$.

Finally, for a given sawtooth amplitude of $2h = 30\,mm$, it appears that for $x/c < 0.4$, the streamwise turbulence is reduced for a smaller sawtooth periodicity λ, while it is increased further downstream relative to a larger sawtooth amplitude. In the far wake at $x/c = 0.66$, this condition is contrary to the noise reduction criteria presented in Section 4.2.1, where it is shown that the smaller the periodicity λ, the greater is the noise reduction.

Geiger [47] shows that the streamwise turbulence can vary by up to about $20\,\%$ at $x/c = 0.61$ behind a serrated trailing edge, depending on the serration geometry. Unfortunately, no measurements were made further upstream in his work or measurements further downstream in this thesis, but this indicates that significant variations of the unsteady velocity can occur within the wake region investigated in this thesis. Geiger also shows that overall the levels of TKE are reduced compared to a straight trailing edge, for both short and long serrations, when $x/c > 1$. This is shown to be due to a faster decay of the TKE due to the increased mixing in the presence of serrated trailing edges.

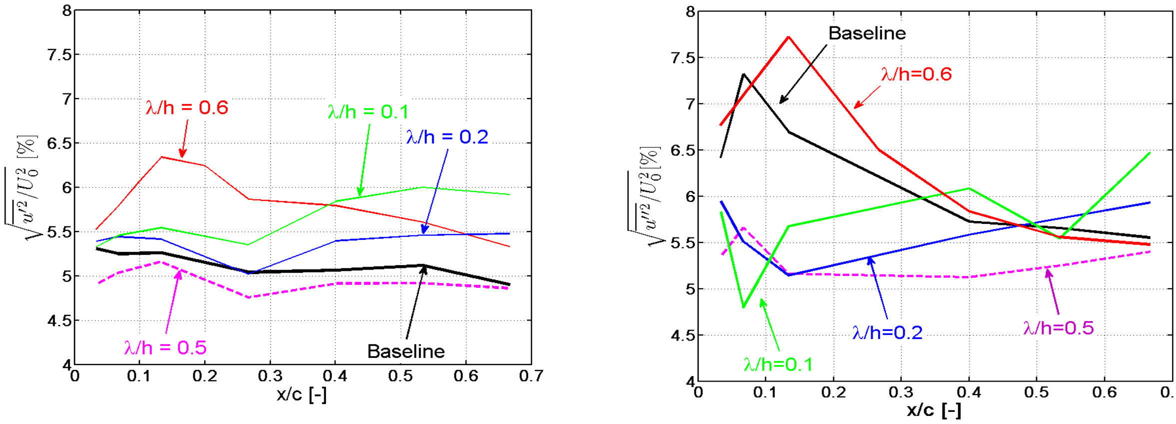

(a) Integrated over the wake width.

(b) At the wake center-line ($x = 0$ is at the airfoil trailing edge).

Figure 4.24: Variation of the turbulence levels normalized by U_0 for the straight edge and the four serrations $\lambda/h = 0.1$, $\lambda/h = 0.2$, $\lambda/h = 0.5$ and $\lambda/h = 0.6$.

This thesis now focuses on the variation of the streamwise turbulence wake profiles along the span of a single sawtooth, from the root to the tip.

Figure 4.25 presents the wake turbulence profiles behind the serrated edge $\lambda/h = 0.5$, measured along the tip of the sawtooth, the root, and the edge located at half the amplitude h, denoted as the 'middle' of the wetted edge below. In the very near wake at $x/c = 0.03$ and $x/c = 0.13$ (see Figures 4.25a and b), as the probe moves along the span of the airfoil, from the tip to the root of the sawtooth, the trajectory of the turbulence is gradually shifted downwards. Further downstream, at $x/c = 0.40$ and $x/c = 0.66$ (see Figures 4.25c and d), less and less differences are observed as the turbulence mixes out and the spreading of the wake becomes more uniform along the span.

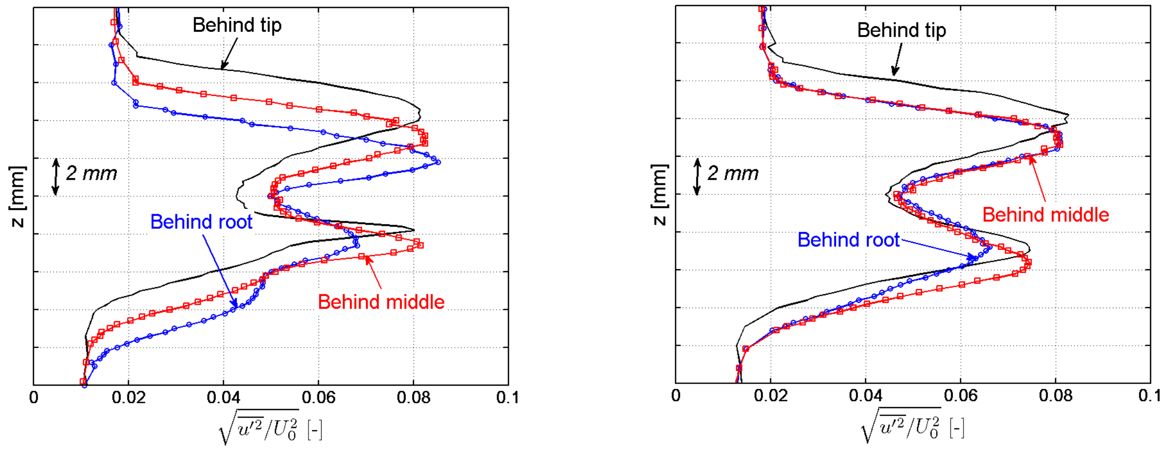

(a) $x/c = 0.03$.

(b) $x/c = 0.13$.

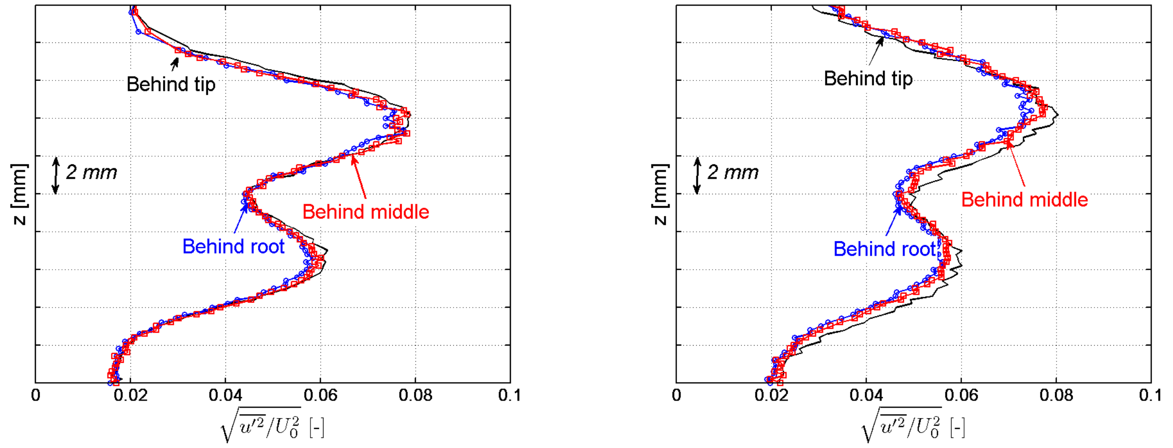

(c) $x/c = 0.40$.

(d) $x/c = 0.66$.

Figure 4.25: Spanwise variation of the turbulence in the wake measured behind the serrated edge $\lambda/h = 0.5$, $x = 0$ is at the airfoil trailing edge.

Figure 4.26 shows the integrated turbulence normalized by U_0 measured behind the shorter serration $\lambda/h = 0.5$, along the tip of the sawtooth (point 1), the root (point 3) and the middle of the wetted edge (point 2). The variation of the turbulence levels with downstream distance is almost identical but the levels vary. As expected, the levels are lower behind the root, where the mixing of the turbulence starts the earliest, followed by the middle of the edge and the tip of the sawtooth. This is also confirmed by Geiger's measurements, which showed that the production of TKE is dominant behind the tip of the serrations at the trailing edge. However, he also mentions that as the wake spreads downstream, the production of TKE decreases by almost a factor 10 but also moves from behind the tip of the sawtooth to behind the root (or 'valley' as used in [47]) of the sawtooth.

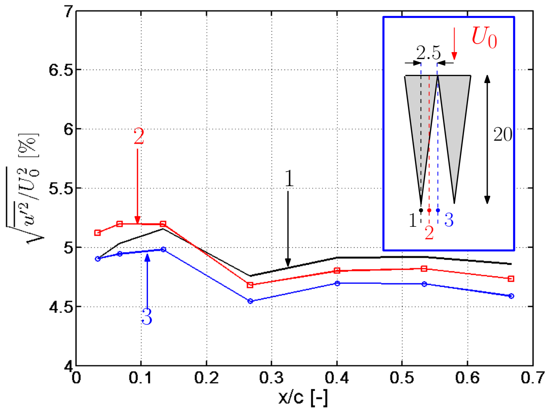

Figure 4.26: Spanwise variation of the turbulence integrated over the wake width, normalized by U_0 and measured behind the serrated edge $\lambda/h = 0.5$ along the tip, the middle and the root of one sawtooth ($x = 0$ is at the airfoil trailing edge).

4.5.3.3 Turbulent length scales

In order to investigate the variation of the turbulence length scales in the wake, a space-time correlation analysis was used to extract the unsteady velocity profiles from the hot wire data. This method allows the separation of the high turbulence regions in the wake from the low turbulence velocity background signal. It assumes frozen turbulence and is based on a measurement of the correlation between successive time samples acquired by the same probe. Figure 4.27 presents the temporal auto correlation function of the streamwise turbulence velocity $R_{uu}(x, y, z, \delta x)$, for time stationary signals at $x/c = 0.03$ and 0.63 (where $x = 0$ is at the airfoil trailing edge), where $R_{uu}(x, y, z, \tau)$ is defined in Equation 4.5.

$$R_{uu}(x, y, z, \tau) = E\left[u(x, y, z, t).u(x, y, z, t + \tau)\right] \tag{4.5}$$

where E denotes the expectation, $u(x, y, z, t)$ is the instantaneous streamwise velocity measured with the hot wire at a position (x, y, z) in the wake. $R_{uu}(x, y, z, \delta x)$ is plotted across the wake where frozen turbulence has been assumed and $\delta x = U_c\tau$. Thus, the frozen turbulence assumption allows an estimate for the streamwise spatial correlation to be performed from the temporal correlation function. $R_{uu}(x, y, z, \delta x)$ is shown for the straight baseline edge as well as for the short serration $\lambda/h = 0.5$. The value of $R_{uu}(x, y, z, \delta x)$ at $\delta x = U_c\tau = 0$ corresponds to the mean square turbulence velocity $R_{uu}(x, y, z, 0) = \overline{u'^2}(x, y, z)$. The convection velocity U_c of the turbulent eddies in the wake is taken as the velocity at the maximum mean wake deficit located at the centre-line. The two peaks of the turbulence in the wake correspond to the wake shear layers and a comparison between the baseline and serrated edge shows discrepancies in the near wake and more similar profiles in the far wake, as mentioned above. The auto correlation function was also computed for the three serrations $\lambda/h = 0.1$, 0.2 and 0.6 but is not shown here for brevity. They are used below to estimate the turbulent integral length scales.

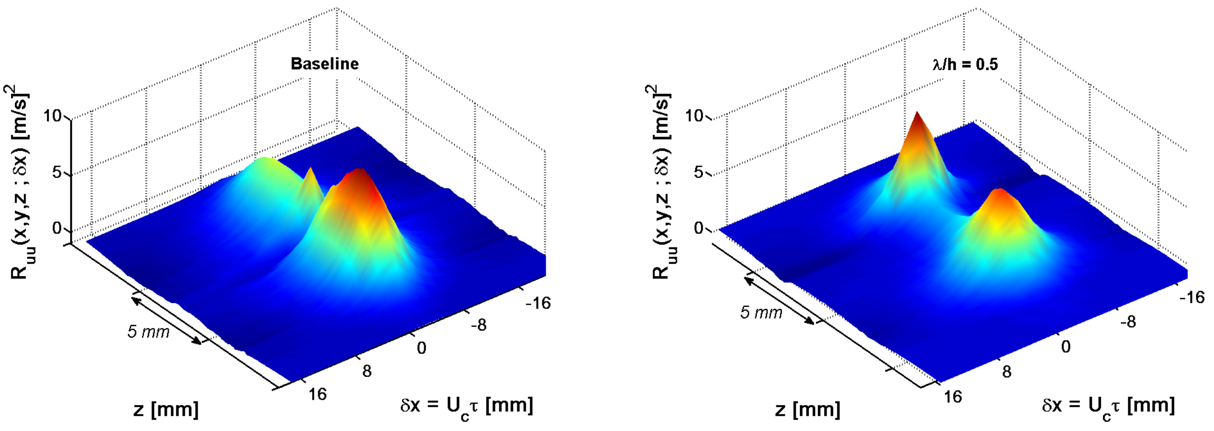

(a) Straight edge at $x/c = 0.03$.

(b) Serrated edge $\lambda/h = 0.5$ at $x/c = 0.03$.

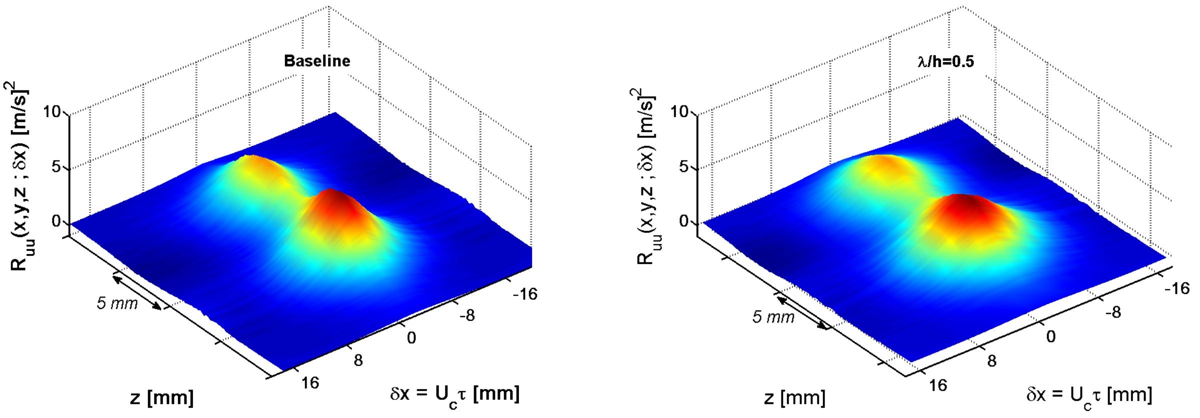

(c) Straight edge at $x/c = 0.66$.

(d) Serrated edge $\lambda/h = 0.5$ at $x/c = 0.66$.

Figure 4.27: Instantaneous auto correlation functions $R_{uu}(x, y, z; \delta x)$.

An important quantity for characterizing the turbulence in the wake is the integral turbulence length scale $\Lambda_{uu}(x, y, z)$. By assuming frozen turbulence the integral time scale can be used to deduce the turbulence integral length scale from Equation 4.6.

$$\Lambda_{uu}(x,y,z) = \frac{U_c \int R_{uu}\left(x,y,z,\tau\right) d\tau}{R_{uu}\left(x,y,z,0\right)} \tag{4.6}$$

Alternatively, the turbulence length scale can be estimated from experimental data using the value of $\tau_{1/2}$ for which $R_{uu}\left(x,y,z,\tau_{1/2}\right)/R_{uu}\left(x,y,z,0\right) = 0.5$. Assuming that the turbulent eddies are frozen and convected at the freestream velocity U_c, the length scale can be estimated using Equation 4.7.

$$\Lambda_{uu}(x,y,z) = U_c \tau_{1/2} \tag{4.7}$$

Figure 4.28 shows the normalized auto correlation function $R_{uu}\left(x,y,z,\delta x\right)/R_{uu}\left(x,y,z,0\right)$ as a function of $\delta x = U_c \tau$ for the sharp edge and the four serrated edges $\lambda/h = 0.1$, 0.2, 0.5 and 0.6, at $x/c = 0.03$ and 0.63. Note that the maximum of $R_{uu}\left(x,y,z,\delta x\right)/R_{uu}\left(x,y,z,0\right)$ is not centered at $\tau = 0$ because the velocity data in the wake were sampled at $20\,kHz$ only, thus preventing a high precision estimate of the time lag. Nevertheless, the resolution obtained with these measurements provides accurate enough data to allow comparison of the change in turbulence length scale between the sharp and the serrated trailing edges.

Figure 4.28, shows a 'slice' of the auto correlation functions of Figure 4.27, taken at the centre-line. Using Equation 4.7 to estimate the integral length scales in the wake, and as shown in Figure 4.30a below, it suggests that Λ_{uu} is increased by 22 % and 12 % in the far wake of the sharper serrations $\lambda/h = 0.1$ and $\lambda/h = 0.2$, respectively. Conversely, it is reduced by 7 % and 11 % in the far wake of the serrations $\lambda/h = 0.5$ and $\lambda/h = 0.6$, respectively.

In addition, Figure 4.28a shows that the typical distance Λ_{uu} over which the correlation function has dropped by 50 % is about $2.5\,mm$, which is much smaller than the amplitude $2h = 20\,mm$ of the sawtooth trailing edges. This observation is important evidence that the eddys close to the trailing edge are largely uncorrelated over the sawtooth. Therefore, it is believed that this is the reason why Howe's model, which assumes perfect frozen turbulence along the edges of the sawtooth, largely over-predicts the noise reduction using sawtooth serrations. This will be further discussed in Chapter 5.

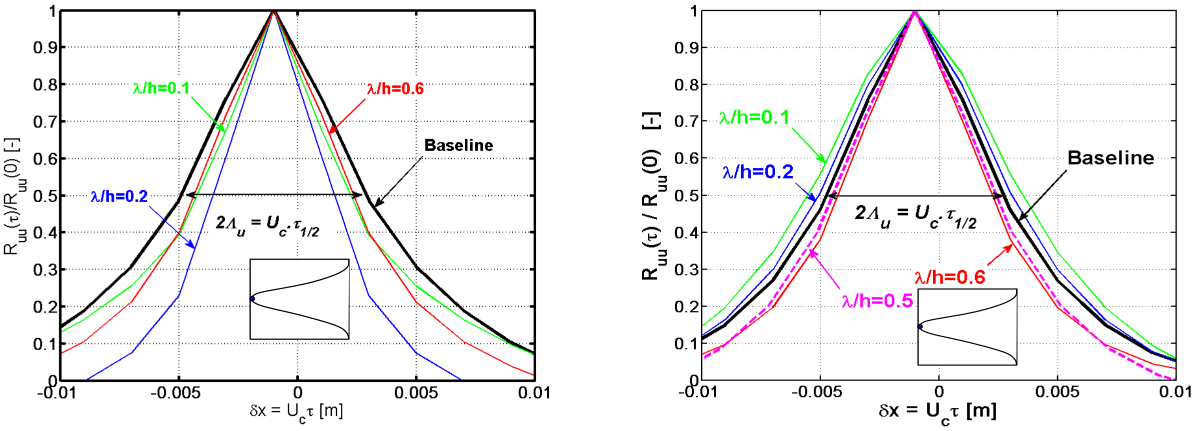

(a) At $x/c = 0.03$.

(b) At $x/c = 0.63$.

Figure 4.28: Instantaneous auto correlation function $R_{uu}(x, y, z, \tau)$ in the wake downstream, at the centre-line.

Using Von Karman's longitudinal velocity spectrum given in Equation 2.9 and $\phi_{uu}(k_x)^{VK} = U_0\,\phi_{uu}^{VK}(\omega)$, it can be shown that:

$$\phi_{uu}(k_x)^{VK} \to \frac{\overline{u'^2}\Lambda}{\pi}, \quad k_x \to 0, \tag{4.8}$$

where $k_x = \omega/U_0$ is the streamwise wave number. The velocity spectra shown in Figures 4.29a are a comparison of the baseline velocity spectrum measured at $x/c = 0.66$ and of the Von Karman spectrum $\phi_{uu}(k_x)^{VK}$. The input data used to predict the Von Karman velocity spectrum are obtained from the above analysis. Although the turbulence in the wake is not isotropic, the general shape is generally well predicted. The interesting feature of this spectrum is that at low frequencies, when $k_x \to 0$, Equation 4.8 shows that the turbulent velocity spectrum is only a function of the turbulence parameters $\overline{u'^2}$ and Λ_{uu}. This shows that the levels of the low frequency plateau observed for all serrated trailing edges in Figure 4.29a can be directly related to the product $\overline{u'^2}\Lambda_{uu}$.

Therefore, it can be observed in Figure 4.29b that at low frequencies, the level of the turbulence spectrum is increased when the length scale and the unsteady velocity (see Figure 4.24b) are increased relative to the baseline, i.e., for the sharper serration. Conversely the level of the plateau decreases by up to 2 dB for the large base serration $\lambda/h = 0.6$ and the shorter serration $\lambda/h = 0.5$, when $\overline{u'^2}$ and Λ_{uu} are decreased. The high frequency content is reduced for all serrated edges except $\lambda/h = 0.6$ and overall, the shorter serration $\lambda/h = 0.5$ decreases the turbulence the most above $2\,kHz$.

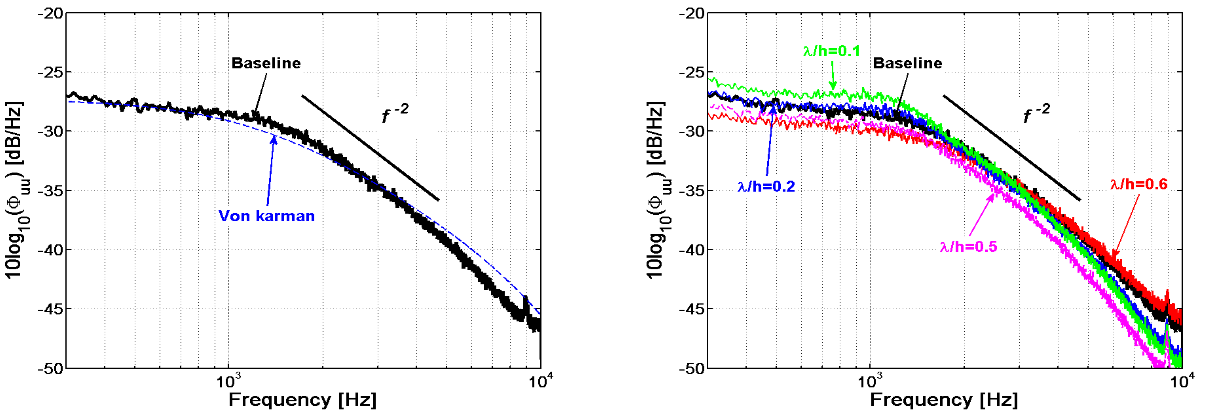

(a) Comparison of the straight edge with the Von Karman spectrum.

(b) Comparison of the straight edge spectrum with the four serrated edges $\lambda/h = 0.1$, $\lambda/h = 0.2$, $\lambda/h = 0.5$ and $\lambda/h = 0.6$.

Figure 4.29: Wake velocity spectra in the wake at $x/c = 0.63$, at the centre-line.

The turbulence length scales, obtained using Equation 4.7 are presented in Figure 4.30a behind the baseline airfoil and the four trailing edge serrations $\lambda/h = 0.1$, 0.2, 0.5 and 0.6. It can be seen that in the wake region of interest, i.e., from $x/c = 0.03$ to 0.66, the trends previously observed at $x/c = 0.66$ appear to be the same as the wake spreads. Therefore, the length scales are increased by up to 20 % behind the sharper serrations $\lambda = 0.1$ and $\lambda/h = 0.2$ compared to the baseline airfoil, but reduced by up to about 25 % behind the serrations $\lambda/h = 0.5$ and $\lambda/h = 0.6$. Geiger [47] also mentions that the spreading of the wake increases with the increasing amplitude of the sawtooth, which is in accordance with a larger length scale. This also suggests that shorter serrations are more effective at reducing the turbulent length scales than longer serrations. The increase of the turbulence length scale observed for the sawtooth $\lambda/h = 0.1$ and 0.2 relative to the sawtooth $\lambda/h = 0.6$ also shows that for a given amplitude $2h$, the sharper serration tends to further increase the turbulent length scale.

In addition, all curves in Figure 4.30a appear to be almost parallel as x/c increases, and it is assumed that this trend continues further downstream.

Figure 4.30b shows the variation of the turbulence length scale as the wake spreads between measurements performed behind the tip, the root and the middle of the sawtooth, for serrations $\lambda/h = 0.2$ and 0.5. While the rate of growth of the length scales is reasonably similar across the span, it appears that for $x/c > 0.4$, the length scales can be ranked as follow: $\Lambda_{root} > \Lambda_{middle} > \Lambda_{tip}$, which is consistent with the early mixing of the wake in the valleys of the serrations. However, Geiger mentions that the spreading rate of the wake is the fastest behind the tip and the slowest behind the root. Therefore, the spanwise distribution of length scales is expected to gradually become more uniform as the wake spreads.

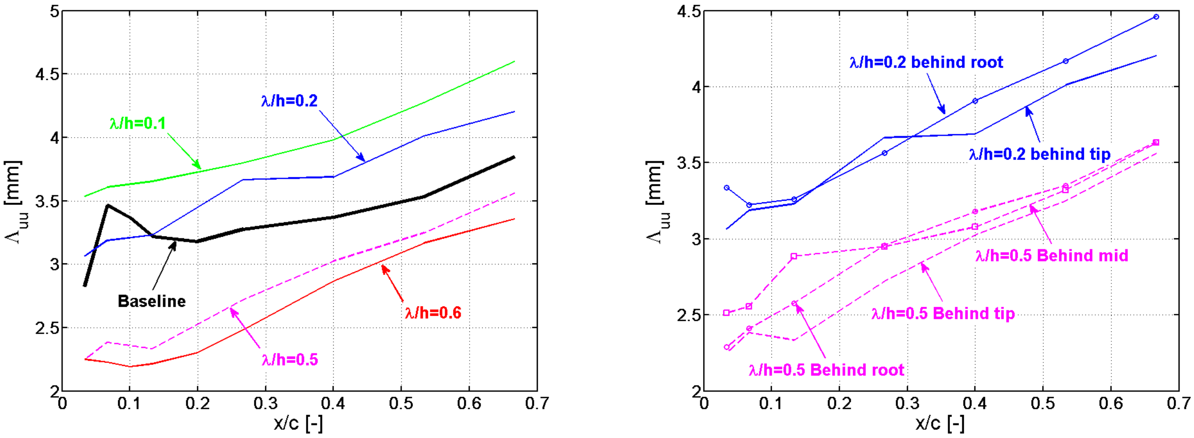

(a) for a straight edge and the four serrations $\lambda/h = 0.1$, $\lambda/h = 0.2$, $\lambda/h = 0.5$ and $\lambda/h = 0.6$.

(b) Spanwise variation measured for the two serrations $\lambda/h = 0.2$, and $\lambda/h = 0.5$.

Figure 4.30: Variation of the turbulence length scale Λ_{uu} with downstream distance relative to the airfoil chord x/c.

Figure 4.31 shows contour levels of the auto correlation function $R_{uu}(x, y, z, \tau)$, normalized by $R_{uu}(x, y, z, 0)$, for the baseline trailing edge and the three serrations $\lambda/h = 0.1$, 0.2 and 0.6 measured along the tip of one sawtooth at $x/c = 0.63$. The width of the wake is indicated by the horizontal double arrow for each trailing edge profile. As the turbulence is not fully mixed, two length scales can be identified; one above, and one below the wake centre-line. It can be seen that for the large base serration $\lambda/h = 0.6$, the width of the wake tends to increase while the turbulent length scales tends to decrease, as seen in Figure 4.30a. By contrast, for the sharp serrations $\lambda/h = 0.1$ and $\lambda/h = 0.2$ the width of the wake remains reasonably identical compared to the baseline case but the turbulent length scales increase, as shown in Figure 4.30a.

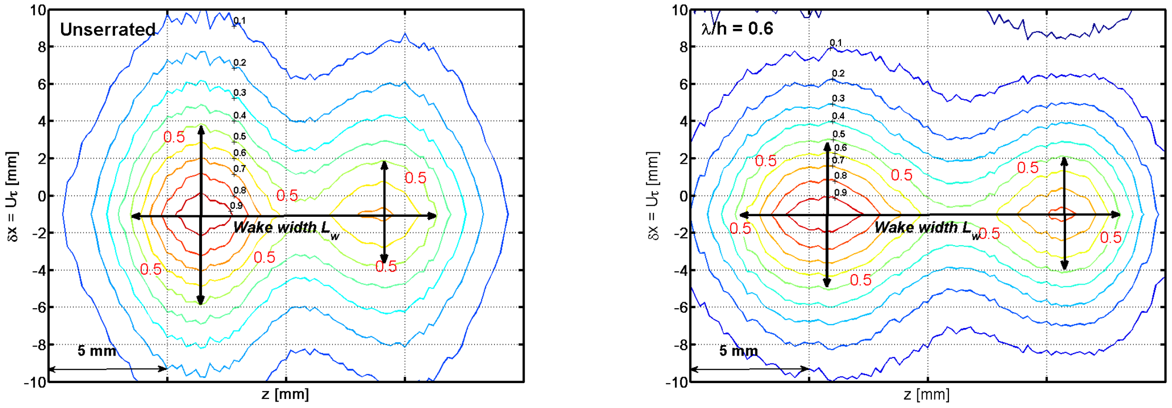

(a) Straight edge.

(b) Serration $\lambda/h = 0.6$.

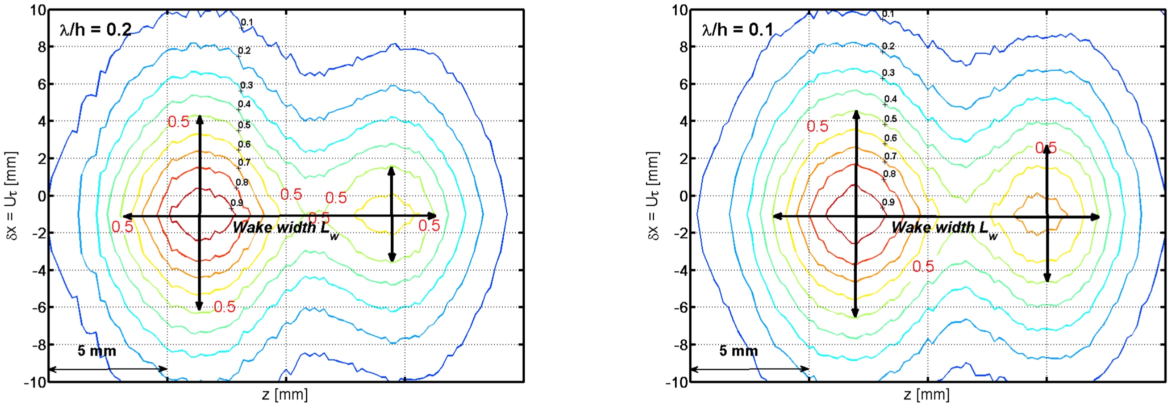

(c) Serration $\lambda/h = 0.2$.

(d) Serration $\lambda/h = 0.1$.

Figure 4.31: Contours of the normalized instantaneous auto correlation functions $R_{uu}(x, y, z, \tau)/R_{uu}(x, y, z, 0)$ at $x/c = 0.66$.

Finally, this Section shows that the airfoil aerodynamic performance is changed by the presence of trailing edge serrations. In addition, the conditions that define a specific sawtooth geometry as an effective treatment to reduce airfoil trailing edge noise appear to be in contrast with a gain in the aerodynamic performances. A good aero-acoustic balance was found using the serration $\lambda/h = 0.3$, i.e., $\lambda = 3\,mm$ and $2h = 20\,mm$ for the flow conditions and airfoil used in this study. This sawtooth was selected as the best trailing edge treatment in the FP7 European project FLOCON and was subsequently tested for noise and aerodynamic performances on a linear cascade by Finez *et al* [42]. Their results are in very good agreement with the ones described in this Chapter. This trailing edge treatment is also used in the tandem airfoil test presented in Chapter 7.

4.6 Summary

This Chapter reports measurements of the trailing edge noise reduction obtained using thirty seven serration geometries on a NACA65(12)-10 airfoil and at relatively low Mach numbers, from $M = 0.06$ to $M = 0.24$. Throughout this Chapter, the far field acoustic pressure are compared to the theoretical noise reduction predictions proposed by Howe [66].

Noise reductions of up to 5 dB over a wide frequency range were measured with serrated trailing edges, for a range of jet speeds and sawtooth geometries. However, large variations in the noise reduction were also measured between serrated edges. Therefore, the investigation was focused on determining the geometrical and flow parameters important to optimize the noise reduction. It was found that, as predicted by Howe, the sharper the serration, the greater is the noise reduction, although the levels of noise reduction obtained were much lower than the analytical ones (by at least 15 dB).

It was shown for the first time that noise reduction occurs when $h/\delta > 0.25$ and $f\delta/U_0 < 1$, and that within that range the larger the amplitude of the serration $2h$ and the smaller the periodicity of the sawtooth λ, the greater is the noise reduction. When $h/\delta < 0.25$, the amplitude of the serration is too small and turbulent eddys pass over the sawtooth without significant interaction. Experimental data also show that extraneous sources of noise in the high frequency range, due to the presence of a cross-flow in between the teeth of the serration, masks the considerable noise reductions predicted by the theoretical model. The noise increases at frequencies above some critical frequency, which is shown to depend only on $f\delta/U_0 \approx [0.7 - 1]$ and weakly depend on the serration geometry. This Strouhal number dependency was also later reported by Finez [42] on a linear cascade arrangement fitted with NACA65(12)-10 airfoils. As the airfoil angle of attack increases, the level of the high frequency noise increases. As the cross-flow becomes stronger, due to the stronger pressure gradients between either sides of the airfoil, then so does the level of high frequency noise.

This study also focuses on the effect of the sawtooth serrated edges on steady and unsteady aerodynamics around the airfoil. While no significant influence of the serrated edges on the lift was recorded, an increase of the drag was reported, gradually increasing with reducing the sawtooth periodicity λ (up to 10 % measured). Particular attention was paid to the measurements of the boundary layer profiles over a single sawtooth. While Howe assumes that the boundary layer flow remains unaffected by the serrated edge, it was shown that the boundary layer thickness gradually increases by up to 12 %, from the root to the tip of the sawtooth, relative to the straight edge. It was also shown that the peak of turbulence is shifted away from the airfoil surface, which was also subsequently measured by Finez using PIV on a linear cascade arrangement. Close to the root of the sawtooth, small differences are observed between the baseline and the serrated edge indicating that the serrations have no significant upstream effects on the development of the boundary layer.

The turbulence in the wake, which is of concern for airfoil turbulence interaction noise, was also measured at various spanwise locations downstream of the trailing edge. Different trajectories of the mean wake were measured behind each serrated edge. Due to the spanwise non uniformity of the serrations, the mixing of the turbulence, in the very near wake is largely non-uniform along the span. However, as shown in this Chapter, and by Geiger [47], the differences tend to even out further downstream. A reduction of the turbulence in the wake by up to $10\,\%$, and of the turbulence integral length scale by $25\,\%$, for the shorter serrated edge of amplitude $2h = 20\,mm$ and periodicity $\lambda = 5\,mm$ was revealed. It was also shown that the turbulence and integral length scales increase compared to the baseline as the serration gets sharper.

Overall, this Chapter shows that although greater noise reductions are obtained for a sharper sawtooth in the low frequency range $f\delta/U_0 < St_\delta$, a larger high frequency noise increase occurs when $f\delta/U_0 > St_\delta$, with $St_\delta \sim 1$. By contrast, the aerodynamic performances associated with a sharper serration, i.e., drag, turbulence and integral length scales in the wake, are generally increased relative to the baseline case.

Chapter 5

Mechanisms of sawtooth serrated trailing edge noise reduction

In this Chapter, the physical mechanisms responsible for the change in the trailing edge noise radiation due to the introduction of sawtooth serrated trailing edges are investigated.

It is well known that the generation of broadband trailing edge noise from an airfoil occurs when the hydrodynamic fluctuating pressure of the turbulent boundary layer is scattered into acoustic energy by the edge discontinuity and subsequently radiated to the far field [7, 62, 68]. Broadband noise reductions of up to about 5 dB were obtained in various studies [17, 30, 27, 36, 42, 55, 56, 54, 59, 66, 71, 82, 88, 92] when using a sawtooth geometry at the airfoil trailing edge. Furthermore, most of these studies reported a significant increase in the noise at high frequencies [17, 36, 42, 71, 88]. Only Howe [65, 66] has considered this problem using analytical methods, which as know from Chapter 4, substantially over-predict the levels of noise reduction. It is shown in Chapter 4 that when using sawtooth trailing edge serrations, broadband noise reduction occurs when $f\delta/U_0 < St_\delta$ while broadband noise increase occurs when $f\delta/U_0 > St_\delta$, where St_δ has been found to be close to unity, depending on angle of attack and serration geometry. The mechanisms responsible for this reduction and increase in the trailing edge noise radiation are presently unknown and explained in detail in this Chapter.

In order to study the mechanism of noise reduction and noise increase due to sawtooth serrations, the distribution of the unsteady surface pressure was measured over one side of a single sawtooth. The results are compared to a straight edge and used in conjunction with the acoustic and aerodynamic data presented in Chapter 4 to deduce the physical mechanisms involved in trailing edge noise reduction.

This Chapter is divided into two parts. The first relates to the mechanisms of noise reduction by the use of trailing edge serrations at low frequencies, $f\delta/U_0 < St_\delta$. The second part concerns the mechanisms of noise increase at high frequencies $f\delta/U_0 > St_\delta$.

5.1 Mechanisms of noise reduction: $f\delta/U_0 < St_\delta$

5.1.1 Background

In Chapter 4 broadband noise reductions of up to about 5 dB were obtained in the low frequency range $f\delta/U_0 < St_\delta$, where $St_\delta \sim 1$. However, apart from Howe's theoretical model [65, 66], no studies have investigated the mechanisms responsible for such noise reductions. In an attempt to relate the near field modifications to the far field noise reductions predicted using DNS computations, Jones *et al* [71] reported noise reductions of between 6 to 10 dB in the far field and found that the boundary layer parameters over a straight edge and over a sawtooth serration are almost unchanged at the very low Reynolds number $Re_c = 50,000$ and $M = 0.4$. This suggests that the surface pressure close to the edge is not significantly affected by the presence of the serrated edge and therefore supports Howe's assumption that the boundary layer pressure remains unchanged compared to a straight trailing edge.

This finding contradicts the finding of Chapter 4 and Gruber *et al* [55, 56], which shows that close to the tip of the sawtooth, the boundary layer thickness δ is gradually increased (by up to 12 % at the tip of the sawtooth) and that the region of maximum streamwise mean square velocity is gradually 'pushed' away from the airfoil surface. Finez [42] subsequently measured a similar change in the boundary layer on a blade in a cascade configuration using PIV measurements. The measurements gathered in this thesis therefore suggest that introducing trailing edge sawtooth serrations causes significant changes to the boundary layer structure.

Although various experimental studies [47, 15] reported measurements of the mean and unsteady flow velocity in the wake of serrated edges (see Chapter 4), no further information is available in the literature as to how the flow in the boundary layer is affected by the introduction of sawtooth serrations.

Equation 1.1, which is quite general and applies to any distribution of random dipole sources, including that produced with trailing edge serrations, suggests that a reduction of the far field acoustic pressure occurs by either a reduction of the boundary layer pressure $\phi_{qq}(\omega)$ or the spanwise correlation length $l_y(\omega)$.

Therefore, the only potential mechanisms responsible for the noise reduction are:

- A reduction of the strength of the sources, i.e., a reduction in the difference in unsteady pressure across the airfoil in the vicinity of the trailing edge.
- A reduction of the correlation length l_y of the surface pressure, particularly close to the edges where scattering occurs.

5.1.2 Measurements of the surface pressure over a single sawtooth

In order to quantify the behaviour of the surface pressure across the trailing edge, with and without trailing edge serrations, simultaneous measurements of the far field pressure and of the unsteady surface pressure over a single sawtooth were made.

These results are presented in this Section together with some of the acoustic and aerodynamic data of Chapter 4 to understand the mechanisms of the noise reduction due to sawtooth serrations.

5.1.2.1 Experimental setup

In order to measure in detail the surface pressure distribution across one side of a single sawtooth, measurements were made on one side of a flat plate attached to the lower side of the wind tunnel nozzle. The flow over the flat plate is therefore in the form of a wall jet.

The wall jet is sketched in Figure 5.1 and fitted in turn with a sawtooth trailing edge and a straight trailing edge. Surface pressure measurements were performed using Remote Microphone Probes (see Chapter 2 and Perennes *et al* [94]) on the surface of a single sawtooth. The use of a wall jet, rather than an airfoil in the potential core for this experiment, is because it allows the use of numerous RMPs very close to the trailing edge, with the capillary tubes extending down below the flat plate outside the flow. The wall jet configuration allows the surface pressure to be taken as close as $0.85\,mm$ from the edge using RMPs connected underneath the trailing edge surface, as shown in Figure 5.2. The pressure spectrum in the far field was also simultaneously recorded at the three mean flow velocities $U_0 = 10$, 20 and $30\,m/s$ using the polar array of 19 B&K microphones described in Chapter 2. The sound power spectrum per unit span $PWL(f)$ was also calculated using Equation 2.2, which integrates the measured mean square pressure between radiation angles of 50^o and 110^o.

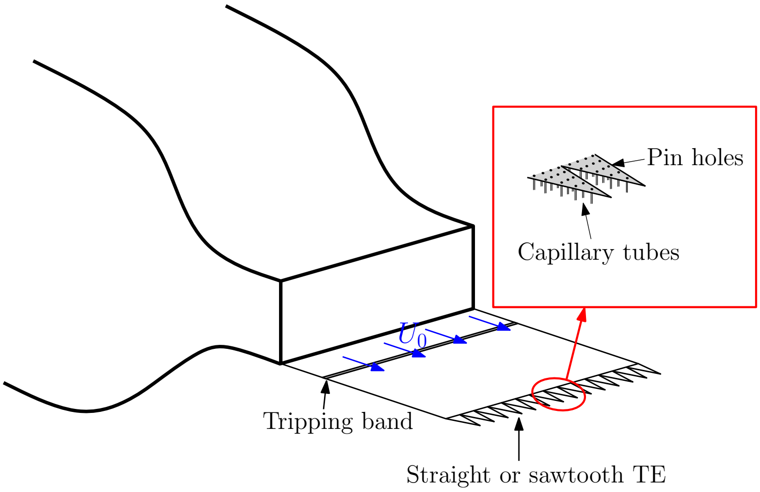

Figure 5.1: Wall jet experiment.

The sawtooth serration geometry used for this study has dimensions of $\lambda = 9\,mm$, and $2h = 30\,mm$ ($\lambda/h = 0.6$ in Table 4.1). Although this particular sawtooth geometry did not provide the best noise reduction measured on the the NACA65(12)-10 airfoil (see Chapter 4), the relatively large area of a single sawtooth allowed for at least twenty pressure tappings to be made. The sharper serration $\lambda/h = 0.3$, for which the best noise performance was measured, did not allow enough measurement points to be located over the surface to obtain detailed information of the variations of the near field pressure between straight and serrated edges.

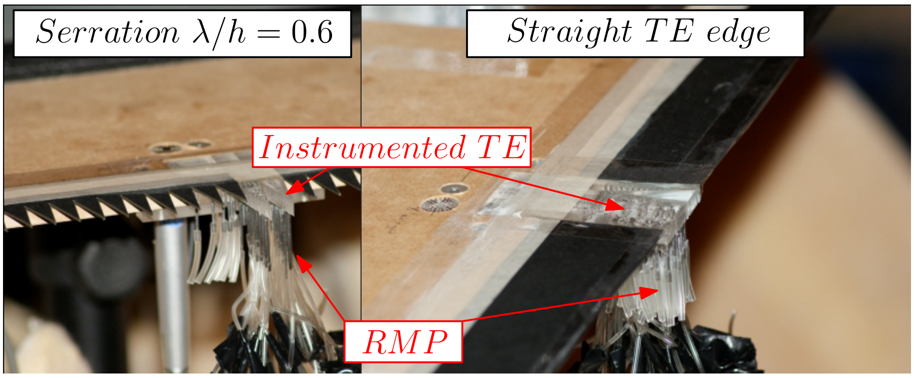

(a) Instrumented sawtooth in a serrated and a straight edge configuration.

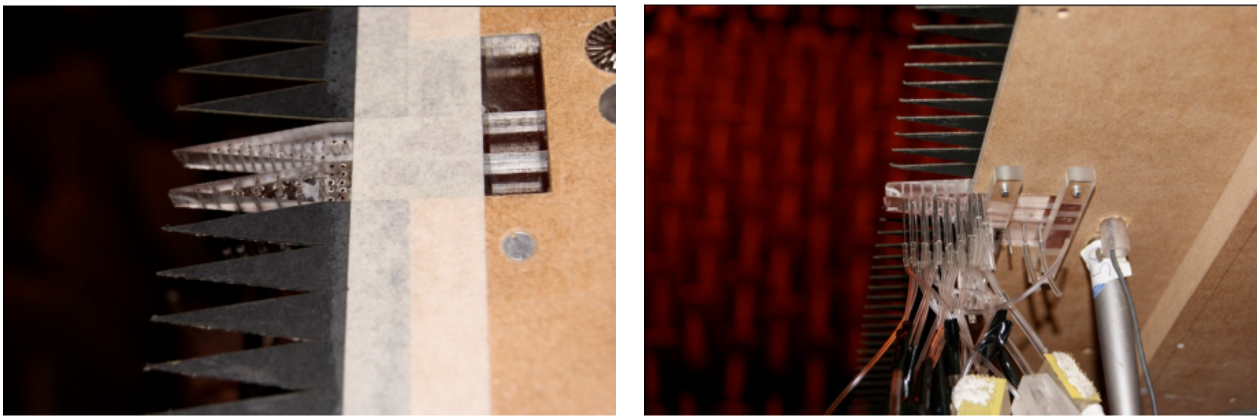

(b) Top view of the instrumented perspex sawteeth.

(c) Bottom view of the instrumented perspex sawteeth with the array of RMP connected to one sawtooth, and the reference B&K microphone.

Figure 5.2: Photographs of the wall jet experiment setup.

Figure 5.2 shows the trailing edge of the wall jet, fitted in turn with the serration $\lambda/h = 0.6$ (see Figure 5.2b) and with the straight edge (see Figure 5.2a). The flat plate is tripped at a location $50\,mm$ upstream of the trailing edge using rough tape of about $0.8\,mm$ thickness to ensure a fully developed turbulent boundary layer at the trailing edge. Figure 5.3 is a sketch of the flat plate fitted with the instrumented sawtooth, centered at the mid-span plane, which is composed of a perspex main body with two adjacent serrations and three detachable perspex triangles that can be fitted to the main body to change the edge from a straight edge (see Figure 5.3a) to a serration (see Figure 5.3b). The trailing edge is completed along the span using add-on flat plate inserts cut into stiff cardboard of $0.8\,mm$ thickness. The perspex parts are $5\,mm$ thick. Forty pin holes are distributed over the two adjacent sawtooth to provide the data necessary to estimate the changes in pressure, convection speed and correlation lengths over the sawtooth compared with a straight edge.

This arrangement therefore allows the detailed measurement of the surface pressure distribution over a single sawtooth and a straight edge using exactly the same set of RMPs without requiring the capillary tubes to be removed and re-attached.

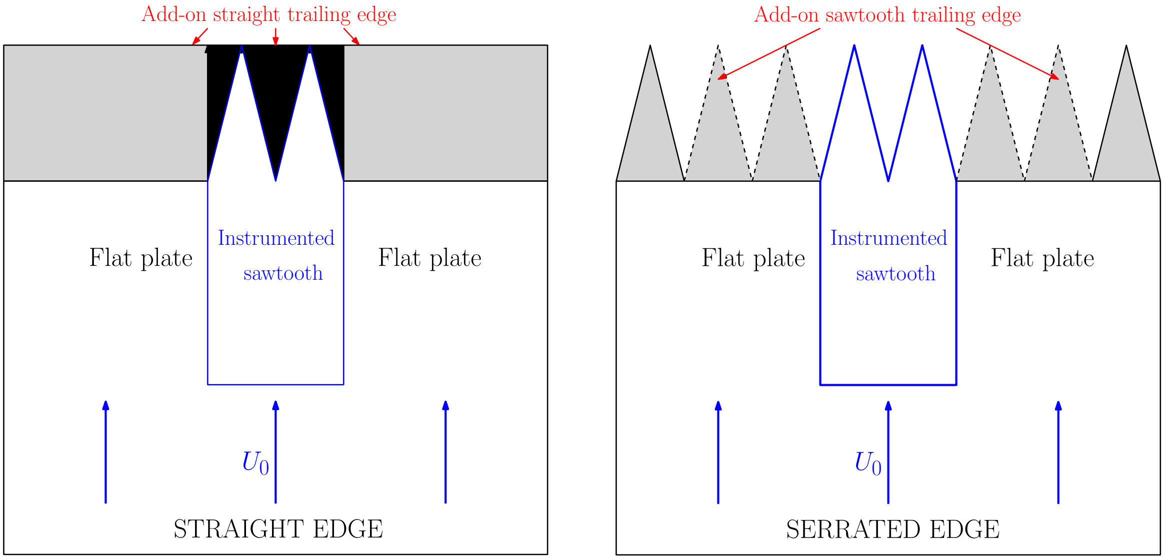

(a) Straight edge configuration.

(b) Serrated edge configuration.

Figure 5.3: Interchangeable trailing edge with instrumented perspex sawtooth.

As shown in Figure 5.2, the unsteady surface pressure is measured using RMPs as described in Chapter 2 and by Perennes [94], where the acoustic pressure is remotely measured by miniature Knowles microphones. Metal tubes of $0.4\,mm$ internal diameter are inserted into the main body outside the flow of the instrumented sawtooth and are flush mounted to the surface. The RMPs are connected underneath the main body using flexible tubes, as described in Chapter 2. A broadband in-situ calibration (see Chapter 2) was also carried out to correct the measured surface pressure signals for the time delay induced by the design of the RMP. In addition, it was found that about a third of the RMP were malfunctioning and due to the careful manufacturing process required, could not be replaced in time for the experiment.

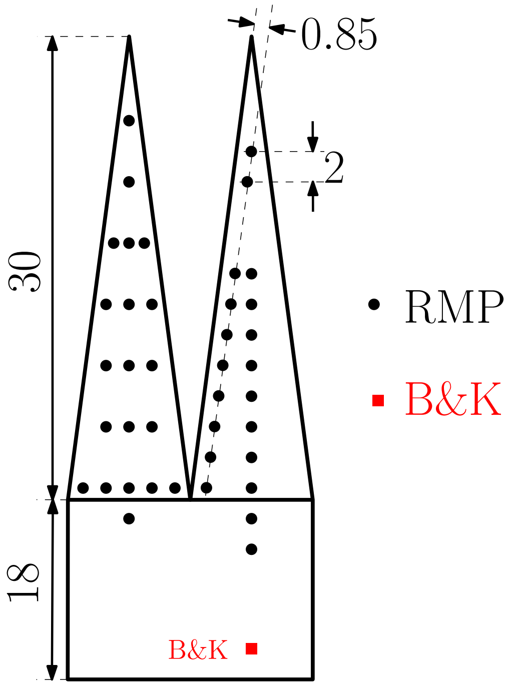

Figure 5.4: Sketch of the instrumented sawtooth showing the distribution of the pressure tapping over the two adjacent sawteeth - All units in mm.

Figure 5.4 shows the layout of the pin holes over the two adjacent sawteeth. A total of twenty surface pressure probes were used in order to map the unsteady surface pressure over a straight edge and a serrated edge. Measurements of the surface pressure were divided into two configurations, one for each sawtooth. A reference 1/2" B&K microphone is also mounted flush upstream of the instrumented module to ensure consistency and repeatability between measurements so that small differences due to slightly different flow speeds could be removed.

5.1.2.2 Sound power reduction

Figure 5.6a shows the sound power spectrum $PWL(f)$ defined in Equation 2.2 measured over the wall jet fitted in turn with a straight edge and the sawtooth serration $\lambda/h = 0.6$, at the three mean flow velocities, $U_0 = 10$, 20 and $30\,m/s$. The jet background noise is measured with no flat plate attached and is also plotted. It shows that the signal to noise ratio is limited to 5 dB over most of the frequency range. Figure 5.5 provides a comparison between trailing edge noise measurements from the wall jet and from the NACA65(12)-10 airfoil in the potential core, and shows that the trailing edge noise due to the wall-jet is between 3 dB and 6 dB below that of the airfoil, which is consistent with the flow passing over only one side.

Figure 5.6a shows that broadband noise reductions of up to 1 and 2.5 dB occur at $U_0 = 10$ and $20\,m/s$ respectively, in the frequency range 500 Hz to 5 kHz. It appears that on a wall jet, the influence of the sawtooth serration $\lambda/h = 0.6$ on the sound power radiation is negligible at $U_0 = 30\,m/s$. Therefore, further analysis of the noise data is restricted to the flow velocity

$U_0 = 20\,m/s$, where the greatest noise reduction occurs. The cause of this strong flow speed dependence is currently unknown.

Figure 5.6b compares the sound power reduction spectrum $\Delta PWL(f)$, defined in Equation 4.2, obtained using the sawtooth $\lambda/h = 0.6$ on a wall jet and on the NACA65(12)-10 airfoil at $U_0 = 20\,m/s$ (see Chapter 4). The sound power reduction $\Delta PWL(f)$ in the wall jet configuration is restricted to frequencies between 500 Hz and 5 kHz. Above 1 kHz, the noise reduction obtained on the wall jet matches closely that on the airfoil, as shown in Figure 5.6b. Below this frequency, background noise due to the jet masks any noise reduction. Therefore, Figure 5.6b shows that the noise reduction using sawtooth trailing edges is not the same in the present case as in an airfoil configuration (see Chapter 4). The main reasons are that the flow is one sided and the jet background noise is more intimately associated with the TE noise in a flat plate configuration than on an airfoil. In addition, the high frequency amplification does not occur because there is no cross flow.

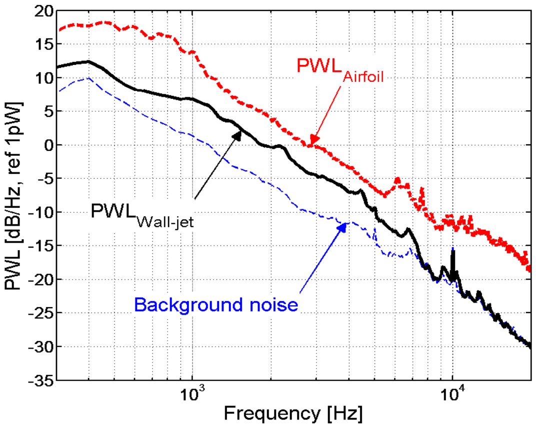

Figure 5.5: Trailing edge noise measured on a wall jet and on an airfoil at $U_0 = 20\,m/s$.

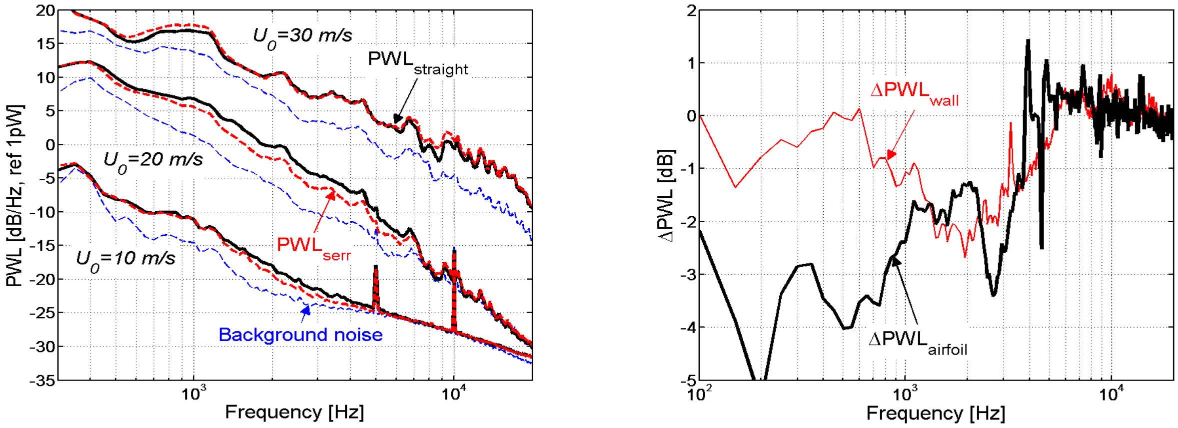

(a) PWL at $U_0 = 10$, 20 and 30 m/s.

(b) Comparison of ΔPWL on a wall jet and on the NACA65(12)-10 airfoil.

Figure 5.6: Sound power reduction due to the sawtooth trailing edge $\lambda/h = 0.6$.

5.1.2.3 Repeatability of the surface pressure data

A key requirement of this test rig is that the surface pressure spectrum is repeatable and consistent. This Section estimates the variability in the surface pressure data due to the transformation of the trailing edge from a serration to a straight edge and back to a serration again. Extensive repeatability tests, not shown here for brevity, have revealed that the surface pressure probes used in a remote configuration are much more sensitive to mounting than when used flush to the surface. This is believed to be related to the use of flexible tubes, whose geometry and length may vary when manipulated. In this experiment, for practical reasons, flexible tubes were also used between the pinhole and the microphone. However, a careful in-situ broadband calibration of the RMPs, as described in Chapter 2, allows good quality data to be taken. It is noteworthy that the possibility of changing the trailing edge geometry from a straight edge to a serration without having to change the arrangement of the surface pressure probes over the surface reduces measurement errors considerably.

Figure 5.7 shows the results of a repeatability test conducted by comparing the distribution of the surface pressure over the serrated edge at $U_0 = 20\,m/s$. Note that between the changes of geometry of the edge, as described above, the RMPs were not disconnected from the perspex sawtooth. The surface pressure spectra are shown for the four locations marked in Figure 5.7, i.e., from the base to the tip of the sawtooth. It can be seen that at all locations, the level of consistency is typically 2 dB over most of the frequency range, where noise reductions are obtained, but can be as high as 5 dB, as seen in Figure 5.7c for location 3. Furthermore, the discrepancies appear to grow from the base to the tip of the sawtooth. The surface pressure sensed by the RMP is believed to be sensitive to the possible motion of the flexible tubes when the instrumented sawtooth was manipulated. However, at all locations, the spectrum rolls off as f^{-5} at high frequencies, which is consistent with a turbulent boundary layer.

Another striking feature of Figure 5.7 is that as the tip of the sawtooth is approached, a broadband hump from 100 Hz to 1 kHz, gradually dominates the surface pressure spectrum by up to about 15 dB at the tip. This peak is discussed in the next Section.

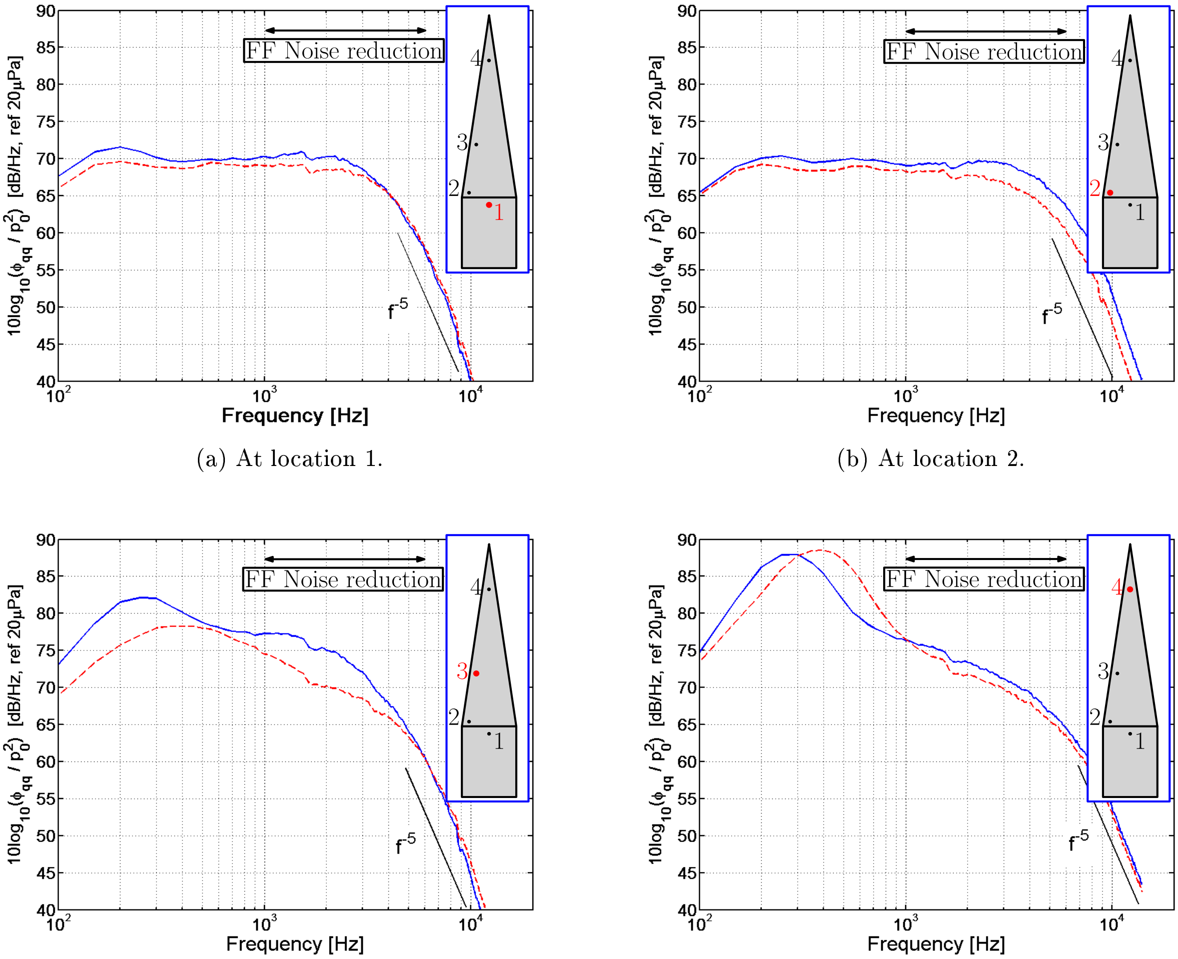

(a) At location 1. (b) At location 2.

(c) At location 3. (d) At location 4.

Figure 5.7: Consistency of surface pressure measurements over the sawtooth $\lambda/h = 0.6$ at $U_0 = 20\,m/s$.

5.1.2.4 Unsteady surface pressure over a single sawtooth

This Section investigates the changes in the unsteady surface pressure, due to the presence of the sawtooth serration at the trailing edge. Equation 5.1 defines the difference in the surface pressure level spectrum $\Delta SPL_{qq}(f)$, measured between a sawtooth trailing edge and a straight trailing edge plate, where $\phi_{qq}(f,\mathbf{y})|_{\mathbf{s}}$ is the pressure spectral density measured at position $\mathbf{y}$ over the serrated trailing edge and $\phi_{qq}(f,\mathbf{y})|_{\mathbf{b}}$ is the pressure spectral density measured at position $\mathbf{y}$ over the straight edge baseline plate.

$$\Delta SPL_{qq}(f,\mathbf{y}) = 10\log_{10}\left(\frac{\phi_{qq}(f,\mathbf{y})|_{\mathbf{s}}}{\phi_{qq}(f,\mathbf{y})|_{\mathbf{b}}}\right), \tag{5.1}$$

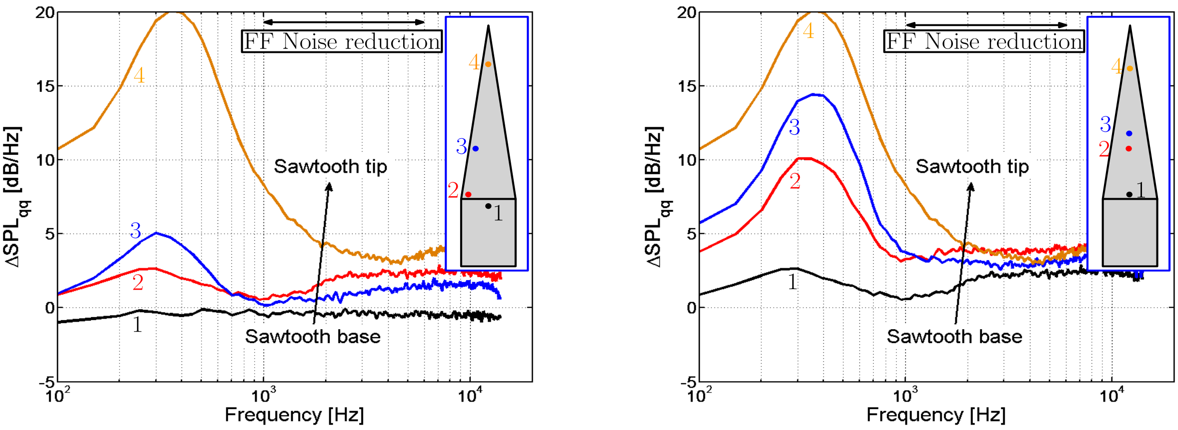

(a) Along the edge.

(b) In the direction of the flow.

Figure 5.8: Surface pressure difference ΔSPL_{qq} between the sawtooth and the straight trailing edge, at $U_0 = 20\,m/s$.

Figure 5.8 is a plot of $\Delta SPL_{qq}(f)$ at the four locations marked along the edge (Figure 5.8a) and in the direction of the flow (Figure 5.8b). At the base of the sawtooth, i.e. location 1, the difference in the surface pressure levels remains within 2 dB and therefore is within the range of repeatability of about 2 dB discussed in the previous Section. However, as the measurement point is gradually moved from the base to the tip of the sawtooth, the pressure gradually increases by up to about 15 dB with a broadband hump between 100 Hz and 2 kHz, centered at 350 Hz. At higher frequencies, the difference in the surface pressure spectrum also shows an increase due to the sawtooth trailing edge of up to about 4 dB. Note that although this increase is within the range of errors of 2 to 5 dB described in the previous Section for this experiment, the pressure increase is gradual and systematic, which indicates a physical process rather than a random measurement error.

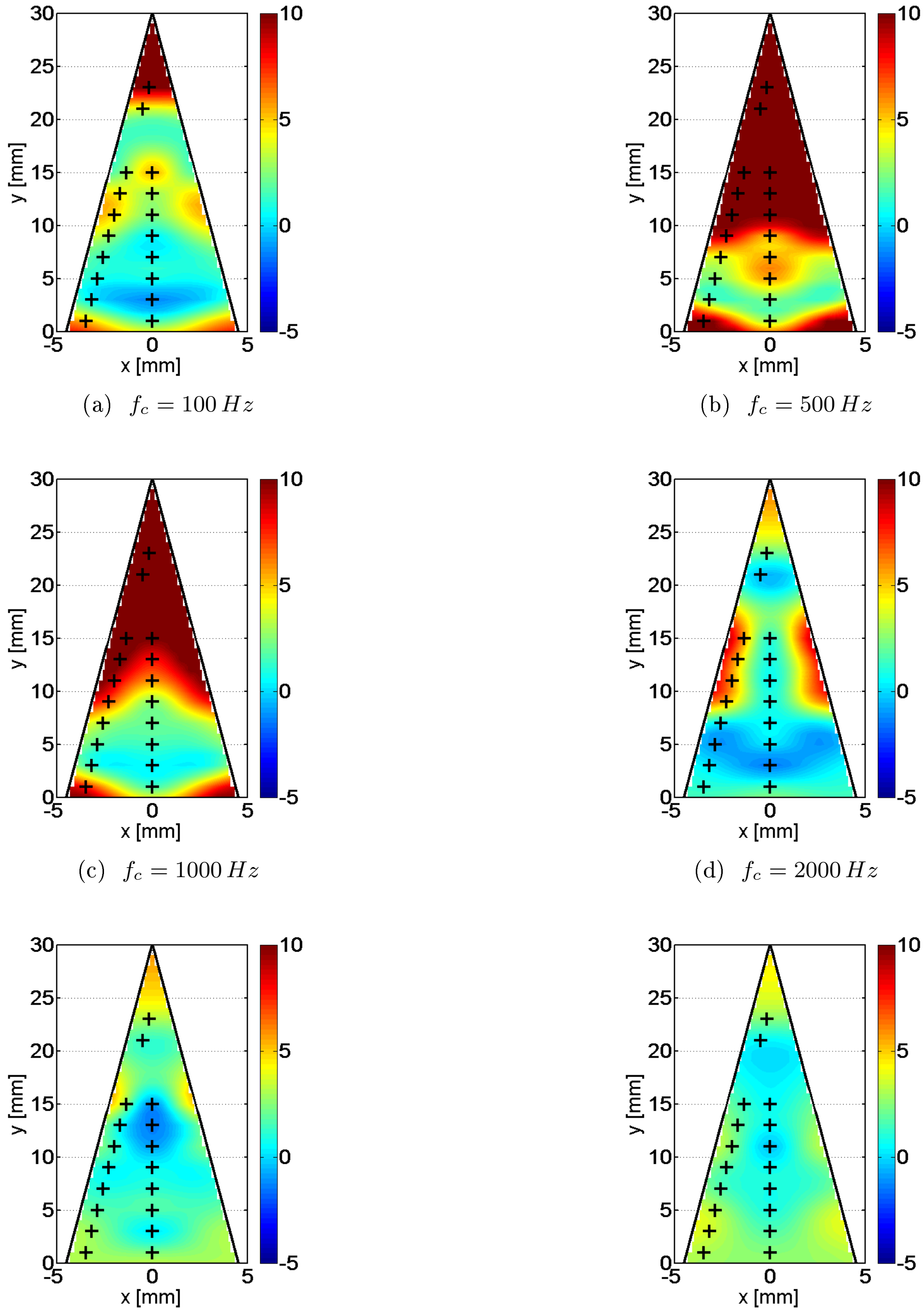

(a) $f_c = 100\,Hz$ (b) $f_c = 500\,Hz$

(c) $f_c = 1000\,Hz$ (d) $f_c = 2000\,Hz$

(e) $f_c = 5000\,Hz$ (f) $f_c = 10000\,Hz$

Figure 5.9: Variation of the unsteady pressure difference ΔSPL_{qq} over a single sawtooth in third octave bands.

Figure 5.9 shows the distribution over a single sawtooth of the difference in the surface pressure level spectrum $\Delta SPL_{qq}(f)$ given in Equation 5.1 at $U_0 = 20\,m/s$ and for the six third octave bands with centre frequencies 0.1, 0.5, 1, 2, 5 and 10 kHz. The measurement locations are indicated with crosses and the pressure data set was interpolated to the edges of the sawtooth using radial basis functions [1]. This extrapolation method introduces some artifacts that should not be considered in the interpretation. Therefore, the comments below only focus on the general trends observed from the analysis of the surface pressure data, at the measurements points marked by the crosses. Also, note that the distribution of the surface pressure was only measured on one side of the sawtooth (where the crosses are) and therefore the data was mirrored to make it symmetrical about the centre-line for presentation purposes. As already indicated by Figure 5.8, the surface pressure difference ΔSPL_{qq} gradually increases from the base to the tip of the sawtooth. The increase in the surface pressure as the tip of the sawtooth is approached, is increased at the three centre frequencies 0.1, 0.5 and 1 kHz due to the broad hump identified in Figure 5.8. At 2 kHz and above, the surface pressure increases more smoothly from the base to the tip of the sawtooth. It is noteworthy that the surface pressure difference appears to be greater close to the edges of the sawtooth (see Figures 5.9d to f). Overall, the surface pressure always increases in the presence of the sawtooth trailing edge, even in the frequency range between 1 kHz and 5 kHz where far field noise reductions are obtained. This increase is further discussed in Section 5.1.3 and is attributed to higher levels of multiple back-scattered pressures in the serration compared to a straight edge, particularly near the tip where the two edges become progressively closer as the tip is approached.

5.1.2.5 Variation of the phase velocity over a single sawtooth

Using the data recorded from pairs of streamwise sensors with constant separation distance $\eta_x = 2.5\,mm$, the phase spectrum can be used to estimate the phase speed at which the pressure appears to propagate over the sawtooth. Note that, close to the edge, the speed of the pressure perturbation is the net result of the convected boundary layer pressure and the scattered pressure, which is back-scattered in the opposite direction to the flow and which generally travels supersonically. Figure 5.10 shows the typical unwrapped phase gradient obtained between two sensors located in the boundary layer near the tip of the sawtooth. Using Equation 3.2, the phase velocity $U_{ph}(f)$ of the turbulent eddies in the vicinity of the edge can be estimated over both the straight edge and the serrated edge. It can be seen in Figure 5.10 that the gradient is steeper over a sawtooth trailing edge up to about 2 kHz, implying a slower phase speed of the turbulence near the edge. For frequencies above 4 kHz the phase speed becomes identical over a straight edge and over a serration.

---

[1] Using the matlab functions available on the Matlab File Exchange community: http://www.mathworks.com/matlabcentral/fileexchange/22173-radial-basis-function-network

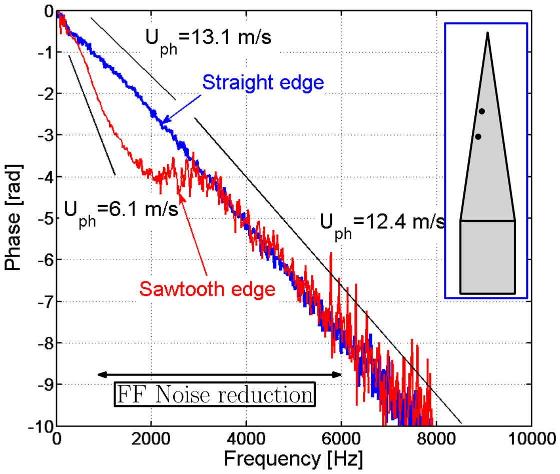

Figure 5.10: Variation of the phase speed at the tip of a straight edge and of the sawtooth $\lambda/h = 0.6$, at $U_0 = 20\,m/s$.

Figure 5.11 shows the variation of the normalized phase velocity U_{ph}/U_0, calculated using Equation 3.2, where $U_0 = 20\,m/s$. Results are presented over the sawtooth in the direction of the flow and along the edge of the sawtooth. It is clearly shown that the presence of the sawtooth causes a reduction in the phase speed of the turbulent eddies as the tip of the serration is approached in the frequency range where noise reductions were measured, i.e., up to about 5 kHz. At higher frequencies, the normalized phase speed merges with that calculated over the straight edge and equals 0.6 to 0.7, as expected from Chapter 4. The ratio U_{ph}/U_0 drops to about 0.35 close to the tip of the sawtooth. The frequency bandwidth over which the phase speed is reduced also increases as the tip of the sawtooth is approached. Direct comparisons between the left and right columns of Figure 5.11 suggest that this dip is more pronounced close to the edge than along the height of the sawtooth. This shows further evidence of a strong back-scattering effect due to the presence of edges in the vicinity of the sensor and is discussed in Section 5.1.3. The closer the edge, the stronger the scattering and hence the larger the frequency bandwidth in which the phase speed is reduced.

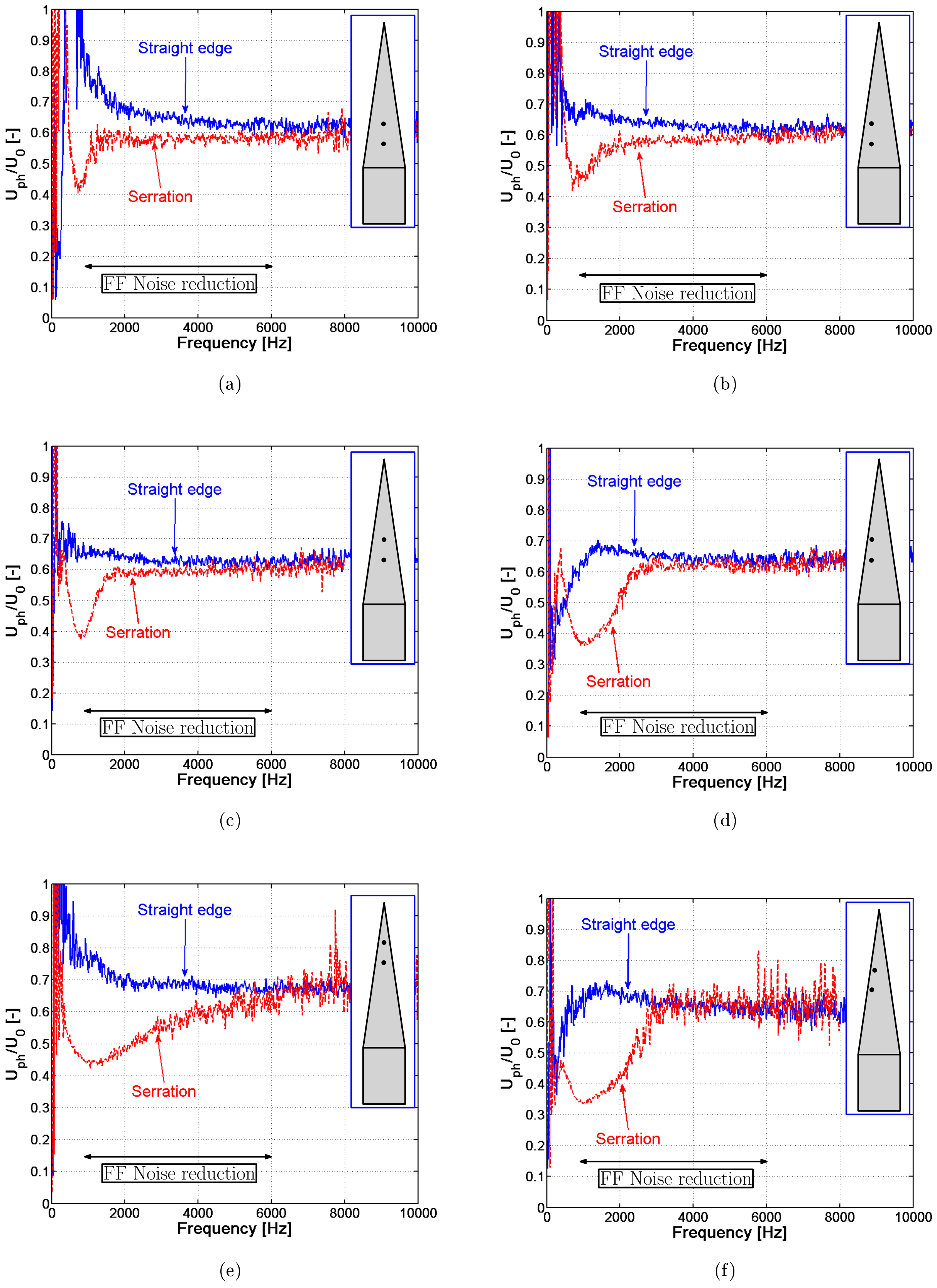

(a)

(b)

(c)

(d)

(e)

(f)

Figure 5.11: Variation of the normalized phase speed U_{ph}/U_0 over a single sawtooth in the direction of the flow (left), along the wetted edge (right). The arrow indicates the frequency range of TE noise reduction.

5.1.2.6 Variation of the coherence over the sawtooth

This Section investigates the changes in the coherence $\gamma^2(f,\eta_x)$ in the streamwise direction and $\gamma^2(f,\eta_y)$ in the spanwise direction between pairs of sensors over a single sawtooth. The coherence γ^2 is calculated using Equation 5.2, where $\phi_{12}(f,\eta)$ is the cross spectrum between a pair of sensors separated by a distance η and $\phi_{11}(f)$ and $\phi_{22}(f)$ are the auto spectra measured by each sensor. The spanwise correlation length $l_y(f)$, along which the sources located at the trailing edge radiate with some coherence to the far field, is defined in Equation 5.3 as the integral of the coherence $\gamma^2(f,\eta_y)$ over the separation distance η_y. This was calculated on a straight edge airfoil in Chapter 3 using surface pressure measurements distributed along the airfoil span. However, in the current experiment, about a third of the surface pressure sensors provided non-reliable data and the correlation length cannot be estimated accurately. In this study, the behaviour of the coherence between pairs of sensors, as an indicator of the changes in the correlation of the sources distributed near the edge, is investigated.

$$\gamma^2(f,\eta) = \frac{|\phi_{12}(f,\eta)|^2}{\phi_{11}(f)\,\phi_{22}(f)} \tag{5.2}$$

$$l_y(f) = \int\limits_0^{\infty} \sqrt{\gamma^2(\eta_y,f)}\,d\eta_y \tag{5.3}$$

Figures 5.12 and 5.13 show the comparison of the coherence γ^2 measured in the boundary layer over the sawtooth and the straight edge.

Pairs of sensors distributed along a line parallel to the edge, and separated by a distance $\eta_x = 2.5\,mm$, are used in turn to estimate the variation of the coherence γ^2 from the base to the tip of the sawtooth (see Figure 5.12). Figure 5.12 illustrates that the coherence is reduced by up to 15 % in the frequency range 1.5 to 5 kHz along the edge, corresponding to the frequency range in which the sound power reduction occurs and where the decrease in the phase speed is observed in the phase spectra shown in Figure 5.11. However, at frequencies below 1.5 kHz, where the peak in the surface pressure is observed in Figures 5.7 to 5.9, the coherence is gradually increased as the sensors are moved towards the tip of the sawtooth. This is also believed to be evidence of a strong back-scattering from the edges as the back-scattered acoustic pressure will be coherent over larger distances compared to that due to pure turbulence, which is limited by the decay time of the eddys. Section 5.1.3 provides further interpretation of these results.

Figure 5.13 shows the variation of the spanwise coherence (in the direction perpendicular to the flow) as the pair of sensors is moved from the base to the tip of the sawtooth. The coherence between pairs of sensors located along a line perpendicular to the flow direction shown in Figure 5.13 shows that the coherence is typically smaller by 0.2 compared with the straight edge fitted to the wall jet. Direct comparisons of the spanwise coherence measured on the NACA65(12)-10 baseline airfoil at $U_0 = 20\,m/s$ and presented in Chapter 3 indicate that in the particular case of the wall jet experiment, the spanwise coherence, and therefore the associated correlation length is very likely to be small already. Poor signal to noise ratio in some RMPs may also destroy the broadband coherence. The strong back-scattering from the edges can also be seen as the pair of sensors approaches the tip of the sawtooth.

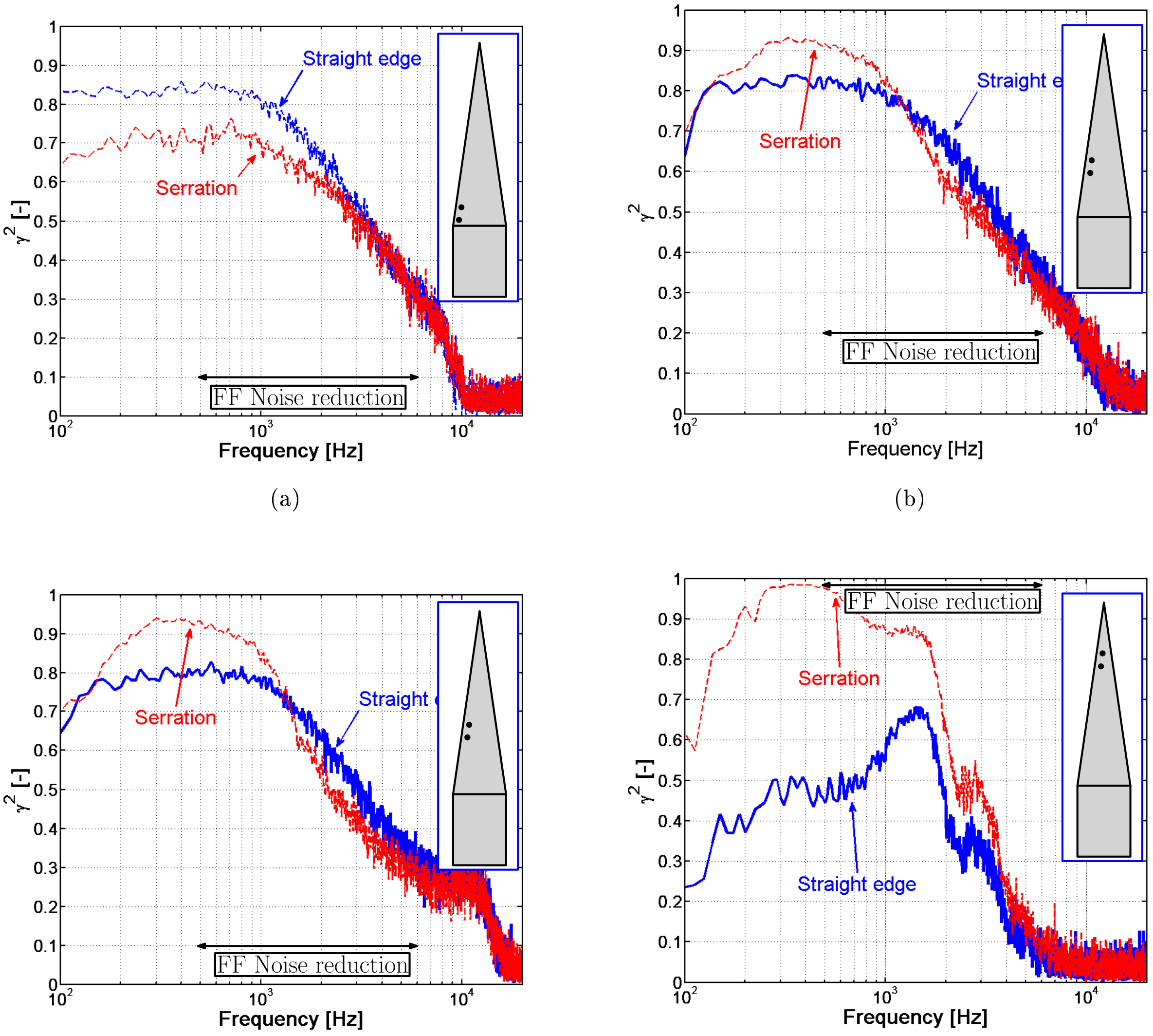

(a)

(b)

(c)

(d)

Figure 5.12: Variation of the coherence between pairs of sensors located along the edge of a single sawtooth.

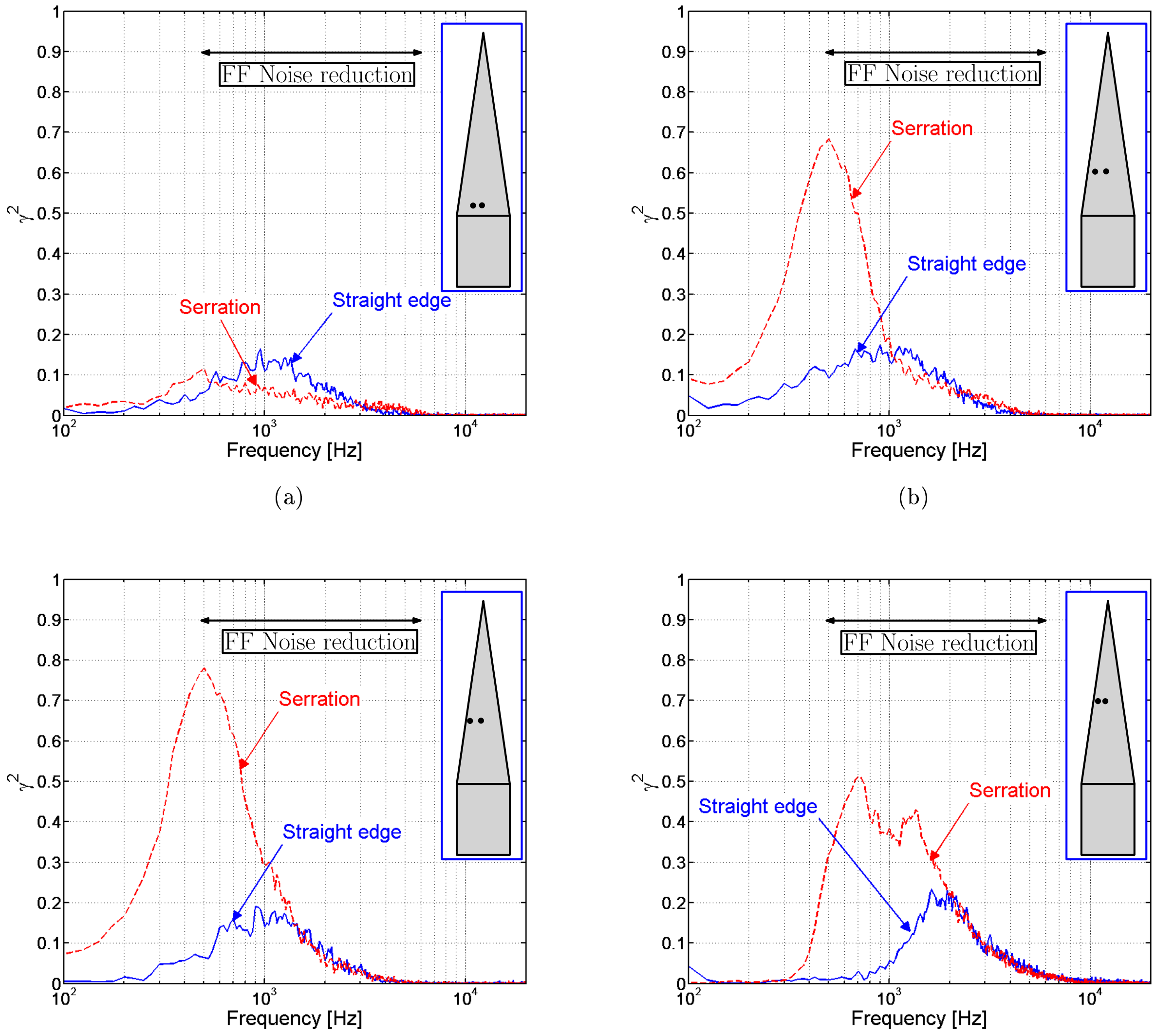

(a)

(b)

(c)

(d)

Figure 5.13: Variation of the spanwise coherence between pairs of sensors over a single sawtooth.

5.1.3 Trailing edge back-scattering

In this Section the results from the experimental campaign presented in the previous Sections, aimed at measuring simultaneously far field noise reductions and modifications to the surface pressure in the close vicinity of the sawtooth trailing edge, are discussed.

Noise reductions of up to 2.5 dB, from 0.5 to 5 kHz were measured on the wall-jet experiment presented in Section 5.1.2.2 at $U_0 = 20\,m/s$. Theory of sound radiation from a surface distribution of random dipole sources (see Equation 1.1) indicates that the far field noise reductions can be caused by either a reduction of the surface pressure spectrum ϕ_{qq} or a reduction of the spanwise correlation length l_y. The results of the wall jet experiments and of the data presented in Chapter 4 show that in the presence of a sawtooth trailing edge:

1. Significant noise reductions occur in the low frequency range $f\delta/U_0 < St_\delta$ while the noise is increased at the high frequencies $f\delta/U_0 > St_\delta$, where $St_\delta \sim 1$ (see Chapter 4).
2. The region in the boundary layer of peak of turbulence is 'pushed' away from the surface, and the boundary layer thickness increases by up to 12 % at the tip of the sawtooth (see Chapter 4).
3. The surface pressure spectrum is significantly increased over the sawtooth serration, even in the frequency range where noise reductions occur (see Section 5.1.2.4). In addition, it is further increased as the tip of the sawtooth is approached.
4. The phase speed of the pressure disturbance close to the serrated trailing edge is considerably reduced compared to a straight edge in the frequency range where noise reductions occur. This is most likely due to the strong interaction of the convected turbulence pressure with the back-scattered pressure field from the edge. The phase speed is further reduced close to the edges (see Section 5.1.2.5), which may be due to the effects of multiple scattering as the edges become closer as the tip is approached.
5. The streamwise coherence and the coherence along the edges of the sawtooth decreases by up to 15 % in the frequency range where noise reductions occur. However, it is increased at low frequencies, where the strong increase due to a coherent back-scattering by the edge is measured in the surface pressure spectrum (see Section 5.1.2.6).

The pressure difference $\Delta P(x)$ between the two sides of the trailing edge due to an incident boundary layer from one side, P^+_{bl} may be expressed in the form:

$$\begin{cases} \Delta P(x) = P^+(x) - P^-(x) \\ P^+(x) = P^+_{bl}(x) + P^+_{scat}(x) \\ P^-(x) = P^-_{scat}(x) \end{cases} , \tag{5.4}$$

where $P^+_{scat}(x)$ and $P^-_{scat}(x)$ are the scattered pressures on the side of the boundary layer and the other side respectively. At the trailing edge, due to the Kutta condition, $\Delta P(x_{TE}) = 0$.

The use of RMPs to measure the surface pressure distribution on one side of the trailing edge limits the measurements to $P^+_{bl}(x) + P^+_{scat}(x)$ only. The large increase in the difference of the surface pressure spectra measured over the sawtooth with respect to a straight trailing edge, (see Section 5.1.2.4) must therefore be due to the scattered pressure $P^+_{scat}(x)$ only. A corresponding increase in scattered pressure $P^-_{scat}(x)$ must therefore be present on the other side to ensure that the Kutta condition is satisfied. The existence of a much longer edge length with $\Delta P = 0$ ensures weak radiation to the far field compared to a straight edge.

Therefore, the increase in the unsteady surface pressure over the sawtooth is a strong further indication of back-scattering of pressure occurring near the edges. Figure 5.14 illustrates the reason for the increase observed in the surface pressure difference ΔSPL_{qq} as the tip of the sawtooth is approached and is most likely caused by the relative proximity of the two edges compared to a straight edge, which become progressively closer together as the tip is approached.

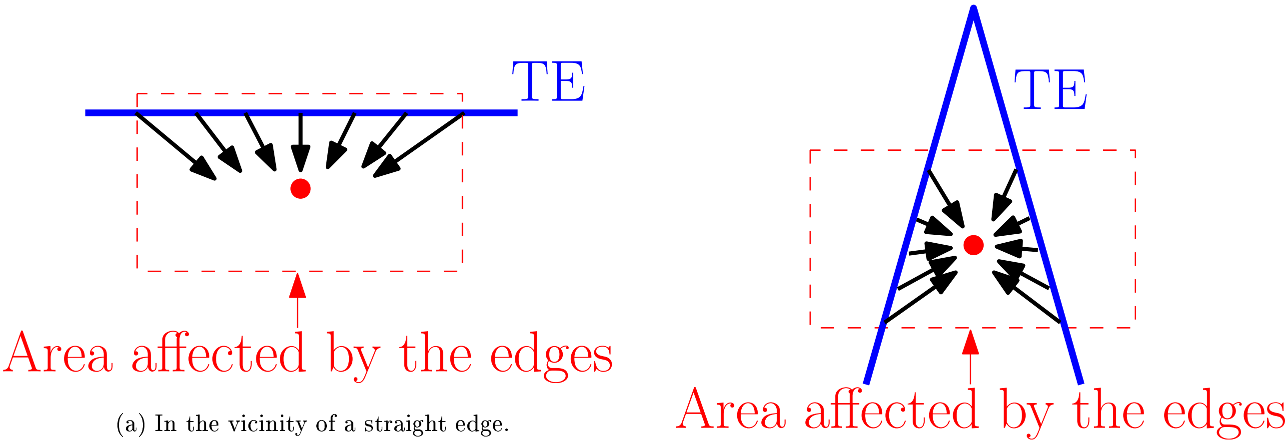

(a) In the vicinity of a straight edge.

(b) In the vicinity of a serrated edge.

Figure 5.14: Back-scattering from the edge.

In the case of a straight edge, Brooks *et al* [18] show that the scattered pressure on both sides of the airfoil at the trailing edge is 0.5 of the pressure due to the boundary layer in the absence of the edge. On the side of the flow, therefore, the pressure at the trailing edge is reduced by 50% by the presence of the edge. Moreover, they showed, along with others, that the back-scattered pressure decays away upstream from the trailing edge at a rate that increases with increasing frequency.

On the surface of a narrow-angle sawtooth, however, it is speculated that multiple back-scattering of waves between the two sides will occur, leading to an amplification of the pressure. This effect is speculated to become more pronounced as the tip is approached and the two sides come closer together, leading to stronger multi-scattering effects between the two sides. This effect is likely to be more pronounced at low frequencies, as observed in the data, where the decay rate of back-scattered waves is smaller.

Despite the large increase in the surface pressure on one side (compared to a straight edge), the Kutta condition at the trailing edge suggests that a similar variation in surface pressure should also be present on the other side. For the narrow-angle sawtooth, therefore, the pressure difference over much of the area of the sawteeth is small (or zero at the trailing edge), leading to weaker radiation compared to a straight edge.

The reduction of the phase speed, which increases in frequency bandwidth as the tip of the sawtooth is approached, is also a direct consequence of the back-scattered acoustic field, which will be more coherent and therefore stronger than the convected turbulence when the sensor is closer to the edge. This results in a considerable slowing of the phase speed of Fourier components of the turbulence in the frequency bandwidth where noise reductions occur. In addition, the drop in coherence in the frequency range where noise reductions occur is another indicator of the reduction of the phase speed, as presented in Section 5.1.2.6, and suggests that the correlation length along the edge is decreased compared to that of a straight edge.

This Section clearly shows that a significant reduction of the phase speed of the eddys occurs in the presence of an oblique edge, in the frequency band where noise is reduced. This behaviour is most likely due to a strong interaction between the boundary layer incident pressure and the acoustic pressure scattered by the edges. Therefore, as suggested by Howe [66], this indicates that the decrease of the speed at which the scattering of the energy would normally take place, due to the obliqueness of the edge, is a strong mechanism of noise reduction. The modifications of the boundary layer turbulent velocity profiles measured in Chapter 4 are likely to be of second order although they may still contribute to the noise reduction measured in the presence of a sawtooth.

These measurements therefore support Howe's conjecture relating the phase cancellation of the various wave number turbulence components along the oblique edge. The reason why Howe's prediction substantially over-predicts the noise reduction, however, is that he assumes perfectly frozen turbulence, leading to perfect interference between radiation from the serration root and from the tip. Experimental evidence has been presented in this thesis that indicates, for sufficiently long serrations, that the turbulence cannot be regarded as frozen (unlike a straight edge). These evidence are:

1. No oscillations in the radiation spectrum are ever measured, as predicted by theory.
2. The streamwise coherence is generally low, which is a consequence of the decay time of the eddys.
3. The length scale of the streamwise turbulence is about $2.5\,mm$, as seen in Figure 4.28, compared to the length of the serrations which is $30\,mm$, and therefore $\Lambda_{uu} \ll 2h$, i.e. the turbulent eddys are largely uncorrelated over the sawtooth trailing edge.

5.2 Mechanisms of noise increase: $f\delta/U_0 > St_\delta$

Despite reducing the noise in the low frequency range $f\delta/U_0 < St_\delta$, it was shown in Chapter 4 that airfoil serrated edges increase the noise by up to 5 dB at high frequencies. This was also reported in various experimental studies [17, 36, 42, 88, 92, 71] but is not predicted by Howe's analytical model [66]. In this thesis, experimental data is presented to show that the increase in the high frequency radiation levels is due to an extraneous source of noise caused by a cross-flow through the valleys of the sawtooth. Following the observations of Chapter 4, where it is shown that the high frequency noise increase increases with increasing airfoil angle of attack, this observation is consistent with the cross-flow being forced through the valleys of the sawtooth and that its intensity is dependent on the static pressure difference at the trailing edge. In order to verify the relation between the cross-flow and the noise increase at high frequencies, this section reports the results of an experiment aimed at visualizing the cross flow using smoke in the vicinity of the trailing edge. Hot wire measurements of the streamwise velocity in the boundary layer and very near wake velocity spectra on a sawtooth and a straight edge airfoil are also presented to show that the frequency St_δ, above which noise is increased divides the spectrum above which the turbulence velocity increases.

5.2.1 Sawtooth serration cross flow

This section describes the results of smoke visualization tests aimed at qualitatively analysing the flow over a straight and a serrated trailing edge. A smoke wand was used, which generates a point source of smoke, to understand the behaviour of the flow in the close vicinity of the serration. The mean flow velocity was $U_0 = 40m/s$ and the airfoil fitted with the serration $2h = 20mm$ and $\lambda = 5mm$, was at 5^o angle of attack. First, in order to check that the flow remains attached along the airfoil chord upstream of the trailing edge, the smoke wand is located upstream of the airfoil leading edge (see Figure 5.15a). This is to ensure that the smoke follows the boundary layer on both pressure and suction sides and merges at the trailing edge. This is verified in Figure 5.15a, confirming that the flow is attached on the pressure and suction sides. In order to study the flow in the close vicinity of the serration, the smoke wand was placed on the pressure side of the airfoil, in the boundary layer upstream of the trailing edge, so that no smoke is generated on the suction side of the airfoil (see Figure 5.15b). Note that the smoke wand was positioned further enough from the trailing edge so as not to disturb the flow past the trailing edge. Figure 5.15c shows the flow past a straight edge, where smoke exclusively originates from the pressure side and leaves the airfoil surface tangentially to follow the airfoil wake. By contrast, Figure 5.15d shows the flow leaving the serrated edge with the smoke wand on the pressure side. Part of the flow is forced through the valleys of the sawtooth, starting from the root of the serrations, where locally the wake begins to mix. This cross-flow phenomenon is believed to be the reason for the noise increase at high frequencies when using sawtooth serrated trailing edges.

The reason for this cross-flow is believed to be two fold. First, at the root of the serration the wake starts mixing. Secondly, at the trailing edge, the pressure difference responsible for the noise radiation is sucking air from the pressure side, partly creating this cross flow effect which then develops in the wake along the edges of the sawtooth.

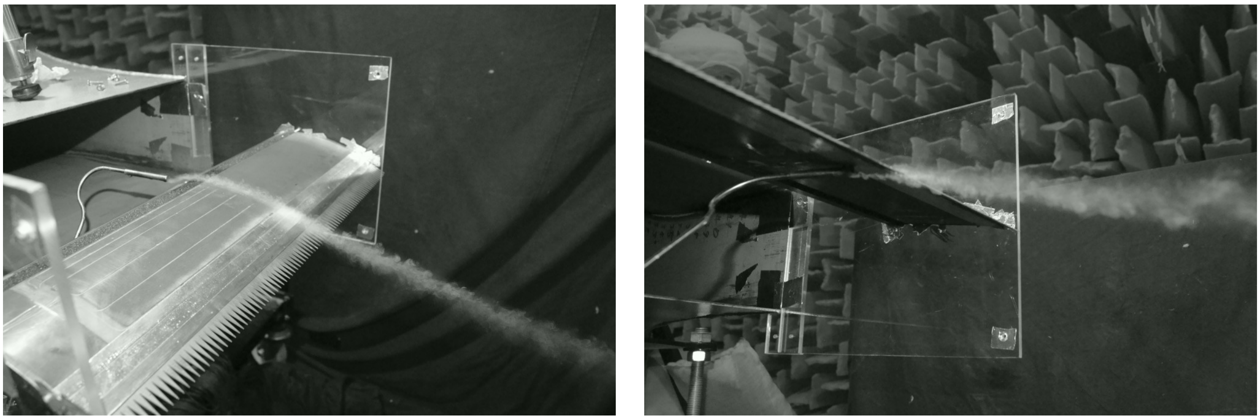

(a) Flow around the airfoil. (b) Smoke wand on the pressure side of the airfoil.

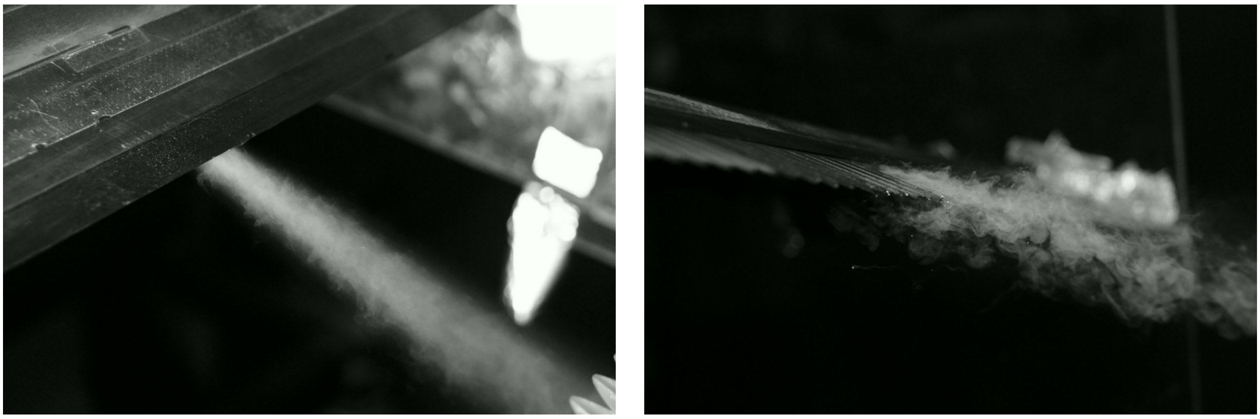

(c) Flow past a straight edge at 5^o AoA. (d) Flow past a sawtooth serrated edge at 5^o AoA.

Figure 5.15: Flow visualization smoke around a sawtooth serrated trailing edge.

5.2.2 Variation of the boundary layer and wake velocity spectra with mean flow velocity

As mentioned previously, the cross-flow phenomenon observed in Section 5.2.1 is believed to be the cause of the high frequency noise radiation increase due to sawtooth trailing edges. In order to confirm this hypothesis, this section verifies that the turbulence in the valleys of the serration is increased above the same frequency at which the noise is increased, whereas no such increase is observed in the boundary layer turbulence.

Measurements of the flow in the boundary layer and in the wake of the airfoil trailing edge serration were performed using a single hot wire probe, at $U_0 = 20m/s$ and also for a flow velocity blow-down, where hot wire data is acquired as the mean flow velocity is steadily decreased from $U_0 = 40m/s$ to zero. Data were recorded at 5^o angle of attack and for a serration with $2h = 20mm$ and $\lambda = 5mm$. Figure 5.17 shows $\Delta\Phi_{uu,w}$ in the wake and $\Delta\Phi_{uu,bl}$ in the boundary layer as defined in Equation 5.5.

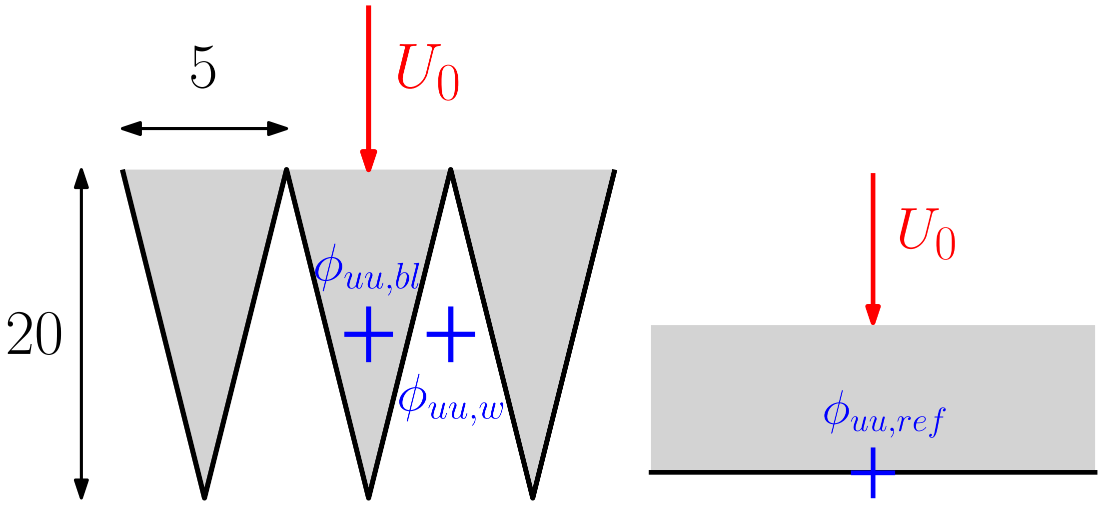

(a) Sawtooth trailing edge.

(b) Straight reference trailing edge.

Figure 5.16: Hot wire measurement locations shown by crosses.

$$\Delta\Phi_{uu,w} = 10\log_{10}\left(\frac{\phi_{uu,w}}{\phi_{uu,ref}}\right) \quad \text{and} \quad \Delta\Phi_{uu,bl} = 10\log_{10}\left(\frac{\phi_{uu,bl}}{\phi_{uu,ref}}\right), \tag{5.5}$$

where ϕ_{uu} denotes the streamwise velocity spectral density and $\phi_{uu,w}$ is measured in the wake in the valley of the sawtooth serrated trailing edge, $\phi_{uu,bl}$ is measured in the boundary layer over a single sawtooth and $\phi_{uu,ref}$ is measured in the boundary layer over a straight edge baseline airfoil. All measurements locations are marked in Figure 5.16 and were taken at the same chordwise distance of $0.15\,m$ and the same distance from the airfoil surface of about $\delta/2$.

Figure 5.17a shows that $\Delta\Phi_{uu,w}$ follows the same Strouhal number dependence as the noise radiation presented in Figure 5.17c, i.e., the turbulence is increased when $St_\delta > 1$ and the turbulence is decreased when $St_\delta < 1$. Figure 5.17b shows that $\Delta\Phi_{uu,bl}$ varies very little ($\pm 0.5\,$dB) between the straight edge case and the serrated edge case. Comparing Figures 5.17a and b indicates that the noise radiation increase due to the introduction of sawtooth serrations is strongly linked to the behaviour of the turbulence in the wake and not in the boundary layer.

In addition, Figure 5.18a also shows the velocity spectrum in the boundary layer over the straight edge, compared to that of the boundary layer over a single sawtooth and that of the very near wake in between two sawteeth, at $U_0 = 20 m/s$. The velocity spectrum has a very similar shape to that of the sawtooth boundary layer. The frequency above which the sound power level spectrum $PWL(f)$ is increased, as seen in Figure 5.18b, closely matches that in the turbulent velocity spectrum of Figure 5.18a.

Generally, the behaviour of the velocity spectrum, while moving along the airfoil chord, past the trailing edge and in the wake, has been investigated, but for brevity not shown here. As the hot wire was traversed along the airfoil suction side towards the trailing edge, the low frequencies of the velocity spectrum increase and the high frequencies decrease due to adverse pressure gradients. While passing into the wake, the velocity spectrum shape remains unchanged but is lower in value.

Therefore, as none of the behaviour pointed in Figures 5.17 and 5.18 has been observed over a straight edge, this confirms that the high frequency noise increase is due to increased turbulence activity in the valleys of the sawtooth.

Finally, Figures 5.17a and 5.18a also show that the turbulence in the valleys of the sawtooth is reduced by a maximum of about 3 dB for $f\delta/U_0 < 1$ over a large range of mean flow velocities, hence exhibiting roughly the same levels of reduction as the noise (see Figures 5.17c and 5.18b). However, as mentioned above, the turbulence reduction at low frequencies was observed to be due to the flow passing from the boundary layer to the wake, past a straight edge. Therefore, this turbulence reduction in Figures 5.17a and 5.18a is not believed to be a principal mechanism in the trailing edge noise reduction due to sawtooth serrations.

Observations similar to that of Figure 5.17 were made in the jet noise community using serrations and flow control by microjets, where energy is removed from large eddies by destroying their coherence, which is partly compensated by energy added to small scales [23].

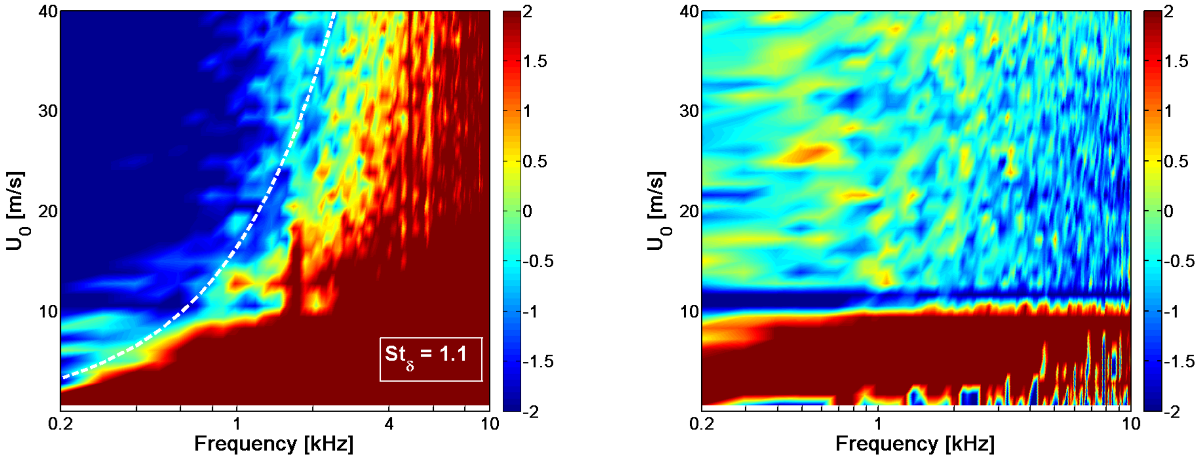

(a) Wake turbulence $\Delta\Phi_{uu,w}$ as defined in Equation 5.5

(b) Boundary layer turbulence $\Delta\Phi_{uu,bl}$ as defined in Equation 5.5.

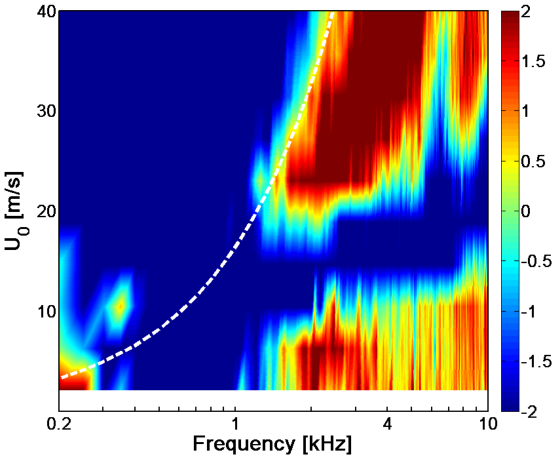

(c) ΔPWL as defined in Equation 4.2.

Figure 5.17: Evidence of cross-flow using the blow-down technique, airfoil at 5^o AoA and $U_0 = 20\,m/s$. The dashed curve shows the Strouhal dependency $St_\delta = f\delta/U_0 \sim 1$.

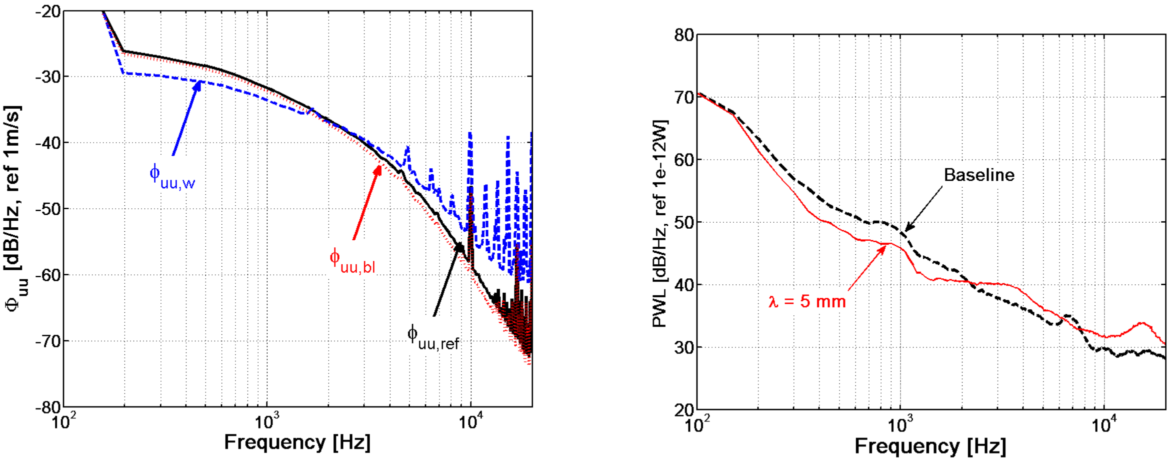

(a) Streamwise velocity spectrum measured at positions listed in Figure 5.16.

(b) Sound power spectrum PWL.

Figure 5.18: Evidence of cross-flow, airfoil at 5^o AoA and $U_0 = 20\,m/s$.

Finally, results of CFD predictions of the flow in between the sawtooth are briefly reviewed. Figure 5.19 shows the results from a 3D LES computation of the flow around the NACA65(12)-10 fitted with the sawtooth serration $\lambda/h = 0.3$ that was provided by the company Avio as part of the European project FLOCON [113]. To analyze the flow through the serrations, velocity vectors are extracted on a plane normal to the serration plate. Values of the normal velocity component are shown in the valleys of the sawtooth at the root, at the mid-height and at the tip of the serrations in Figure 5.19. Small recirculation bubbles are visible near the serration edges and it is shown that the low-pressure suction side recirculation bubbles entrain the flow from the pressure side. The presence of a strong velocity component normal to the trailing edge can clearly be seen at the three cross sections and therefore Figure 5.19 provides further evidence of the cross-flow discussed in this Section. It is also reported by Avio [113] that the stream wise vorticity develops near the serrated edge, and that it is twice as large as the normal component of the velocity.

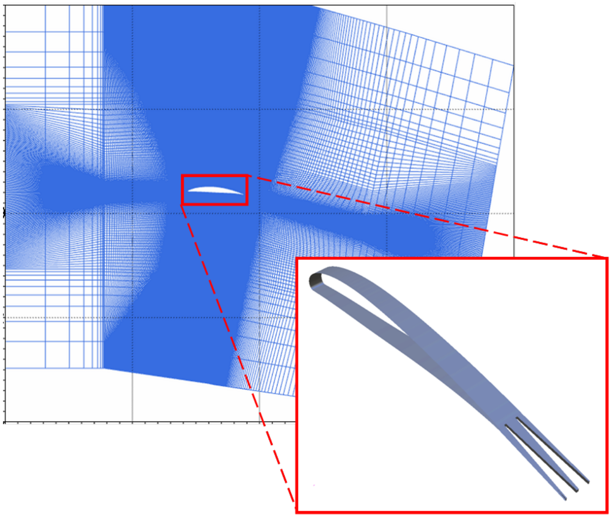

(a) Mesh and geometry of the serrated NACA65(12)-10 airfoil.

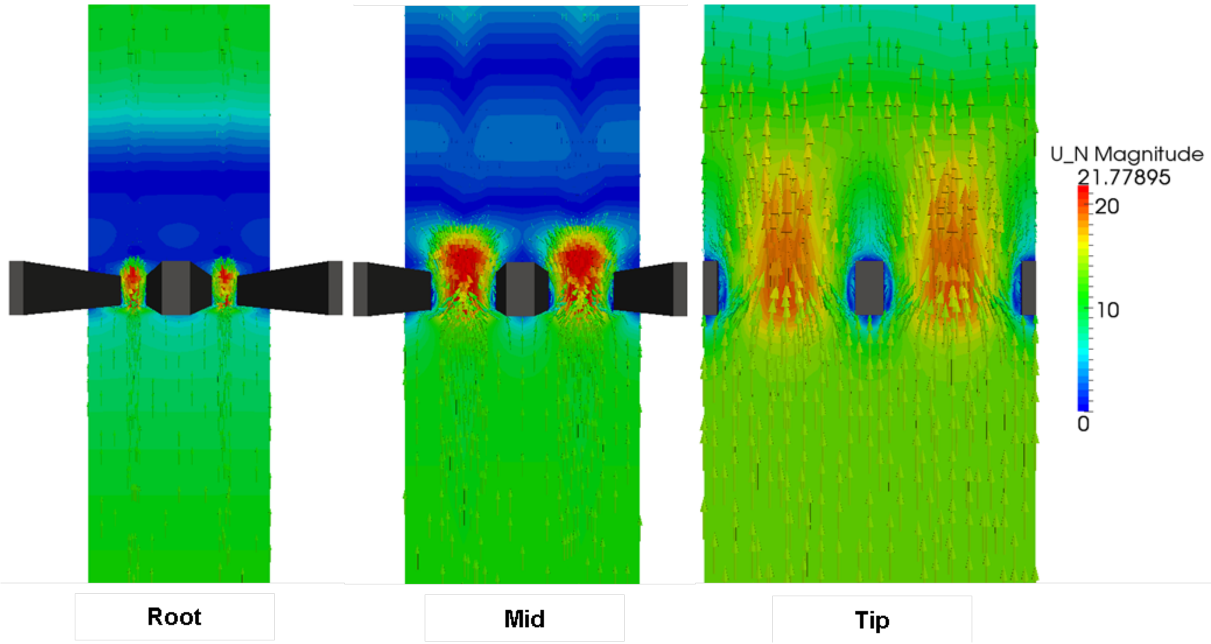

(b) Velocity component normal to the serration plate.

Figure 5.19: Evidence of cross-flow from 3D LES [113] (Avio SpA courtesy).

5.3 Summary

This Chapter focuses on the understanding of the mechanisms responsible for the change in the noise radiation obtained using trailing edge serrations and reported in Chapter 4 and by other researchers [17, 30, 27, 36, 42, 55, 56, 54, 59, 66, 71, 82, 88, 92].

In order to investigate the noise reduction that occurs when $f\delta/U_0 < St_\delta$ (see Chapter 4), an experimental study aimed at simultaneously measuring the far field noise reduction and the modifications of the near field in the vicinity of the trailing edge was conducted in a wall jet configuration. Broadband noise reductions of up to about 2.5 dB in the far field were measured up to 5 kHz, together with significant modifications of the surface pressure, turbulence convection velocities and correlation lengths in the boundary layer over a single sawtooth.

The dominant noise reduction mechanism appears to be a reduction of the phase speed at which the turbulence is convected near the edge, up to a half of the speed in the frequency range where noise reduction occurs. A reduction of up to 15 % in the coherence measured along the edge of the sawtooth also occurs in the frequency band where the noise is reduced to the far field.

This reduction of the scattering is in accordance with Howe's theory [65, 66], which was shown in Chapter 4 however, to over-predict the measured noise reductions by at least 15 dB. The main failure of Howe's model therefore appears to be the assumption of perfect destructive interference over the whole sawtooth between incident and scattered pressure fields whereas it was shown that the streamwise correlation length (about $2\,mm$ from Figure 4.28) is considerably shorter than the serration length $2h$ needed for noise reductions.

The large increase in the surface pressure over the whole of the sawtooth, i.e., by up to 15 dB near the tip is speculated to be due to a back-scattering of the pressure by the trailing edge. However, this large increase of the measured surface pressure cannot be related as such, to the far field radiation due to cancellation with the scattered pressure field underneath the wall-jet that could not be measured. The increase in the boundary layer thickness and the shift of the peak of turbulence away from the surface is believed to be of second order compared to the reduction in the scattering efficiency.

The increase in noise observed in Chapter 4, and by other researchers [17, 36, 42, 88, 92, 71], is a downside to the use of serrated edges as a means of trailing edge noise reduction in real applications such as for example slats, wind turbine blades or cooling fan blades. The mechanisms causing the noise increase when $f\delta/U_0 > St_\delta$ (see Chapter 4) were investigated using smoke visualization that showed evidence of a cross flow, forced through the valleys of the serrated trailing edge. Furthermore, measurements of the flow over a sawtooth and in the valley of a serrated edge has shown that the frequency above which noise is increased, i.e., $f\delta/U_0 > St_\delta$ was also identified in the velocity spectrum. The turbulence also appears to be increased at high frequencies when $f\delta/U_0 > St_\delta$. In addition, as the level of high frequency noise increases with increasing airfoil angle of attack (see Chapter 4), it is believed that the intensity of the cross flow is driven by the pressure difference at the trailing edge that is responsible for the radiation of trailing edge noise. The higher the pressure drop at the trailing edge, the greater is the intensity of the cross flow and the level of noise increase when $f\delta/U_0 > St_\delta$. The evidence of a cross-flow is supported by a 3D LES calculation provided by Avio [113] that shows a strong velocity component normal to the airfoil surface in the valleys of the sawtooth.

Chapter 6

Towards trailing edge noise reduction: Alternative trailing edge treatments

This Chapter presents alternative trailing edge geometries to the sawtooth serrations introduced in Chapter 4 for reducing airfoil trailing edge noise. Three treatments designed to introduce some flow permeability across the trailing edge, are first presented in Section 6.1 and are periodic along the airfoil span. These are the slits, sawtooth with holes and slitted sawtooth. A random trailing edge geometry aimed at reducing the scattering efficiency at the trailing edge is also presented.

As in Chapter 4, noise performance is presented for each treatment and compared to a baseline straight edge and the sawtooth serration $\lambda/h = 0.3$, which was shown to provide the maximum noise reduction, with minimal aerodynamic impact, in Chapter 4.

All trailing edge treatments are manufactured from stiff cardboard of $0.8\,mm$ thickness using a laser and inserted into the blunt slotted trailing edge of the NACA65(12)-10 airfoil, as for the sawtooth serrations (see Chapter 2).

It is worth noting that as these trailing edge inserts are fitted to the airfoil in the same way as the sawtooth serrations, and considering that measurements representative of the changes in lift are only available upstream of the airfoil trailing edge, no significant changes to the steady pressure are expected from the measured data (see static distribution along the sawtooth serrated airfoil in Chapter 4). For this reason, and for brevity, the static pressure distribution, which was measured for the slits and the slitted sawtooth, are not presented.

6.1 Alternative periodic trailing edges

In this Section, the noise reduction measured for three geometries of periodic trailing edges are presented: slits, sawteeth with holes, slitted sawteeth.

6.1.1 Slits

Herr [59, 58] introduced fibre-type trailing edge extensions, i.e. brushes, as a means of reducing trailing edge noise. Broadband noise reductions were measured on a NACA0012 airfoil and on a flat plate in the DLR's Aeroacoustic Wind Tunnel in Braunschweig. The vortex shedding noise from the blunt baseline trailing edge was suppressed using brushes and broadband reductions of up to about 9 dB were measured. In the present context of broadband noise reduction, it is noteworthy that Herr's baseline airfoil investigation was dominated by a strong tonal component (due to vortex shedding) and that the TE brushes therefore appeared to provide more spectacular results as real broadband noise control.

It was found that the noise reduction was mostly dependent on the geometry of brushes (length, diameter, spacing) rather than on the flow conditions (Reynolds number, mean flow speed, chord length and angle of attack). Herr identified that the spacing between adjacent brushes was a crucial parameter for providing maximum noise reductions, i.e., typically smaller than $0.1\,mm$. Increasing this spacing to $0.1\,mm$ provided a decrease of the broadband noise reduction capability of about 5 dB, which she attributed to the necessity of the spacing to be of the order of the viscous sublayer thickness. The length of the trailing edge treatment was also found to be a critical parameter of the order of the boundary layer thickness (δ to 2δ). Finally, a negligible high frequency excess noise was reported in this study.

Finez [41] subsequently used brushes on a NACA65(12)-10 airfoil and reported noise reductions of about 3 dB from 600 Hz to 2 kHz, while a recirculating bubble noise near the leading edge dominated the noise emission at higher frequencies. Finez also showed through wake space time correlation measurements that the correlation length related to the near wake velocity was decreased by 25 % due to the trailing edge brushes. The large discrepancies on the measured potential noise reduction between Herr's and Finez's studies suggests a strong sensitivity of the treatment implementation. However, it was shown in both studies that brushes larger than the boundary layer thickness, and with a separation distance as small as possible were required to obtain noise reductions.

Finally, Ortmann [91] reported numerically that while trailing edge brushes have an adverse effect on the airfoil aerodynamic, slits comparable to brushes but with a rectangular section had little adverse to slightly beneficial effects on the aerodynamic performance.

This thesis now focuses on the capability of slit trailing edges to reduce broadband noise.

6.1.1.1 Geometry

Figure 6.1 shows the geometry of the slit trailing edges completely defined by an amplitude $2h$, a slit width d_2, and the distance between adjacent slits d_1. A total of seven slit trailing edge inserts, whose values of $2h$, d_1 and d_2 are listed in Table 6.1, were tested in turn for noise reduction. As discussed in Chapter 2, the effect of the material, i.e., stiff cardboard and metal, proved no significant difference to the noise radiation and therefore the results from both metal and cardboard inserts are compared altogether below. Note that due to manufacturing limitations (width of the laser beam), a slit width of the order of 0.1 mm or smaller, presented as a critical condition for maximum noise reduction by Herr [59], was not achieved in this study and therefore smaller noise reductions are expected.

Figure 6.2 shows a picture of the cardboard slit trailing edges listed in Table 6.1, together with a close-up of the trailing edge 1 of Table 6.1.

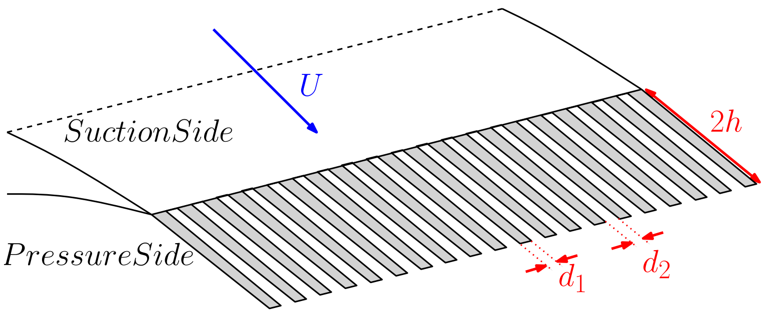

	$2h$	d_1	d_2	Material
1	30	0.5	0.5	Card
2	30	1	0.5	Card
3	30	1	1	Card
4	30	2	0.5	Card
5	20	1	1	Card
6	20	2	0.5	Metal
7	20	5	0.5	Metal

Figure 6.1: Geometry of the slitted trailing edge inserts, all units in mm.

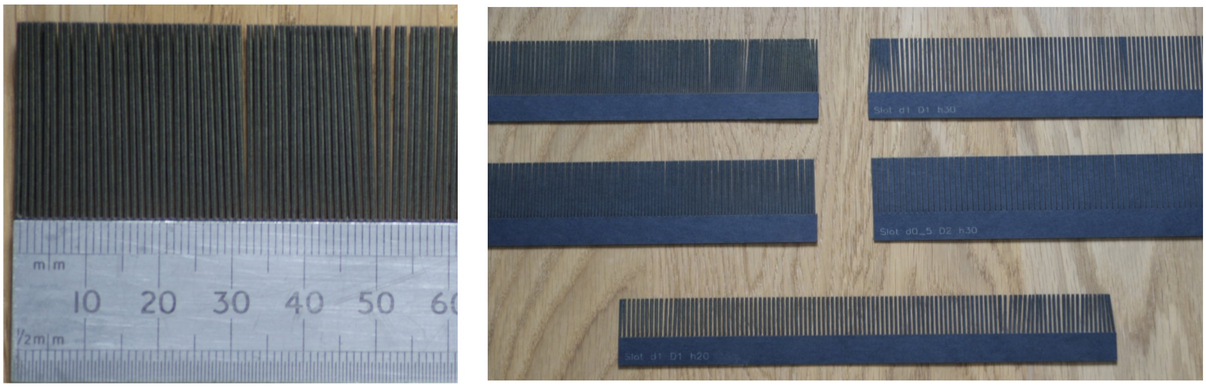

(a) Slit 1 in Table 6.1.

(b) Slits cut in thick cardboard.

Figure 6.2: Picture of the slitted trailing edge inserts.

6.1.1.2 Sound power reduction

The influence of the three parameters $2h$, d_1 and d_2 on the sound power level PWL, defined by Equation 2.2, radiated between 50^o and 110^o to the trailing edge, are presented in Figure 6.3 using the set of slit inserts listed in Table 6.1. Sound power spectral densities are presented at 15^o angle of attack and for the three velocities U_0 =20, 40 and 60 m/s.

Figure 6.3a shows that for $d_1 = d_2 = 1\,mm$, broadband sound power reduction of up to 2 dB occurs for the longer slits of amplitude $2h = 30\,mm$ only. The shorter slits do not provide a significant noise reduction. Table 2.3 indicates that the boundary layer thickness measured at the very trailing edge of the baseline airfoil is $9.4\,mm$. Therefore, it appears that noise reduction only occurs when the amplitude of the slits is at least a certain fraction of the boundary layer thickness, i.e., when $2h > \delta$. This is in accordance with Herr's [59] and Finez's [41] statements that a minimum length of brushes of the order of the boundary layer thickness is required to obtain noise reduction. The longer slits appear to be effective at weakening the sound emission at the lowest speed only, while an increase of broadband noise can be clearly observed at U_0= 40 and $60\,m/s$.

Figure 6.3b shows that for fixed values of $d_1 = 1\,mm$ and $2h = 30\,mm$, the smaller the slit width d_2, the greater is the broadband noise reduction below $6\,kHz$ for all mean flow velocities. This observation is consistent with Herr's results [59] where it was shown that an almost-zero slit width was required to maximize the noise reduction. At higher frequencies, as observed for the sawtooth serrations in Chapter 4, the noise is increased by up to about 5 dB for the smallest slit width ($d_2 = 0.5\,mm$) and by up to 2 dB for $d_2 = 1\,mm$.

Figure 6.3c and d illustrate the influence of the separation distance between slits d_1 for fixed values of the slit width $d_2 = 0.5\,mm$ and slit length of $2h = 20\,mm$ and $2h = 30\,mm$, respectively. It is shown that, generally, the smaller the distance between adjacent slits, the greater is the maximum broadband sound power reduction, for both slit lengths and all mean flow speeds. Conversely, the high frequency noise excess appears to increase for smaller separation distances d_1. This trend is believed to be consistent with the behaviour of the noise increase related to sawtooth serrations (see Chapter 4), where the noise gradually increases as the sawtooth becomes narrower.

Generally, as mentioned above the noise reduction levels obtained using slit treatments are significantly lower than the ones obtained by Herr [59]. Considering the almost-zero slit width required to obtain good noise reductions, as reported by Herr, the lack of effectiveness of the slits tested in this study is believed to be due to the width of the slits being too large. However, the conditions described by Herr to reduce the noise, i.e., satisfy a minimum slit length $2h$ and minimize the slit width d_2 are well observed. In addition, the current study suggests that the smaller the separation distance between adjacent slits d_1, the greater is the noise reduction. This trend could be due to either an increased number of slits at the trailing edge, or the condition $d_1 = d_2$ to be satisfied to maximize the trailing edge noise reduction.

6.1.2 Serrations with holes

Sawtooth serrations with holes are now used to tackle the high frequency noise increase observed with sawtooth serrations, which is shown to be due to a cross flow in the valleys of the sawtooth in Chapter 5. This cross flow is believed to be forced through the valleys of the sawtooth by the pressure difference between the pressure and suction side of the airfoil close to the wetted edges. Therefore, one way to reduce its intensity was to drill holes through the sawtooth in order to

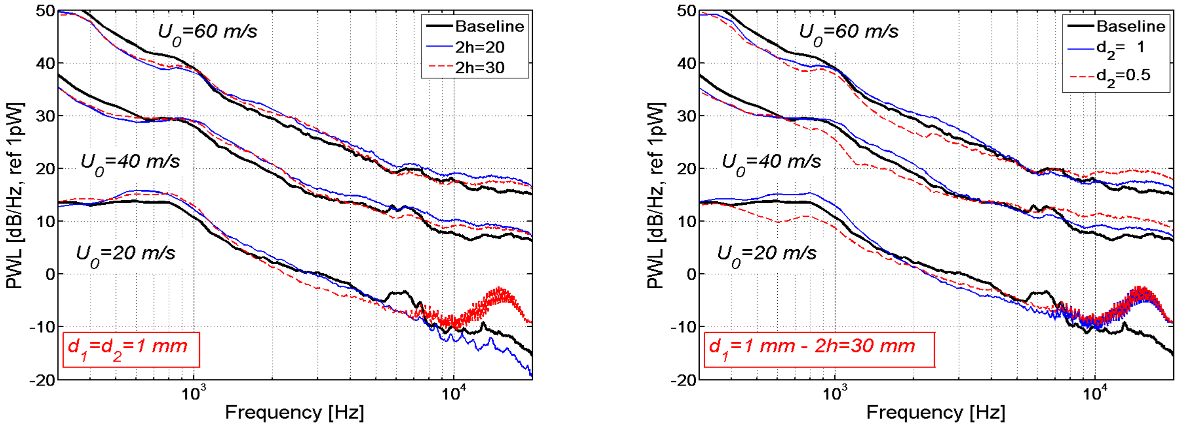

(a) Varying the amplitude of the slits $2h$

(b) Varying the width of the slits d_2.

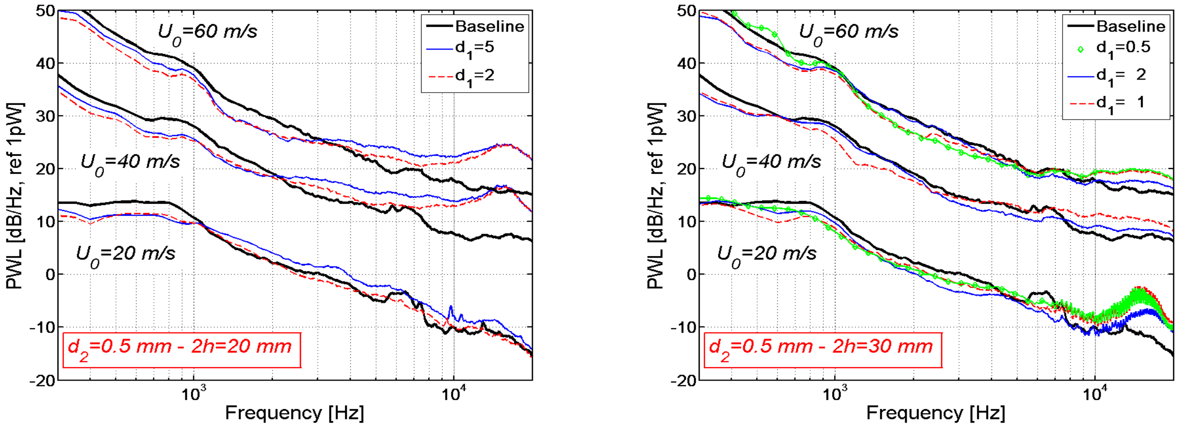

(c) Varying the distance between adjacent slits d_1, with $2h = 20\,mm$.

(d) Varying the distance between adjacent slits d_1, with $2h = 30\,mm$.

Figure 6.3: Sound power level PWL of the slit trailing edges, as listed in Table 6.1, at 15^o AoA.

alleviate the total pressure difference across the airfoil trailing edge and hence reduce the flow speed through the valleys.

6.1.2.1 Geometry

The sawtooth serration $\lambda/h = 0.6$ was chosen as the main periodic pattern and Figure 6.4 shows a sketch of this sawtooth where the holes are distributed in lines perpendicular to the airfoil chord line. As in Chapter 4, the parameters defining the sawtooth serration are the periodicity of the sawtooth λ and the amplitude of the sawtooth $2h$. These parameters are taken to be constant and equal to $\lambda = 9\,mm$ and $2h = 30\,mm$ ($\lambda/h = 0.6$). Note that this sawtooth does not provide the best noise reduction of all sawteeth tested in Chapter 4 but allows superposition of other patterns. Due to manufacturing limitations, the smaller sawtooth $\lambda/h = 0.3$, chosen as the best treatment in Chapter 4 did not allow for a detailed parametric study of the effect of increasing the open area, to be carried out.

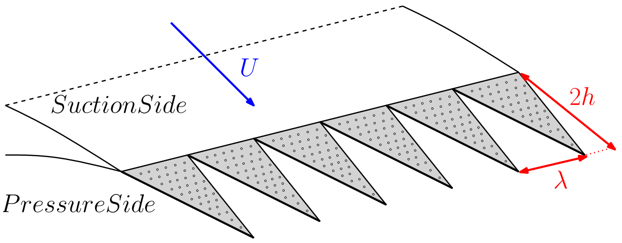

	$2h$	λ	OA	Material
1	30	9	8 %	Card
2	30	9	11 %	Card
3	30	9	20 %	Card
4	30	9	22 %	Card
5	30	9	24 %	Card
6	30	9	26 %	Card

Figure 6.4: Geometry of the sawtooth trailing edges with holes, all units in mm.

Six trailing edges, listed in Table 6.4, were manufactured with various open area OA over the airfoil trailing edge, where OA is defined as:

$$OA = \frac{n\pi r^2}{\lambda h}, \tag{6.1}$$

where n is the number of holes over one sawtooth and r is the hole radius. Figure 6.5a is a close-up view of the trailing edge $OA = 24\,\%$ and Figure 6.5b shows the set of sawtooth serrations with holes cut in stiff cardboard. The diameter of the holes is fixed and equal to $1\,mm$. The open area OA is therefore increased by increasing the number of holes n in one sawtooth.

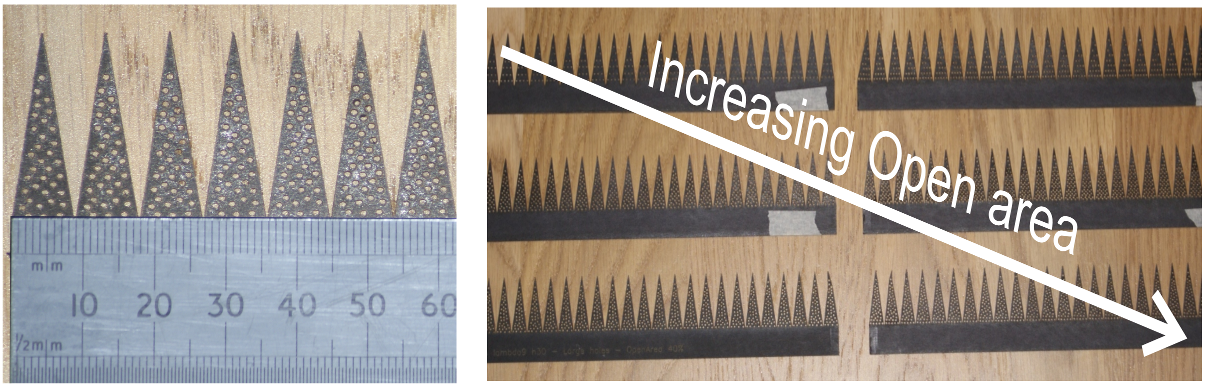

(a) Trailing edge $OA = 24\,\%$.

(b) Sawtooth trailing edges with holes cut in thick cardboard.

Figure 6.5: Picture of the sawtooth trailing edge inserts with holes.

6.1.2.2 Sound power reduction

Figure 6.6 shows a comparison of the sound power level PWL, defined by Equation 2.2, radiated between 50^o and 110^o to the trailing edge, with varying open area OA, from 8 % to 26 %. The airfoil is at 5^o angle of attack and the measurements were performed at the two flow velocities of $U_0 = 40\,m/s$ and $U_0 = 80\,m/s$. Data are presented over the low and mid frequency bandwidth 300 Hz to 7 kHz (Figure 6.6a and c), and over the high frequency bandwidth 7 kHz to 20 kHz (Figure 6.6b and d). The power spectrum of the baseline straight edge and of the sawtooth $\lambda/h = 0.6$ are also included for comparison.

Figures 6.6a and c show that at lower frequencies, below 400 Hz, noise reductions limited to 1 dB are obtained due to the dominance of jet noise. For frequencies higher than 1 kHz at $U_0 = 40\,m/s$ and 2 kHz at $U_0 = 80\,m/s$, the sawtooth serrations with smaller open areas OA appear to provide noise reduction of up to 2 dB at $U_0 = 40\,m/s$ and up to 5 dB at $U_0 = 80\,m/s$, while the sound power level is increased by up to 3 dB for the sawtooth serrations with the larger open areas. At frequencies higher than 2 kHz and 4 kHz at $U_0 = 40\,m/s$ and $U_0 = 80\,m/s$ respectively the noise is gradually increased and the sawtooth serrations with the lowest open area gives a maximum increase of up to about 10 dB (see Figures 6.6b and d).

Generally, Figure 6.6 shows that the presence of holes in the sawtooth $\lambda/h = 0.6$ provides a consistent reduction of up to 4 dB of the noise radiation compared to the solid sawtooth trailing edge up to about 7 kHz but conversely further increases the noise at high frequencies by at least 3 dB.

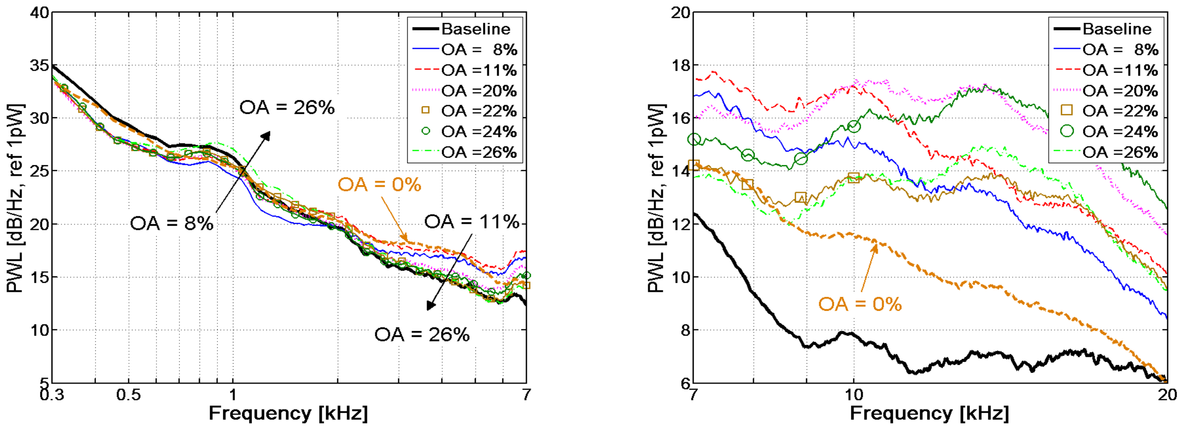

(a) $U_0 = 40\,m/s$ from $300\,Hz$ to $7\,kHz$. (b) $U_0 = 40\,m/s$ from $7\,kHz$ to $20\,kHz$.

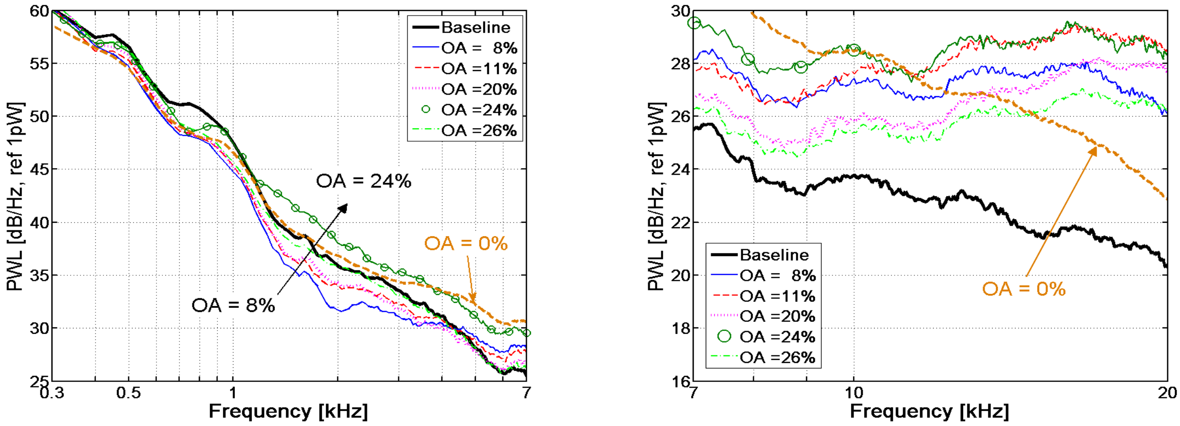

(c) $U_0 = 80\,m/s$ from $300\,Hz$ to $7\,kHz$. (d) $U_0 = 80\,m/s$ from $7\,kHz$ to $20\,kHz$.

Figure 6.6: Sound power level PWL of the sawtooth trailing edges with holes, as listed in Table 6.4, at 5^o AoA.

Figure 6.7 shows the change in sound power level ΔPWL, defined in Equation 4.2, as the airfoil angle of attack is increased from 0^o to 15^o. The results are presented at $U_0 = 40\,m/s$ and for the sawtooth serrations with open area $OA = 8\,\%$ and $11\,\%$. The noise reduction obtained in the mid-frequency range using these treatments appears to be weakly dependent on airfoil angle of attack. The high frequency noise excess increases between 1 and 2 dB with increasing airfoil angle of attack, depending on the open area through the sawtooth. Direct comparisons with Figure 4.14a show that although the absolute levels of noise excess are increased compared to the sawtooth $\lambda/h = 0.6$, the presence of holes decreases the dependency of the high frequency excess noise on angle of attack. This is believed to be due to the presence of micro-jets that are forced through the holes and may weaken this dependency.

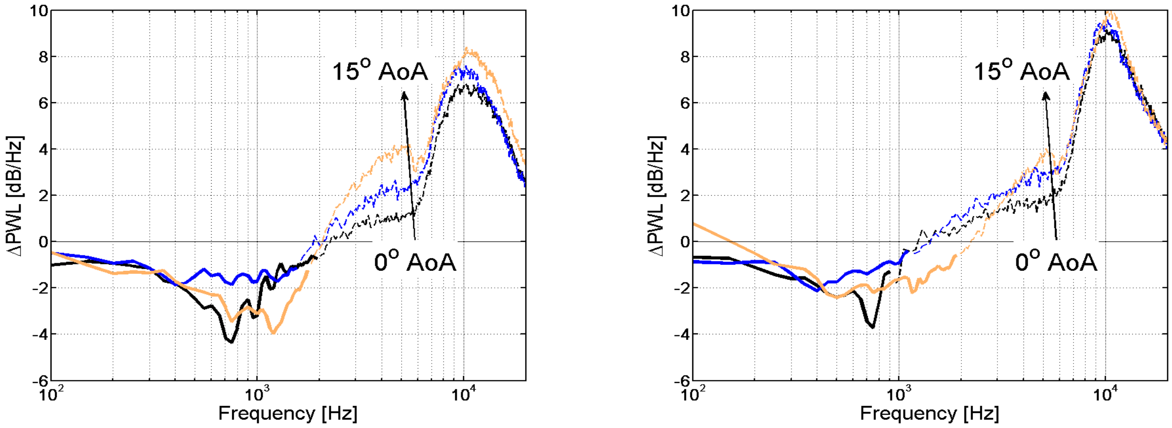

(a) $OA = 8\,\%$.

(b) $OA = 11\,\%$.

Figure 6.7: Change in ΔPWL, presented as a function of frequency and angle of attack α_g at $U_0 = 40\,m/s$.

Generally, it appears that the effectiveness of the holes at the trailing edge to reduce broadband noise requires a fine tuning of the open area. Considering that the noise reduction obtained in the mid-frequency range is weaker than the noise reduction obtained using the sawtooth $\lambda/h = 0.3$ (see Figure 4.3) and that the high frequency noise is further increased, this type of treatment was not further investigated in this study.

However, future work should include a detailed study of the influence on the sound radiation of the holes through a straight edge, through a sharper serration and also the effect of the hole's diameter and the importance of their distribution over the sawtooth.

For the aim of reducing the high frequency noise excess, the presence of holes through the sawtooth serration is therefore not an effective strategy. Section 6.1.3 below presents another treatment where slits are cut through the sawtooth serration in the direction of the flow.

6.1.3 Slitted sawtooth

The sawtooth serrations with slits is a geometry that superposes the solid sawtooth serration presented in Chapter 4 as the main periodic pattern with smaller slits cut into the trailing edge in the direction of the flow (as presented above in Section 6.1.1). This trailing edge geometry was also designed to tackle the high frequency noise increase observed with sawtooth serrations. Therefore, the intensity of the cross flow in the valleys of the sawtooth is reduced by cutting slits through the sawtooth serration, in the direction of the flow. As for the sawtooth with holes, the slitted sawtooth is believed to distribute the pressure difference across the trailing edge by introducing flow permeability. In addition, another potential effect is to further reduce the noise radiation due to coherent sources along the trailing edge by increasing the length of the wetted edges and reducing the phase speed and the correlation length of the turbulence that is convected past the trailing edge (see Chapter 5).

6.1.3.1 Geometry

As for the sawtooth with holes, the sawtooth serration $\lambda/h = 0.6$ was chosen as the main periodic pattern. Figure 6.8 shows a sketch of the slitted sawtooth where slits are cut through the sawtooth in the direction of the flow. Note that the sawtooth serration $\lambda/h = 0.6$ does not provide the best noise reduction of all sawtooth tested in Chapter 4 but allows superposition of other patterns. Due to manufacturing limitations, the smaller sawtooth $\lambda/h = 0.3$, chosen as the best treatment in Chapter 4 did not allow for a detailed parametric study of the effect of varying the slit parameters, to be carried out.

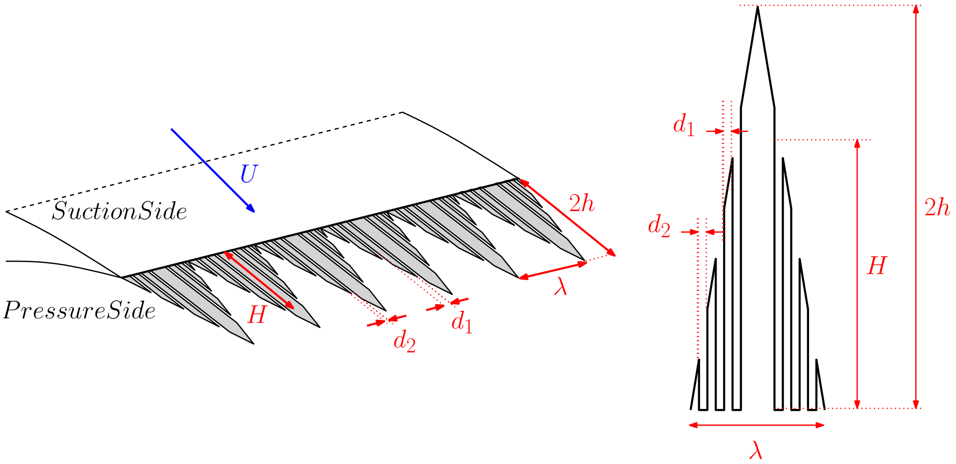

	$2h$	λ	d_1	d_2	H	Material
1	30	9	0.5	0.5	5	Card
2	30	9	0.5	0.5	10	Card
3	30	9	0.5	0.5	15	Card
4	30	9	0.5	0.5	18.5	Card
5	30	9	0.5	0.5	25	Card
6	30	9	1.5	0.5	10	Card

Figure 6.8: Geometry of the slitted sawtooth trailing edges - all units in mm.

As in Chapter 4, the parameters defining the sawtooth serration are the periodicity of the sawtooth λ and the amplitude of the sawtooth $2h$. These parameters are taken to be constant and equal to $\lambda = 9\,mm$ and $2h = 30\,mm$. The width of the slits is defined by d_2 and the depth of the slits by H. The distance between adjacent slits is given by d_1.

Six slitted sawtooth trailing edges, listed in Table 6.8, were manufactured with various values of H and d_1. Following the results given in Section 6.1.1 on the slit trailing edges, the width of the slits is kept constant and as small as possible, i.e., equal to $d_2 = 0.5\,mm$. Note that the depth H

is defined for the slits close to the height of the triangle. As the slits move away from the height of the triangle, their depth is truncated to the base of the trailing edge.

Figure 6.9a is a close up view of the slitted sawtooth 5 of Table 6.8, where $d_1 = d_2 = 0.5\,mm$ and $H = 25\,mm$. Figure 6.9b shows the set of slitted sawtooth serrations manufactured from stiff cardboard.

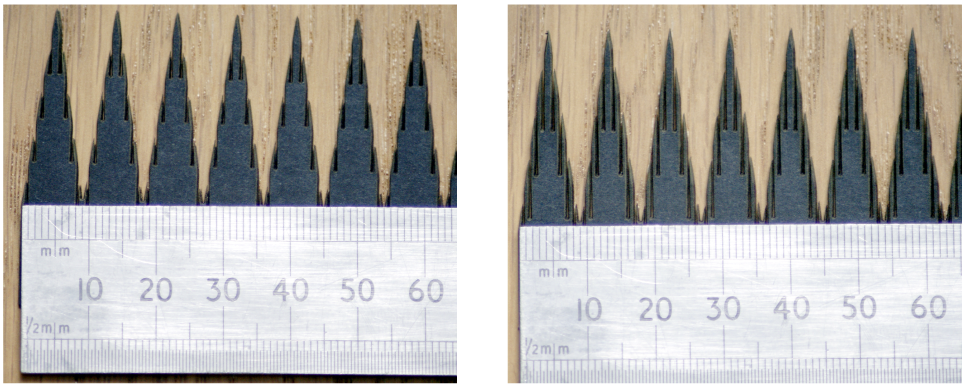

(a) $H = 5\,mm$ (b) $H = 10\,mm$

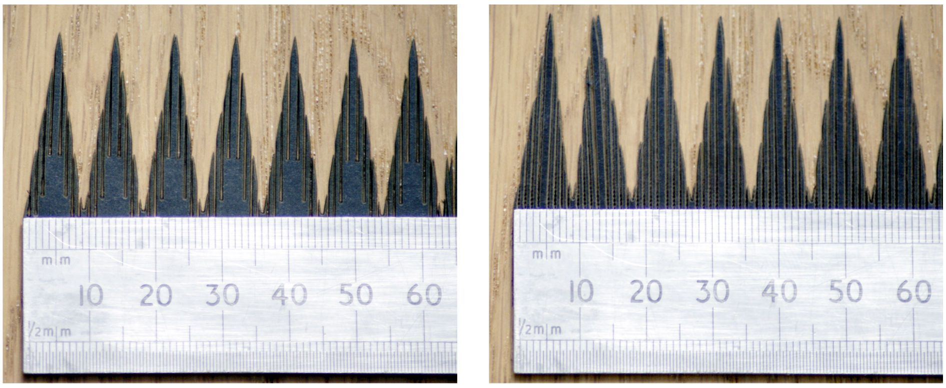

(c) $H = 15\,mm$ (d) $H = 25\,mm$

Figure 6.9: Picture of the slitted sawtooth trailing edge inserts, where $d_1 = d_2 = 0.5\,mm$ as listed in Table 6.8.

6.1.3.2 Sound power reduction

Figure 6.10 shows a comparison of the sound power level PWL, defined by Equation 2.2, radiated between 50^o and 110^o to the trailing edge, with varying slit depths, from $H = 5$ to $25\,mm$. The airfoil is at 5^o angle of attack and the measurements were performed at the two flow velocities of $U_0 = 40\,m/s$ and $U_0 = 80\,m/s$. Data are presented over the low and mid frequency bandwidth 300 Hz to 7 kHz (Figure 6.10a and c), and over the high frequency bandwidth 7 kHz to 20 kHz (Figure 6.10b and d). The power spectrum of the baseline straight edge and of the sawtooth $\lambda/h = 0.6$ are also included for comparison.

Figures 6.10a and c show that at lower frequencies, below 400 Hz, noise reductions limited to 1 dB are obtained due to the dominance of jet noise. For frequencies higher than 500 Hz at $U_0 = 40\,m/s$ and 1 kHz at $U_0 = 80\,m/s$, the slitted sawtooth provide broadband noise reduction up to 5 dB at $U_0 = 40\,m/s$ and $U_0 = 80\,m/s$. It is striking that the noise reduction gradually improves as the depth of the slits H is increased from 5 to 25 mm. The addition of the slits to the sawtooth serration $\lambda/h = 0.6$ also provides up to 6 dB of noise reduction compared to the sound power level radiated by the sawtooth with no slits. At higher frequencies, Figures 6.10b and d illustrate the same phenomenon where for the deeper slits, i.e., H =18.5 and 25 mm, the trailing edge noise is reduced up to 10 kHz at $U_0 = 40\,m/s$ and up to 15 kHz at $U_0 = 80\,m/s$. For frequencies above 15 kHz, the noise increase is limited to a maximum of 0.5 to 1 dB. At high frequencies, the presence of the slits on the sawtooth therefore almost completely removes the disadvantageous noise increase reported in all sawtooth serration geometries in Chapter 4 and in the work of other researchers [36, 42, 82, 88, 92].

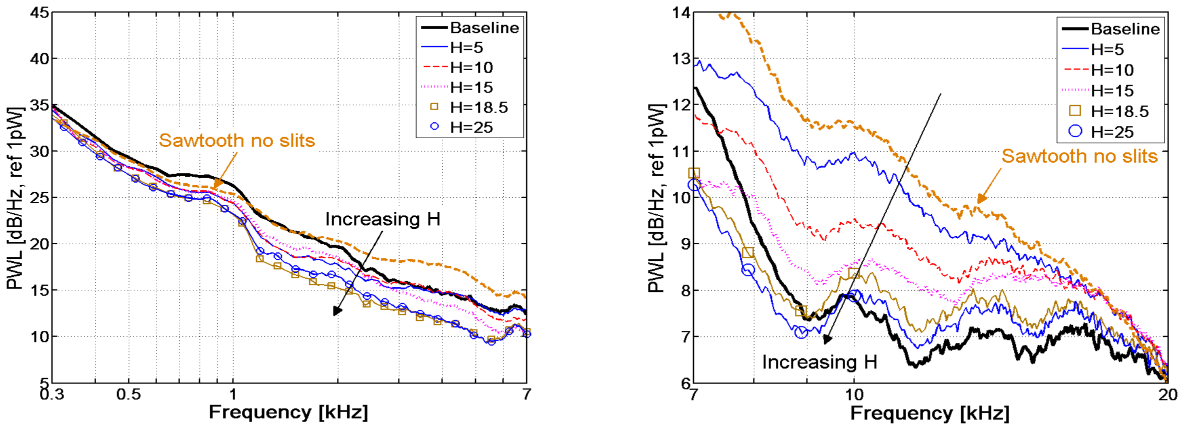

(a) $U_0 = 40\,m/s$ from 300 Hz to 7 kHz. (b) $U_0 = 40\,m/s$ from 7 kHz to 20 kHz.

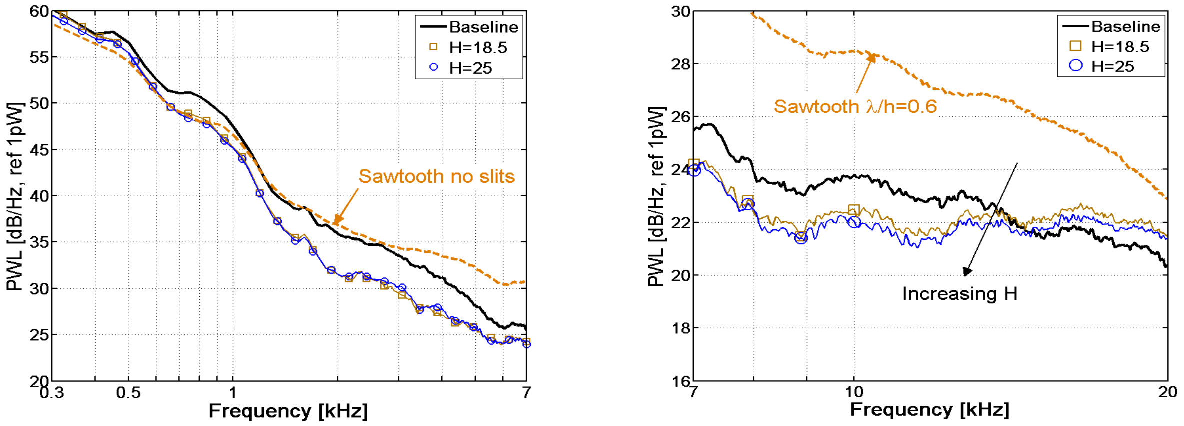

(c) $U_0 = 80\,m/s$ from 300 Hz to 7 kHz. (d) $U_0 = 80\,m/s$ from 7 kHz to 20 kHz.

Figure 6.10: Sound power level PWL of slitted serrated trailing edges 1 to 5 with $d_1 = d_2 = 0.5\,mm$ (as in Figure 6.8), at 5^o AoA.

Figure 6.11 shows the change in sound power level ΔPWL, defined in Equation 4.2, as the airfoil angle of attack is increased from 0^o to 15^o. The results are presented for the slitted sawtooth serrations 1 and 5 in Table 6.8, where $H = 5$ and $25\,mm$, respectively and at $U_0 = 40\,m/s$ (also at $U_0 = 80\,m/s$ for the trailing edge 5). The noise reduction obtained in the mid-frequency range using the slitted sawtooth treatments appears to slightly increase, in the region of the peak of noise reduction, as the airfoil angle of attack is increased. As for the sawtooth serrations, it can be seen in Figure 6.11a, that for the shallowest slits ($H = 5\,mm$), the high frequency noise excess is gradually increased by up to 3 dB as the angle of attack increases. However, the high frequency noise increase becomes less than 1 dB, at both U_0 =40 and $80\,m/s$, and independent of angle of attack when the depth of the slit is maximized to $H = 25\,mm$.

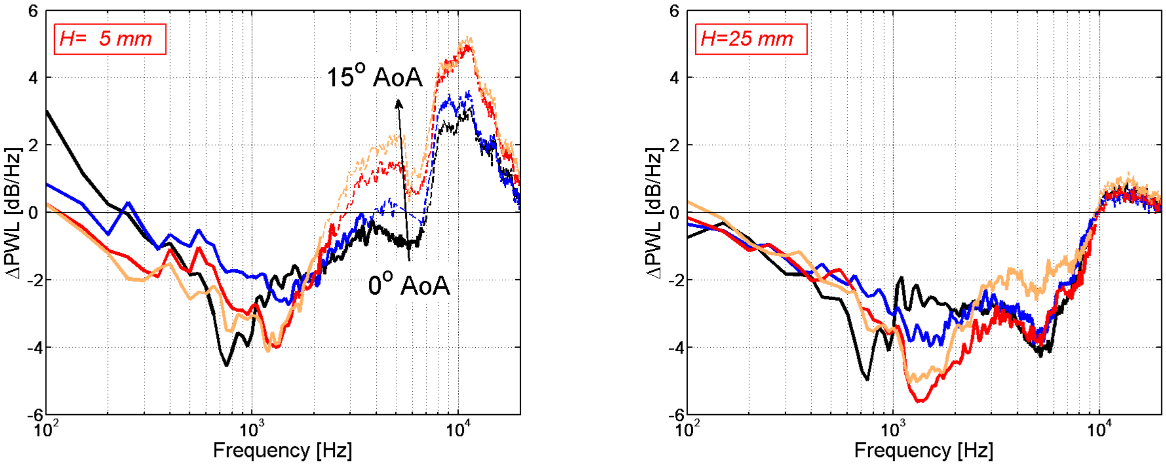

(a) $H = 5\,mm$ at $U_0 = 40\,m/s$. (b) $H = 25\,mm$ at $U_0 = 40\,m/s$.

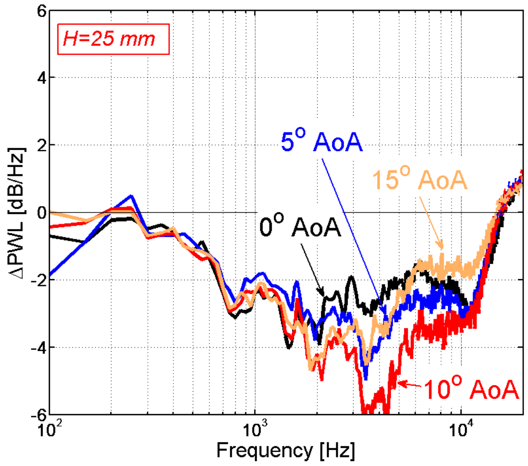

(c) $H = 25\,mm$ at $U_0 = 80\,m/s$.

Figure 6.11: Change in ΔPWL, presented as a function of frequency and angle of attack α_g.

Figure 6.12 shows a comparison of the sound power level PWL due to the baseline airfoil and the two slitted sawtooth 2 and 6 listed in Table 6.8, where the separation distance between two adjacent slits is changed from $d_1 = 0.5$ to $1.5\,mm$ ($d_2 = 0.5\,mm$ and $H = 10\,mm$ remain constant) at $U_0 = 40\,m/s$ and at 5^o and 15^o angle of attack. The smaller separation distance of $d_1 = 0.5\,mm$ appears to provide an additional 1 dB over the whole frequency range and for both airfoil angles of attack. This observation is consistent with that observed in Section 6.1.1 and suggests that this is due to either the number of slits per sawtooth or the condition $d_1 = d_2$ being satisfied.

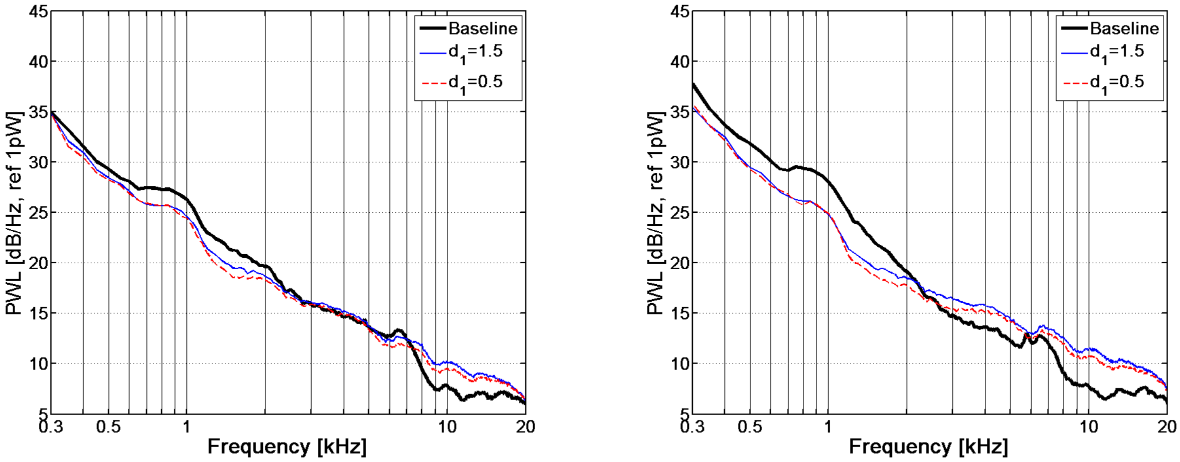

(a) 5^o AoA.

(b) 15^o AoA.

Figure 6.12: Sound power level PWL of slitted serrated trailing edges 2 to 6 with $d_2 = 0.5\,mm$ and $H = 10\,mm$ (as in Figure 6.8), at $U_0 = 40\,m/s$.

Figure 6.13 shows the variation of the overall sound power level reduction $\Delta OAPWL$, defined in Equation 4.1, with increasing depth of the slits, H. In order to give an accurate representation of the noise performance across the audible frequency range, the integration is performed over the three frequency bands [0.1 - 1], [1 - 7] and [7 - 20] kHz. The depth of the slits H marked as zero represents the sound power reduction obtained using the solid sawtooth serration $\lambda/h = 0.6$.

In the lower frequency band, between 100 Hz and 1 kHz, the noise reduction, limited to about 1 dB, is not affected by the presence of the slits, at all flow velocities. For higher frequencies, the general trend shown in Figure 6.13 is that the averaged sound power reduction is improved by increasing the depth of the slits H. The positive effect of cutting slits into the sawtooth is striking in the mid-frequency range, between 1 and 7 kHz, where maximum noise reductions of 3 to 4 dB are obtained at all mean flow velocities, and the slits provide an additional noise reduction of up to 2 dB on the solid sawtooth serration. However, it is in the higher frequency range between 7 and 20 kHz that the slitted serration are the most effective by reducing the overall sound power radiation by up 2 dB relative to the baseline airfoil and up to about 4 dB compared to the solid sawtooth trailing edge at $U_0 = 80\,m/s$.

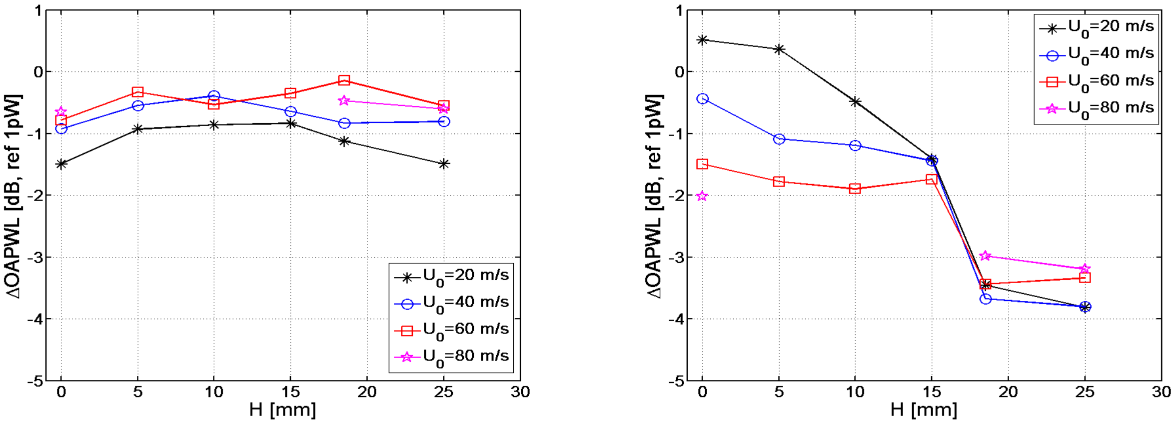

(a) Averaged from 100 Hz to 1 kHz.

(b) Averaged from 1 kHz to 7 kHz.

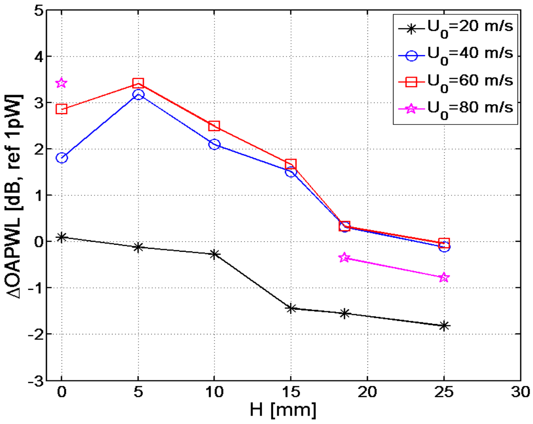

(c) Averaged from 7 kHz to 20 kHz.

Figure 6.13: Overall Averaged Sound Power Level difference $\Delta OAPWL$ of slitted serrated trailing edges 1 to 5 listed in Table 6.8 as a function of the depth of the slits H, at 5^o AoA.

Generally, the slitted sawtooth tested in this study appear to provide an effective solution to the high frequency noise increase observed in the radiation of airfoil trailing edge noise from sawtooth trailing edges (see Chapter 4 and other studies [17, 36, 88, 92, 42]). The depth of the slits H has been shown to be a critical parameter in order to maximize the broadband sound power reduction in the mid-frequency range, and to minimize the noise excess at high frequencies. The separation distance between adjacent slits d_1 was also proven to be an important parameter, though less crucial than H.

This trailing edge design has been patented through Rolls Royce (patent no GB1121753.6).

6.2 Non periodical trailing edge pattern

The non periodical trailing edge geometry was designed to reduce the scattering effect of the turbulence by the edge discontinuity, by introducing a random pattern. It is believed that the non uniformity of the trailing edge across the span should largely contribute to maximizing the edge length and reducing the phase speed and correlation lengths at the airfoil trailing edge (see Chapter 5).

6.2.1 Geometry

Figure 6.14 shows the geometry of the profile applied to the airfoil trailing edge, as defined in Equation 6.2

$$\left\{ \begin{array}{c} x_n = n\delta x \\ y_n = y_0 + g(0, \sigma_0) \end{array} \right. , \tag{6.2}$$

where $g(0, \sigma_0)$ is a random variable that follows a normal distribution with zero mean and standard deviation σ_0 and y_0 is a constant chosen so that the surface area of the treated airfoil is identical to that of the baseline airfoil. The random pattern applied to the airfoil trailing edge is therefore shown in Figure 6.14. Table 6.14 shows the set of four trailing edge inserts manufactured using the laser cut process described in Chapter 2. Two standard deviations σ_0 and $\sigma_0/2$, which define the average peak to peak distance, or the maximum amplitude of the trailing edge geometry were chosen to be of the order of the sawtooth amplitude, i.e., about 30 and 15 mm respectively. The sampling of the signal along the span was chosen as $\delta x = 1.5$ and 3 mm, i.e., identical to the periodicity of the sharper sawtooth serrations tested in Chapter 4. This type of trailing edge geometry is referred to hereon as a 'random' trailing edge.

Figure 6.15a is a close up view of the trailing edge 3 in Table 6.14, where $\sigma = \sigma_0/2$ and $\delta x = 1.5\,mm$. Figure 6.15b shows the set of random trailing edges cut in stiff cardboard and fitted to the NACA65(12)-10 airfoil in-situ.

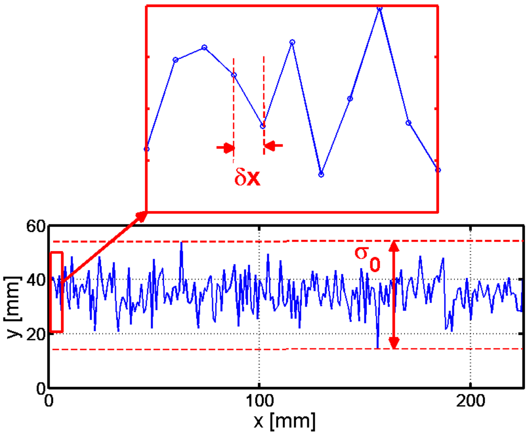

	$2h$	σ	δx	Material
1	30	σ_0	1.5	Card
2	30	σ_0	3	Card
3	30	$\sigma_0/2$	1.5	Card
4	30	$\sigma_0/2$	3	Card

Figure 6.14: Definition of parameters σ_0 and δx and geometry of the 'random' trailing edges - all units in mm.

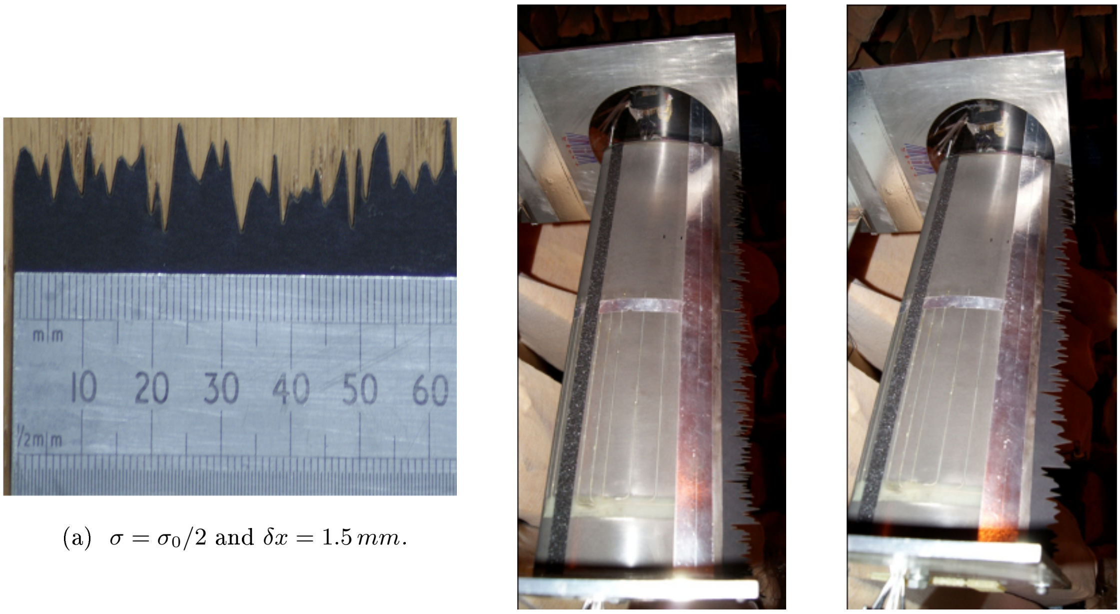

(a) $\sigma = \sigma_0/2$ and $\delta x = 1.5\,mm$.

(b) $\sigma = \sigma_0$ and $\delta x = 1.5\,mm$.

(c) $\sigma = \sigma_0$ and $\delta x = 3\,mm$.

Figure 6.15: Picture of the random trailing edge inserts.

6.2.2 Sound power reduction

Figure 6.16 shows a comparison of the sound power level PWL, defined by Equation 2.2, radiated between 50^o and 110^o to the trailing edge, with varying σ and δx. The airfoil is at 5^o angle of attack and the measurements were performed at the two flow velocities of $U_0 = 40\,m/s$ and $U_0 = 80\,m/s$. Data are presented over the low and mid frequency bandwidth 300 Hz to 7 kHz

(Figure 6.16a and c), and over the high frequency bandwidth 7 kHz to 20 kHz (Figure 6.16b and d). The power spectrum of the baseline straight edge is also included for comparison.

It is clear that the critical parameter for this trailing edge geometry is the amplitude of the random design σ rather than the sampling along the span. Figures 6.16a and c show that at lower frequencies, below 1 kHz, jet noise dominates. For frequencies higher than 1 kHz at $U_0 = 40\,m/s$ and 1.5 kHz at $U_0 = 80\,m/s$, the random trailing edges with largest amplitude (σ_0) provide a broadband noise reduction of up to 3 dB limited to the frequency range [1 - 3] kHz and [1.5 - 5] kHz, respectively. In that frequency range, the influence of the sampling of the signal along the span is not significant. For frequencies above and up to 20 kHz, the noise radiation becomes comparable to that of a straight edge for the trailing edge with parameters σ_0 and $\delta x = 3\,mm$, while it increases by up to 1 dB when $\delta x = 1.5\,mm$ (and $\sigma = \sigma_0$). The two trailing edges with smaller amplitude $\sigma_0/2$ appear to provide a noise reduction of up to 3 dB over a broader frequency range from 1 to 12 kHz and 2 to 20 kHz at $U_0 = 40$ and $80\,m/s$, respectively. Similarly, the influence of the parameter δx is limited to small variations of about 0.5 dB only.

It is noteworthy that no significant trailing edge noise increase is observed at high frequencies and that the sound power level is even reduced by up to 3 dB at 10 kHz and 1 dB at 20 kHz.

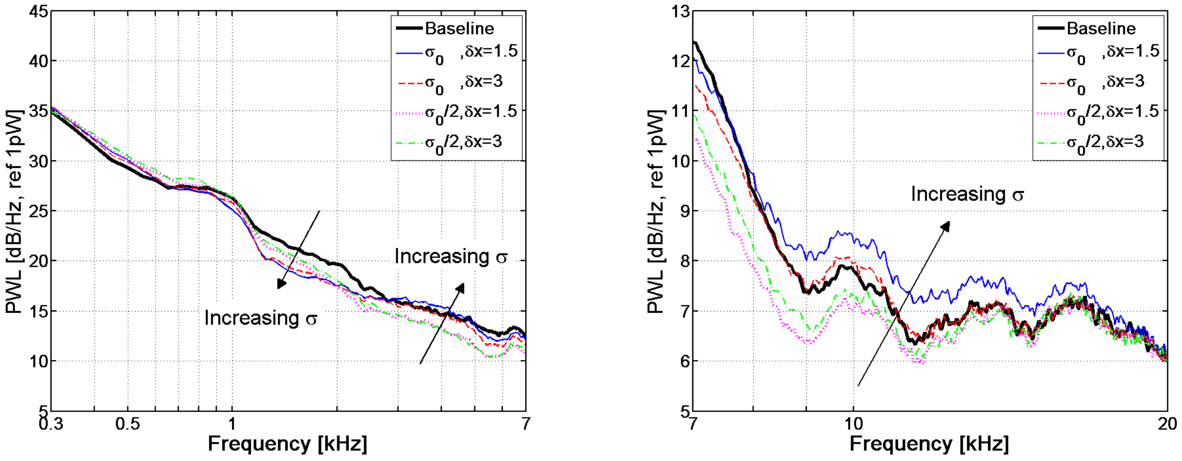

(a) $U_0 = 40\,m/s$ from $300\,Hz$ to $7\,kHz$.

(b) $U_0 = 40\,m/s$ from $7\,kHz$ to $20\,kHz$.

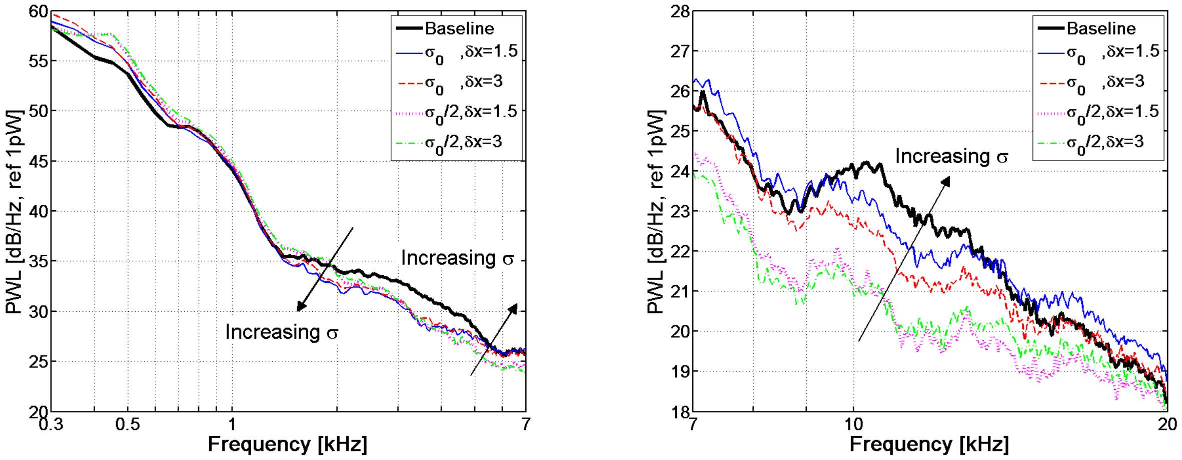

(c) $U_0 = 80\,m/s$ from $300\,Hz$ to $7\,kHz$.

(d) $U_0 = 80\,m/s$ from $7\,kHz$ to $20\,kHz$.

Figure 6.16: Sound power level PWL of the random trailing edges, at 5^o AoA.

Figure 6.17 shows the change in sound power level ΔPWL, defined in Equation 4.2, as the airfoil angle of attack is increased from 0^o to 15^o. The results are presented at $U_0 = 40\,m/s$ for the random trailing edges 2 and 4 in Table 6.14, where $\sigma = \sigma_0$ and $\sigma_0/2$, respectively ($\delta x = 3\,mm$ is fixed). The striking feature in this figure is that the noise reduction spectra at all angles of attack collapse within 0.5 dB over most of the frequency range suggesting that the change in noise is independent of airfoil angle of attack. For the trailing edge 2, Figure 6.17a shows that the noise is increased by about 1.5 dB from 2 to 4 kHz at 15^o angle of attack, which is believed to be a possible flow effect (local flow separation or boundary layer instability) occurring only at the higher angle of attack and for this specific trailing edge geometry.

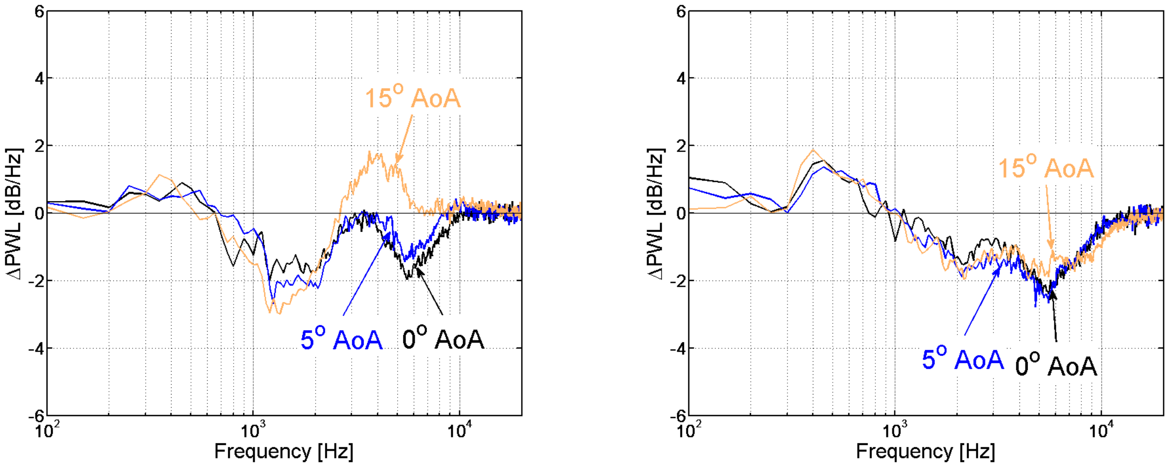

(a) $\sigma = \sigma_0$.

(b) $\sigma = \sigma_0/2$.

Figure 6.17: Change in ΔPWL of random trailing edges 2 and 4 as listed in Table 6.14 with $\delta x = 3\,mm$, presented as a function of frequency and angle of attack α_g, at $U_0 = 40\,m/s$.

Generally, the random trailing edges provide a reasonable broadband noise reduction of up to 3 dB with no excess noise at high frequencies.

6.3 Comparison with sawtooth serrations

The novel trailing edge treatments described in this Chapter are now compared in detail and to the sawtooth serration giving the maximum noise reduction in Chapter 4, i.e., with dimensions of $\lambda = 3\,mm$ and $2h = 20\,mm$ ($\lambda/h = 0.3$). Note that the sawtooth with holes are not included in the comparisons due to the poor noise reduction described in Section 6.1.2.

Figure 6.18 shows a comparison of the sound power level PWL, defined by Equation 2.2, radiated between 50^o and 110^o to the trailing edge of the sawtooth serration $\lambda/h = 0.3$, the slit trailing edge 1 in Table 6.1 ($d_1 = d_2 = 0.5\,mm$, $2h = 30\,mm$), the slitted sawtooth 5 in Table 6.8 ($d_1 = d_2 = 0.5\,mm$, $H = 25\,mm$) and the random trailing edge 4 in Table 6.14 ($\sigma = \sigma_0/2$, $\delta x = 3\,mm$). The airfoil is at 5^o and 15^o angles of attack. Data are presented over the low and mid frequency bandwidth 300 Hz to 7 kHz (Figure 6.18a and c), and over the high frequency bandwidth 7 kHz to 20 kHz (Figure 6.18b and d). The power spectrum of the baseline straight edge is also included for comparison. The measurements are presented at $U_0 = 40\,m/s$ in Figure 6.18 and at $U_0 = 80\,m/s$ in Figure 6.19. Note that the noise reduction from the slit trailing edges was not measured at $U_0 = 80\,m/s$.

Figure 6.18a shows that the slitted sawtooth geometry provides a greater broadband noise reduction than any other geometry, from 500 Hz to 7 kHz. It appears that up to 2 kHz, the noise reduction obtained from the sawtooth serration $\lambda/h = 0.3$ closely follows the slitted sawtooth. For frequencies above 2 kHz, the benefits from the sawtooth serration appear to gradually deteriorate up to about 8 kHz where the noise is increased at higher frequencies. The slits are most effective from 2 to 7 kHz giving up to 4 dB broadband reduction. It appears that the slitted sawtooth benefits the best of both the sawtooth serration and the slits and provides the maximum noise reduction of about 5 dB from 500 Hz to 7 kHz. For the higher frequencies seen in Figure 6.18b, the random trailing edge affords the best noise reduction of about 0.5 dB, while the slitted serration increases the noise by no more than 0.5 dB. Figure 6.18c and d show that the comparisons described at 5^o angle of attack are also valid at 15^o, though the high frequency noise is increased by a maximum of 1 dB in the presence of slitted serrations.

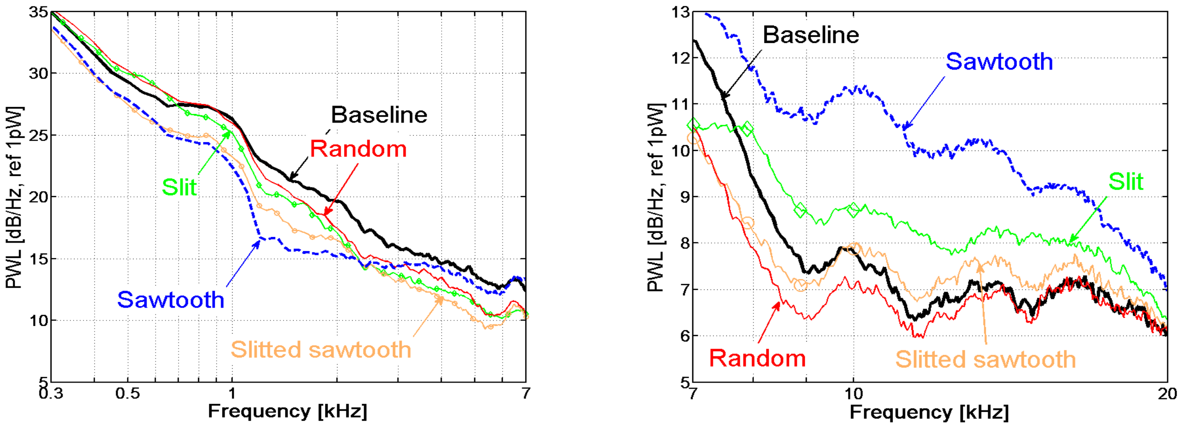

(a) At 5^o AoA from 300 Hz to 7 kHz.

(b) At 5^o AoA from 7 kHz to 20 kHz.

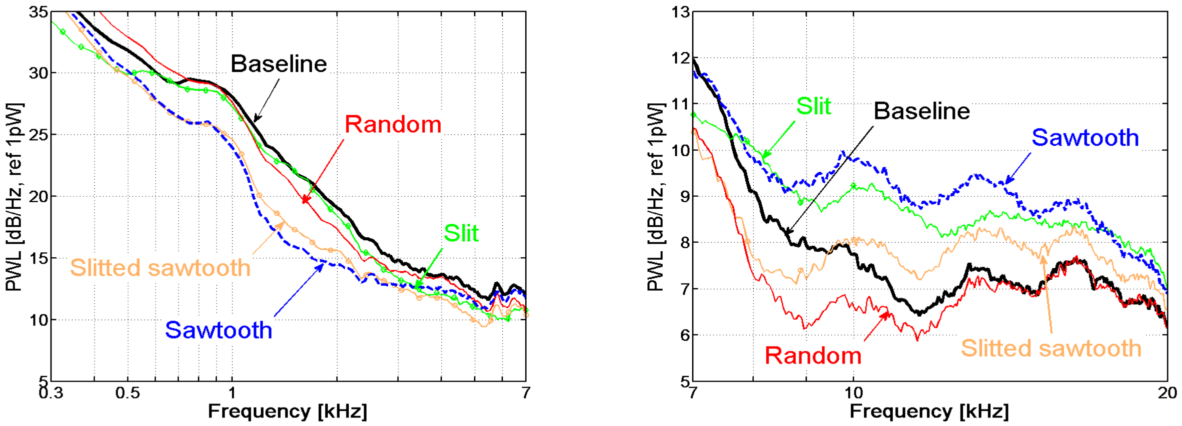

(c) At 15^o AoA from 300 Hz to 7 kHz.

(d) At 15^o AoA from 7 kHz to 20 kHz.

Figure 6.18: Sound power level PWL as a function of frequency at $U_0 = 40\,m/s$.

Figures 6.19 show that the slitted sawtooth geometry performs best at $U_0 = 80\,m/s$ compared to the sawtooth serration and the random trailing edge. A broadband noise reduction is measured from 500 Hz to 15 kHz and is maximum and equal to about 5 dB between 2 to 7 kHz. The effectiveness of the slitted serration at $U_0 = 80\,m/s$ and high angle of attack is of great importance as it is proven in this Chapter and in Chapter 4 that other trailing edge treatments can be adversely affected by changes of the flow conditions.

Although providing a weaker noise reduction, the effectiveness of the random trailing edge to reduce broadband noise appears to be little affected by the changes of angle of attack and mean flow velocity. It also provides the best noise reduction at high frequencies, which may be due to the higher (spatial) frequency content of the random pattern.

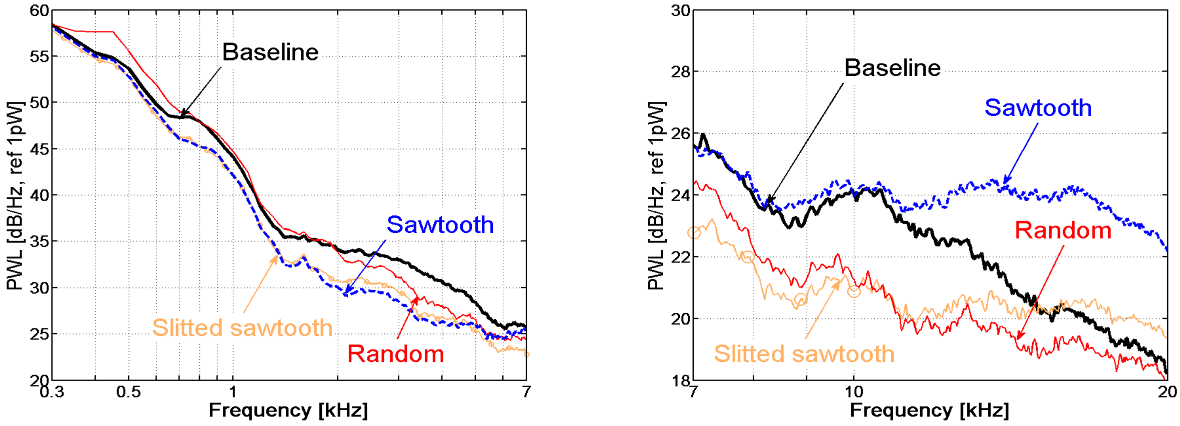

(a) At 5^o AoA from $300\,Hz$ to $7\,kHz$. (b) At 5^o AoA from $7\,kHz$ to $20\,kHz$.

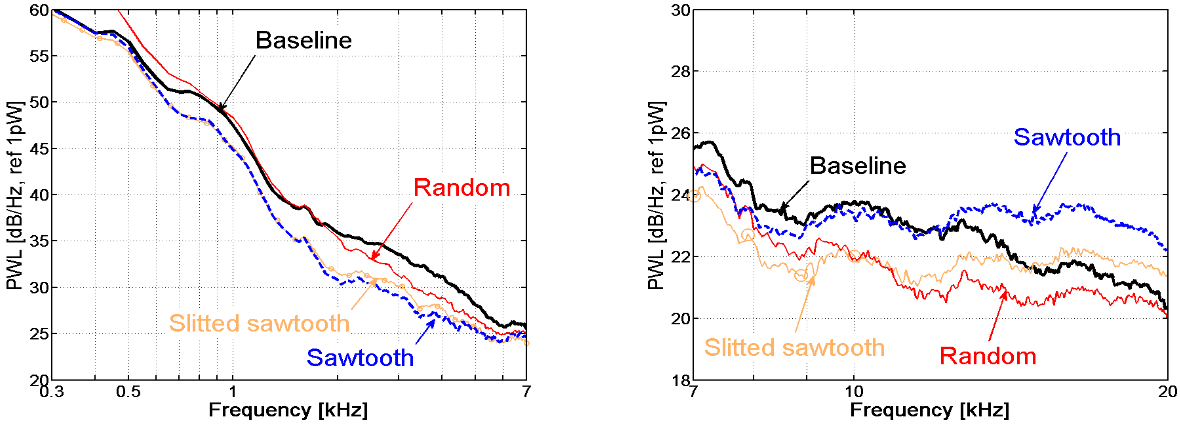

(c) At 15^o AoA from $300\,Hz$ to $7\,kHz$. (d) At 15^o AoA from $7\,kHz$ to $20\,kHz$.

Figure 6.19: Sound power level PWL as a function of frequency at $U_0 = 80\,m/s$.

Finally, Figure 6.20 shows the mean flow velocity dependency of the change in sound power level ΔPWL defined in Equation 4.2. It can be seen that for all trailing edge treatments, the frequency above which noise is increased can be identified by a constant Strouhal number $St_\delta \sim 1$, as given in Equation 4.3. This is true for the periodic patterns, i.e., the slits, the sawtooth with holes and the slitted sawtooth, and also for the random trailing edge geometry, although it is less clear for the latter as the noise is not increased but only identical to that of the baseline straight edge for frequencies higher than $f\delta/U_0 > 1$.

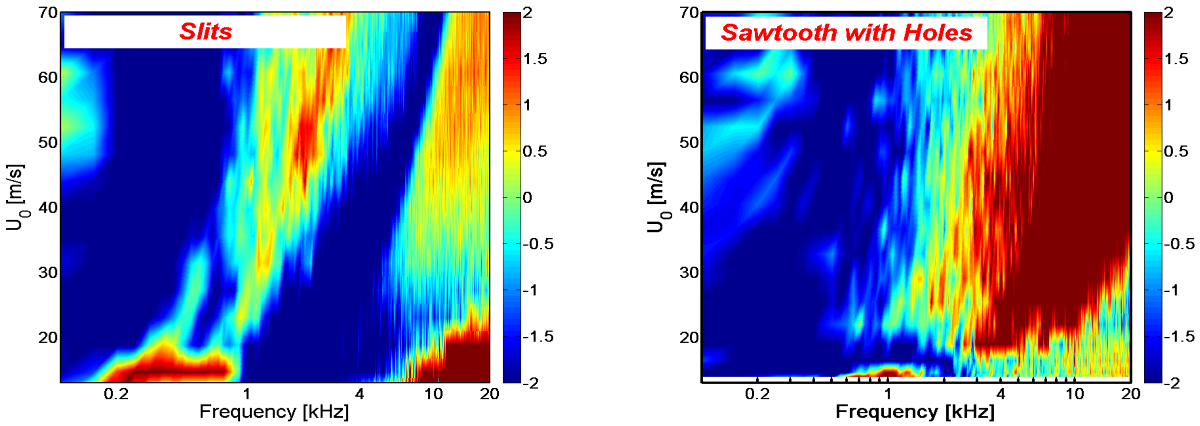

(a) Slit $(d_1 + d_2)/h = 0.07$.

(b) Sawtooth with holes $OA = 15\,\%$.

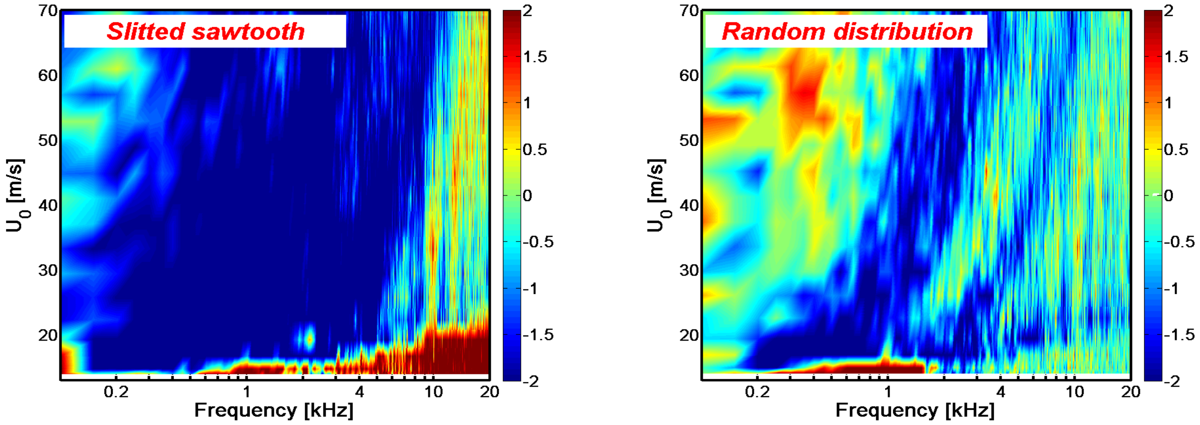

(c) Slitted sawtooth $d_1 = d_2 = 0.5\,mm$, $H = 25\,mm$.

(d) Random distribution $\sigma = \sigma_0$, $\delta x = 3\,mm$.

Figure 6.20: Sound power level change ΔPWL as a function of frequency and mean flow velocity U_0 at 5^o AoA.

6.4 Summary

This Chapter presents and assesses the noise performance of four trailing edge geometries to reduce airfoil trailing edge noise. A brief summary is given below:

Slits:

Slit trailing edges were investigated. These have been previously used by Herr [59], where broadband noise reductions of up to 10 dB were reported. In the current study, the broadband noise benefits from slit trailing edges is limited to about 2 dB when the length of the slits is $2h = 30\,mm$, and when the width of the slit and the separation between adjacent slits are $0.5\,mm$. It is worth noting that Herr states that for the slits to be effective at reducing the trailing edge noise radiation, their width must be of the order of the sub-layer thickness, i.e., typically smaller than

0.1 mm. Due to manufacturing limitations, a minimum slit width of 0.5 mm was achieved in the current study and is therefore substantially less than the suggested size, investigated by Herr. Another major difference with Herr's experiment is the presence of high frequency excess noise observed in this work (as with the sawtooth serrations in Chapter 4) but not reported in Herr's study. These discrepancies are partly attributed to the large variation in the Reynolds number tested in each study, i.e., [0.2 - 0.8] $\times 10^6$ in this study and [1.1 - 7.9]$\times 10^6$ in Herr's study.

Serrations with holes:

The sawtooth serration with holes provided relatively poor noise reductions of up to maximum 2 dB compared to the straight edge airfoil, and over a smaller frequency range relative to all the other trailing edge geometries tested. A high frequency noise increase of up to 12 dB was also reported. The likely cause of this is the size of the holes. However, it is shown that introducing flow permeability by means of holes across the sawtooth introduces a consistent broadband noise reduction of up to 4 dB over the solid sawtooth. It was also shown that a fine tuning, which was not further investigated here, appears to be required to benefit from an additional noise reduction through the implementation of holes at the airfoil trailing edge.

Slitted serration:

The slitted serrations were presented as another method to introduce flow permeability at the airfoil trailing edge. It is shown that the depth of the slits superposed to the main sawtooth is a critical parameter controlling the noise reduction capability of this geometry. In addition, minimizing both the width of the slits, and the distance between adjacent slits per sawtooth also appear to provide additional noise reductions. Significant noise benefits were obtained with broadband reductions of up to 5 dB compared to the baseline airfoil, across most of the frequency range. Additional noise reductions of up to 1 dB at $U_0 = 40$ and 80 m/s were obtained compared to the best performing trailing edge sawtooth of Chapter 4 ($\lambda/h = 0.3$). In addition, the high frequency noise excess was found to be less than 1 dB for all flow conditions. The major advantage of this trailing edge design is that the broadband noise reductions associated appear to be weakly dependent on the flow conditions, i.e., the mean flow velocity U_0 and the airfoil angle of attack. This trailing edge geometry has been patented (patent no GB1121753.6).

Random edges:

Random trailing edge geometries were designed to break down the periodic pattern at the trailing edge and reduce the phase speed and the spanwise correlation lengths that control the coherent radiation of the sources distributed along the trailing edge. A series of random pattern was therefore generated and distributed along the airfoil trailing edge. The amplitude of the edge perturbation was controlled by the standard deviation of the random white noise signal. The sampling of the signal along the airfoil span was chosen to be similar to the periodicity of the sawtooth serrations presented in Chapter 4, i.e., 1.5 and 3 mm. Broadband noise reductions of up to 3 dB were obtained over the large frequency band from 1 kHz to 10 kHz. It is worth noting that this trailing edge design does not increase the noise at higher frequencies and that the noise reduction appears to be non-significantly sensitive to changes of angle of attack.

By way of a summary, this Chapter presents alternative trailing edge geometries to the sawtooth serrated edge to reduce boundary layer turbulence trailing edge noise. The random trailing edges gave reasonable broadband noise reductions, with no increase of noise at high frequencies. The most effective design is the slitted sawtooth, where slits are superposed on a conventional sawtooth. It is believed that with the appropriate technology, the noise reduction performance of this trailing edge design can be further improved by reducing the size of the sawtooth and consequently the size of the slits that are superposed onto it. As suggested by Herr [59], a maximum slit width of the order of the sub-layer thickness, i.e., typically less than $0.1\,mm$ could considerably improve the noise performance of this treatment.

The noise performance of the treatments applied at the trailing edge of the single airfoil for reducing trailing edge noise are summarized in Table 6.1.

	Low frequency NR	High frequency NI
Sawtooth	$> 5\,\mathrm{dB}$	$> 5\,\mathrm{dB}$
Slit	$1 \rightarrow 5\,\mathrm{dB}$	$> 5\,\mathrm{dB}$
Sawtooth + holes	$\pm 1\,\mathrm{dB}$	$> 5\,\mathrm{dB}$
Slitted sawtooth	$> 5\,\mathrm{dB}$	$< 1\,\mathrm{dB}$
Random	$1 \rightarrow 3\,\mathrm{dB}$	$0\,\mathrm{dB}$

Table 6.1: Summary of the noise performance of the various trailing edge treatments tested for noise reduction, for both the low frequency Noise Reduction (NR) and the high frequency Noise Increase (NI).

Chapter 7

Noise reduction using serrated trailing and leading edges in a tandem airfoil experiment

This chapter describes an experimental study of the simultaneous use of leading edge and trailing edge serrations for reducing the broadband noise (self noise and interaction noise) from two airfoils in a tandem configuration. As detailed in Section 7.1 below, and as shown in Chapter 4, trailing edge serrations have been used previously to reduce broadband self noise in isolated airfoil tests and to reduce the turbulence in the wake. The basic tandem geometry is shown below in Figure 7.1 together with the three dominant broadband sources, where $W_{sn_1}(f)$ and $W_{sn_2}(f)$ are the trailing edge self noise power spectrum radiated from the upstream airfoil and the downstream airfoil, respectively, and $W_i(f)$ is the interaction noise power spectrum radiated from the downstream airfoil.

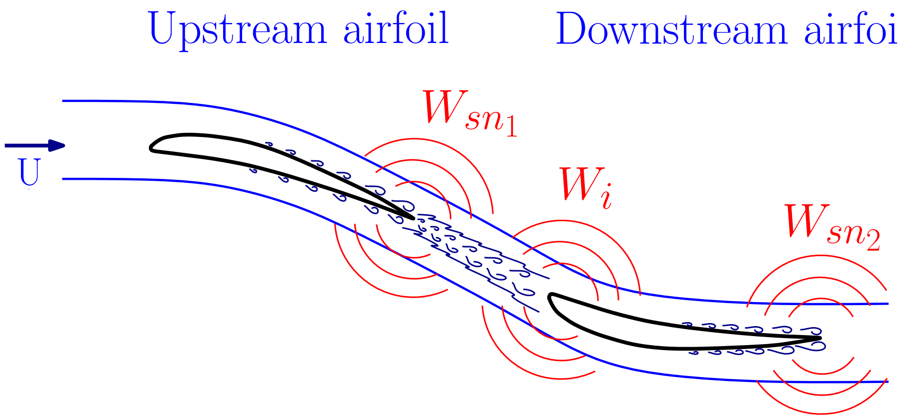

Figure 7.1: Self noise and interaction noise sources in a tandem airfoil configuration.

The objectives of this experiment are to:

- Quantify the relative contributions to the total noise reduction from the trailing edge noise from the upstream airfoil and the downstream airfoil, and the interaction noise from the downstream airfoil (due to its interaction with the wake shed from the upstream airfoil).
- Quantify the reductions in leading edge and trailing edge noise due to the introduction of leading edge and trailing edge serrations.
- Decompose the interaction noise reduction into its contributions from the reduction of the turbulent wake, due to trailing edge serrations, and the reduction due to a reduced leading edge response in the presence of leading edge serrations.

This study therefore combines, for the first time, a leading edge serration and a trailing edge serration, in order to reduce trailing edge and leading edge noise simultaneously. The self noise of the upstream airfoil will be reduced through a weakening of the scattered efficiency at the trailing edge by the introduction of trailing edge serrations. The leading edge noise of the downstream airfoil will be reduced by the simultaneous reduction of the wake turbulence impinging on the downstream airfoil together with the reduced scattering efficiency at the leading edge due to the introduction of leading edge serrations. An example of a direct application for this is the rotor - stator broadband interaction in a turbofan aircraft engine.

7.1 Background

Trailing edge serrations have been used previously in experiments aimed at reducing broadband self noise on isolated airfoils and cascade arrangement by several researchers, such as Oerlemans [88], Dassen [36], Parchen [92], Finez [42], Moreau [82] and Gruber [55, 54, 56] (see also Chapter 4). It was shown in Chapters 4 and 5 that Howe's model [65, 66] for serrated trailing edges consistently over-predicted the noise reduction compared to experiments. Geiger [47] and Gruber [55] (see also Chapter 4) performed hot wire measurements behind a serrated trailing edge airfoil to quantify their effect on wake turbulence. Geiger reported that although the TKE can be increased by up to 20 % depending on serration geometry, it is reduced overall for $x/c > 1$ ($x = 0$ is at the trailing edge) due to a faster decay compared to a straight edge. Geiger also reported an increase of the spreading of the wake behind a serrated trailing edge. It is also reported in Chapter 4 that the turbulence behind a sharp serrated edge ($2h = 30\,mm$, $\lambda < 5\,mm$) is increased by up to 20 % at $x/c = 0.66$. However, it appears that it is reduced by up to 10 % for shorter serrations ($2h = 20\,mm$) while the turbulence integral length scale Λ_{uu} decreases by up to 25 % within the range $0.03 < x/c < 0.66$.

As part of the FP7 European project FLOCON, a set of leading edge serrated airfoils was designed and manufactured by the company ONERA to reduce broadband interaction noise [35] on isolated airfoils. Measurements were performed in the ISVR wind tunnel and broadband noise reductions of up to 6 dB were measured for flow velocities ranging from $U_0 = 20$ to $60\,m/s$.

7.2 Sources of broadband noise

Figure 7.2 shows the tandem configuration of baseline sharp edge airfoils in the ISVR's wind tunnel.

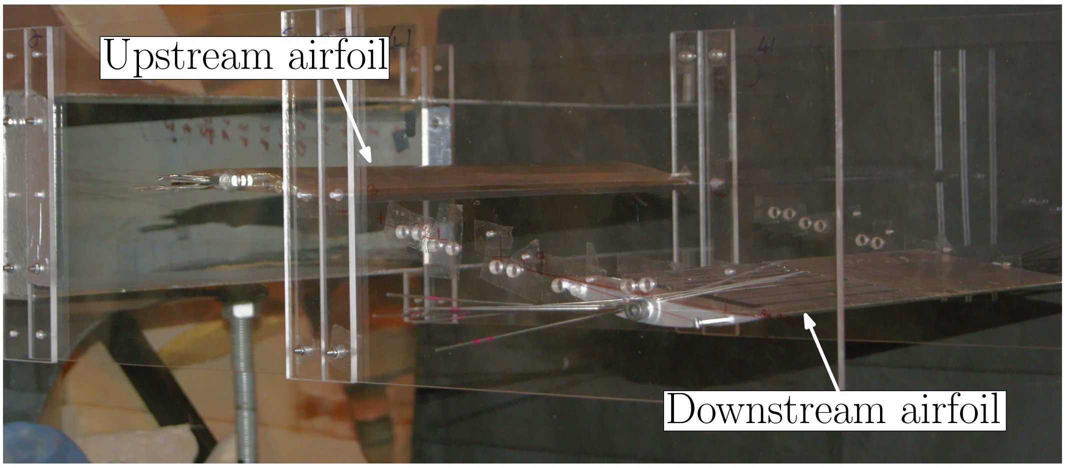

Figure 7.2: Photograph of the baseline tandem airfoils in the open-jet test section.

Figure 7.1 depicts the three sources of broadband noise radiated to the far field. The overall power $W_t(f)$ is the sum of the trailing edge self noise from both airfoils $W_{sn}(f)$, the interaction noise due to the turbulent wake from the upstream airfoil impinging on the leading edge of the downstream airfoil $W_i(f)$, and $W_b(f)$ the background noise due to the isolated jet (see Equation 7.1 below).

$$W_t(f) = W_{sn}(f) + W_i(f) + W_b(f), \tag{7.1}$$

The trailing edge self noise is the sum of the trailing edge self noise radiated from the upstream airfoil $W_{sn_1}(f)$ and the downstream airfoil $W_{sn_2}(f)$, as shown in Equation 7.2 below.

$$W_{sn}(f) = W_{sn_1}(f) + W_{sn_2}(f) \tag{7.2}$$

In an attempt to split the reduction in interaction noise into the contribution from the reduction in wake turbulence and from the reduction in leading edge response, the sound power due to the downstream airfoil leading edge noise, $W_i(f)$, is separated into its contribution from the normal component mean square velocity at the leading $\overline{w'^2}(f)$ and the blade response $R(f)$ (see Equation 7.3 below).

$$W_i(f) = \overline{w'^2}(f)R(f) \tag{7.3}$$

In these experiments, where the streamwise component of the velocity spectrum in the wake was measured, $\overline{u'^2}$ is therefore used as an approximation to $\overline{w'^2}$ in Equation 7.3, with the assumption that the wake turbulence is nearly isotropic and the mean square velocity and the integral length scales are of the same order in all directions. As a result, the overall sound power radiated by the two airfoils in a tandem airfoil configuration can be separated as the sum of the three sources identified in Figure 7.1.

$$W_t(f) = W_{sn_1}(f) + W_{sn_2}(f) + \overline{u'^2}(f)R(f) + W_b(f) \tag{7.4}$$

In this study it is assumed that the interaction noise with the upstream airfoil is negligible since the flow impinging upon the upstream airfoil leading edge has a turbulence intensity of less than 0.4 %. This assumption is verified in the beamforming results shown in Chapter 2 and the good comparisons of the measured noise directivity obtained with Amiet's trailing edge noise model shown in Chapter 3.

7.3 Source decomposition on the baseline tandem airfoils

The aim of this Section is to decompose the contribution of the three noise sources depicted in Figure 7.1 to the overall noise. The experimental procedure used to separate the sources is based on Equations 7.2 to 7.3 given in Section 7.2.

7.3.1 Method for the separation of the broadband noise sources

By a systematic process of spectral substitution of the noise power radiated by the upstream airfoil alone, with the downstream airfoil alone, and with both together, the self noise from individual airfoils and the interaction noise was identified. This procedure is repeated with and without serration treatment so that the effect of serrations on self noise and interaction noise can be quantified. To identify each source, the following steps are taken:

1 - The total broadband noise $W_t(f)$ is measured in a tandem configuration.

2 - The self noise of the upstream airfoil $W_{sn_1}(f)$ is measured in isolation.

3 - The self noise of the downstream airfoil $W_{sn_2}(f)$ is measured in isolation (keeping 5^o angle of attack for consistency with the tandem configuration).

4 - Interaction noise is estimated by spectral substitution from Equation 7.4, $W_i(f) = W_t(f) - W_{sn_1}(f) - W_{sn_2}(f) - W_b(f)$.

5 - Finally, interaction noise is further broken down into its reduction in the blade response, $R(f) = W_i(f)/\overline{u'^2}(f)$, where $R(f)$ is the downstream airfoil response function, either with a straight edge or a leading edge serration, and $\overline{u'^2}(f)$ is the streamwise turbulent spectrum in the wake, measured at the leading edge of the downstream airfoil.

7.3.2 Tandem airfoil setup

7.3.2.1 Geometrical parameters

The two airfoils used in this test were NACA65(12)-10 airfoil profiles with dimensions of 150 mm chord and 450 mm span (see Chapter 2). Noise measurements were performed using the polar array of 19 B&K microphones described in Chapter 2, at mean flow velocities of U_0 =20, 40, 60 and 80 m/s. The sound power was calculated using Equation 2.2. Both airfoils were positioned at 5^o angle of attack relative to their respective incoming flow directions, as illustrated in Figure 7.3. The upstream airfoil used in this study is the same as that used in Chapters 2 to 6, comprising a main steel body and a detachable trailing edge used for both the baseline and serrated trailing edge noise study. The downstream airfoil is made of aluminium with a straight leading edge and a sharp trailing edge, as shown in Figure 7.2.

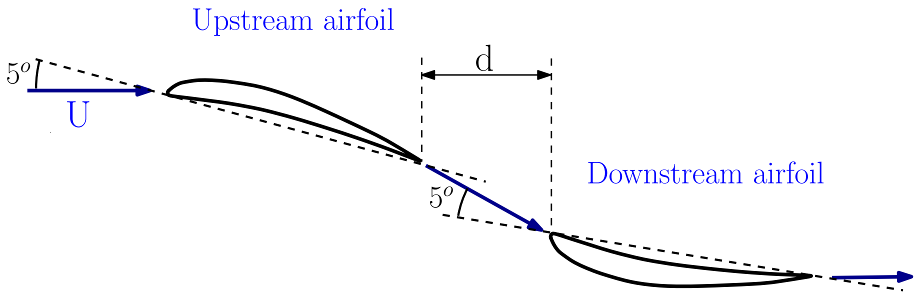

Figure 7.3: Geometrical arrangement of the tandem airfoils with the flow.

The leading edge of the upstream airfoil is located at one chord distance from the jet exit, while the downstream airfoil can be moved axially (using the arrangement discussed below) in order to measure the effect of the wake spreading on the sound power radiation. Table 7.1 lists the five normalized axial separation distances d/c, referred to by P_1 to P_5, for which the sound power was measured.

	P_1	P_2	P_3	P_4	P_5
d/c	0.13	0.33	0.67	1	1.33

Table 7.1: Axial separation distance between upstream and downstream airfoils, normalized by the airfoil chord c.

7.3.2.2 Positioning of the downstream airfoil

In this Section the description of the setup of the tandem airfoils relative to one another is presented. The different combinations of serrations fitted to the pair of airfoils are also presented to show that, as mentioned in Chapter 4 and by Geiger [47], the trajectory of the wake shed from the upstream airfoil varies with the trailing edge geometry and therefore, the downstream airfoil has to be located accordingly.

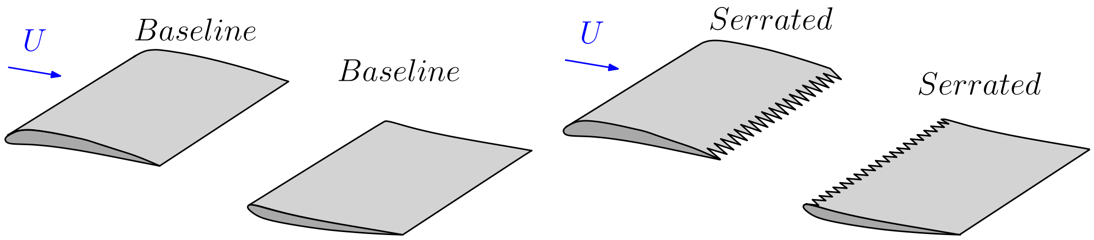

(a) Baseline trailing edge - Baseline leading edge.

(b) Serrated trailing edge - Serrated leading edge.

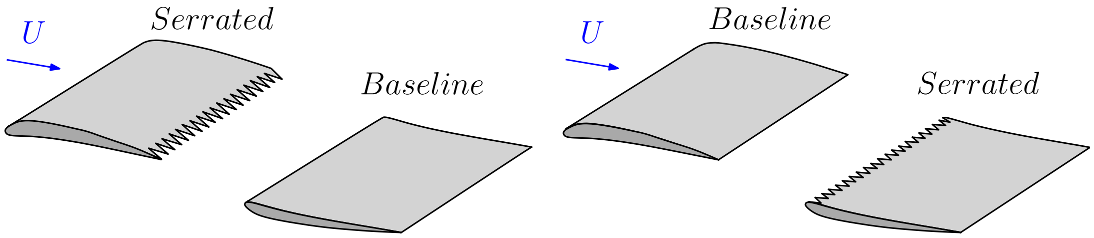

(c) Serrated trailing edge - Baseline leading edge.

(d) Baseline trailing edge - Serrated leading edge.

Figure 7.4: Tandem airfoil configurations tested.

Four combinations of pairs of upstream and downstream airfoils, with and without edge treatments, were tested as depicted in Figure 7.4 in order to quantify the contribution to the noise reduction of the trailing edge serrations, the leading edge serrations and the reduction of the turbulence in the wake. One leading edge serration and two trailing edge serrations were fitted in turn to the downstream and upstream airfoils respectively. From hereon, the baseline airfoils are referred to by B, while the leading edge and trailing edge serrations are referred to by S. As mentioned in Section 7.4 below, a slitted sawtooth trailing edge was also tested as a means of reducing both the noise and wake turbulence on the upstream airfoil and is referred to by $Slitted\,S$. These serration geometries are presented in Section 7.4 below.

Due to the different trajectories of the wake behind each trailing edge geometry, and to obtain accurate comparisons of the effect of each treatment on the sound power level, it is essential that the centre-line of the wake from the upstream airfoil impinges on the leading edge of the downstream airfoil, for each separation distance listed in Table 7.1. This was made possible by locating the trajectory of the wake centre-line as it convects downstream, by measuring the wake profile at each of the positions P_1 to P_5 listed in Table 7.1.

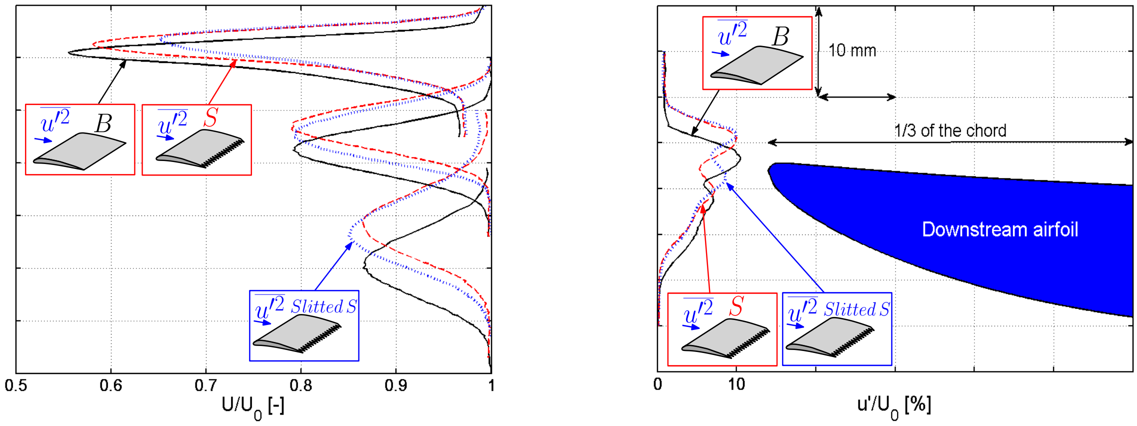

(a) Normalized mean wake deficit at positions P_1, P_3 and P_5.

(b) Turbulence intensity at P_1 showing the airfoil size relative to the wake width.

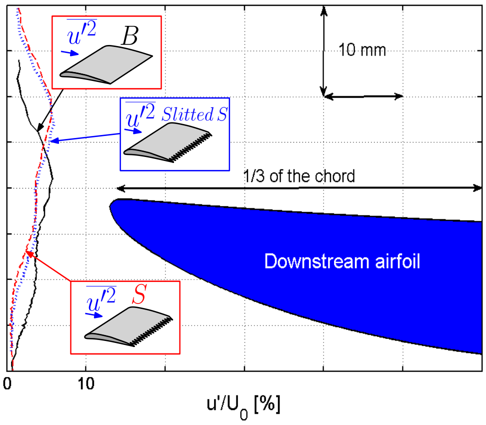

(c) Turbulence intensity at P_5 showing the airfoil size relative to the wake width.

Figure 7.5: Hot wire velocity data behind the upstream airfoil trailing edge.

Figure 7.5a shows the normalized mean wake velocity at positions P_1, P_3 and P_5. For each position, a shift in the wake centre-line is observed between all three trailing edge geometries. The mixing of the wake starts in between the teeth, i.e., at $x/c = -0.07$ and $x/c = -0.1$ for the serration and the slitted serration, respectively, where $x = 0$ is at the tip of the serrations. This shift needs to be accounted for to achieve accurate positioning of the downstream airfoil.

In order to assess the accuracy with which the airfoil leading edge must be located along the trajectory of the wake centre-line, it is useful to compare the size of the leading edge relative to the wake width. In Figure 7.5b the turbulent wake profile is presented together with the downstream airfoil shown to scale, at position P_1, where the wake is the thinnest and in Figure 7.5c at position P_5, where the wake is the widest. Note that Figures 7.5b and c are only shown for qualitative purposes since the alignment of the airfoil is different for each trailing edge. The leading edge of the downstream airfoil is shown to be smaller than the wake width at P_1 and P_5.

For consistency, and due to the wake spreading shift between all treatments, the leading edge of the downstream airfoil was aligned with the location of the maximum wake deficit for each trailing edge treatment applied to the upstream airfoil (within ±0.1 mm) using the following procedure.

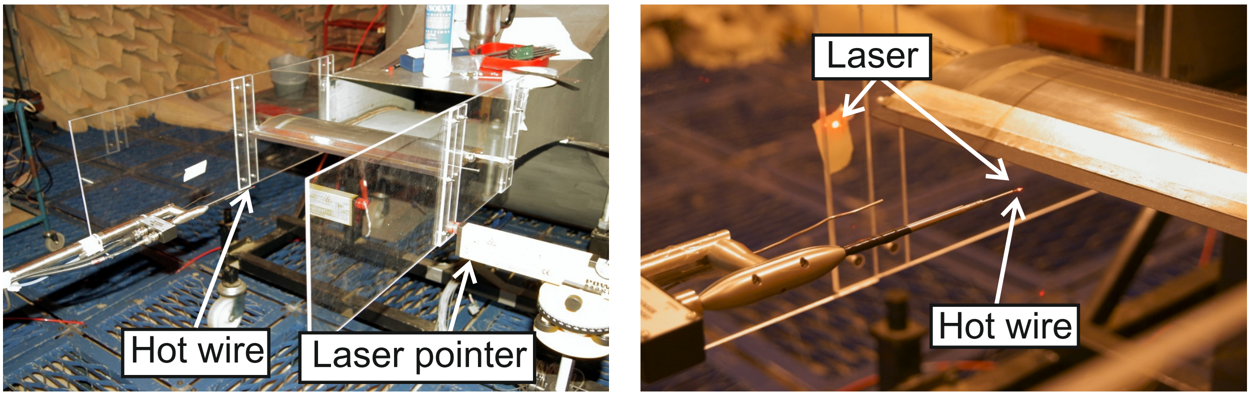

(a) Use of a leveled laser with the hot wire to locate the position of the wake centre-line.

(b) Laser targeting the tip of the hot wire.

Figure 7.6: Setting up the airfoil tandem experiment.

A set of fixing holes were drilled into the perspex side plates for each of the axial positions given in Table 7.1. The locations of the fixing holes were identified for each trailing edge treatment and for each axial distance d, using a hot wire positioned at the coordinate of the maximum wake deficit, in the mid-span plane of the airfoil. As shown in Figure 7.6, a levelled laser was pointed at the tip of the wire probe and the position of the leading edge was marked accordingly on the side plates. The fixing holes of the downstream airfoil were drilled in the side plates to ensure a 5^o angle of attack to the flow deflected by the upstream airfoil.

7.3.2.3 Smoke visualization

To verify that two airfoils were correctly aligned, and to ensure that both airfoils remained in the potential core of the jet, flow visualization tests were performed using a smoke wand, as shown in Figure 7.7. The smoke wand generates a point source of smoke upstream of the two airfoils. The smoke passes around the upstream airfoil, leaving its trailing edge tangentially. It is convected smoothly in the wake and around the downstream airfoil, ensuring that both airfoils are in the potential core of the jet. The smoke can clearly be seen to pass around the leading edge of the downstream airfoil. This test was performed for each axial separation distance.

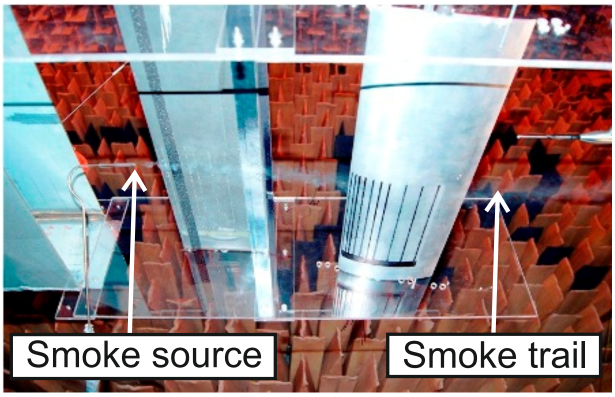

Figure 7.7: Flow visualization around the tandem airfoil configuration.

7.3.3 Self noise measurements setup

Self noise measurements performed on isolated airfoils are presented here for both the downstream baseline and serrated leading edge airfoils, as a means of isolating the self noise contribution to the overall noise. Measurements of the self noise of the upstream airfoil were performed following the same setup used for the isolated airfoil study described in Chapter 2 and is therefore not further mentioned here.

In order to decompose the total noise radiation from the tandem airfoils into the sources of noise in Equation 7.4, the trailing edge noise of the upstream and downstream airfoils were measured separately in the potential core of a clean jet at 5^oangle of attack. Figures 7.8a and b show the position of the baseline and treated downstream airfoils in the jet for the measurement of self noise. The leading edge of the downstream airfoil is located at three chord distance, i.e., $0.45\,m$, from the jet exit section. Without jet deflection due to the upstream airfoil, the downstream airfoil was moved to the centre of the potential core. For consistency with the tandem airfoil configuration, the isolated airfoil was positioned at 5^o angle of attack to the jet, with the pressure side facing upwards. Flow visualization using a smoke wand and hot wire measurements were performed in order to ensure that the airfoil was still in the potential core of the jet and that the shear layers were not interacting with the airfoil body. The baseline downstream airfoil was tripped for the isolated self noise measurements to avoid flow separation and the growth of instabilities in the boundary layers.

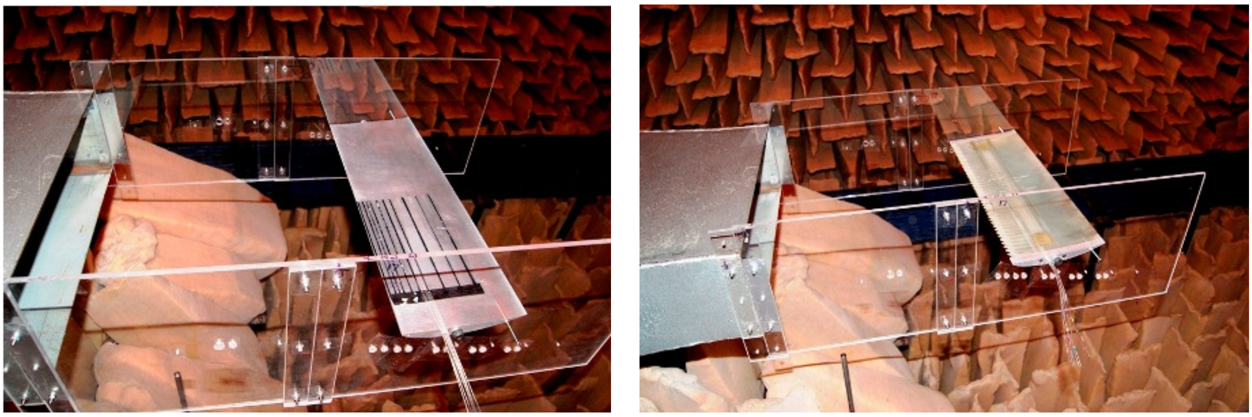

(a) Baseline airfoil. (b) Serrated leading edge airfoil.

Figure 7.8: Self noise measurement of the downstream airfoil.

7.3.4 Tripping the airfoils

In this thesis all isolated airfoil experiments were performed using a tripping band on both pressure and suction sides of the airfoil to force the flow into the fully turbulent state as described in Chapter 2. In the tandem airfoil configuration, the same tripping band was used on the baseline and treated upstream airfoils, i.e., between 10 and 20 % of the chord from the leading edge on both pressure and suction sides. However, as mentioned in Section 7.4 below, the inclusion of the leading edge serrations does not allow for the use of a tripping band at the same position as that used previously. The importance of boundary layer tripping was therefore investigated.

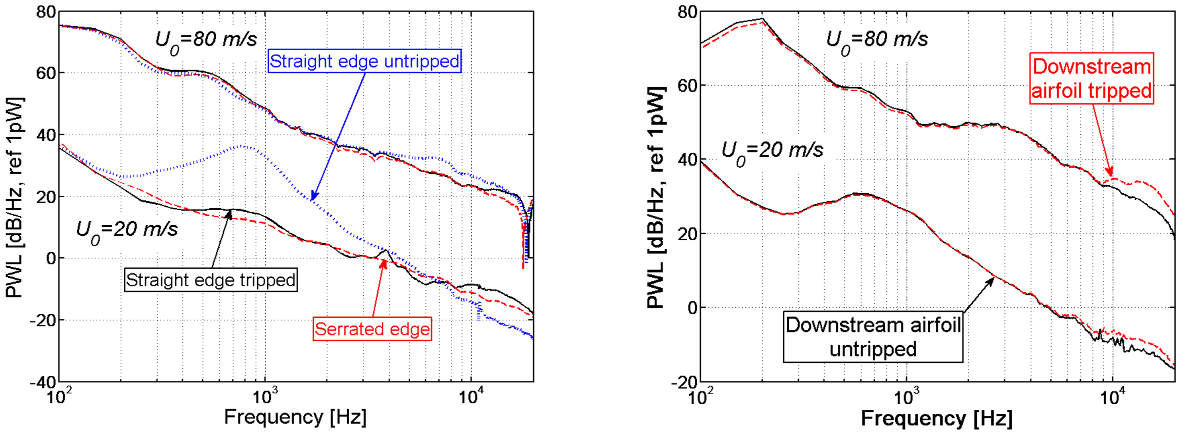

(a) PWL for the isolated airfoils. (b) PWL for the tandem airfoils.

Figure 7.9: Effect of the tripping of the downstream airfoil at $U_0 = 20\,m/s$ and $U_0 = 80\,m/s$.

On the isolated airfoil, the presence of the tripping band prevents the occurrence of the characteristic spectral broad hump in the noise radiation, due to boundary layer instabilities (see Figure 7.9a). It is also clear in Figure 7.9a that the noise radiation from the serrated leading edge airfoil is very similar to the tripped baseline airfoil when the trailing edge noise source is dominant. As reported by FLUOREM [45] from CFD computations performed using the Turb'flow RANS code, the presence of the leading edge serrations generates counter-rotating vortices that forces the boundary layer flow to remain attached, even without a tripping band (see Figure 7.10). Therefore the boundary layer does not separate and the trailing edge noise measurements are very similar to a tripped baseline airfoil.

In the tandem arrangement, the presence of the tripping band on the baseline downstream airfoil increases the noise by up to 6 dB at high frequencies, as shown in Figure 7.9b, and therefore, the baseline downstream airfoil was not tripped during the tandem tests.

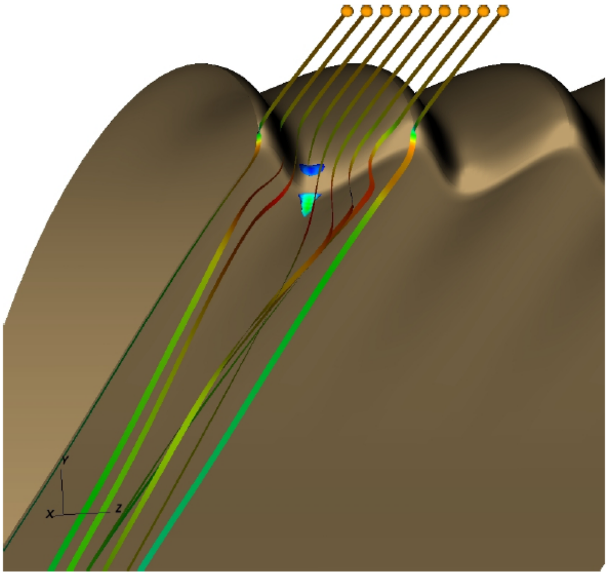

Figure 7.10: Streamlines ribbons colored by velocity modulus for 3D RANS ONERA wavy edge at 5^o angle of attack. Outer limit of the recirculation zone is materialized as an iso-surface (iso-value of axial velocity $u = -10^{-5}\,m/s$) colored by TKE (taken from FLUOREM [45]).

7.3.5 Typical decomposition results for the baseline airfoils

Using the procedure described in Section 7.3.1, the sound power radiated from the baseline tandem airfoil configuration was decomposed into the three noise sources shown in Figure 7.2. The relative contributions of the trailing noise from each airfoil to the overall self noise is shown in Figure 7.11 at $U_0 = 20\,m/s$ and $U_0 = 80\,m/s$.

The self noise radiated from both isolated airfoils is closely matched, within about 3 dB, with the largest difference occurring at low frequencies. The minor differences in the lower frequency range is partly attributed to the difference in flow conditions at the axial location of the airfoil in the jet, i.e., one chord distance from the jet exit for the upstream airfoil, and 3 chords distance from the jet exit for the downstream airfoil. Also, the microphone array faces the suction side of the

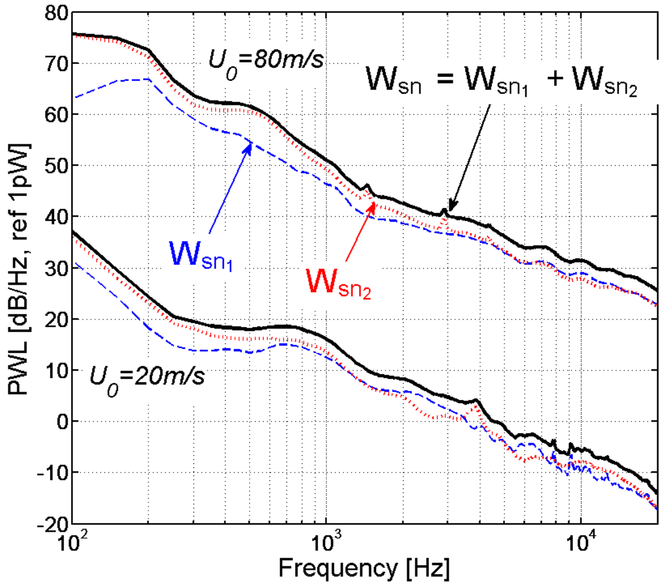

Figure 7.11: Similarity of the self noise measured on both isolated airfoils.

upstream airfoil but the pressure side of the downstream airfoil, which could account for small differences in the noise radiation due to the airfoil camber.

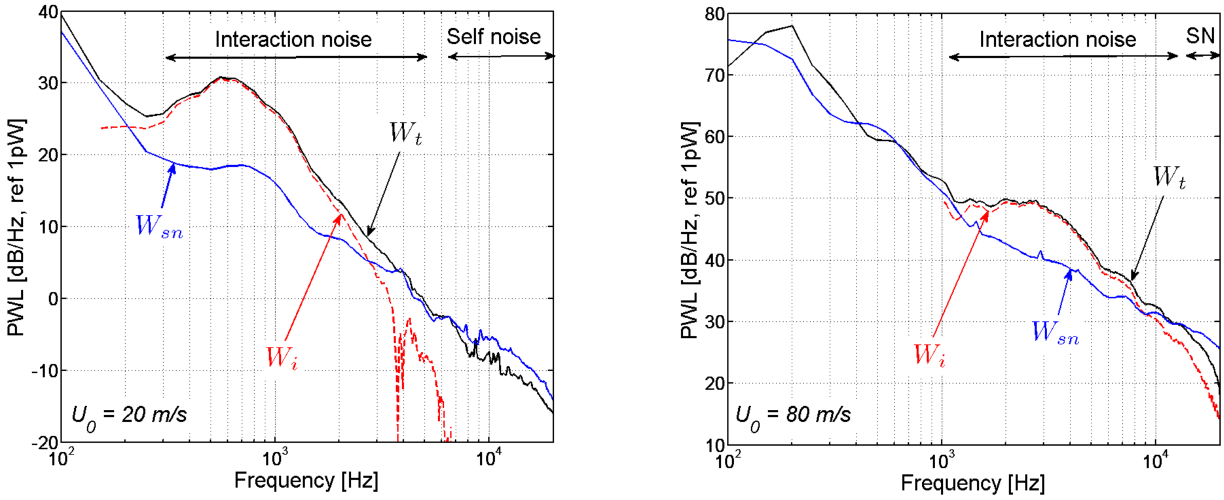

(a) $U_0 = 20\,m/s$.

(b) $U_0 = 80\,m/s$.

Figure 7.12: Separation of the noise sources in the P_3 tandem airfoil configuration.

Figures 7.12a and b show the overall sound power spectrum $W_t(f)$ measured on the baseline tandem airfoils at $U_0 = 20\,m/s$ and $U_0 = 80\,m/s$, respectively, together with their contribution from the sum of the trailing edge noise spectra $W_{sn_1}(f) + W_{sn_2}(f)$ and the turbulence interaction noise spectrum $W_i(f)$.

At $U_0 = 20\,m/s$, interaction noise dominates the total noise radiation between 300 Hz and 1 kHz by more than 10 dB, while the trailing edge noise dominates at frequencies greater than 7 kHz.

Comparing Figures 7.12a and b shows that the peak of interaction noise is velocity dependent and is shifted from 600 Hz at $U_0 = 20\,m/s$, to 2.5 kHz at $U_0 = 80\,m/s$. At $U_0 = 80\,m/s$, the interaction noise dominates the self noise radiation in the frequency range of interest.

7.4 Serrated trailing edge and leading edge treatments

This study uses trailing edge and leading edge serrations simultaneously to reduce the sound power level radiated from a tandem airfoil configuration. Note the serrations are applied to the trailing edge of the upstream airfoil and to the leading edge of the downstream airfoil, hence reductions in $W_{sn_1}(f)$ and $W_i(f)$ are obtained in this experiment. The trailing edge of the downstream airfoil remains unchanged, and therefore $W_{sn_2}(f)$ is assumed to be unaffected by any changes in the leading edge geometry of the downstream airfoil.

Two serrated type trailing edges are used as means of reducing both self noise and wake turbulence from the upstream airfoil. One is a sawtooth serration, previously used to reduce broadband noise on isolated airfoils in Chapter 4; the other is a slitted sawtooth serration, previously used to reduce broadband noise on isolated airfoils in Chapter 6. Their respective geometries are described below.

The noise reduction obtained using the leading edge serrations on an isolated airfoil are also shown to assess the noise performance of this geometry when the turbulence is controlled and generated by means of grids, as described by Polacsek [35] using data obtained by the author.

7.4.1 Upstream airfoil treatment: Trailing edge serrations

The sawtooth serration geometry giving the largest sound power reduction on the single airfoil profile was selected for the tandem airfoil test and has dimensions of $2h = 20\,mm$ and $\lambda = 3\,mm$ (see Chapter 4 and Figure 7.13a). Also tested as a trailing edge treatment on the upstream airfoil was the most effective of the slitted sawtooth serrations described in Chapter 6 with dimensions of $2h = 30\,mm$ and $\lambda = 9\,mm$, $d_1 = d_2 = 0.5\,mm$ and $H = 25\,mm$ (see Figure 7.13b). The geometry of the trailing edge is changed by means of flat plate inserts of thickness $0.8\,mm$ cut in stiff cardboard, as described in Chapter 2.

Chapters 4 and 6 provide further details on the noise and aerodynamic performance of these two trailing edge treatments.

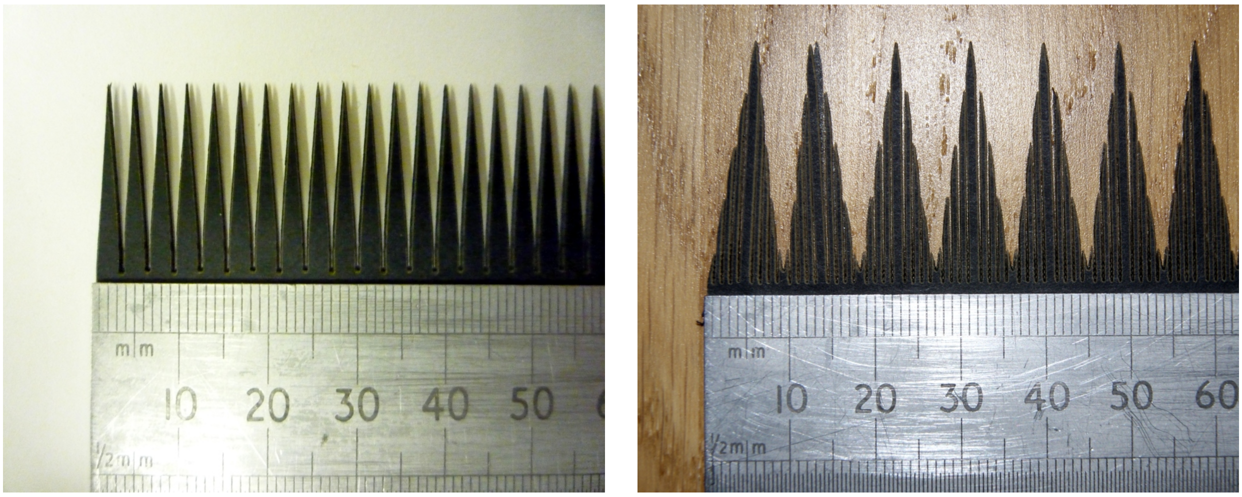

(a) Sawtooth 4 in Table 4.1 ($\lambda/h = 0.3$). (b) Slitted sawtooth 5 in Table 6.8.

Figure 7.13: Serrated trailing edge treatments fitted to the upstream airfoil.

7.4.2 Downstream airfoil treatment: Leading edge serrations

As part of the FP7 European project FLOCON, ONERA proposed a leading edge sinusoidal serration design aimed at reducing interaction noise. Three designs of sinusoidal serrations with parameters h and λ shown in Figure 7.14a, were tested in the ISVR's open-jet wind tunnel on isolated airfoils, where controlled isotropic turbulence is generated by means of grids (see Chapter 2). The serrated leading edge airfoils are referred to by LE_1 ($h = 10\,mm$, $\lambda = 5\,mm$), LE_2 ($h = 10\,mm$, $\lambda = 10\,mm$) and LE_3 ($h = 15\,mm$, $\lambda = 10\,mm$) and were manufactured using a rapid prototyping process. These parameters were chosen by ONERA to be close in size to the integral length scale of the turbulence impinging on the airfoil leading edge generated by the bi-planar grid, i.e., $\Lambda_{uu} = 5$ and $6\,mm$ for the two grids used in turn in Chapter 2.

Figures 7.14b and c show a side view and a top view of the airfoil LE_3 chosen for the tandem experiment. The sinusoidal serrations smoothly blend into the airfoil shape and therefore, a tripping band could not be positioned on the surface, as discussed in Section 7.3.4.

7.4.3 Leading edge serrations for turbulence interaction noise reduction on an isolated airfoil.

As reported by Polacsek [35] and based on the measurements conducted in the ISVR wind tunnel by Gruber, all three leading edge serrated airfoils reduced the sound power radiation by at least 4 dB over most of the mid and high frequency range. The airfoil LE_3, with geometrical parameters $h = 15\,mm$ and $\lambda = 10\,mm$, was found to be the most effective at reducing broadband interaction noise by an additional 1 dB and was chosen as the downstream airfoil treatment for the tandem

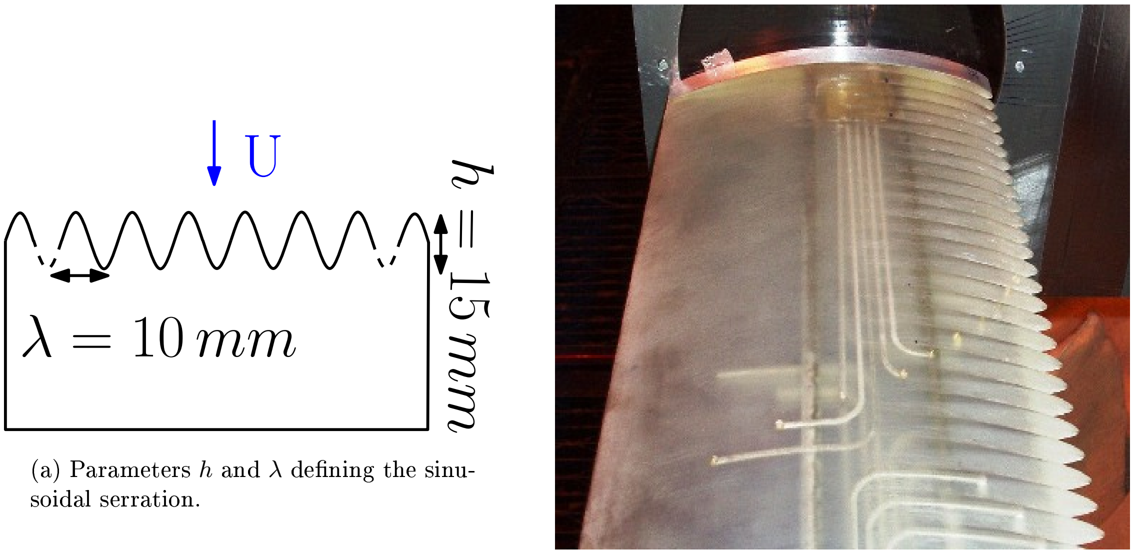

(a) Parameters h and λ defining the sinusoidal serration.

(b) Side view of airfoil LE_3 in ISVR's open-jet wind tunnel.

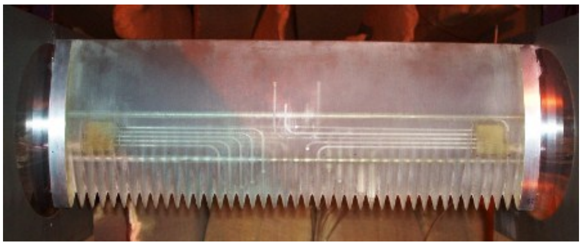

(c) Top view.

Figure 7.14: Leading edge serrated airfoil designed by ONERA [35].

test. This Section summarizes the noise reduction results obtained using the leading edge serrations LE_3 on the isolated NACA65(12)-10 airfoil in order to estimate the airfoil response function R, given in Equation 7.3 for the baseline leading edge and the serrated leading edge. Measurements were performed using, in turn, two bi-planar grids to generate controlled turbulence (see Chapter 2) in the ISVR open-jet wind tunnel.

The broadband sound power reductions reported by Polacsek [35] are shown below for completeness. Figure 7.15a shows the sound power level spectrum $PWL(f)$, defined in Equation 2.2, measured on the isolated serrated leading edge airfoil and baseline leading edge airfoil, at $U_0 = 20$, 40 and $60\,m/s$. Figure 7.15b shows the sound pressure level spectrum $SPL(f)$, defined in Equation 2.1 and measured at 90^o to the airfoil trailing edge. Broadband reductions of up to 6 dB are obtained using serrated leading edges from 0.5 to 20 kHz, depending on the mean flow velocity.

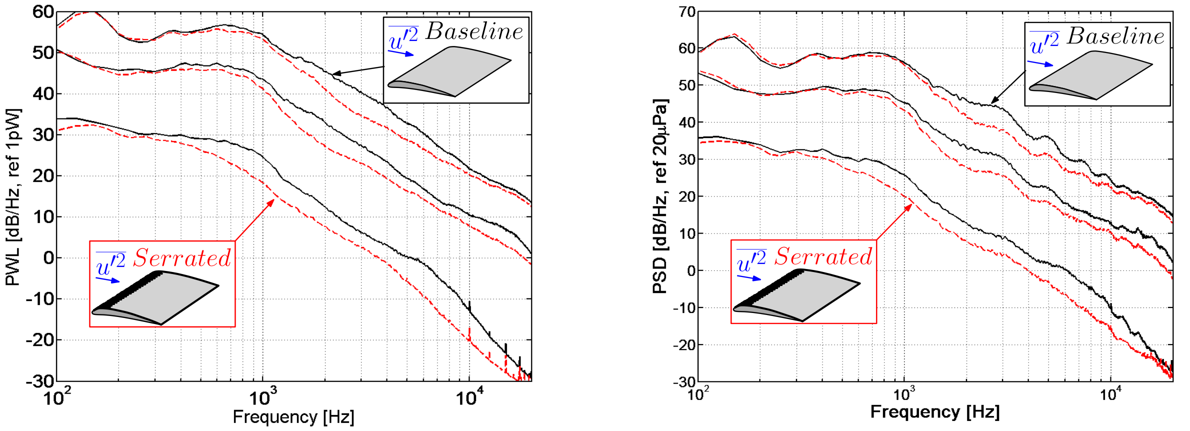

(a) Sound power level spectrum $PWL(f)$ as given in Equation 2.2.

(b) Sound pressure level $SPL(f)$ measured at 90^o as given in Equation 2.1.

Figure 7.15: Reduction of turbulence interaction noise using the leading edge serrations depicted in Figure 7.14.

Equation 7.3 is now used to decompose the interaction noise spectrum and isolate the airfoil response function $R(f) = W_i(f)/\overline{u'^2}$ for both serrated and straight leading edges. In addition, the two grids described in Chapter 2 are used in turn to generate two slightly different turbulence characteristics in the incoming flow. The streamwise turbulence spectra used for this calculation are measured at the airfoil leading edge in the middle of the jet.

Figure 7.16a shows the airfoil response $R(f)$ for each turbulence grid at $U_0 = 40\,m/s$ for both the straight and the serrated leading edge LE_3. It can be seen that $R(f)$ varies by no more than 1 dB over the whole frequency range, for both turbulence grids. The discrepancies most likely arise from the difference in turbulence length scales from the two grids and from random error. Interestingly, Figure 7.16a shows that the response of the serrated leading edge airfoil is weaker by up to 8 dB over the whole frequency range with negligible reductions occurring below about 1 kHz where jet noise dominates. Figure 7.16b shows the airfoil response $R(f)$ for grid 2, with turbulence parameters $TI = 2.1\,\%$ and $\Lambda_{uu} = 5\,mm$ (see Chapter 2), at the three mean flow velocities $U_0 = 20$, 40 and $60\,m/s$ and for both serrated and straight leading edges. The reduction in noise appears weakly dependent on the flow speed, with a maximum reduction of 8 dB above 1 kHz.

Therefore, it is shown that the presence of leading edge serrations provides broadband reductions of the airfoil response function $R(f)$ of up to 8 dB.

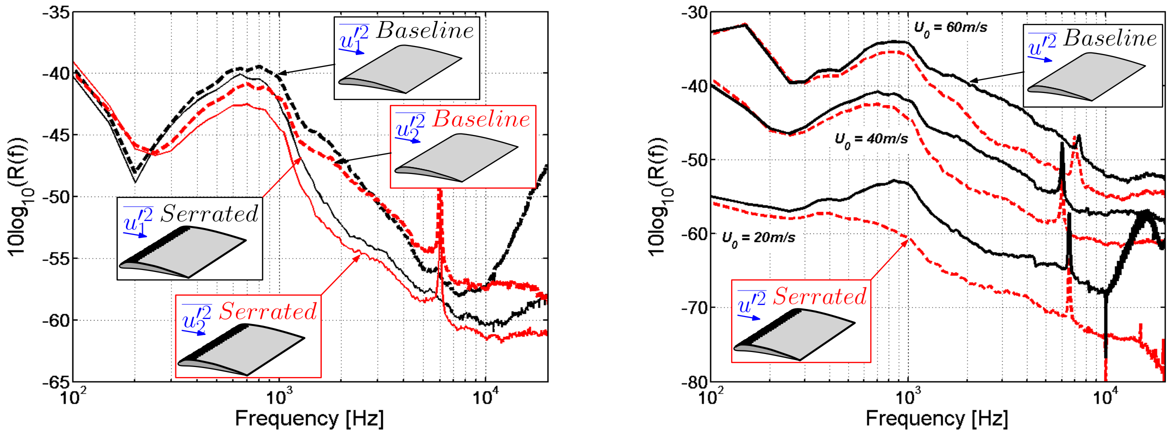

(a) At $U_0 = 40\,m/s$ for two bi-planar grids generating in turn turbulence with characteristics: $TI_1 = 2.5\,\%$ and $\Lambda_{uu,1} = 6\,mm$, $TI_2 = 2.1\,\%$ and $\Lambda_{uu,2} = 5\,mm$.

(b) At $U_0 = 20$, 40, $60\,m/s$ with grid 2 fitted inside the nozzle of the open-jet.

Figure 7.16: Estimation of the airfoil response function $R(f)$ on an isolated baseline and serrated leading edge airfoil, as given in Equation 7.3.

This work now attempts to compare the airfoil response function $R(f) = W_i(f)/\overline{u'^2}$, defined in Equation 7.3, for the case of an isolated airfoil (using grid-generated turbulence) with that in a tandem airfoil configuration (with impinging turbulence from the wake interacting with the airfoil leading edge). As mentioned above, the turbulence velocity spectrum is measured in the middle of the jet, at the airfoil leading edge in the isolated airfoil case. In the tandem configuration, the turbulence spectrum is integrated around $\pm 2\,mm$ of the wake centre-line, at the leading edge of the downstream airfoil.

Therefore, Figure 7.17 shows a comparison of $R(f)$ obtained at $U_0 = 20\,m/s$ using the leading edge serrated airfoil LE_3 in isolation, with grid 2 as a turbulence generator, and in a tandem airfoil arrangement at P_5, where turbulence is shed from the upstream airfoil. Figure 7.17 shows the airfoil response $R(f)$ obtained with the three trailing edge geometries described in the previous Sections fitted to the upstream airfoil trailing edge, i.e., a straight TE, a sawtooth TE and a slitted sawtooth TE.

The estimate of the airfoil response $R(f)$ is seen to deviate by no more than 2 dB up to 6 kHz in the frequency range where interaction noise dominates, between the isolated airfoil case and the three tandem airfoil cases. Therefore, it is reasonable to assume that the change in the turbulence characteristics between the isolated test (where the turbulence is homogeneous and isotropic) and the tandem airfoil test (where the turbulence naturally develops in the wake of the upstream airfoil) should not affect the noise reduction efficiency due to the serrated leading edge airfoil.

The close match between the airfoil response spectra in the tandem configuration, independently of the upstream trailing edge geometry also suggests that it should be possible to isolate the effect of the reduction of the wake turbulence on the overall tandem airfoil noise reduction.

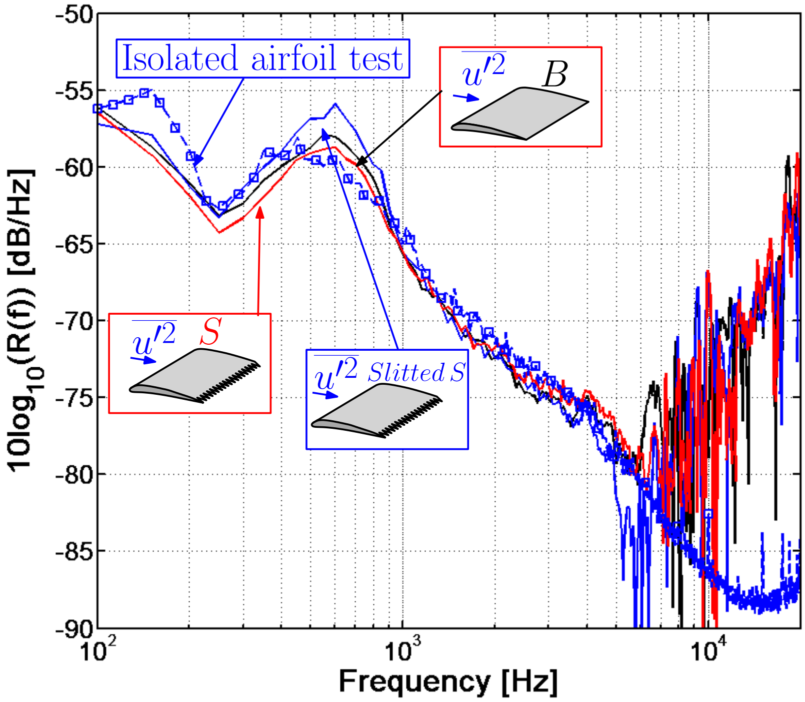

Figure 7.17: Estimation of the airfoil response function $R(f)$, defined in Equation 7.3, of the serrated leading edge airfoil in isolation and in a tandem configuration at $U_0 = 20\,m/s$.

7.5 Tandem test results

This Section presents the results and analysis of the tandem experimental data. The overall noise from the two airfoils in tandem is first broken down into the component sources, as shown in Equation 7.4. The sound power reduction is investigated for both combinations of trailing edge serrations with leading edge serrations and trailing edge slitted serrations with leading edge serrations. Data will be presented at $U_0 = 20\,m/s$ and $U_0 = 80\,m/s$ and for the airfoil separation distances d listed in Table 7.1. Finally, the contribution of each source of noise to the measured sound power reduction is discussed. First, the results of the overall noise reduction obtained with the simultaneous use of serrations at the upstream airfoil trailing edge and the downstream airfoil leading edge are discussed.

7.5.1 Sound power reduction using serrated trailing and leading edges

Figure 7.18 shows a photograph taken from above of the fully treated tandem airfoil configuration, where the upstream airfoil is fitted with the slitted serrated trailing edge and the downstream airfoil is fitted with leading edge serrations. A comparison of the sound power level spectra $PWL(f)$, given in Equation 2.2, measured on the baseline tandem arrangement and on the two fully treated tandem configurations (the upstream airfoil is treated in turn with the sawtooth serration and with the slitted sawtooth serration) is shown in Figure 7.19, for the two mean flow velocities $U_0 = 20$ and $80\,m/s$. Overall sound power reductions of up to 5 dB are obtained with the sawtooth trailing edge serrations and up to 8.5 dB using slitted sawtooth serrations at $U_0 = 80\,m/s$. The effect of the fully treated tandem arrangement has negligible effects at low frequencies, below the broad spectral hump characteristic of interaction noise. For both treated configurations the maximum sound power reductions occur at frequencies where the interaction noise was shown to be dominant. However, the use of the slitted sawtooth provides an additional 3.5 dB on the overall noise reduction at $U_0 = 80\,m/s$ compared to the sawtooth trailing edge.

The following Sections are therefore dedicated to isolating the effects of the trailing edge treatment, of the leading edge treatment and that due to the change in the characteristics of the wake turbulence, on the total sound power reduction.

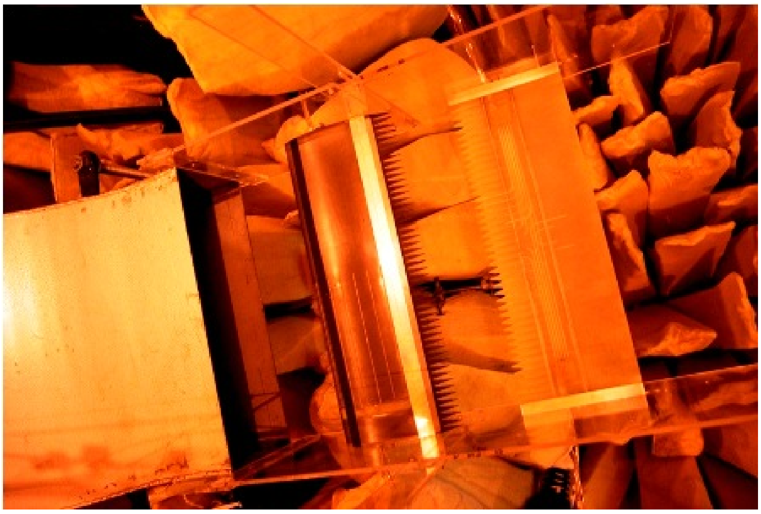

Figure 7.18: Fully treated tandem airfoils in the test section of the open jet wind tunnel.

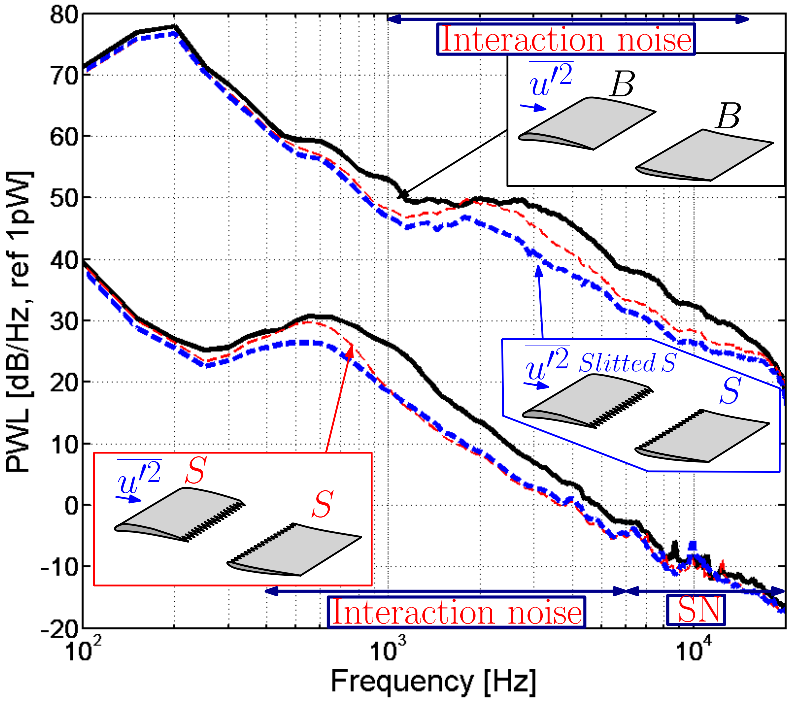

Figure 7.19: Total sound power reduction obtained when combining trailing edge serrations and leading edge serrations in a tandem airfoil configuration, at $U_0 = 20\,m/s$ and $U_0 = 80\,m/s$, at position P_3.

7.5.1.1 Contribution of individual sources of noise to the overall Sound PowerPWL

This thesis now attempts to split the overall noise reduction into its contributions from self noise reductions and interaction noise reductions. Interaction noise is further decomposed into its contribution from the reduced wake turbulence and the leading edge response due to leading edge serrations.

This Section investigates the individual contributions of the serrated trailing edge and leading edge treatments, to the overall noise reduction $W_t(f)$, using the source decomposition procedure described in Section 7.2. The following quantities are therefore introduced to estimate the contribution of each source of noise to the overall sound power reduction spectrum, where W is defined in Equation 2.2.

$$\Delta PWL_t(f) = 10\log_{10}\left(\frac{W_t(f)|_{\mathbf{s}}}{W_t(f)|_{\mathbf{b}}}\right) \tag{7.5}$$

$$\Delta PWL_{sn}(f) = 10\log_{10}\left(\frac{W_{sn}(f)|_{\mathbf{s}}}{W_{sn}(f)|_{\mathbf{b}}}\right) \tag{7.6}$$

$$\Delta PWL_i(f) = 10\log_{10}\left(\frac{W_i(f)|_{\mathbf{s}}}{W_i(f)|_{\mathbf{b}}}\right) \tag{7.7}$$

$$\Delta PWL_R(f) = \Delta PWL_i(f) - 10\log_{10}\left(\frac{\overline{u'^2(f)}\Big|_{\mathbf{s}}}{\overline{u'^2(f)}\Big|_{\mathbf{b}}}\right), \tag{7.8}$$

where $\Delta PWL_t(f)$ refers to the total sound power spectrum reduction due to trailing edge and leading edge serrations on the tandem airfoils, $\Delta PWL_{sn}(f)$ is the sound power spectrum reduction due to the reduction of the upstream trailing edge noise, $\Delta PWL_i(f)$ is the sound power spectrum reduction due to the reduction in interaction noise and $\Delta PWL_R(f)$ is the sound power spectrum reduction due to the reduction of the downstream airfoil response only, in the presence of leading edge serrations. Unfortunately, the velocity spectra of Equation 7.8 were measured at $U_0 = 20\,m/s$ only. Therefore, the Von Karman spectrum for longitudinal turbulence, defined in Equation 2.9 is used to predict the velocity spectra in the wake at $U_0 = 80\,m/s$, using the streamwise turbulence intensity TI and turbulence integral length scale Λ_{uu} estimated from the hot wire measurements presented in Section 7.5.2 below.

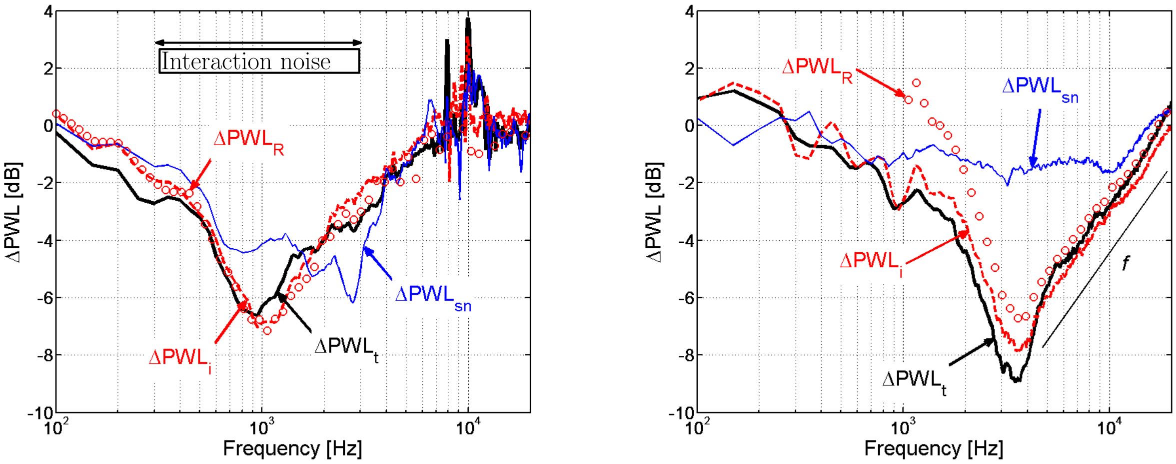

(a) At $U_0 = 20\,m/s$.

(b) At $U_0 = 80\,m/s$.

Figure 7.20: Contribution of individual noise sources to the overall sound power reduction using slitted sawtooth TE and serrated LE.

Figure 7.20 shows the difference in the sound power level spectrum $\Delta PWL(f)$ defined in Equations 7.10 to 7.8, at the two mean flow velocities $U_0 = 20$ and $80\,m/s$, and for the tandem airfoils fitted with upstream trailing edge slitted sawtooth and downstream leading edge serrations. At both velocities, it is clear that the overall sound power reduction $\Delta PWL_t(f)$ follows closely the reduction obtained from the interaction noise source $\Delta PWL_i(f)$. This is expected as it was shown that interaction noise dominates self noise over most of the frequency range (see Section 7.5.2). This is true even at the low velocity $U_0 = 20\,m/s$, where both the trailing edge self noise reduction $\Delta PWL_{sn}(f)$ and the interaction noise reduction $\Delta PWL_i(f)$ appear very closely matched. At frequencies close to 6 kHz, self noise dominates, which explains the increase in power at higher frequencies when $f\delta/U_0 > 1$ from Chapter 4. At the higher velocity $U_0 = 80\,m/s$, the interaction noise source alone contributes to the overall sound power reduction by more than 6 dB compared to the trailing edge noise source.

In order to estimate the contribution of the reduction of the turbulence in the wake, the contribution to the overall sound power reduction spectrum of the reduction in the interaction noise $\Delta PWL_i(f)$ and the reduction in the airfoil response only $\Delta PWL_R(f)$, (see Equations 7.7 and 7.8 respectively), were calculated. It is shown that at $U_0 = 20\,m/s$, both $\Delta PWL_i(f)$ and $\Delta PWL_R(f)$ are closely matched and therefore contributions from the modification of the turbulence in the wake are non-significant. However, at $U_0 = 80\,m/s$, the Von Karman model is used with the turbulence intensity TI and the length scale Λ_{uu}, measured at $U_0 = 20\,m/s$, to estimate the turbulence spectrum in the wake (see Equation 2.9). It is therefore assumed that these turbulence parameters are independent of the mean flow velocity, which was verified in Chapter 2. It is shown in Figure 7.20b that the small modifications of the turbulent parameters in the wake shown below in Section 7.5.2 provide an additional 2 dB to the overall tandem sound power reduction. Note that this value of 2 dB under-predicts the actual additional reduction of 3.5 dB due to the slitted sawtooth rather than the sawtooth trailing edge, as seen in Figure 7.19 at $U_0 = 80\,m/s$. However, the turbulent spectrum in the wake was not measured at this velocity, and therefore the Von Karman spectrum may under-estimate the reductions of the turbulence that occur at the downstream airfoil leading edge in the presence of the upstream sawtooth slitted trailing edge.

Overall, most of the sound power reduction measured on the fully treated tandem airfoils originates from the reduction of the downstream airfoil response due to leading edge serrations, while the contributions from the self noise reductions are mainly masked by the interaction noise source, which dominates over most of the frequency range. The geometry of the trailing edge sawtooth fitted to the upstream airfoil is shown to contribute an additional 2 dB to the overall noise reduction in the presence of the slitted sawtooth. The additional reduction of 3.5 dB due to the slitted sawtooth rather than the sawtooth trailing edge (see Figure 7.19 at $U_0 = 80\,m/s$) may therefore be partly due to a weaker response of the downstream airfoil to the turbulence shed from the slitted sawtooth rather than the sawtooth trailing edge, as deduced from the sensitivity of the airfoil response $R(f)$ due to various turbulence characteristics shown in Figure 7.17.

Note that results are similar for the case of the tandem airfoils with the upstream sawtooth trailing edge and are therefore not shown here for brevity.

7.5.1.2 Contribution to the overall noise reduction by the self noise sources

The previous Section has demonstrated that most of the noise reduction originates from a reduction in the interaction noise source due to the use of the leading serrations on the downstream airfoil. This work now attempts to isolate the contribution to the overall noise reduction by the upstream trailing edge treatment when the downstream airfoil is fitted with leading edge serrations.

Therefore, the noise reduction is compared against separation distance d, for the straight trailing edge and the two serrated trailing edges, by means of the overall sound power level $OAPWL$ integrated between 100 Hz and 20 kHz and defined in Equation 7.9.

$$OAPWL = 10\log_{10}\sum_i \left(\frac{W(f_i).\Delta f}{W_0}\right) \quad , 100\,Hz < f_i < 20\,kHz, \tag{7.9}$$

where $W(f_i)$ is the sound power spectrum given in Equation 2.2, and $W_0 = 10^{-12}$W.

Figure 7.21 shows the $OAPWL$ calculated for both combinations of fully treated tandem airfoils plotted against the normalized turbulence length scale Λ_{uu}/λ in the wake of the upstream airfoil (λ is the periodicity of the leading edge serrations). The tandem configuration composed of the upstream airfoil straight trailing edge and the downstream airfoil serrated leading edge is also shown for comparisons. Note that the normalized turbulent length scale is varied in Figure 7.21 by variations of the integral length scale Λ_{uu} only, while the sawtooth periodicity is constant and equal to 10 mm.

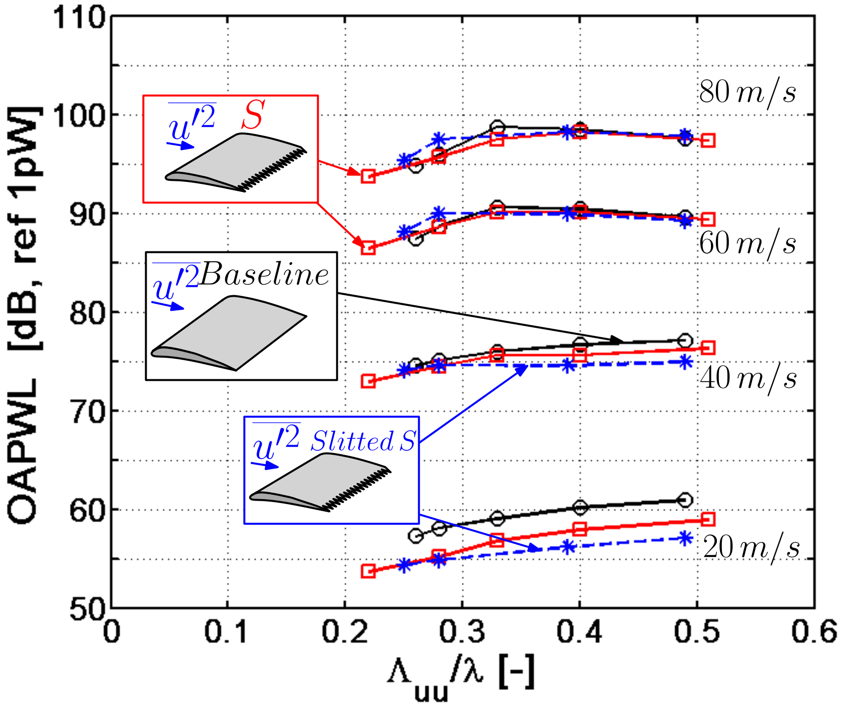

Figure 7.21: Sound power level $OAPWL$ (see Equation 7.9), integrated over the frequency band [0.1 - 20] kHz, against the normalized turbulent length scaleΛ_{uu}/λ, where λ is the periodicity of the leading edge serrations and Λ_{uu} the integral length scale of the incoming turbulence in the wake, at the four velocities $U_0 = 20$, 40, 60 and 80 m/s.

It is shown that $OAPWL$ generally decreases with decreasing Λ_{uu}/λ, for the four mean flow velocities, $U_0 = 20$, 40, 60 and 80 m/s. In addition, at $U_0 = 20\,m/s$ and $U_0 = 40\,m/s$, the slitted serrated trailing edge provides an additional 1.5 dB reduction compared to the arrangement with a conventional serrated trailing edge, and up to 5 dB relative to the baseline tandem airfoil. However, at $U_0 = 60\,m/s$ and $U_0 = 80\,m/s$, all three trailing edges appear to contribute similarly to the overall noise reduction to the tandem arrangement with leading edge serrations present. This is because the $OAPWL$ is dominated by the low frequency background noise at high velocities.

The overall sound power level also appears to drop faster when $\Lambda_{uu}/\lambda < 0.3$, while it is reasonably flat when $\Lambda_{uu}/\lambda > 0.3$. This indicates that the effectiveness of the serrated leading edges to reduce noise is most effective when the periodicity of the serrations are greater than about three times the integral length scale of the incoming turbulence (see Equation 7.10).

$$\lambda \gtrsim 3\Lambda_{uu} \tag{7.10}$$

Finally, Figure 7.21 shows that at low velocities, when trailing edge noise is the dominant noise source above 3 kHz, the sawtooth and slitted sawtooth provide additional noise reductions of up to 3 dB and 5 dB relative to the straight trailing edge, respectively, to the overall sound power level. However, as the frequency above which self noise dominates increases, i.e., when the jet speed increases, the contributions of the trailing edge treatments to the overall sound power level become less significant.

7.5.1.3 Effect of separation distance d on the overall sound power reduction

Figure 7.22 shows the overall sound power level reduction $\Delta PWL_t(f)$, defined in Equation 7.10, measured at the two positions P_3 and P_5 listed in Table 7.1, at the two mean flow velocities $U_0 = 20$ and $80\,m/s$. The results are compared for both pairs of airfoils fitted in turn with the sawtooth trailing edge and the slitted sawtooth trailing edge. Note that the low frequency noise is dominated by jet noise and therefore masks any noise reduction.

At low flow speeds of $U_0 = 20\,m/s$ (see Figures 7.22a) the maximum noise reduction occurs when the upstream airfoil is fitted with slitted sawtooth serrations rather than sawtooth serrations. Although the overall noise reduction varies by up to about 3 dB with separation distance d across the frequency range 100 Hz to 20 kHz, the relative noise performance of each combination of upstream sawtooth and slitted sawtooth trailing edge (with downstream serrated leading edge) of tandem airfoils is not significantly affected by the separation distance d. As discussed previously, at low velocities, the overall noise reduction is not significantly affected by the upstream trailing edge geometry, leading to maximum noise reductions of 8 dB at position P_3. At $U_0 = 80\,m/s$, the use of the slitted sawtooth in place of sawtooth serrations at the upstream trailing edge provides an additional noise reduction of up to 3.5 dB from 300 Hz to 15 kHz at position P_5. According to the results shown in the previous Section, this additional noise reduction is most likely to be due to reduced turbulence in the wake rather than a reduced trailing edge noise, as at $U_0 = 80\,m/s$, interaction noise dominates in the frequency range where this additional noise reduction occurs.

Finally, as discussed in the previous Section, Figure 7.22 suggests that the greatest noise reductions are obtained when the length scale Λ_{uu} is less than $1/3$ of the leading edge serration period λ, i.e., in the current experiment, when the distance d is small.

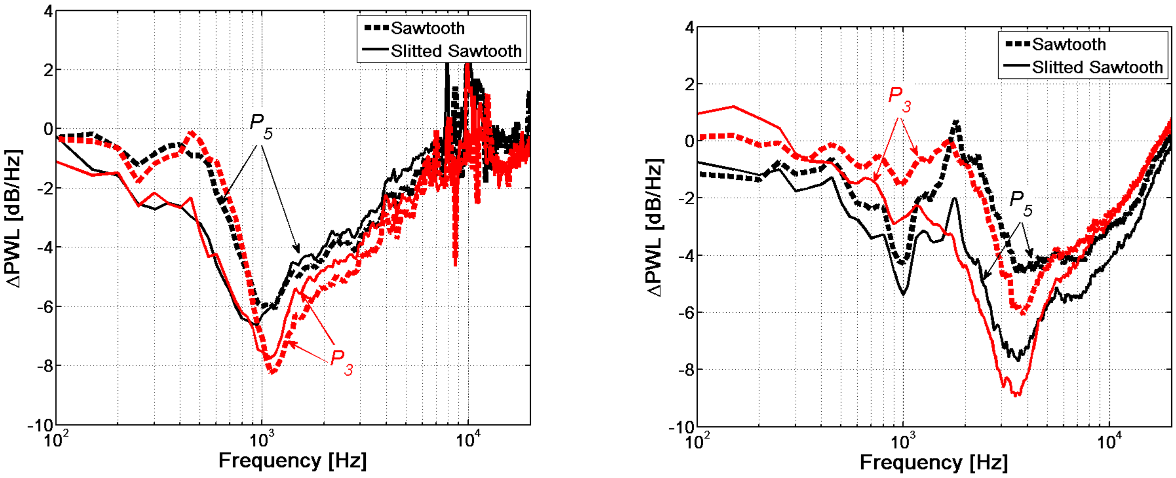

(a) At $U_0 = 20\,m/s$.

(b) At $U_0 = 80\,m/s$.

Figure 7.22: Overall sound power reduction $\Delta PWL_t(f)$, defined in Equation 7.10, with the downstream airfoil at positions P_3 and P_5.

7.5.1.4 Effect of the mean flow velocity U_0 on the overall noise reduction

This thesis now attempts to characterize the dependence of the noise reduction on the mean flow velocity. Using the blowup test technique, detailed in Chapter 2, the behaviour of the sound power level reduction ΔPWL_t, defined in Equation 7.10, is presented in Figure 7.23 against frequency and mean flow velocity. Note that the limits of $\pm 2\,\text{dB}$ on the plot are set manually for maximum contrast to emphasize the behaviour of the transition frequency between power reduction and power increase and do not refer to maximum and minimum changes in power.

As seen in Chapter 4 and in Figure 7.23, the jet background noise dominates the low frequency region, while the high frequencies are dominated by trailing edge noise, where the noise increases above a certain frequency based on the constant Strouhal number $St_\delta \sim 1$ (see Chapter 4). Figure 7.23 also shows that the noise reduction, due to slitted serrated trailing edge and serrated leading edges in the tandem test, appear to occur when $St < 1.2$, very close to the value of unity reported for isolated airfoils in Chapter 4. In the tandem configuration, this frequency bandwidth is dominated by interaction noise as mentioned above.

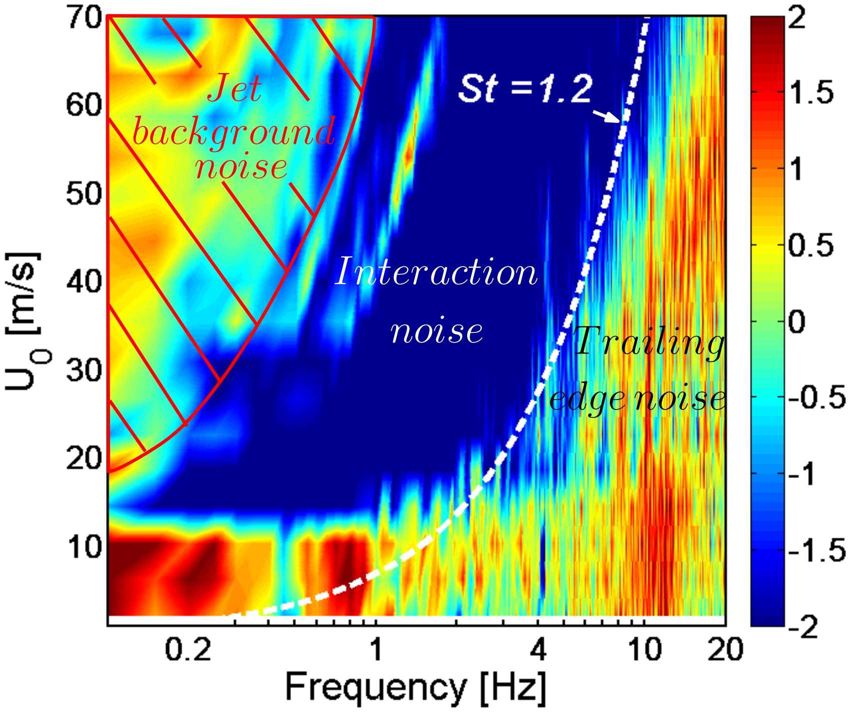

Figure 7.23: Typical sound power reduction$\Delta PWL_t(f)$, defined in Equation 7.10, obtained with upstream slitted sawtooth TE and downstream LE serrations, against frequency and mean flow velocity at P_3.

7.5.2 The effect on overall broadband noise of varying the axial separation distance d between the two airfoils

This Section investigates the variation of the measured turbulence velocity spectrum $\phi_{uu}(f)$ and sound power level spectrum $PWL(f)$, defined in Equation 2.2, for different values of axial separation distance d between the two airfoils shown in Table 7.1, where P_1 is at $d/c = 0.13$ and P_5 is at $d/c = 1.33$.

7.5.2.1 Effect of d on the turbulence velocity spectrum

Figure 7.24 shows the variation with d of the measured turbulence intensity and turbulence length scales in the wake estimated from space-time velocity correlation measurements, as described in Chapter 4. Results are shown for the baseline trailing edge, the sawtooth trailing edge and the slitted sawtooth trailing edge. Note that the hot wire measurements were performed along the tip of the serrations. It is shown in Chapter 4 that despite the strong spanwise non uniformity of the wake immediately behind a serrated airfoil, the rapid mixing of the turbulence implies that, for a given serration geometry, the velocity profiles along the span converge beyond about $x/c = 0.4$ in the wake behind the airfoil trailing edge. Figure 7.24a shows that all three trailing edges exhibit a similar trend in the decay of the streamwise turbulence intensity TI with increasing separation d.

The turbulence intensity at the wake centre-line varies little behind the sawtooth serrated trailing edge and the straight edge. However, larger differences of up to 8 % increase in the near wake and 5 % reduction further downstream occur behind the slitted serrated trailing edge.

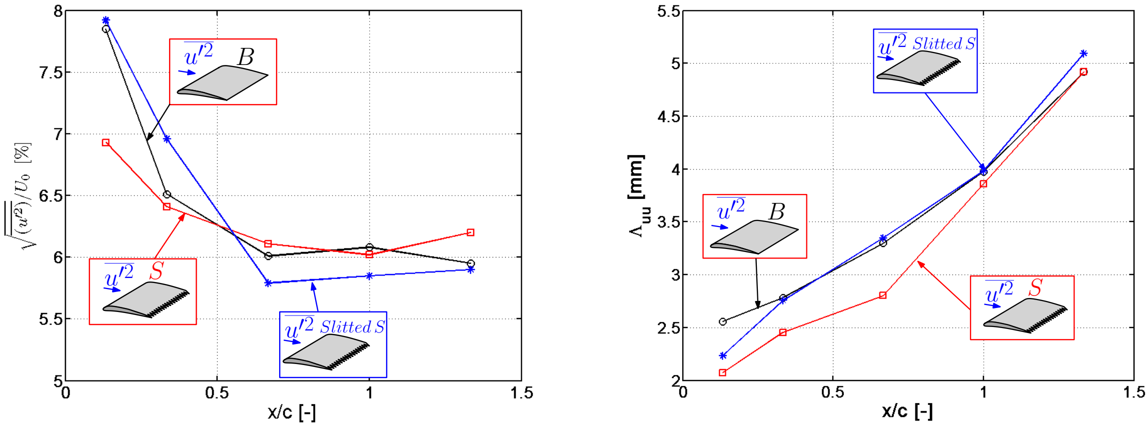

(a) Streamwise turbulence intensity $TI = \sqrt{\overline{u'^2}}/U_0$.

(b) Integral length scale Λ_{uu} estimated from velocity space-time correlation measurements (see Chapter 4).

Figure 7.24: Variation of the streamwise turbulence parameters in the wake with separation distance d, at $U_0 = 20\,m/s$.

Figure 7.24b shows the variation of turbulence length scales estimated from the procedure used in Chapter 4, versus downstream distance. The length scales in the wake behind the sawtooth serration is decreased by up to 20 % for distances of up to P_3 and converges with the length scales for the straight edge further downstream. The length scales on the wake centre-line behind the slitted sawtooth appear to follow closely the straight edge results. In Chapter 4, it was shown that the length scales tend to be decreased when the serration amplitude is small, i.e., $2h = 20\,mm$, and increased when the serration periodicity is decreased. In this tandem airfoil test, the sawtooth serration has a smaller amplitude $2h$ than the slitted sawtooth, and also a larger effective periodicity λ if the slits cut into the slitted serration geometry are accounted for. Therefore, the findings of Chapter 4 are consistent with that shown in Figure 7.24b.

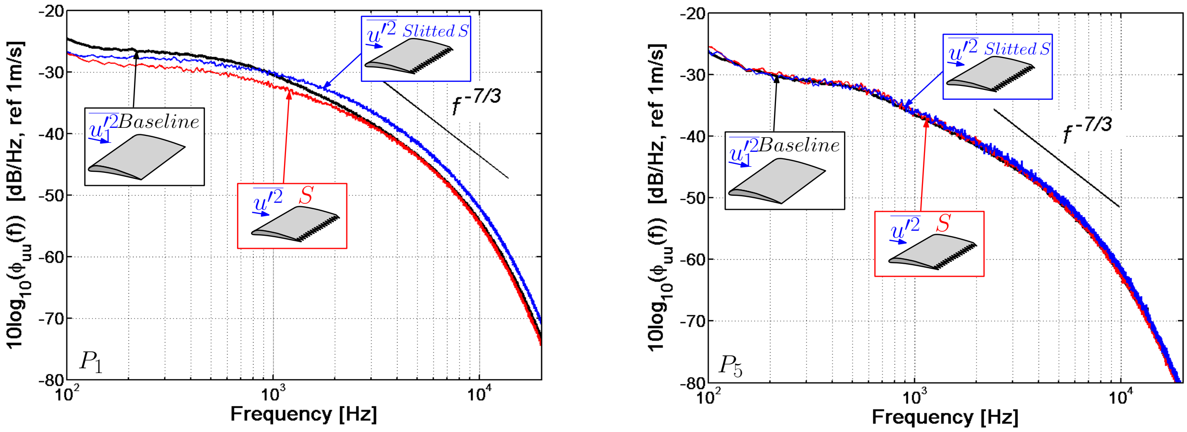

(a) At P_1.

(b) At P_5.

Figure 7.25: Turbulence spectra measured at $U_0 = 20\,m/s$, at the wake centre-line.

Figure 7.25 show a comparison of the streamwise turbulent spectra measured behind the tip of the serrations, in the wake of the baseline airfoil, the sawtooth serrated airfoil and the slitted sawtooth airfoil. Measurements were taken at the wake centre-line at $U_0 = 20\,m/s$ and at the two positions P_3 and P_5. It can be seen that at position P_3 the turbulence in the wake of the sawtooth trailing edge is reduced by 2 dB up to 1 kHz and by up to 1 dB for the slitted sawtooth trailing edge. At frequencies above 2 kHz the turbulence behind a sawtooth serration is identical to that behind the straight edge while it is increased by up to 2 dB behind the slitted sawtooth serration. At position P_5, the spectrum of the wake turbulence behind all three trailing edges is identical.

7.5.2.2 Comparison of the sound power and velocity spectra

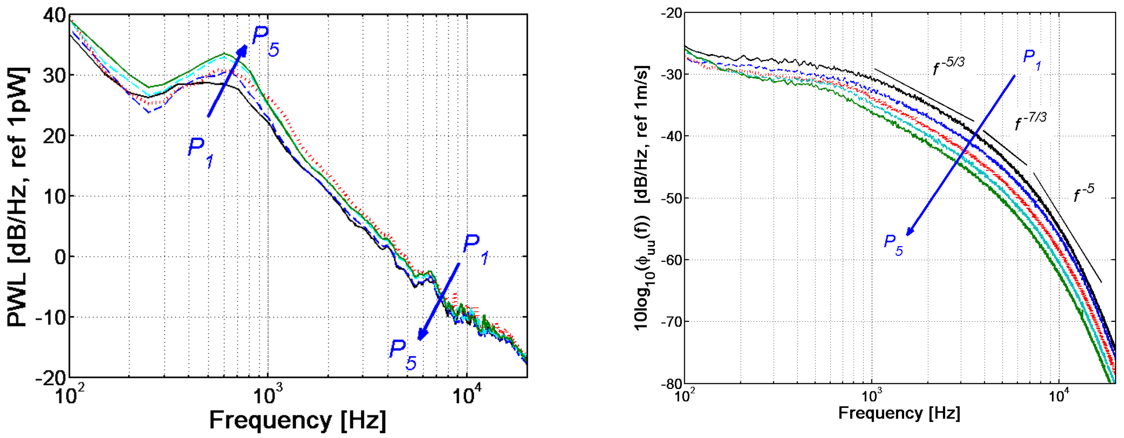

(a) Variation of sound power level $PWL(f)$.

(b) Variation of measured streamwise turbulent spectrum $\phi_{uu}(f)$.

Figure 7.26: Effect of separation distance d on the sound power level spectrum $PWL(f)$ and the velocity spectrum $\phi_{uu}(f)$, at $U_0 = 20\,m/s$

Figure 7.26a shows the variation of the sound power level spectrum $PWL(f)$ with increasing airfoil separation distance d for $U_0 = 20\,m/s$, while Figure 7.26b shows the corresponding variation of the measured turbulence velocity spectrum $\phi_{uu}(f)$ at the centre-line of the wake from the upstream baseline airfoil. As the separation distance d increases, the power level of the broad hump, centred on about 600 Hz increases by up to 5.5 dB, while the level of the high frequency power decreases by up to 1 dB. This behaviour increase cannot be observed in the velocity spectrum of Figure 7.26b. The power and velocity spectra behave differently at high frequencies due to the masking effect caused by the dominance of the self noise discussed in Section 7.3.5.

7.6 Summary

This Chapter describes an experimental campaign, which assesses the noise reduction obtained using simultaneously serrated trailing edges and serrated leading edges in a tandem airfoil configuration. Two types of serrated trailing edge treatments are applied to the upstream airfoil, i.e., a sawtooth serration and a slitted sawtooth serration, both selected for their noise performance measured on isolated airfoils (see Chapters 4 and 6), where broadband noise reductions of up to 5 dB were measured. The leading edge serrated airfoil was designed and manufactured by ONERA [35] and is shown to give broadband interaction noise reductions of up to 6 dB on isolated profiles and for a range of incoming turbulence characteristics.

In the tandem airfoil configuration, the following points were highlighted in this Chapter:

- The overall noise radiation is dominated by interaction noise over most of the frequency range. Trailing edge noise dominates the high frequency power spectrum at low mean flow velocity. The frequency at which they are roughly equal is $f\delta/U_0 \approx 1.4$.
- The overall noise reduction is dominated by the reductions in interaction noise, at all velocities and positions of the downstream airfoil P_1 to P_5.
- The reduction of the downstream airfoil response $R(f)$ due to leading edge serrations contributes most to the overall noise reduction.
- Additional reductions of the overall noise radiation of up 3.5 dB are provided by the use of the slitted sawtooth trailing edge rather than the sawtooth trailing edge on the upstream airfoil at the high flow velocity $U_0 = 80\,m/s$. This is shown to be most likely due to modifications of the wake parameters, i.e., notably a faster decay of the turbulence intensity behind the slitted sawtooth trailing edge.
- Both the length scales Λ_{uu} and the unsteady velocity $\overline{u'^2}$ in the wake are affected by the serrated edges in the near wake (up to $x/c \sim 0.4$). Further downstream, the values converge with the turbulence wake characteristics behind the straight edge.

Chapter 8

Conclusions and Future work

8.1 Conclusions

This thesis presents, for the first time, an extensive experimental study of the trailing edge noise reduction obtained using sawtooth serrations and discusses the mechanisms responsible for it. Measurements are compared to Howe's theory, which predicts the noise reduction from a sawtooth trailing edge [66]. In addition, novel trailing edge geometries were manufactured and tested to address the high frequency noise increase observed with sawtooth serrations. Finally, tandem airfoil noise reduction is also investigated by using trailing edge and leading edge serrations simultaneously on a pair of airfoils.

This work was supported by the 7^{th} Framework European Project FLOCON: Adaptive and passive FLOw CONtrol for fan broadband noise reduction.

8.1.1 Broadband noise reduction using sawtooth serrated TE and its mechanisms

The broadband trailing edge noise reductions obtained using thirty seven sawtooth serration geometries on a NACA65(12)-10 airfoil were reported at the four flow speeds of $U_0 = 20$, 40, 60 and $80\,m/s$ and a range of angles of attack (see Chapter 4). The noise data is compared to the straight trailing edge airfoil presented in Chapter 3.

Based on Howe's formulation, the geometrical parameters and the flow parameters that control the noise reduction were verified experimentally to be the non-dimensional frequency $f\delta/U_0$ and the sawtooth amplitude to boundary layer thickness ratio h/δ. It was found that noise reductions of up to 5 dB occur when $f\delta/U_0 < St_\delta$, where St_δ is close to unity, and when $h/\delta > 0.25$. Within these limits, the noise reduction was found to increase as the sawtooth becomes sharper, as predicted by Howe. It is shown experimentally in Chapter 5, that a large reduction of the scattering efficiency at the trailing edge is responsible for the noise reductions obtained using sawtooth serrations. Detailed measurements of the variation of the surface pressure over a single sawtooth showed evidence of a reduction in the phase speed by nearly 50 %, in the frequency range where noise reductions were measured. In addition, a reduction of up to 15 % in the coherence measured along the edge of the sawtooth was also measured in the frequency bandwidth where the noise is reduced in the far field.

However, the surface pressure was found to increase over a single sawtooth compared to a straight trailing edge. This increase in surface pressure was amplified as the tip was approached. This is speculated to be due to multiple back-scattering effects of the turbulence by the edges. This effect is shown in the data to be more pronounced at low frequencies, where the decay rate of the back-scattered waves is smaller, and also increases as the tip is approached due to the two sides coming closer together. However, the Kutta condition at the trailing edge suggests that a similar variation in the surface pressure should occur on the other side of the trailing edge, resulting in a small pressure difference over the sawtooth area compared to a straight edge and hence weaker radiation to the far field.

Flow measurements and smoke visualization tests have shown that, when the non-dimensional frequency $f\delta/U_0$ is greater than St_δ, the noise increases by up to 5 dB because of the presence of a cross-flow being forced through the valleys of the sawtooth. Flow velocity measurements showed that the frequency above which noise is increased, i.e. $f\delta/U_0 > St_\delta$ was also identified in the velocity spectrum in the valleys of the sawtooth. The noise increase is also found to be more pronounced as the angle of attack increases, which is because the intensity of the cross-flow is driven by the pressure difference at the trailing edge that is responsible for the radiation of trailing edge noise. For sufficiently small sawteeth amplitude compared to the boundary layer thickness, i.e., $h/\delta < 0.25$, it was found that the noise radiation is the same as a straight trailing edge, across the whole frequency range for all values of $f\delta/U_0$. This behaviour is not predicted by Howe's model.

Comparisons with Howe's analytical model for predicting the noise reduction from sawtooth trailing edges therefore shows that his assumption that the noise reductions result from a strong reduction of the scattering efficiency of turbulence by the edges is correct. However, Howe assumes that the turbulent eddies are perfectly frozen as convected past the oblique edges, which result in perfect destructive coherent interferences along the edges. Detailed measurements of the correlation function over one side of a single sawtooth show that this frozen assumption is incorrect for a sawtooth serration and results in Howe's theory over-predicting the measured noise reductions by at least 15 dB. Experimental data confirm that the eddy decay time is much smaller than the time for it to convect over the length of the sawtooth $2h/U_c$.

8.1.2 Aerodynamic considerations

Steady and unsteady aerodynamic data were also measured in the boundary layer and in the wake of some sawtooth trailing edges to assess the effects on lift, drag and turbulence in the boundary layer and in the wake. The aerodynamic data are compared to the straight trailing edge airfoil presented in Chapter 3.

While no significant influence of the serrated edges on the lift was measured, an increase of the drag of up to 10 % was reported, which gradually increased as the sawtooth periodicity λ was reduced.

The boundary layer thickness is shown to gradually increase, by up to 12 %, from the root to the tip of the sawtooth, relative to the straight edge. It is also shown that the peak of turbulence is 'pushed' away from the airfoil surface by the sawteeth. Locally, the turbulence close to the edge is therefore weaker than compared to a straight edge. This is believed to maybe partly contribute to the noise reduction, although the main contributions are thought to originate from the reduced scattering mentioned in the previous Section.

The turbulence in the wake, which is of concern for airfoil turbulence interaction noise, was also measured and a reduction of the streamwise turbulence intensity by up to 10 % was reported for the wider and shorter serrations. In addition, the turbulence integral length scale is shown to be reduced by 25 % for the shorter serrated edge of amplitude $2h = 20\,mm$ and periodicity $\lambda = 5\,mm$.

Finally, as the serration gets sharper, the drag, the turbulence intensity and the integral length scales were found to increase compared to the baseline, which is in contrast with the trends observed for the noise performance. In this thesis, a balance between noise and aerodynamics performance was found with the sawtooth $\lambda/h = 0.3$, where $\lambda = 3\,mm$ and $2h = 20\,mm$.

8.1.3 Novel TE geometries for TE noise reduction

Four novel trailing edge geometries were designed and tested for addressing the high frequency noise increase observed with conventional sawtooth serrations, namely slits, sawtooth with holes, slitted sawtooth and random trailing edges.

Slit trailing edges provide broadband noise reductions of up to 2 dB when the length of the slits is sufficiently large, typically $2h = 30\,mm$, and the width of the slit and the separation between adjacent slits are minimal, typically $0.5\,mm$. The presence of high frequency noise increase was also observed in this work (as with the sawtooth serrations in Chapter 4).

The sawtooth with holes provided a poor noise reduction of up to maximum 2 dB compared to the straight edge airfoil, and over a restricted frequency range relative to all the other trailing edge geometries tested. A high frequency noise increase of up to 12 dB was also reported, which is almost certainly due to turbulent flow through the holes.

The slitted serrations are shown to be a superior alternative geometry to sawtooth trailing edges, for reducing trailing edge noise. It is shown that the depth of the slits controls the noise reduction and that minimizing both the width of the slits, and the distance between adjacent slits per sawtooth increases the noise reductions. Significant broadband noise reductions of up to 5 dB were obtained compared to the baseline airfoil. Additional noise reductions of up to 1 dB at $U_0 = 40$ and $80\,m/s$ were obtained compared to the best trailing edge sawtooth of Chapter 4 ($\lambda/h = 0.3$). In addition, the high frequency noise excess was found to be less than 1 dB for all flow conditions. The major advantage of this trailing edge design is that the broadband noise reductions associated appear to be weakly dependent on the mean flow velocity U_0 and the airfoil angle of attack. This trailing edge geometry has been patented (patent no GB1121753.6).

The random trailing edges are shown to provide broadband noise reductions of up to 3 dB between 1 kHz and 10 Hz but with the significant advantage that it does not increase the noise at higher frequencies. The noise reduction obtained with the random trailing edges also appears to be weakly dependent on the airfoil angle of attack.

8.1.4 Tandem airfoil TE and LE noise reduction

Finally, the noise reduction obtained using simultaneously serrated trailing edges and serrated leading edges in a tandem airfoil configuration is reported in this thesis. Two types of serrated trailing edge treatments are applied to the upstream airfoil, i.e., a sawtooth serration and a slitted sawtooth serration. The leading edge serrated airfoil was designed and manufactured by ONERA [35]. Broadband noise reductions of between 5 dB and 8.5 dB are reported.

In addition, it is shown over most of the frequency range that overall noise radiation is dominated by interaction noise, while trailing edge noise dominates the high frequency power spectrum at low mean flow velocity. Therefore, the overall noise reduction is dominated by the reductions in interaction noise, and particularly by the reduction of the downstream airfoil response $R(f)$ due to leading edge serrations. However, additional reductions of the overall noise radiation of up 3.5 dB are provided by the use of the slitted sawtooth trailing edge rather than the sawtooth trailing edge on the upstream airfoil at the high flow velocity $U_0 = 80\,m/s$. This is shown to be most likely due to modifications of the wake parameters, i.e., notably a faster decay of the turbulence intensity behind the slitted sawtooth trailing edge.

8.2 Future work

The recommendations for future work are listed below:

1. Detailed measurements of the modifications of the lift and drag due to the trailing edge geometries used in this thesis using a force balance.
2. Detailed simultaneous measurements of the unsteady surface pressure on both sides of a single sawtooth would be useful to investigate the validity of the Kutta condition at the trailing edge in the presence of serrations to establish definitively the noise reduction mechanism at low frequencies.

3. Design and test a slitted sawtooth trailing edge with a sharper reference sawtooth geometry, such as for example $\lambda/h = 0.3$ and reduce the width of the slits, ideally $d_1 = d_2 < 0.1\,mm$.
4. Investigate the effect of the trailing edge porosity on the noise reduction by manufacturing a sawtooth trailing edge using porous materials.
5. Reproduce the tandem airfoil experiment on a rotating fan rig by modifying the trailing edge of the fan blades and the leading edge of the outlet guide vanes.

Bibliography

[1] Flocon - adaptative and passive flow control for fan broadband noise reduction - description of work.

[2] http://en.wikipedia.org/wiki/biomimetics.

[3] http://www.wind-energy-the-facts.org/en/scenarios-and-targets/chapter-6-the-global-wind-energy-outlook-scenarios/ (last accessed in 02/2012).

[4] M. Abramowitz and I.A. Stegun. *Handbook of mathematical functions with formulas, graphs, and mathematical tables*, volume 55. Dover publications, 1964.

[5] JL Adamczyk. The passage of an infinite swept airfoil through an oblique gust. Technical report, NASA, 1974.

[6] RK Amiet. Acoustic radiation from an airfoil in a turbulent stream. *Journal of Sound and Vibration*, 41(4):407–420, 1975.

[7] RK Amiet. Noise due to turbulent flow past a trailing edge. *Journal of Sound and Vibration*, 47(3):387–393, 1976.

[8] RK Amiet. Effect of the incident surface pressure field on noise due to turbulent flow past a trailing edge. *Journal of Sound and Vibration*, 57:305, 1978.

[9] RK Amiet. Refraction of Sound by a Shear Layer. *Journal of Sound and Vibration*, 58:467, 1978.

[10] T. Bachmann, S. Klän, W. Baumgartner, M. Klaas, W. Schröder, H. Wagner, et al. Morphometric characterisation of wing feathers of the barn owl tyto alba pratincola and the pigeon columba livia. *Frontiers in zoology*, 4(1):23, 2007.

[11] S. Bereketab, H. Wang, P. Mish, and WJ Devenport. The surface pressure response of a naca 0015 airfoil immersed in grid turbulence. volume 1: Characteristics of the turbulence. Technical report, NASA, 2000.

[12] J.J. Bertin and M.L. Smith. *Aerodynamics for engineers.* Inc, 1998.

[13] V. Blandeau. *Aerodynamic Broadband Noise from Contra-Rotating Open Rotors.* PhD thesis, ISVR, 2011.

[14] V.P. Blandeau, P.F. Joseph, G. Jenkins, and C.J. Powles. Comparison of sound power radiation from isolated airfoils and cascades in a turbulent flow. *The Journal of the Acoustical Society of America*, 129:3521, 2011.

[15] A. Borgoltz. *Modifications of Coherent Structures in Fan Blade Wakes for Broadband Noise Reduction*. PhD thesis, Virginia Polytechnic Institute and State University, 2007.

[16] J. Boudet, N. Grosjean, and M.C. Jacob. Wake-airfoil interaction as broadband noise source: a large-eddy simulation study. *International Journal of Aeroacoustics*, 4(1):93–116, 2005.

[17] KA Braun, N. van der Borg, AGM Dassen, F. Doorenspleet, A. Gordner, J. Ocker, and R. Parchen. Serrated trailing edge noise (steno). In *EWEC-CONFERENCE*, pages 180–183, 1999.

[18] TF Brooks and TH Hodgson. Trailing edge noise prediction from measured surface pressures. *Journal of Sound Vibration*, 78:69–117, 1981.

[19] T.F. Brooks, D.S. Pope, and M.A. Marcolini. Airfoil self-noise and prediction. *NASA reference publication*, 1218:l, 1989.

[20] MK Bull. Wall-pressure fluctuations beneath turbulent boundary layers: some reflections on forty years of research. *Journal of Sound and Vibration*, 190(3):299–315, 1996.

[21] D. Casalino, F. Diozzi, R. Sannino, and A. Paonessa. Aircraft noise reduction technologies: A bibliographic review. *Aerospace Science and Technology*, 12(1):1–17, 2008.

[22] J. Casper and F. Farassat. Broadband trailing edge noise predictions in the time domain. *Journal of Sound and Vibration*, 271(1-2):159–176, 2004.

[23] T. Castelain, J.C. Béra, and M. Sunyach. Noise reduction of a mach 0.7–0.9 jet by impinging microjets. *Comptes Rendus Mecanique*, 334(2):98–104, 2006.

[24] D.M. Chase. Noise radiated from an edge in turbulent flow. *AIAA Journal*, 13:1041–1047, 1975.

[25] D.M. Chase. Modeling the wavevector-frequency spectrum of turbulent boundary layer wall pressure. *Journal of Sound and Vibration*, 70(1):29–67, 1980.

[26] DM Chase. The character of the turbulent wall pressure spectrum at subconvective wavenumbers and a suggested comprehensive model. *Journal of Sound and Vibration*, 112(1):125–147, 1987.

[27] T.P. Chong, P. Joseph, and M. Gruber. An experimental study of airfoil instability noise with trailing edge serrations. In *Proceedings of the 16th AIAA/CEAS Aeroacoustics Conference, Stockholm, Sweden*, 2010.

[28] TP Chong, PF Joseph, and P. Davies. A Parametric Study of Passive Flow Control for a Short, High Area Ratio 90 deg Curved Diffuser. *Journal of Fluids Engineering*, 130:111104, 2008.

[29] TP Chong, PF Joseph, and P. Davies. Design and performance of an open jet wind tunnel for aero-acoustic measurement. *Applied Acoustics*, 70(4):605–614, 2009.

[30] TP Chong, PF Joseph, and M. Gruber. On the noise and wake flow of an airfoil with broken and serrated trailing edges. In *Proceedings of the 17th AIAA/CEAS Aeroacoustics Conference, Portland, Oregon*, 2011.

[31] GM Corcos. The structure of the turbulent pressure field in boundary layer flows. *Journal of Fluid Mechanics*, 18(3):353–378, 1964.

[32] DG Crighton and FG Leppington. On the scattering of aerodynamic noise. *Journal of Fluid Mechanics*, 46(03):577–597, 1971.

[33] DG Crighton and FG Leppington. Scattering of aerodynamic noise by a semi-infinite compliant plate. *Journal of Fluid Mechanics Digital Archive*, 43(04):721–736, 2006.

[34] N. Curle. The influence of solid boundaries upon aerodynamic sound. *Proceedings of the Royal Society of London. Series A. Mathematical and Physical Sciences*, 231(1187):505–514, 1955.

[35] Vincent Clair Thomas Le Garrec Guillaume Dufour Hugues Deniau Cyril Polacsek, Gabriel Reboul. Turbulence-airfoil interaction noise reduction using wavy leading edge: an experimental and numerical study. In *18th ICSV conference*, 2011.

[36] AGM Dassen, R. Parchen, J. Bruggeman, and F. Hagg. Results of a wind tunnel study on the reduction of airfoil self-noise by the application of serrated blade trailing edges . In *Proc. of the European Union Wind Energy Conference and Exhibition, Göteborg*, pages 800–803, 1996.

[37] W.J. Devenport, J.K. Staubs, and S.A.L. Glegg. Sound radiation from real airfoils in turbulence. *Journal of Sound and Vibration*, 329(17):3470–3483, 2010.

[38] M. Drela. XFOIL - An analysis and design system for low Reynolds number airfoils, 1989.

[39] A.C. Faszer, T.P. Hynes, C. Blaabjerg, and H. Shin. Acoustic beamforming and holography measurements of modified boundary layer trailing-edge noise. In *12th AIAA/CEAS Aeroacoustics Conference*. American Institute of Aeronautics and Astronautics, 2006.

[40] G.C. Fernandes, M. Weinmann, and R.D. Sandberg. Applicability of rans models for accurate computation of flow over airfoils with serrated trailing edges. In *ECCOMAS CFD 2010*, 2000.

[41] A. Finez, E. Jondeau, M. Roger, and M.C. Jacob. Broadband noise reduction with trailing edge brushes. In *16th AIAA/CEAS Aeroacoustics Conference*, 2010.

[42] Roger M. Jondeau E. Finez A., Jacob M. Broadband noise reduction of a linear cascade with trailing edge serrations. In *17th AIAA/CEAS Aeroacoustics Conference*, 2011.

[43] MR Fink and DA Bailey. Airframe noise reduction studies and clean-airframe noise investigation. Technical report, NASA, 1980.

[44] Lionel Gamet and Thibault Turpin. Noise prediction for no-treatment baseline configuration parametrized naca65-1210 airfoil. Technical report, FP7 FLOCON, WP2 - Task 2.4, D2.2, FLUOREM, 2009.

[45] Turpin T. Gamet L. Parametrized aeroacoustics optimization applied to a naca65-1210 airfoil. noise prediction for baseline configuration, onera wavy le and isvr serrated te. Technical report, FLOCON - FLUOREM, D2.10, 2011.

[46] A. Garcia Sagrado, T. Hynes, and H. Hodson. Experimental investigation into trailing edge noise sources. In *12th AIAA/CEAS Aeroacoustics Conference*, 2006.

[47] D.H. Geiger. Comparative Analysis of Serrated Trailing Edge Designs on Idealized Aircraft Engine Fan Blades for Noise Reduction. Master's thesis, Virginia Tech, 2004.

[48] T. Geyer, E. Sarradj, and C. Fritzsche. Measurement of the noise generation at the trailing edge of porous airfoils. *Experiments in fluids*, 48(2):291–308, 2010.

[49] T. Geyer, E. Sarradj, and C. Fritzsche. Porous airfoils: noise reduction and boundary layer effects. *International Journal of Aeroacoustics*, 9(6):787–820, 2010.

[50] T. Geyer, E. Sarradj, and C. Fritzsche. Porous airfoils: noise reduction and boundary layer effects. *Noise Notes*, 10(2):11–38, 2011.

[51] S.A.L. Glegg and C. Jochault. Broadband self-noise from a ducted fan. *AIAA journal*, 36(8):1387–1395, 1998.

[52] M. Goody. Empirical spectral model of surface pressure fluctuations. *AIAA journal*, 42(9):1788–1794, 2004.

[53] RR Graham. The silent flight of owls. *J Roy Aero Soc*, 38:837–843, 1934.

[54] M. Gruber, M. Azarpeyvand, and P. Joseph. Airfoil trailing edge noise reduction by the introduction of sawtooth and slitted trailing edge geometries. In *20th ICA conference*, 2010.

[55] M. Gruber, P. Joseph, and TP. Chong. Experimental investigation of airfoil self noise and turbulent wake reduction by the use of trailing edge serrations. In *16th AIAA/CEAS Aeroacoustics Conference*, 2010.

[56] M. Gruber, P. Joseph, and TP. Chong. On the mechanisms of serrated airfoil trailing edge noise reduction. In *17th AIAA/CEAS Aeroacoustics Conference*, 2011.

[57] M. Herr. Experimental study on noise reduction through trailing edge brushes. *New Results in Numerical and Experimental Fluid Mechanics V*, -:365–372, 2006.

[58] M. Herr. Design criteria for low-noise trailing-edges. In *13 th AIAA/CEAS Aeroacoustics Conference(28 th AIAA Aeroacoustics Conference)*, volume 3470, pages 21–23, 2007.

[59] M. Herr. A noise reduction study on flow-permeable trailing-edges. In *Conference Proceedings of the Eighth ONERA-DLR Aerospace Symposium (ODAS)*, volume 17, page 19, 2007.

[60] M. Herr and W. Dobrzynski. Experimental investigations in low-noise trailing-edge design. *AIAA journal*, 43(6):1167–1175, 2005.

[61] J. Hinze. Turbulence, 1972.

[62] MS Howe. A review of the theory of trailing edge noise. *Journal of Sound and Vibration*, 61(3):437–465, 1978.

[63] MS Howe. On the added mass of a perforated shell, with application to the generation of aerodynamic sound by a perforated trailing edge. *Proceedings of the Royal Society of London. A. Mathematical and Physical Sciences*, 365(1721):209–233, 1979.

[64] MS Howe. The influence of surface rounding on trailing edge noise. *J. Sound and Vib*, 126:5, 1988.

[65] MS Howe. Aerodynamic noise of a serrated trailing edge. *Journal of Fluids and Structures*, 5(1):33–45, 1991.

[66] MS Howe. Noise produced by a sawtooth trailing edge. *The Journal of the Acoustical Society of America*, 90:482, 1991.

[67] MS Howe. *Acoustics of fluid-structure interactions*. Cambridge Univ Pr, 1998.

[68] MS Howe. Trailing edge noise at low Mach numbers. *Journal of Sound and Vibration*, 225(2):211–238, 1999.

[69] F.V. Hutcheson, T.F. Brooks, C.L. Burley, and D.J. Stead. Measurement of the noise resulting from the interaction of turbulence with a lifting surface. In *AIAA Conference*, number June, pages 05–08, 2011.

[70] M.C. Jacob, J. Boudet, D. Casalino, and M. Michard. A rod-airfoil experiment as a benchmark for broadband noise modeling. *Theoretical and Computational Fluid Dynamics*, 19(3):171–196, 2005.

[71] Lloyd E. Jones and Richard D. Sandberg. Numerical investigation of airfoil self-noise reduction by addition of trailing-edge serrations. In *16th AIAA/CEAS Aeroacoustics Conference*, 2010.

[72] F.E. Jorgensen. How to measure turbulence with hot-wire anemometers–a practical guide. Technical report, DANTEC Dynamics, 2002.

[73] V. Jurdic, P. Joseph, and J. Antoni. Investigation of Rotor Wake Turbulence Through Cyclostationary Spectral Analysis. *AIAA journal*, 47(9):2022–2030, 2009.

[74] S. Klan, T. Bachmann, M. Klaas, H. Wagner, and W. Schroder. Experimental analysis of the flow field over a novel owl based airfoil. *Animal Locomation*, -:413, 2010.

[75] R.A. Kroeger. Low speed aerodynamics for ultra-quiet flight. Technical report, DTIC Document, 1972.

[76] T.A. Leitch, CA Saunders, and WF Ng. Reduction of unsteady stator-rotor interaction using trailing edge blowing. *Journal of sound and vibration*, 235(2):235–245, 2000.

[77] M.J. Lighthill. On sound generated aerodynamically. i. general theory. *Proceedings of the Royal Society of London. Series A. Mathematical and Physical Sciences*, 211(1107):564, 1952.

[78] M.J. Lighthill. On sound generated aerodynamically. ii. turbulence as a source of sound. *Proceedings of the Royal Society of London. Series A. Mathematical and Physical Sciences*, 222(1148):1, 1954.

[79] G.M. Lilley. A study of the silent flight of the owl. In *19th AIAA/CEAS Aeroacoustics Conference*, volume 2186, 2004.

[80] P.F. Mish. *Mean Loading and Turbulence Scale Effects on the Surface Pressure Fluctuations Occurring on a NACA 0015 Airfoil Immersed in Grid Generated Turbulence.* PhD thesis, Virginia Polytechnic Institute and State University, 2001.

[81] P.F. Mish. *An experimental investigation of unsteady surface pressure on single and multiple airfoils.* PhD thesis, Virginia Polytechnic Institute and State University, 2003.

[82] D.J. Moreau, L.A. Brooks, and C.J. Doolan. Flat plate self-noise reduction at low-to-moderate reynolds number with trailing edge serrations. In *Proceedings of ACOUSTICS 2011, Gold Coast, Australia*, 2011.

[83] S. Moreau, D. Neal, and J. Foss. Hot-wire measurements around a controlled diffusion airfoil in an open-jet anechoic wind tunnel. *Journal of fluids engineering*, 128:699, 2006.

[84] S. Moreau and M. Roger. Back-scattering correction and further extensions of Amiet's trailing-edge noise model. Part II: Application. *Journal of Sound and Vibration*, 323(1-2):397–425, 2009.

[85] S. Moreau, M. Roger, and V. Jurdic. Effect of angle of attack and airfoil shape on turbulence-interaction noise. In *11 th AIAA/CEAS Aeroacoustics Conference(26 th Aeroacoustics Conference); Monterey, CA*. American Institute of Aeronautics and Astronautics, 1801 Alexander Bell Drive, Suite 500, Reston, VA, 20191-4344, USA,, 2005.

[86] S. Moreau and R. Roger. Effect of airfoil aerodynamic loading on trailing edge noise. In *9th AIAA/CEAS Aeroacoustics Conference*, volume 3177, 2003.

[87] S. Moreau, C. Schram, and M. Roger. Diffraction Effects on the Trailing Edge Noise Measured in an Open-jet Anechoic Wind Tunnel. In *13 th AIAA/CEAS Aeroacoustics Conference(28 th AIAA Aeroacoustics Conference)*. American Institute of Aeronautics and Astronautics, 1801 Alexander Bell Drive, Suite 500, Reston, VA, 20191-4344, USA,, 2007.

[88] S. Oerlemans, M. Fisher, T. Maeder, and K. Kögler. Reduction of wind turbine noise using optimized airfoils and trailing-edge serrations. *AIAA journal*, 47:1470–1481, 2009.

[89] S. Oerlemans and P. Migliore. Aeroacoustic wind tunnel tests of wind turbine airfoils. *AIAA Journal*, 3042:–, 2004.

[90] S. Oerlemans, JG Schepers, G. Guidati, and S. Wagner. Experimental demonstration of wind turbine noise reduction through optimized airfoil shape and trailing-edge serrations. In *Proceedings of the European Wind Energy Conference, Copenhagen, Denmark*. NATIONAL AEROSPACE LABORATORY, 2001.

[91] J. Ortmann and J. Wild. Effect of acoustic slat modifications on aerodynamic properties of high-lift systems. *AIAA Paper*, 3842:2006, 2006.

[92] R. Parchen, W. Hoffmans, A. Gordner, and K. Braun. Reduction of airfoil self-noise at low Mach number with a serrated trailing edge. In *International Congress on Sound and Vibration, 6 th, Technical Univ. of Denmark, Lyngby, Denmark*, pages 3433–3440, 1999.

[93] R.W. Paterson. Acoustic radiation and surface pressure characteristics of an airfoil due to incident turbulence. Technical report, NASA, 1976.

[94] S. Perennes and M. Roger. Aerodynamic noise of a two-dimensional wing with high-lift devices. In *Fourth AIAA/CEAS Aeroacoustics Conference*, 1998.

[95] A. Powell. On the aerodynamic noise of a rigid flat plate moving at zero incidence. *The Journal of the Acoustical Society of America*, 31:1649, 1959.

[96] C. Relun. Design and development of a phased microphone array for spatial location of aeroacoustic sources. Technical report, Student project - ISVR / UTC, 2009.

[97] M. Roger and S. Moreau. Broadband self-noise from loaded fan blades. *AIAA journal*, 42(3):536–544, 2004.

[98] M. Roger and S. Moreau. Back-scattering correction and further extensions of Amiet's trailing-edge noise model. Part 1: theory. *Journal of Sound and Vibration*, 286(3):477–506, 2005.

[99] M. Roger and S. Moreau. Extensions and limitations of analytical airfoil broadband noise models. *International Journal of Aeroacoustics*, 9(3):273–306, 2010.

[100] Y. Rozenberg. *Modélisation analytique du bruit aérodynamique à large bande des machines tournantes : utilisation de calculs moyennés de mécanique des fluides*. PhD thesis, LMFA, Ecole Centrale de Lyon, 2007.

[101] Y. Rozenberg, M. Roger, and S. Moreau. Effect of blade design at equal loading on broadband noise. In *12th AIAA/CEAS Aeroacoustics Conference*, 2006.

[102] Y. Rozenberg, M. Roger, and S. Moreau. Rotating blade trailing-edge noise: Experimental validation of analytical model. *AIAA journal*, 48(5):951–962, 2010.

[103] A.G. Sagrado. *Boundary layer and trailing edge noise sources.* PhD thesis, Whittle Laboratory, University of Cambridge, 2007.

[104] A.G. Sagrado, T. Hynes, and H. Hodson. Experimental investigation into trailing edge noise sources. In *12 th AIAA/CEAS Aeroacoustics Conference(27 th AIAA Aeroacoustics Conference); Cambridge, MA*. American Institute of Aeronautics and Astronautics, 1801 Alexander Bell Drive, Suite 500, Reston, VA, 20191-4344, USA,, 2006.

[105] RD Sandberg, ND Sandham, and PF Joseph. Direct numerical simulations of trailing-edge noise generated by boundary-layer instabilities. *Journal of sound and vibration*, 304(3-5):677–690, 2007.

[106] E. Sarradj and T. Geyer. Noise generation by porous airfoils. In *AIAA paper, 13th AIAA/CEAS Aeroacoustics Conference*, 2007.

[107] JG Schepers, A. Curvers, S. Oerlemans, K. Braun, T. Lutz, A. Herrig, W. Wuerz, B.M. López, A. Matesanz, R. Ahrelt, et al. Sirocco: Silent rotors by acoustic optimisation. Technical report, ECN, 2005.

[108] RH Schlinker and RK Amiet. Helicopter rotor trailing edge noise. In *American Institute of Aeronautics and Astronautics, Aeroacoustics Conference, 7th, Palo Alto, CA, Oct. 5-7, 1981, 26 p.*, 1981.

[109] WR Sears. Some aspects of non-stationary airfoil theory and its applications. *J. Aeronaut. Sci*, 8:104–108, 1941.

[110] B.A. Singer, K.S. Brentner, D.P. Lockard, and G.M. Lilley. Simulation of acoustic scattering from a trailing edge. *AIAA paper*, 231:1999, 1999.

[111] P.T. Soderman. Aerodynamic effects of leading-edge serrations on a two- dimensional airfoil. Technical report, NASA, 1972.

[112] P.T. Soderman. Leading-edge serrations which reduce the noise of low-speed rotors. Technical report, NASA, 1973.

[113] Arina R. Torzo D. Acoustic prediction of selected treatment from configuration 1. Technical report, FLOCON - AVIO, D2.5, 2012.

[114] Various. Aeroacoustics of flight vehicles - volume 1: Noise sources. Technical report, NASA, 1991.

[115] Various. Aeroacoustics of flight vehicles - volume 2: Noise control. Technical report, NASA, 1991.

[116] Various. Aeronautics and air transport: Beyond vision 2020 (towards 2050). Technical report, ACARE, June 2010.

[117] J.E.F. Williams and LH Hall. Aerodynamic sound generation by turbulent flow in the vicinity of a scattering half plane. *Journal of Fluid Mechanics*, 40(04):657–670, 1970.

[118] WW Willmarth and FW Roos. Resolution and structure of the wall pressure field beneath a turbulent boundary layer. *J. Fluid Mech*, 22(1):81–94, 1965.

[119] J. Winkler, T. Carolus, and Moreau S. E?ect of trailing edge blowing geometry on broadband noise sources. In *17th AIAA/CEAS Aeroacoustics Conference*, 2011.

[120] J. Winkler, T. Carolus, J. Scheuerlein, and F. Dinkelacker. Trailing-edge blowing on tandem airfoils: Aerodynamic and aeroacoustic implications. In *16th AIAA/CEAS Aeroacoustics Conference*, 2010.

[121] J. Winkler and Moreau S. Les of the trailing-edge ?ow and noise of a naca6512-63 airfoil at zero angle of attack. In *Center for Turbulence Research Proceedings of the Summer Program*, 2008.

[122] Q. Zhou and Joseph P. A frequency domain numerical method for airfoil broadband self-noise prediction. *Journal of Sound and Vibration*, 299:504–519, 2007.